PROSPECTIVITY STUDY OF MINERAL AND GEOTHERMAL ENERGY RESOURCESINPARTS OF SOUTHEASTERN NIGERIAN SEDIMENTARY BASIN

BY

NAME: OKIYI, IJEOMA MILLICENT ***(B.Sc. ACU; M.Sc. OAU)***

REG. NO: 20154988798

A DISSERTATION SUBMITTED TO THE POSTGRADUATE SCHOOL, FEDERAL UNIVERSITY OF TECHNOLOGY, OWERRI.

IN PARTIAL FULFILMENT OF THE REQUIREMENTS FOR THE AWARD OF THE DEGREE OF DOCTOR OF PHILOSOPHY, IN GEOPHYSICS

SEPTEMBER, 2021

CERTIFICATION

This is to certify that this work, "Prospectivity Study of Mineral and Geothermal Energy Resources in Parts of Southeastern Nigerian Sedimentary Basin" was carried out by I, Okiyi, Ijeoma Millicent (20154988798) in partial fulfilment for the award of the degree of Doctor of Philosophy (Ph.D.) in Geophysics in the Department of Geology, School of Physical Sciences, Federal University of Technology, Owerri (FUTO), Nigeria.

.....
Dr. S.I. Ibeneme
Principal Supervisor

30/09/21
.....
Date

.....
Dr. E.Y. Obioha
Co-Supervisor

30/09/2021
.....
Date

.....
Prof. S.O. Onyekuru
Co-Supervisor

30/09/21
.....
Date

.....
Dr. A.I. Opara
Head, Department of Geology

30/09/21
.....
Date

.....
Prof. C.C.Z. Akaolisa
Dean, School of Physical Science

8/12/21
.....
Date

.....
Prof. C.C. Eze
Dean, Postgraduate School

.....
Date

.....
Prof. E.E. Udensi
External Supervisor

.....
Date

DEDICATION

My utmost dedication of this work goes to God on high, whose blessings and good decrees upon me have substantially helped me in triumphing over vicissitudes of life and academic challenges.

ACKNOWLEDGEMENTS

My indebt appreciation goes to my supervisors; Dr. S.I. Ibeneme, Rev. Dr. Y. E. Obioha and Prof. S.O. Onyekuruand my ex-supervisor, Prof. Selemo, A.I. The tutelage I got from you all remains quite unequivocal and my heart-felt gratitude goes out to all of you as I sincerely appreciate your inputs which ensured the success attained in this research work. I appreciate the efforts of all lecturers in Geology Department who went a long way in imparting me positively, I must say you were building blocks for me who have continuously strived and ensured greater attainments in this field of study. Seemingly, you all are and so far have appeared, great geoscience clairvoyants for reverence in the lives of budding geoscientists. I thank the various Heads of Department who in their various tenures, built academic excellence to its zenith, I must really say that I gained from your unquantifiable respective reigns in the Department. In heaviness of heart, I still mourn the demise of Prof. C.A. Ahiarakwem, who in his short tenure as the Head of Department and in his stay in the department, imparted good morals in students. I appreciate this virtue of yours I had the privilege of being a beneficiary too. May you be embraced in the bosom of our Lord and may you all live long, Amen and Amen.

My profound gratitude goes to my parents and siblings who were mainly the pillars of support to me, this kindness and encouragement of theirs, have contributed in seeing me thus far in the programme. I acknowledge the care and support given to me by my husband, Chris, in the course of this research work, may God bless you abundantly. My departmental colleagues have never ceased to be very supportive as well. God bless you all, God bless Geology Department, Federal University of Technology, Owerri and God bless Nigeria.

TABLE OF CONTENTS

LIST OF FIGURES

LIST OF PLATES

LIST OF TABLES

TABLES **PAGE NUMBER**

LIST OF APPENDICES

ABSTRACT

There has been an open search for clean/renewable energy and mineral resources for economic growth using airborne geophysical surveys. High resolution airborne magnetic and radiometric data, five scenes of Landsat 8 remote sensing, SP and VES Schlumberger data of parts of Southeastern Nigerian sedimentary basin were analysed and interpreted with a view to delineate regimented mineral colonies and anomalous zones of geothermal gradient. Reduction to Equator and Vertical Derivative filters were applied to the airborne magnetic data to centre anomaly peaks over causative bodies, define shapes and edges of magnetic sources and map magnetic lineaments. Fast Line-in-sight Atmospheric Analysis for Spectral Hypercube (FLAASH) and subsequent post FLAASH band maths were applied to the remote sensing data to generate the surface reflectance data from which ratio composite and lineament maps were generated. Results showed dominant NE-SW and E-W lineament trends from Landsat and Magnetic data with subordinate NW-SE trend. 50% overlapping data windows selected for spectral analysis were used to delineate anomalous geothermal gradients. The vertical, horizontal and NTilt derivative maps were used to reveal boundaries of mafic intrusives and inclusions which are most likely controlled by the trends of deep-seated magnetic lineaments. The derivative maps were also used to enhance edges of shallow structures. Alteration zones, lithologic/geologic boundaries were revealed by radioelement ratio, ternary and total count maps and Landsat ratio map composites 4/2, 6/5 and 6/7 and PCA plots. The Source Parameter Imaging, 3D Euler Deconvolution and Magnetic Vector Inversion modelling depth estimate filters established depths to, and geometry of, subsurface magnetic structures. Results revealed shallow to deep-seated structures in the depth range of 80 m asl to >7 km bsl which must have aided development of veins and hosted lodes of intrusives and ore bodies. Shallow Curie Point Depth (< 10km), geothermal gradient > 42°C/km and heat flow > 88mW/m^2 from spectral analysis procedure have been earmarked for good geothermal reservoirs. VES geoelectric sections and 2D imaging results beneath two zones of anomalous geothermal gradient between 35 to 45 (°C/km), proposed approximate models of geothermal resources as Hot Dry Rock (HDR) for Alok and geo-pressured model for Amagunze. Cylindrical/lenticular sills, inclined dykes, sparse nodules and spheres were identified from probed windows of the RTE-TMI map as surface to deep-seated models. Ground-truthing these findings, field image and double dipole results indicated mineralization of the study area as true, hence, making it a viable mineral and geothermal prospect environment.

Keywords: Airborne, Magnetics, Radiometrics, Landsat, Geothermal, Lineaments, Mineralization,

CHAPTER ONE

1. INTRODUCTION

There has been a quest to search for clean/renewable energy (geothermal energy) and mineral resources for economic growth in the recent 21st century through airborne geophysical surveys which rely on variation of physical and geochemical properties of targets on the Earth's surface via distribution of magnetic minerals, density, electrical conductivity and radioactive element concentrations and contrasts of other forms of deposits (Tesfaye, 2004). This search quest is to oust the desirous energy towards the liquid black gold (crude oil) exploration and transform the duo for man's benefit. Having considered the entrepreneurial aspect of geophysical exploration for mineral and geothermal energy resources for economic growth, the sustainability of these resources in Southeastern part of the Lower Benue Trough in the solid mineral and energy sectors, this study was considered. Basically, end products of harnessed mineral, oil and gas, aquifer and geothermal reserves e.t.c. are vital parts of our modern life as they have been of great importance throughout history. For example, without quarry of igneous intrusives, some states within the study area would not have gotten stones, gravel and sand (aggregates) for construction. Mineral exploitation is part of the wider extractive industry, but much attention is not being paid to it. The research work suggests that mineral resources as earth's natural reserve, can be harnessed by serious exploration which will benefit government and private agencies.

1.1 Background Information

The area falls within Southeastern sedimentary basin of the Lower Benue Trough, part of the Benue Trough. Beacause of earth's dynamicity originating from convective cells within the mantle (mantle dynamics), this has resulted to plate movement, causing drift of South American and African Continents and consequently, forming an aulacogen (failed arm/ Benue Trough). This is a major geological formation extending about 1,000 km northeast from the Bight of Benin to Lake Chad with about 150 km width (Grant, 1971). The Trough contains about 6,000m thick Cretaceous-Tertiary sediments. It may

include those predating the middle Santonian which have been compressionally deformed, faulted, and uplifted in several places. The geological processes leading to the formation of the Trough have made it viable for geothermal and mineral resource enrichment. The geology of the area comprises of sedimentary and basement formations. The tectonic events which are both deformation and orogenic processes, making ore genesis of Sedex (Sedimentary Exhalatives) more interesting and relevant for mineral exploration in the area.

The importance of aulacogens or ancient rifts as suitable environments for base-metal deposits has been noted by Sawkins (1976), Olade (1980) and Robbins (1983). The mineralization in the study area falls in the category of the Benue Valley mineralization which is attributed to connate brines derived from evaporitic shales of Asu River Group (Orajaka, 1972; Ford, 1981) set into motion by a high geothermal gradient accompanying continental rifting (Olade & Morton, 1985). The Benue Valley-type lead-zinc deposits constitute a distinct category (riftogenic) of sediment- hosted mineralization. Rapid cooling either due to reaction with wall rocks or mixing with meteoric or descending water (atmospheric water from condensation and precipitation) of low salinity (Akande & Mucke, 1993) principally activated mineral deposition by precipitation of ore minerals from chloride and/or sulfide complexes within high-level faults zones. The ore metals are considered to have been leached from alkali feldspars of Precambrian origin within the sediments and/or the Basement Complex as suggested by leadisotope data (Grant, 1971), and the sulphur derived by reduction of sea water sulfate (Olade 1976; Ezepue 1981). The Lower Benue Trough and the Trough at large, like other Sedimentary Basins in Nigeria is found to be endowed with mineral resources. Over twenty mineral resources have so far been reported in the Trough by the Geological Survey of Nigeria Agency and these include; coal, lead-zinc, barytes, limestone, clay, gypsum, phosphate, glass sand, fluorspar, salt, ironstone, uranium, sulphur, graphite, cassiterite, manganese, mica

and silver (Fatoye & Gideon, 2013) but as to where explorable new fields are, it remains liable for more research.

Knowledge of the temperature inside the Earth is still imprecise, the temperature can only be measured in the immediate vicinity of the Earth's surface, in boreholes and deep mines. Conditions are warmer in deep mines and near-surface temperatures increase rapidly with depth by roughly 30 K km^{-1} (Agricola,1530). At this rate, linear extrapolation would give a temperature around 200,000 K at the center of the Earth. Heat flows constantly from its sources within the Earth to the surface. Total heat loss from the Earth is estimated at 44.2 TW, mean heat flow is 65 mW/m^2 over continental crust and 101 mW/m^2 over oceanic crust and the heat of the Earth is replenished by radioactive decay at a rate of 30 TW (Perry, 1895a). The global geothermal flow rates are more than twice the rate of human energy consumption from all primary sources, hence its relevance. (Perry, 1895b).

Heat increase in the earth causes temperature change by an amount (∂T), determined by specific heat at constant pressure and mass of earth's material (m) (Lowrie, 2007) which explains the geothermal gradient. Away from tectonic plate boundaries, it is about 25 °C per km of depth (1°F per 70 feet of depth) near the surface in many parts of the world (Beardemore & Cull, 2001). Increased geothermal gradient is a lot useful in several geological processes such as kerogene maturation, geothermal reserve accumulation, most relevant to this study, in ore-fluid migration, accretion and mineral precipitation. Increasing both temperature and pressure during burial triggers a series of physico-chemical reactions and phase changes that may release water and ions that can become involved in carbonate diagenetic processes in the subsurface. For example, the conversion of gypsum to anhydrite at about less than 1000 m releases significant water that may become involved in solution, cementation or dolomitization (Kendall, 1984). Aside this, build-up of high geothermal gradients aid in catagenetic processes and for type III kerogenes, it leads to the formation of coal. Elevated temperatures over extended time periods to sedimentary organic

materials, lead to catagenesis of organic compounds and formation of oil and gas (Tissot & Welte, 1978). Such is seen in Mamu shales of Enugu bearing coal deposits derived from terrestrial organic matter representing the brackish marsh and fossiliferous pro-delta facies of the Late Campanian-Early Maastrichtian depositional cycle (Reijers & Nwajide, 1998), around 70 Ma. During this time also, the Anambra Basin became silted up with thick vegetation growing in low-lying marshes on a broad delta fan deposited by rivers from the interior which became buried under coarse sands afterwards with increased temperature and pressure, hence the maturation of oil and gas.

This study adopts integrated airborne geophysical techniques encompassing remote sensing survey using Landsat8, aeromagnetic and aero radiometric data from Federal Ministry ofMines and Steel Development, Nigeria, who between 2005 and 2009, engaged the services of Fugro Airborne Surveys Limited to acquire high resolution data of 500 m line spacing and 80 m terrain clearance for most parts of Nigeria. Subsequently, these data were generated at ease with the prevalence of high speed and robust computer programs and were divulged by the Nigerian Geological Survey Agency (NGSA), all in 2010. These highly reliable integrated airborne techniques show good results.

Remote Sensing survey is a Geo-Informatics System which studies objects on earth from Space Satellites based on electromagnetic irradiation from both natural radioactive elements in minerals or other artificial sources giving colours based on the reflection of certain range of wavelengths by electrons in specific state. Also for example, Magnetics and Landsat identify lineations and structures which are good conduits for fluid migration and ore accretion and are factors for orientation of these occurrence

1.2 Problem Statement

There is need for a systematic regional mineral exploration using new tools/data such as airborne radiometric surveys. Application of airborne radiometric technique to regional geologic mapping and mineral exploration in most parts of Nigeria have not been fully exploited and this could be due to

unavailability of high resolution data in the near past. The lithologies and geologic features mark the area a viable zone for mineral and geothermal energy resources. Most mineral exploration works have been disjointed and few because there has been no co-ordinated or systematically planned procedure. There are gaps in the mineral map (Fig. 1.1) because of unfound deposits and this makes an incomprehensive map,

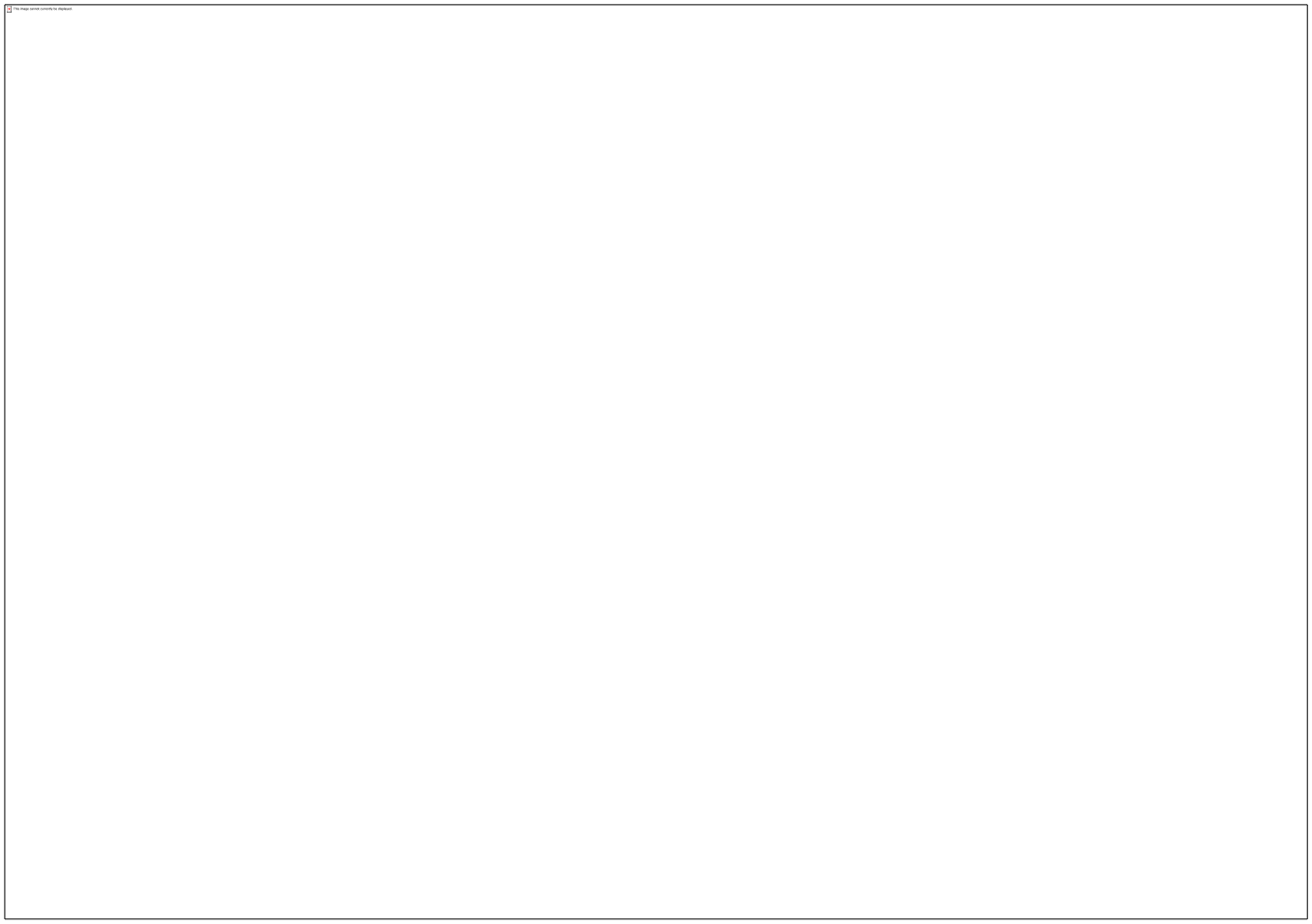

Figure 1.1: Mineral Map of the Study Area
(Adapted from Falade, 2016)

incomplete and not good enough. Several authors in time past had engaged in researching on occurrence of individual deposits in the southeastern Nigerian sedimentary basin. These include; Tattam (1930), Orajaka (1965), Nwachukwu (1974), Olade (1976), Ezepue (1984) who investigated Pb-Zn mineralization in Abakaliki; Etim, Louis, & Maurin (1988), Egboka & Uma (1986), Uma, Onuoha & Egboka (1990), Uma & Loehnert (1992), Omada & Echefu (1996), Uma (1998), who studied brines and Farrington (1952), Olade (1978), Umeji & Can Vachette (1983) who researched on igneous bodies/intrusive. Recently, Obarezi & Nwosu, 2013 studied the structural controls of Pb-Zn mineralization of Enyigba district of Abakaliki and Oha, Onuoha, & Dada (2017) studied the lead-zinc barium mineralization widely distributed in epigenetic fracture-controlled vein deposits of Albian-Turonian sediments.

Lack of proper catalogue of mineral deposits within the Lower Benue Trough and absence of improved localized mineral potential map of the area have created lacunae in preparing an exploration model for this study area.

1. Aim and Objectives

The aim of this research work is to generate an improved mineral exploration model of the study area. To achieve this, the specific objectives are;

1. To analyze and interprete airborne magnetic, radiometric, landsat, SP and VES data of the study area.

2. To integrate various digital data sets including satellite imageries, digital elevation models, aeromagnetic, airborne-radiometric and mineral occurrence data in a Geographical Information System (GIS).
3. To identify the major structural features of the area and relate these structural fabrics to mineralization.
4. To estimate curie point depth, geothermal gradient and heat flow regimes in the area.
5. To propose possible models of the geothermal resources in the area.
6. To produce an improved mineral potential map for the study area.

1.4 Justification of Study

This study encapsulates the search of mineral and geothermal energy resources. Nigeria is enriched with over forty (40) industrial minerals such as marble, gypsum, gemstones, gold, lithium, iron ore, talc e.t.c. (Nwegbu, 2014), scattered in more than 450 different locations across the country. Exploration of these deposits helps economic development and diversifies revenue streams of the country. Solid minerals contribute just 2% of the country's Gross Domestic Product (GDP) and less than 5% of economic minerals are currently being mined while the rest 95% are currently untapped, hence, solid mineral sector needs revatalisation which encourages development of entire regions of mineral occurrences within the country.

On the other hand, geothermal energy is a form of renewable energy and renewable energy sources constitute over 26% of the world's electricity today. According to International Energy Agency (IEA), its share is expected to reach 30% by 2024 (IEA, 2019; McGinn & Schneer, 2019) and this is indeed a pivotal time for renewable energy use. UK has hit an amazing milestone in June 10, 2020, for being a country who celebrated two months of running purely on renewable energy for the first time ever and Nigeria can follow her lead. These are quite quintessential and have informed the essence of this research. With the increasing population and improving industrialization in Nigeria, the need to reduce the use of fossil fuels to the barest minimum, justifies the need to search for clean/geothermal energy enhanced by power plants, for generation of electricity and need to revatalise the solid mineral industry.

1.5. Description of the Project Environment

1.5.1. Location, Accessibility and Scope of Study

The Study area is geographically located between Latitude 5° 30' N and 7°00' N and Longitudes 7° 00' E and 9° 00' E and the area extent is 36,300 km^2, which encompasses environs of Anambra, Enugu, Ebonyi, Imo, Abia, Akwa Ibom and Cross River States. The area is directly bounded by Kogi to the North, Delta and Edo to the West and Bayelsa and Rivers States to the South and to the East by Cameroon. The areas are linked to each other via express and primary roads (Fig.1.2). This research work includes detailed

ground truthing to be carried out in areas of known mineralization as well as areas.

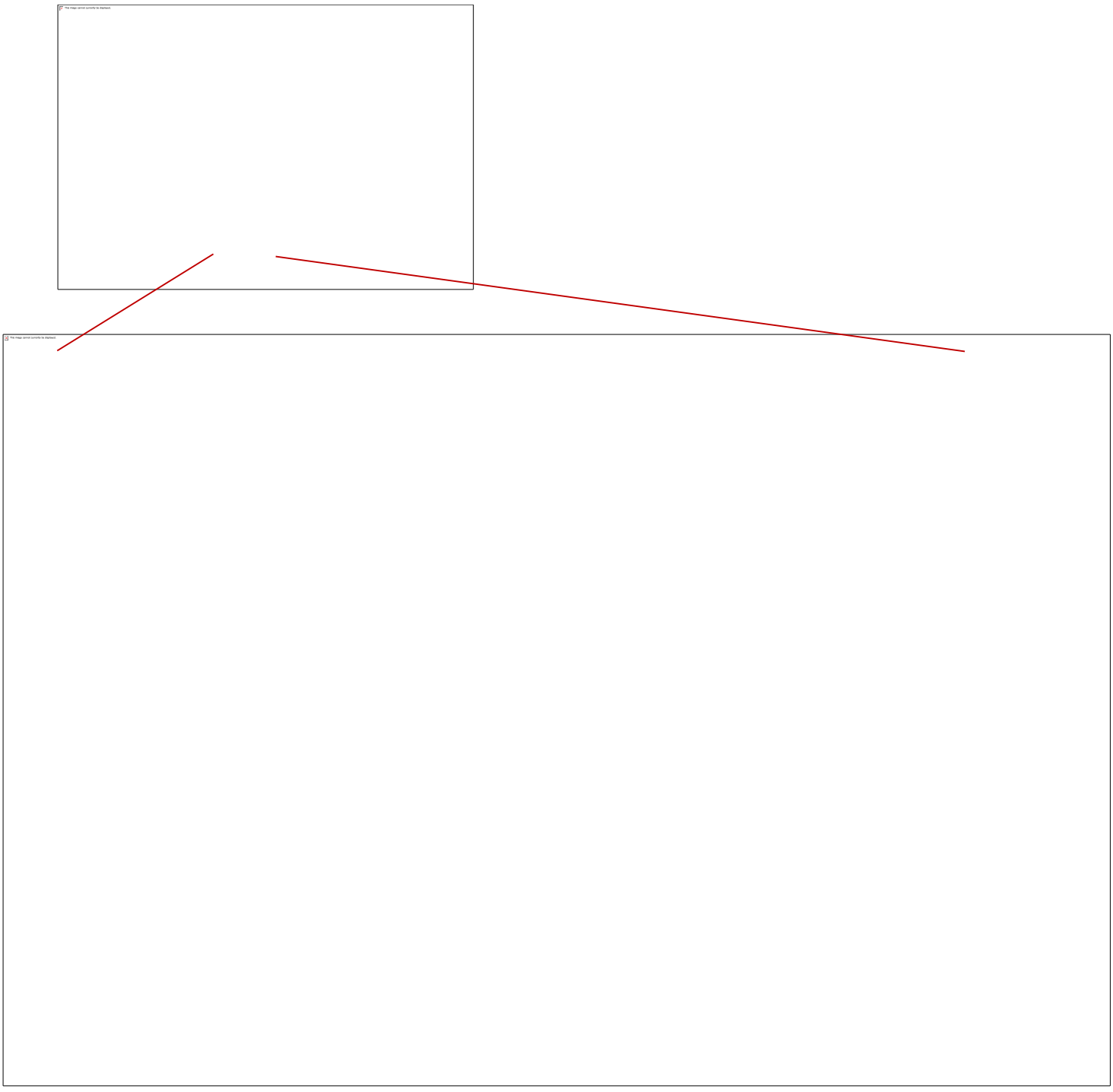

Figure 1.2: Topographical Map of the Study Area (Adapted from Ryan, Carbotte, Coplan, O' Hara, Melkonian, Arko, Weissel, Ferrini, Goodwillie, Nitsche, Bonczkowski & Zemsky, 2009).

which have hitherto been mapped as non-mineralization areas. It will focus mainly at investigating and delineating the mineralization potential vis-a-vis the geothermal energy resource of the study area using integrated Geophysical approaches.

1.5.2 Geology of the Study Area

A. Regional Geologic Setting

Nigeria is situated within the PAN African mobile belt and sandwiched between the West African Craton to the West, the Tuareq Shield to the North and the Congo Craton to the southeast. About half of the total area of Nigeria landmass is underlain by rocks of the Precambrian age known in the country as the Basement Complex. The basement complex is divided into two provinces. The Western Province and the Eastern province. The Western Province is approximately west of longitude 8º E, typified by N-S to NNE-SSW trending schist belts separated from one another by migmatites, gneisses and granites. This trend is believed to be the result of Pan African orogeny involving collision between the West African Craton and the Pan African mobile terrain with eastward dipping subduction zone. The schist belts are differently interpreted as small ocean basins, infilled rift structures or synclinal remnants of an extensive supra crustal cover. The Eastern Province lies approximately east of longitude 8°E and is more nearly NE-SW. When followed eastward into Cameroon, the trend changes to ENE-WSW (e.g Ngaoundere mylonite zone and the schist belts near Batare). The Eastern Province comprises mainly migmatites, gneisses and large masses of Pan-African granitoids (Older Granites) intruded in Jos plateau, by per alkaline granites. Except for smaller schist occurrences around Madagali (Hawal Massif), Toungo and Gayam (Adamawa Massif) and Oban Massif in southeast, the Eastern Province is marked by the absence of major schist belts (Figure 1.3a).

Nigeria is almost equally divided between crystalline basement rocks and Cretaceous to Quaternary sediments and volcanics (Fig.1.3c). The basement complex is commonly described under three lithologic groups, Migmatitie Gneiss Complex group, Schist belts and Older Granites. Migmatite gneiss complex

Figure 1.3a

Figure 1.3b

Regional Geology/Tectonic Setting

Figure 1.5a: Regional Tectonic Setting of Nigeria (Haruna, 2017)

Figure 1.5b: Benue Trough and Related Atlantic Fracture Zones. (After Wrght, 1968).

(MGC) are believed to be the oldest rocks of the Nigeria Basement Complex. Much of the complex is believed to be reworked older crust (probably Liberian in age) which have been further reworked by later orogenies like the Eburnean (2000 + 200 Ma) and the Pan African (600+150 Ma) with addition of the granitoids and the schist belts. Although evidence of sedimentation and deformation during Kibaran (1300-1100 Ma) have been recognized, no magmatic event of this age have been recorded. The Kibaran was followed by ages ranging from 900-450 Ma representing the imprint of the Pan African event which gave rise to migmatite, gneisses, Older Granite intrusives and similar lithologic units. The middle and late Paleozoic age is not represented by any magmatic or sedimentation event. The Mesozoic is marked by uplift and intrusion of a series of anorogenic, alkaline, shallow sub-volcanic intrusive known as the Younger Granites which fall within a N-S narrow belt in the western part of the Eastern Province and extends north ward into Niger Republic (Haruna, 2017). The remaining half is covered by Cretaceous to Quaternary sediments and volcanics (Fig.1.3c). The Cretaceous to Recent sediments are preserved in structurally controlled basins, from the oldest; (Coastal Calabar Flank, the Benue Trough (see1.3d), Bida, Chad Basin, Iullemeden/Sokoto Basin, Dahomey Basin and Niger Delta). The sedimentary successions in these basins are broadly divided into basal continental sandstones, siltstones and mudstones, middle marine shales and limestones intercalating with sandstones and siltstonesand continental/paralic upper sandstone sequence. The middle Cretaceous marked the beginning of sedimentation following the development of early rifts that were initiated in early Jurassic. Marine transgression marked by the growth

of trans-continental seas and epirogenic movements resulted in the formation and infilling of the many basins flanking the basement highs. Periodic sedimentation continued through the Tertiary and Quaternary.

B. Local Geology/Geologic Setting of the Study Area

The 36,300 km^2 area of study interest encompasses environs of Anambra, Enugu, Ebonyi, Imo, Abia, Akwa Ibom and Cross River States which occur within Southeastern Sedimentary Basin of the Lower

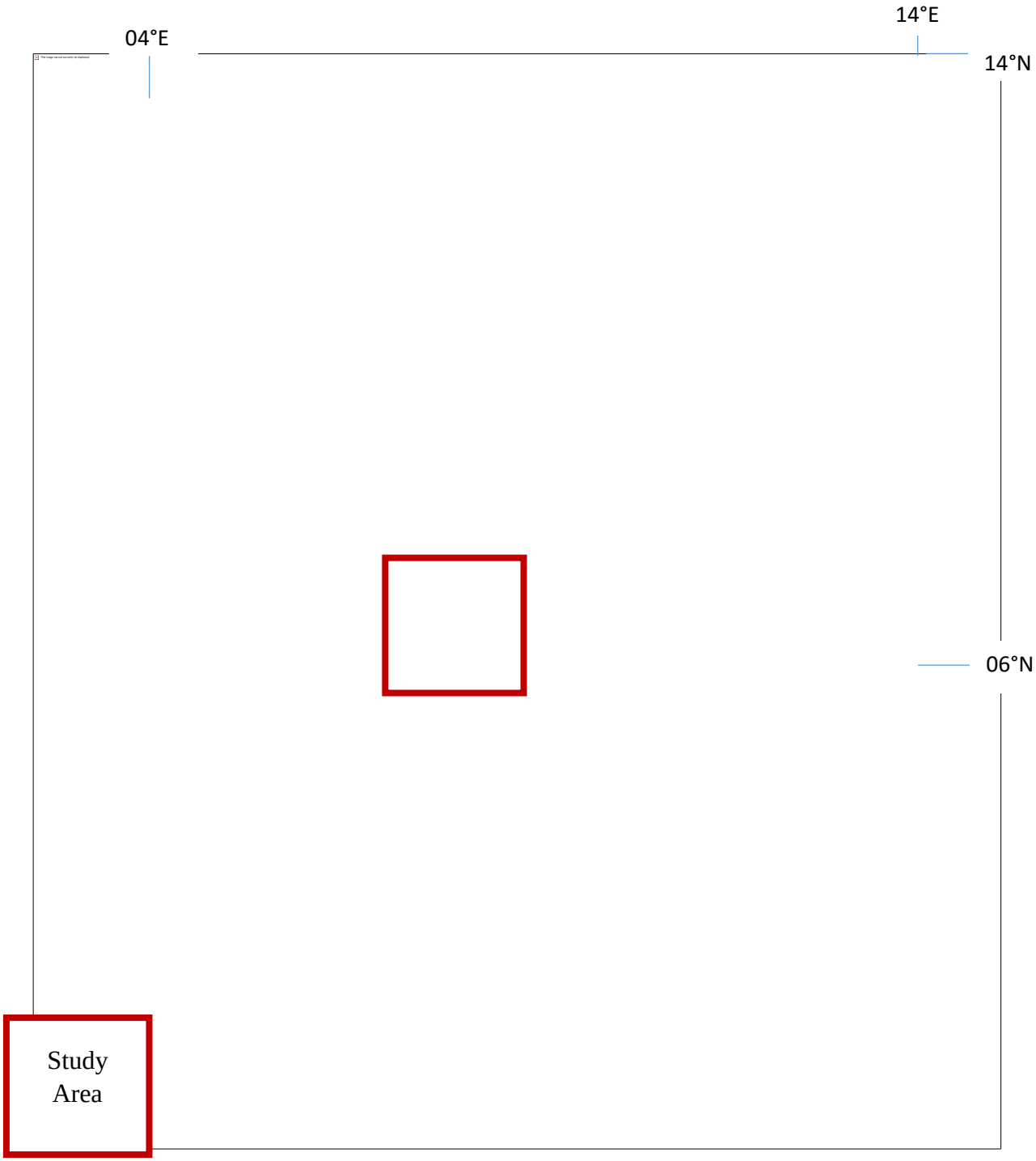

Figure 1.3c: Geologic Map of Nigeria Showing the Sedimentary Basins and the Basement Complexes (Adapted from Taiwo, Towolawi, Olanigan, Olujimi & Arowolo, 2015)

Benue Trough, which is a tensional feature and a rift structure within the Trough. There was proto-rifting of the boundary area between South America and African plates. The rifting started at a triple R (RRR) junction, under present day Niger Delta. At that time, Gulf of Guinea, Benue depression, South Atlantic developed between two of the triple Rs North of the junction, one between South America and along Niger Delta (Petters, 1978). Continuous movement along Atlantic spreading ridge and faults within the ridge offset resulted to physiographic and structural disposition (see Fig1.3b). The area covered by present day Benue valley was also spreading. But separation and sea floor spreading in the Benue Trough seized at late Cretaceous basin. Lately, activities started along the Cameroon plate which has many embryonic spreading ridge. Intracontinental Benue Trough was initiated during the lower Cretaceous in relation with the Atlantic Ocean opening.

The Benue Trough of Nigeria is a rift basin in central West Africa that extends NNE–SSW for about 800 km in length and 150 km in width. The southern limit is the northern boundary of the Niger Delta, while the northern limit is the southern boundary of the Chad Basin (Fig. 1.3d). The Trough contains up to 6,000 m of Cretaceous-Tertiary sediments of which those predating the mid-Santonian have been compressionally folded, faulted, and uplifted in several places. Compressional folding during the mid- Santonian tectonic episode affected the whole of the Benue Trough and was quite intense, producing over 100 anticlines and synclines (Benkhelil, 1989). Major deformational structures include the Abakaliki

anticlinorium and the Afikpo syncline in the Lower Benue Trough.

A. Southern Benue Trough

The Geodynamical and Tectonic processes within the Trough gave rise to the following formations contained in the study area. As described, starting from the bottom.

1. ASU River Group

Sedimentation in the Lower Benue Trough in shallow marine environment, commenced with the marine

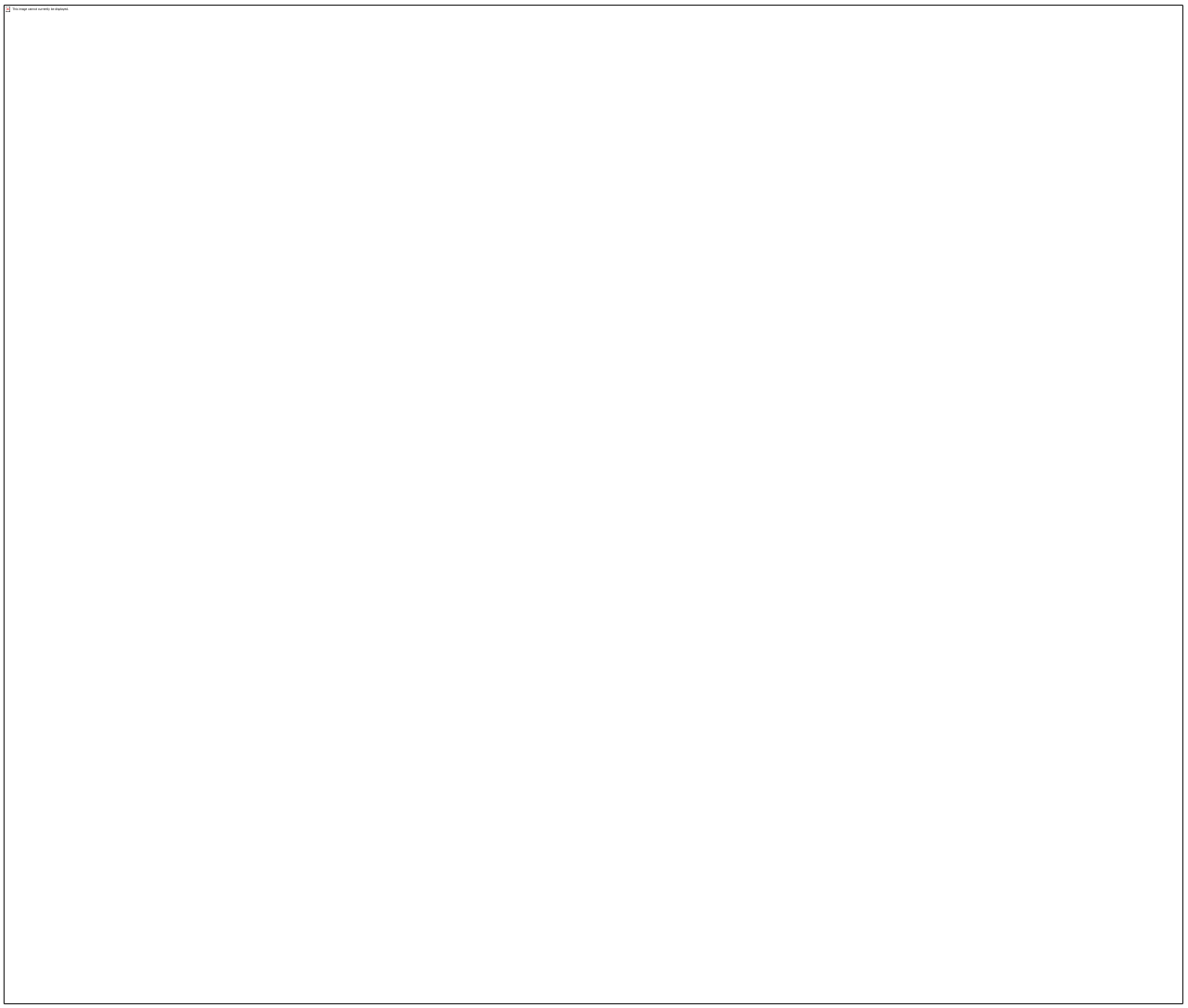

Figure 1.3d: Geological Map (Regional Map) of the Benue Trough Showing the Lower, Middle and Upper Benue Troughs (Adapted from Petters & Ekweozor, 1982)

Neocomian - Albian Asu River Group with some pyroclastics of Aptian – Early Albian age. The sediments predominantly comprise of shales with localized sandstones, siltstones and limestones. The oldest rocks are Abakaliki pyroclastics of the ASU River Group comprising of altered base of basalts, conglomerates, lithic fumes injected during the lower Alptian-Albian (Obaje 2009). They are sediments of the first transgressive cycle of massive thickness compacted into the Lower Benue Trough. (Onu, 2017; Fatoye & Gideon, 2013), due to a yielding bottom condition.

1. Ezeaku Formation

They are formations believed to have been deposited during the Turonian transgression (Cratchley&Jones, 1965). Overlying the Asu River Group is the Cenomanian-Turonian Nkalagu formation consisting of a 900 m thick fossil-rich black shales of New Netim Marl, limestones and siltsones and bedded Awgu Shales with fine-grained carbonaceous limestone beds in close association with subordinate limestone and calcareous sandstones and interfingering regressive sandstones of the Agala and Agbani Formations. There was also contemporaneous silting sequence of unconformably deposited sandstones, limestones, shales and calcareous sandstones of the Odukpani Formation on the folded basement rocks of the Calabar Flank during the Late Albian. (Onu, 2017). The folding was accompanied by igneous activities leading to extrusions and intrusions of andesites and igneous magma. There was a hiatus, the depo-centre of the depo-valley shifted westwards and it became an area of derivational sediments and the trough became a source area to the west of the trough area (Obaje, 2009).

B. Anambra Basin

The Santonian was a period of non-deposition, folding and faulting. The intensive Middle–Santonian deformation and magmatism in the Benue Trough displaced the major depositional axis westward which

led to the formation of the Anambra Basin. Post deformational sedimentation in the Lower Benue Trough, therefore constitutes the Anambra Basin. (Odoma, Obaje, Omada, Idakwo, & Erbacher, 2013).

1. Nkporo Shales

Sedimentation in the Anambra Basin thus commenced with the Early Campanian-Early Maastrichtian of the Enugu and Nkporo Formations (lateral equivalents) which overlie a sequence of Awgu shales and mudstone locally with sandy shales, thin sandstones and shaly limestone beds. The shaly facies grade laterally to sandstones of the Owelli and Afikpo Formations (Obaje, 2009).The Enugu and the Nkporo Shales represent the brackish marsh and fossiliferous pro-delta facies of the Late Campanian-Early Maastrichtian depositional cycle (Reijers & Nwajide, 1998). Deposition of the sediments of the Nkporo/Enugu Formations reflects a funnel-shaped shallow marine setting that graded into channeled low-energy marshes. The best exposure of the NkporoShale is at the village of Leru (Lopauku), 72 km south of Enugu on the Enugu – Portharcourt express road, while that of Enugu Shale is at Enugu, near the Onitsha-Road Flyover (Obaje, 2009).

2. Mamu Formation

The coal-bearing Mamu Formation and the Ajali Sandstone accumulated during this epoch of overall regression of the Nkporo cycle. The Mamu Formation occurs as a narrow strip trending North–South from the Calabar Flank, swinging west around the Ankpa plateau and terminating at Idah near the River Niger. The Mamu Formation is best exposed at theMiliken Hills in Enugu, with well-preserved secions along the road cuts from the King Petrol Station up the Miliken Hills and at the left bank of River Ekulu near the bridge to Onyeama mine (Obaje, 2009).

3. Ajali and Nsukka Formation

The converging littoral drift cells governed the sedimentation and are reflected in the tidal sand waves which are characteristicfor the Ajali Sandstone.The Ajali Formation of cretaceous age consists of red earth

sands which form the false-bedded sandstones. This in turn consists of great thickness of friable but poorly sorted sandstones. The Deltaic facies grade laterally into the overlying marginal marine sandstones of the Ajali and Nsukka Formations.Ajali and Owelli Formations lie on the Mamu Formation and constitute its lateral equivalents in most places. The Ajali Sandstone marks the height of the regression at a time when the coastline was still concave. In Abia State, Ajali Formation spans from Isuochi (Umunneochi LGA) though Uturu, Eluama and Ovim (Isikwuato LGA) where it narrows down to South of Nguzu Afikpo area of Ebonyi State, before running South into Arochukwu L.G.A and it is overlain by Nsukka Formation (Obaje, 2009).

C. Niger Delta Formation

1. Imo Shales and Ameki Group

The Nsukka Formation and the Imo Shale mark the onset of another transgression in the Anambra Basin during the Paleocene which are overlain by the tidal Nanka Sandstone of Eocene age. (Fatoye, Ibitomi, & Omada, 2014). The Imo formation is the outcrop lithofacies equivalent of the Akata formation in the subsurface Niger Delta. (Short & Stable, 1967; Avbovbo, 1978).

The Nanka sand, Nsugbe and Ameki formations are laterally equivalent (Nwajide, 1979) and they occur in the Eocene time. Based on faunal content, their depositional environment has been suggested to be ranging from near shore (barrier-ridge lagoonal complex) to intertidal and subtidal zones of the shelf environments. (Nwajide, 1976; Arua, 1986). The Eocene Nanka Sands mark the return to regressive conditions.The Nanka Formation offers an excellent opportunity to study tidal deposits. Well-exposed, strongly asymmetrical sandwaves suggest the predominance of flood-tidal currents over weak ebb-reverse currents. The presence of the latter are only suggested by the bundling of lamine separated from each other by mud drapes reflecting neap tides. A good outcrop of the Nanka Formation is the Umunya section, 18 km from the Niger Bridge at Onitsha on the Enugu – Onitsha Expressway (Obaje, 2009).

2. The Tertiary Units/Proto-Niger Delta Sequence

The Oligocene/Miocene Ogwashi-Asaba Formation comprises of alternating coarse-grained sandstone, lignite seams and light coloured clays of continental origin (Kogbe, 1976). These Tertiary units constitute the proto-Niger Delta Eocene to Recent sequences in the subsurface (Fatoye & Gideon, 2013). The Ameki group and the Ogwashi-Asaba formation are correlative with the Agbada formation in the surface Niger Delta. (Olajubaje *et al*., 2018). Shales of Ogwashi-Asaba formation contain significant amount of organic matter and may be a potential source for the hydrocarbons in the northern part of the Niger Delta (Reijers & Nwajide, 1998). The Stratigraphic strata of the Southern Sedimentary Basin and Lower Benue Trough at large are elaborated below in Figure1. 4 and Table 1.1 below and the geologic map of the study area is represented in Figure 1.5 below.

1.5.3 Geomorphology of the Study Area

A. Physiography, Climate and Vegetation

The relief of the study area undulates as seen from the low lying Niger Delta formations occurring as much as up to 150 m, next to it, are varying and increasing elevations of some lithologic units within the Anambra Basin, from Nkporo shales with elevations as high as 200 m, Mamu formationwith elevations between 250-350 m up to Ajali sandstone as high as 500 m asl. A sharp change in topography occurs around the shaly, sandstone sediments of the Abakaliki Trough occurring within the Abakaliki-Benue formations between the Asu River groups and Awgu Shales of the Lower Benue Trough. The cross-sections from profiles taken across the geologic map (Fig.1.6a) is indicative of a sharp depression evident from the elevations ranging between 50 -150 m in this group. Occuring higher than the adjacent sediments and volcanics of the Mamfe Basin are the Oban and Adamawa massifs of the Pre-Cambrian Basement Complex whose elevations are as high as 400 m. Figures 1.6b from Shuttle Radar also corroborates the varying elevation of the Study Area.

In Nigeria, the climate is tropical, semi-arid in the far North and progressively rainier southward. There is rainy season due to African monsoon, which is progressively longer and more intense from North to South. In the South, rainy season goes from March to October, in the central part of Nigeria, it goes from April to October, then ceases in October and in the South East which is the wettest area, rainy season goes from

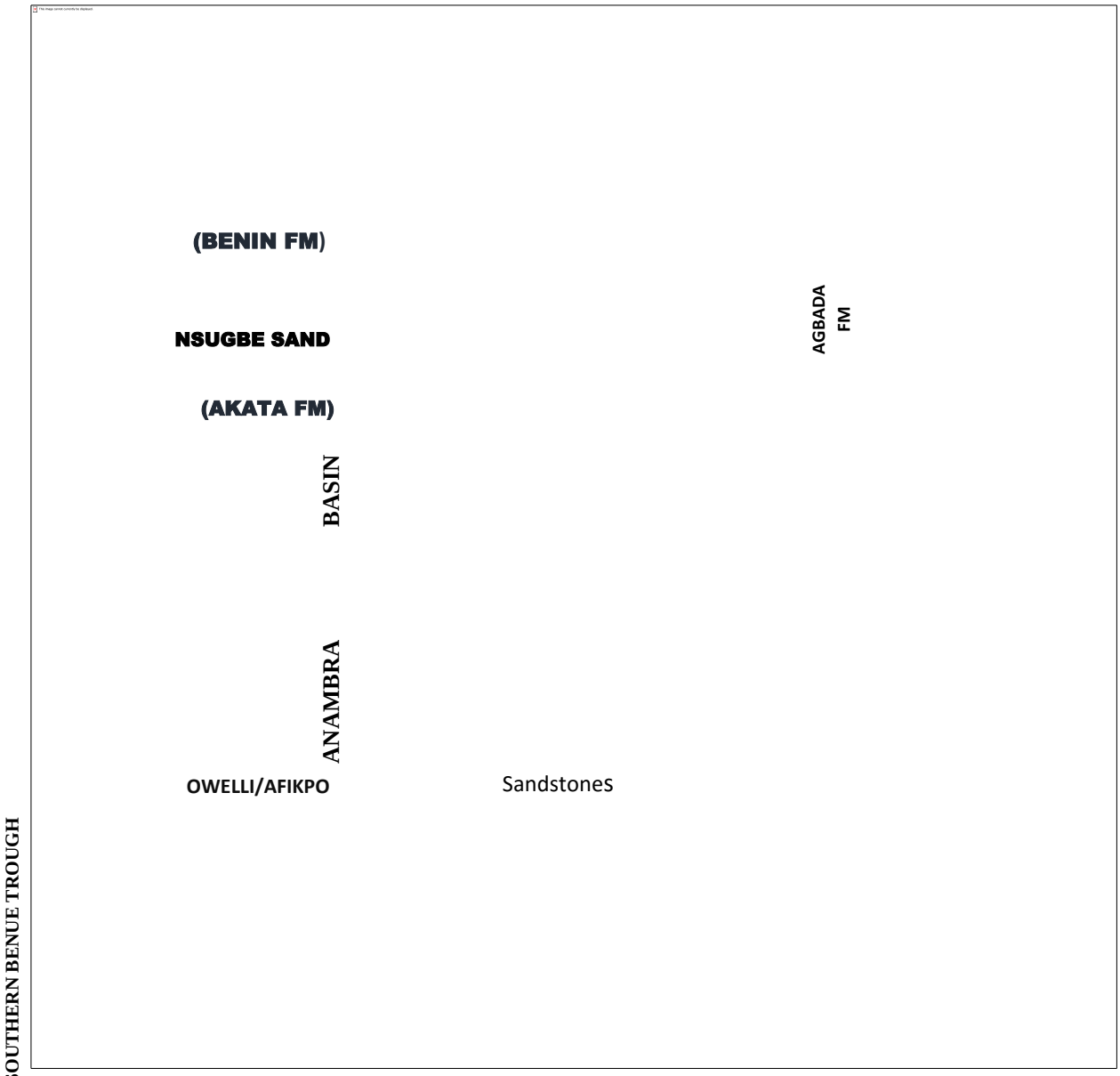

Figure 1.4: Stratigraphic Successions in the Anambra Basin and Southern Benue Trough, Nigeria (Modified after Ladipo, 1988; Akande, Hoffknecht & Erdtmann, 1992 and Nwajide, 2013)

Table 1.1: Lithostratigraphic Successions of the LBT (Modified after Petters, 1982)

Geologic Age	Geologic Formation	Lithologic Description
Pleistocene – Holocene	Alluvium and Quartenary deposits	Unconsolidated freshwater sands and gravels with silt and clay admixtures.
	Beach Ridges	Fine grained greyish white sands
Oligocene Pliocene	Coastal Plain Sands	Sands Coarse to medium grained unconsolidated sands with gravels, ferruginous sandstones and clays.
Oligocene	Ogwashi-Asaba Formation	Gritty clays and pebbly sandstones with lignite layer.
Pliocene Eocene	Bende- Ameke Formation	Sandstone and shale sequence with bouldery and shelly limestone.
Paleocene	Imo Shale Group	Grey Calcareous shales and siltstones with bands of sandstone and ironstone.
Maastrichtian	Nsukka Formation Ajali sandstones Mamu Formation	Alternating sequence of shales and sandstones with coal seams (the coal measures).
	Nkporo Formation	Dark grey shales and soft mudstones with occasional thin beds of sandstones and limestones.
Campano-Maastrichtian	Awgu-Ndeaboh Shale Group	Shales with thin limestone bands and lenticular sand bodies.
Coniacian	New Netim Marl Formation	Thick Marl unit with intercalations of thin bands of dark shales.
	Amaseri Sandstone Formation	

Turonian	Ezillo Formation Ezeaku Formation	Formation highly bio-turbated fine to medium grained calcareous sandstones formation with fossiliferous shales at the base.
	Ekenkpon Shale	Dark grey shales with fine sandstone and siltstone intercalations.
	Asu River Group	Alternating shales, siltstones and limestones with lateral facies changes to sandstones.
Cenomanian		Thick, black and highly fissile shales with intercalations of marls, calcareous mudstones and shale beds.
Ekenkpon Albian	Mamfe Formation	Poorly bedded sandy shales with fine to medium grained sandstone lenses
	Mfamisong Formation	Cross-bedded coarse to medium grained immature sandstones with basal conglomerates and arkoses.
	Awi Sandstone Formation	Masssive bedded, grey chalky limestones with fossils
Aptian-Neocomian		Fluvio-deltaic clastics consisting of grits, sandstones, mudstones and shales.

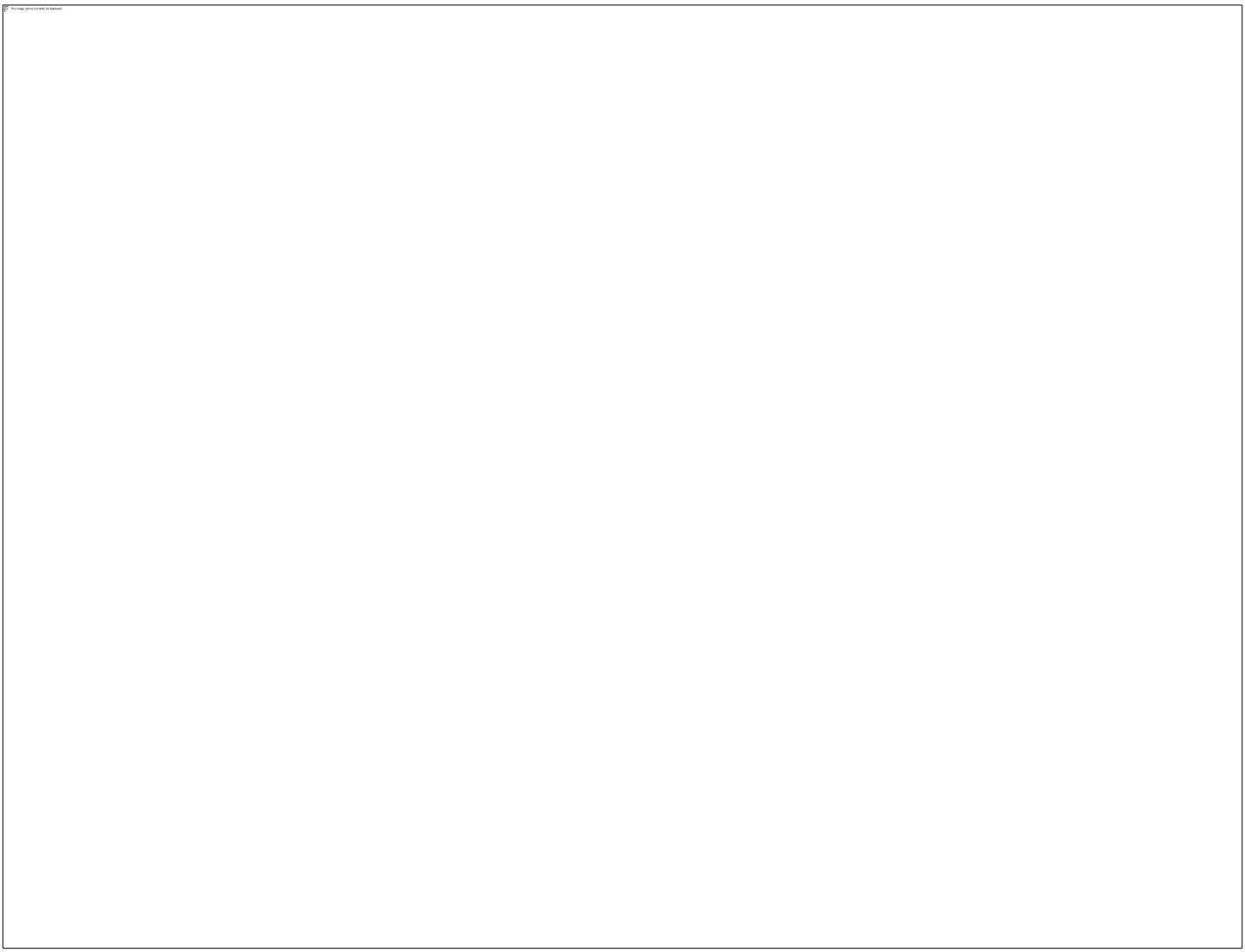

Figure 1.5: Geologic Map of the Study Area {(Digitized from Geologic Map of Nigeria, Nigerian Geological Survey Agency, 2010)}

(a)i

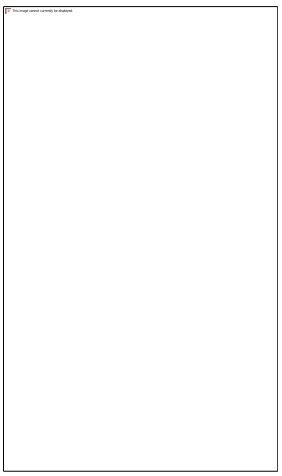

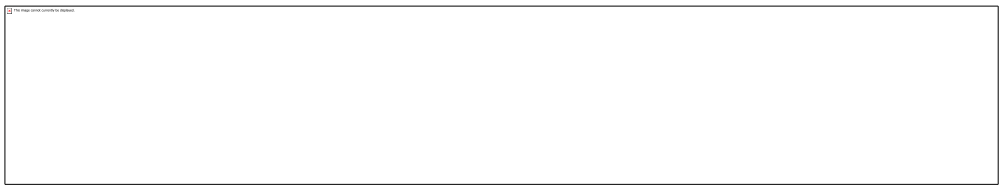

(ii)

Figures 1.6a (i & ii). Geologic Map with Profile Lines and Cross-Sections Generated Across Profile Lines

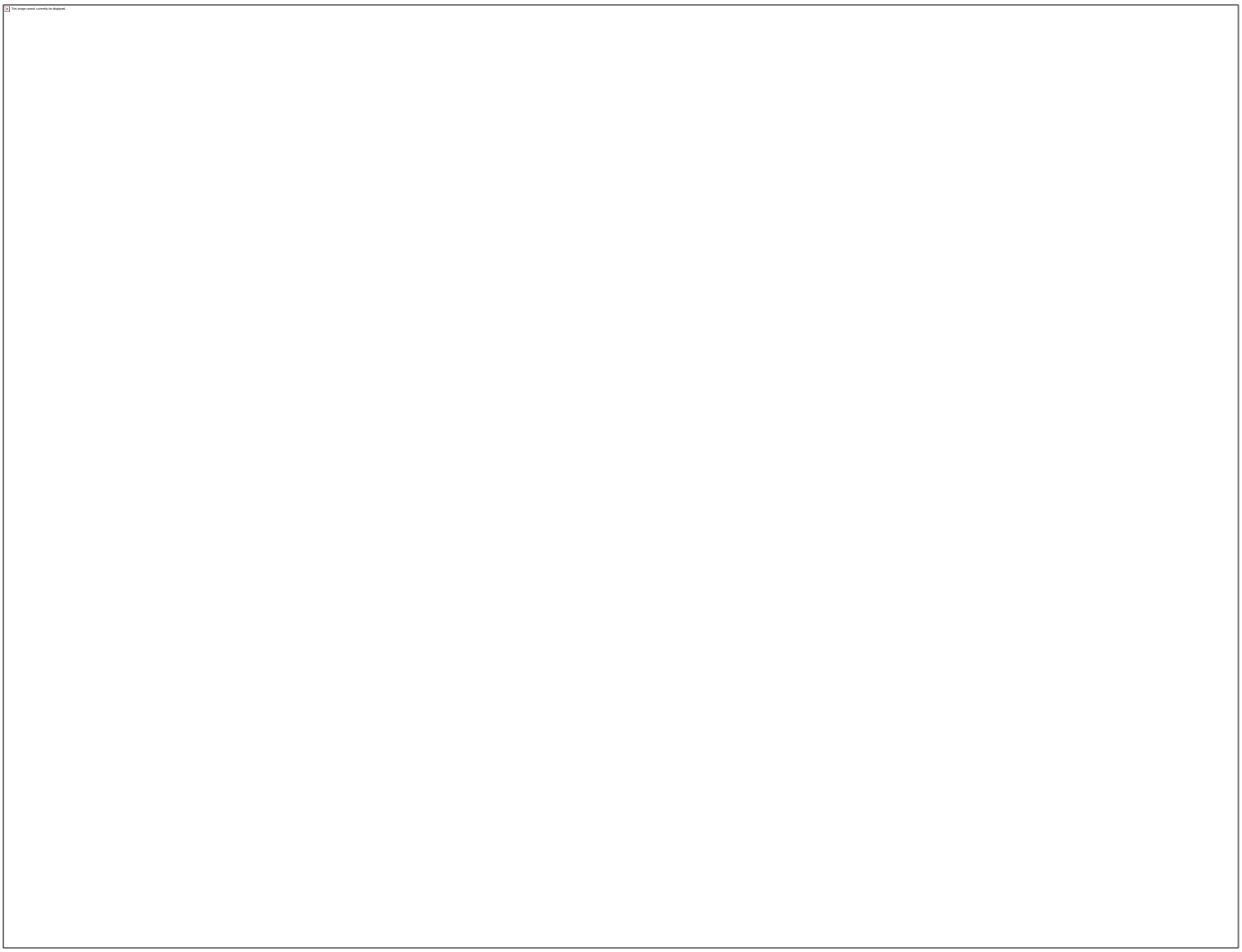

Figure 1.6b: Elevation Map of the Study Area

{Adapted from Shuttle Radar Topographic Mission (SRTM)}

March to November. Annual precipitation ranges between 1000-1500 mm in central Nigeria, exceeds 2,000 mm (80 in) in the South and even exceeds 3000 mm (120 in) in the far South East characteristic of tropic rainforest climates, worldwide. The Southern part of Nigeria experiences heavy and abundant rainfall. These storms are usually convectional in nature due to the region's proximity to the equatorial belt. It also experiences a double rainfall maxima characterized by two high rainfall peaks, with a short dry season in the month of August, commonly referred to as August Break and a longer dry season with temperatures between 20°C to 40°C, falling between November and February after each peaks. With this, vegetation varies considerably because the Savannah is observed in the central part of Nigeria, the rainforests in the South and the mangroves in the Niger Delta and Coastal areas. Humidity remains higher in the South, because of the influence of the sea, while hot, sunny and dry weather conditions return to the Central and Northern parts. Figures 1.7 a&b give better explanation of these. The Study area and its environs have ever green vegetation with eastern prototype mixtures of semi-savannah grasslands, forests and swamps and this stands it out as a distinctive agrarian area and a good source of type III kerogenes

B. Drainage, Soil Type and Superficial Deposits of the Study Area

The study area is well drained by Source Rivers most likely emanating from the Benue River going by the dominant North Easterly trend of the dendritic pattern and other tributaries linked to the Niger Delta coming from the South Atlantic Ocean. The closest source can also be pointed to the Rivers Niger and Northwestern parts of the study areas are most likely drained by Benue and Niger-Benue River confluences respectively.

Regoliths and soil type of a given area are greatly influenced by the lithology of the area which counts from migmatite, banded and granite gneisses, schists, quartz-diorites, shales, marls, sandstones, siltstones, clays, mafics e.t.c. Due to degradational and erosional processes, soils and regoliths are Benue confluence going by the second trend, which is North Westerly (see Figure 1.2). Areas lying as low as 100-150 m

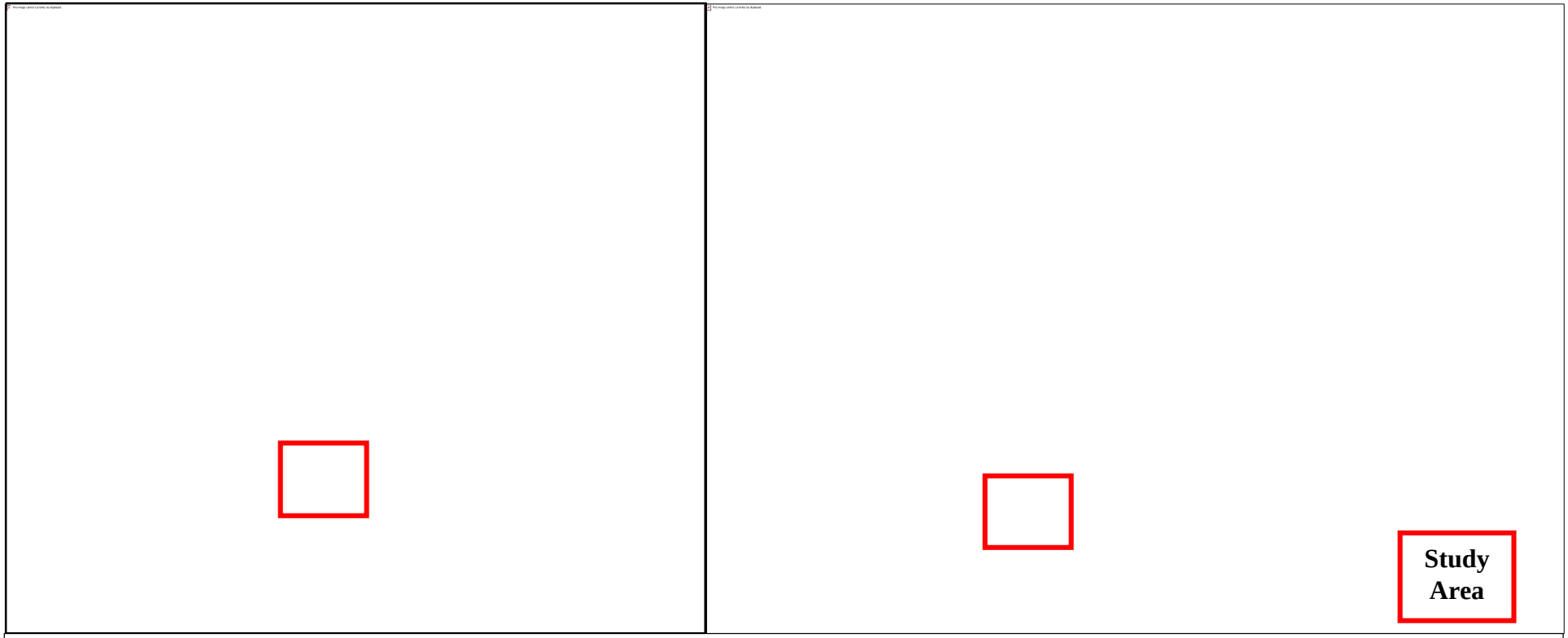

Figure 1.9a Figure 1.9b

Figure 1.7 a&b: Diagrammatic Representation of the Climate Around the Study Area (Adapted from Encarta, Microsoft and archived from The Original, 2009)

-N-B: The Study Area generally has >2000 mm annual rainfall which influences the dominant rainforest and woodland/tall grass vegetation present.

appear more drained and discontinued river channels are indicative of elevated areas, eroded river channels or dried river channels devoid of abundant rainfalls during dry seasons. The area is well drained by Cross River and its tributaries and the drainage pattern is dendritic. The soil within the area varies in a wide range from, clayey, silty, lateritic-shales /grey sandy clay (hydromorphic soils), sandy or clayey loam soil dominant around the Abakaliki environs, hence the soil's suitability towards rice farming and other tuber cultivations. Laterites and alluvium are basically the most recognized superficial deposits in the study area. Due to erosional processes and leaching away of topmost soils. Laterites directly overlay weathered bedrocks and are believed to be of pedogenetic origin and alluvia on the other hand are detrital remnants from water bodies along a flow channel (de Swardt, 1964).

CHAPTER TWO

2.0 LITERATURE REVIEW

This section makes available useful terms and gives insight to the associative terms of the research work, with the aim of giving a broad picture of the basis of the research by making reference to similar results and unsolved problems within the frame of the topic, concept of the basis of the research work, and ideal chosen tools for the achievement of the research. For ease of convenience, this review is grouped into three parts; Conceptual, Theoretical and Empirical frameworks.

2.1 Conceptuaal Framework

Based on the mode of formation of the intercontinental rift basin/Benue Trough, Cratchley & Jones (1965) attributes this to stem from rifting of African and South American plates and extension of the original fracture system which did not open up completely (failed arm). The Trough serves as a containment for deformed Cretaceous sediments and intrusives concealing rift boundaries and localized ore bodies which constitute a distinct category (riftogenic) of sediment-hosted mineralization (Ogundipe & Obasi, 2016). Geodynamics brings about rift formations such as the Trough, which has been a focus of attention for researchers with numerous studies being carried out to understand the causes, modes and importance of the whole lithospheric extension (Benkhelil, 1989). Due to this mode of formation, analysis of the basin geometry allows for proper identification of possible reserves of hydrocarbon, geothermal occurrences and mineral deposits. The importance of aulacogens or ancient rifts as suitable environments for base-metal deposits has been noted by Sawkins (1976), Olade & Morton (1980) and Robbins (1983). The mineralization in the study area falls in the category of the Benue Valley mineralization which is attributed to connate brines derived from evaporitic shales of Asu River Group (Orajaka, 1972; Ford, 1981) set into motion by a high geothermal gradient accompanying continental rifting (Olade & Morton, 1985).

The Trough has extensively been studied in time past using various geophysical techniques with various aims of study attached. Several geophysical methods measure different physical parameters of the earth such as magnetic susceptibility, density, electrical conductivity, radioactive element concentrations e.t.c. (Reeves, 2005 and Telford, Geldart, Sheriff & Keys, 1990). Geophysical methods are adopted for such purposes through the identification of structures such as faults/slips, fractures, folds e.t.c on the overlying sediments, determined by the underlying basement signatures which aid in interpretation. Remote sensing/satellite imageries and geophysical prospecting methods (magnetic and gravity) have found useful applications in the mapping of potential ore bearing linear geological strutures (Nash, Boshier, Coupard, Theron & Wilson, 1980; Goetz & Rowan, 1981; Peters, 1983; Drury, 1986, 1993; Rowan & Bowers, 1995; Hoover, Klein & Campell,1995; Adagunodo, Sunmonu & Adeniji, 2015; Akinlalu, Adelusi, Olayanju, Adiat, Omosuyi, Anifowose & Akeredolu, 2018 and Bamidele, 2020). In geothermal exploration, magnetic measurements also enables location of regions with reduced magnetization due to thermal activity (Georgsson, 2009).

2.2. Theoretical Framework

2.2.1 Magnetic Method

Gao, Xiong, Yu, Zhang, & Wu, 2021 and Sharma, 1987 pointed out that of all geophysical methods, magnetic mapping is the oldest, simplest, most reliable and widely used technique for locating hidden ores. Structures associated with mineral deposits, curie point depths for geothermal gradient and heat flow studies, are estimated using magnetic method (Lawal, 2021; Shaole, Zhixin, Kefa & Jinlin, 2021; Oha, Onuoha, Nwegbu & Abba, 2016, and Obande, Lawal, & Ahmed, 2014). The principles of magnetism help to understand the various modes of responses of earth materials to magnetic field (Dobrin & Savit, 1988). This is so because the Earth acts like a magnet as a result of the ferromagnetic properties of the core and mantle. Hence when a magnetic survey is conducted, earth materials exhibit magnetism based

on their respective magnetic properties/susceptibilities. Anomalies in the local geomagnetic field arising from magnetization by earth's magnetic fields and remanence are measured (Glatzmaier & Roberts, 1995). Trends in magnetic features most often have semblance to the trend of the overlying sediment as sedimentary structures are to a large extent controlled by basement tectonics. Most rock forming minerals are effectively magnetic, nevertheless, some rocks contain sufficient magnetic minerals to yield abundant magnetic signatures and buried ferrous objects do same too.

In Nigeria, the application of airborne magnetics to earth studies, have proved alot useful in exploration and geotechnics. Ezepue (1984) emphasized on how tectonic fissures have influenced the loci of mineralization within the study area and further studies by Ajakaiye (1981) and Ofoegbu (1984, 1985 and 1988) through ground and airborne geophysical techniques over the study area also have revealed long, extensive block faulting and basinal structures in the Trough. Ananaba & Ajakaiye (1987) made a lineament density map of Nigeria using 30 Landsat frames which was done to show evidence of tectonic control on mineralization in Nigeria from lineament density. They corroborated that mineral occurrences in the country are closely related to the lineaments that are linked to offshore trans-oceanic fracture zones, because the lineament density map compared well with primary mineral occurrence map and results showed good correlation between areas of high lineament density and where there are occurrences of most primary minerals. This correlation suggests that primary mineralization is tectonically controlled. Mineralization occurs through conduits in the form of faults, fissures and lineaments by which magma or mineralizing fluids get to the surface as intrusives. These deformations (linear structures) are usually picked by aeromagnetic maps as surface linear features (Anyawu & Mamah, 2013). Results from previous study by Ugwu, Ezema, & Ezeh, 2013, reveal that igneous intrusions with large lateral extents, occurring more at Southeastern parts of the study area accounts for more mineralization, hence the area may not

hold any significance of hydrocarbon potentials due to high temperature that prevailed at the time of ore genesis.

The study area occurs within Southeastern sedimentary basin which airborne magnetic studies have shown that it is tectonically and structurally controlled, of erosional origin and it contains magnetic deposits from exhalatives/extrusives, intrusives, magnetic sediments or magnetic metamorphic units. If the magnetic units in the basement occur at the basement surface, depth determinations will indirectly map the basin floor morphology and so for or several decades, basement depth estimation has helped locate sedimentary basins with significant thicknesses of sediments (Gunn, 1997). Aeromagnetic data may be high or of low resolution and high resolution. Depth to anomalous bodies, structural discontinuities, basement structures and depth, overburden thicknesses e.t.c have all been delineated through the use of airborne magnetic data and have been of study interest within the past few years of which the previous research works below explain some of them. Magnetic data when used in mapping depth to anomalous bodies, invariably maps basin floor, topography, morphology and structure with a relatively high accuracy (Onyedim, Awoyemi, Ariyibi & Arubayi, 2006), and locates mineralized zones as well as evaluates hydrocarbon deposit of the region by calculating sediment thickness (Ikeh, Ugwu, & Asielue, 2017). Either one or more of the physical parameters such as the configuration of the anomalous zone, magnetic susceptibility contrast as well as the depth to the anomalous body yield magnetic anomaly signature characteristics. Very high gradient on aeromagnetic map is usually indicative of difference in magnetic susceptibilities such as that between acidic to ultramafic rocks (intrabasement). Variation of contour gradient on an aeromagnetic map is indicative of suprabasement (Vertical movement) and the shape of the causative body is considered (Reeves, 2005). Short, medium and long wavelengths contribute to the varying magnetic field in the Benue Trough at large. The changes in rock composition within the basement reflect the broad magnetic closures seen on the total magnetic intensity anomaly maps (Ijeh,

Anyadiegwu & Okeiyi, 2018). Depth to basement, faults in the basement surface, and the relief of the basement surface have direct relevance to the depositional and structural history of the study area. From airborne magnetic data obtained over the Benue Trough, long and extensive block faulting revealing basinal structures in the trough were revealed by the analysis done by Ajakaiye, 1981 and Ofoegbu 1984, 1985 and 1988 on them.

These geological structures are often overlain by sediments whose depositional isopachs and/ or structure reflect the underlying basement structure. Thus, through the study of the magnetic basement, information can be provided on the morphology of the sedimentary basin and its structure. Therefore, source depth or location of anomalies can be interpreted from contoured aeromagnetic maps (Ishola, Oluwaseyi, Akerele & Adeogun (2020); Dobrin & Savit (1988). Airborne magnetic survey is relevant in displaying spatial distribution and relative abundance of magnetic and non-magnetic minerals in the lithosphere and accompanying geology and geologic structures within (Ibraheem, Haggag & Tezkan (2019). Igneous features which include intrusive plugs, dykes, sills, lava flows and volcanic centres can occur at any stage of a basin's evolution and preserved at any sedimentary section (Dobrin & Savit, 1988 and Glatzmaier & Roberts, 1995).

Magnetic surveys can be performed on land, sea and air and airborne magnetic survey data are used in this study. Magnetometers working on magnetic induction principles are effective in picking magnetic responses of minerals (Keary, Brooks & Hill, 2002). The speed of operation and resolution of the data are very endearing towards the ease of detecting ore deposits that contain magnetic minerals.

2.2.2 Remote Sensing Technique -LANDSAT VIII

Some authors like, Payamani, Babaei, Dehghan, & Harouni (2020); Frutuoso, Rui, Lima & Teodoro (2021); Sulemana, Quaye-Ballard, Ntori, Awotwi, Okrah, & Asare-Ansah (2020); Ourhzif, Algouti, Algouti, Hadach (2019); Rekhibi, Wadi, & Said (2015) and Grauch, Hudson, Minor & Caine (2006) have proposed that remote

sensing is intensively used nowadays in mineral exploration, and some of the most frequently used remote sensing data for alteration zone mapping and geological extrapolations come from Advanced Space borne Thermal Emission and Reflection Radiometer (ASTER) and Landsat Thematic Mapper (TM). Ran, Zhang, Wei & Zhang **(**2017) have observed that Remote Sensing uses satellite- or aircraft-based sensor technologies to detect and classify objects on Earth, including on the surface, and in the atmosphere and oceans based on propagated electromagnetic radiation. Remote Sensing can be active if it sends out their own energy and records reflected portion of that energy from the earth's surface such as radar imaging systems and it could be passive if it records the reflected energy of electromagnetic radiation or emitted energy from the sun with the use of cameras, video recorders and thermal infrared detectors (Imam, 2019). Whether remote sensing systems are active or passive, all detect and record energy signals from earth surfaces and/or from the atmosphere (Schowengerdt, 2007). Other more complex sensing systems include electronic scanners, linear/area arrays, laser scanning systems, etc. The electromagnetic spectra ranges from short wavelengths of high frequency waves to long wavelengths of low frequency waves. In that range, they include gamma rays, x-rays, ultraviolet (UV) radiation, visible light, Infrared (IR) radiation, microwave radiation and radio waves (Leilesand & Kiefer, 1993). The rainbow of colours occupy the visible spectrum that we see as visible light (sunlight). This portion of the electromagnetic spectrum has wavelengths between 400 and 700 billionths of a meter (0.4–0.7 μm). Although it is a narrow spectrum, the visible spectrum has a great utility in satellite remote sensing and for the identification of different objects by their visible colors in photography (McBratney, Mendoça, & Minasny, 2003). This electromagnetic radiation, E, travels as packets or in quanta of energy in the course of being dispersed. The incident energy quanta is either transmitted, absorbed or reflected and same EM Radiation is directly proportional to the fourth power of its absolute temperature, (Stefan Boltzman law). The Infrared spectrum extends from the visible region to about 1 mm (in wavelength). They can be further partitioned into the near-IR, mid-IR, and far-IR spectrum, which include thermal radiation. IR radiation can be measured by using electronic detectors (Guo, Sun, Jia, Jiang, Jiang, Wang, Xu, Wang, Tian & Wu, 2019). IR images obtained by when sensors can yield important information on the health of crops and also in visualizing forest fires even when they are enveloped in an opaque curtain of smoke. Microwave radiation has a wavelength ranging from approximately 1 mm to 30 cm, they are emitted from earth, objects such as cars and planes, and

atmosphere (Aggarwal, 2004). These microwaves can be detected to provide information, such as the temperature of the object that emitted the microwave. Because their wavelengths are so long, the energy available is quite small compared with visible and IR wavelengths (Joseph, 1996). Therefore, the fields of view must be large enough to detect sufficient energy to record a signal.

Four generations of Landsat instruments (MSS, TM, ETM+ and OLI (and TIRS) have different band designations. Landsat Multispectral Scanner (MSS) imagery consist in four spectral bands with 60 meter spatial resolution. Each image covers approximately an area of 170 km (north-south) by 185 km (east-west). Specific band designations differ from Landsat 1-3 to Landsat 4-5 (USGS, 2015). Landsat Thematic Mapper (TM) images are composed by seven spectral bands with a spatial resolution of 30 meters for Bands 1 to 5 and 7 and for Band 6 (thermal infrared) is 120 meters, but is resampled to 30-meter pixels. Approximate scene size is 170 km (north-south) by 183 km (east-west) (USGS, 2015). Landsat Enhanced Thematic Mapper Plus (ETM+) imagery consists of eight spectral bands with a spatial resolution of 30 meters for Bands 1 to 7 and the Band 8 (panchromatic) resolution is 15 meters. Scene size is approximately 170 km (north-south) by 183 km (east-west) (USGS, 2015).

Landsat-8 is an American Earth observation Satellite and the eighth satellite in the Landsat program. Its ground stations are situated in five locations which are Landsat ground station in South Dakota, Svalbard ground station in Norway, Alice Springs ground station in Australia, Neustrelitz ground station in Germany and Gilmore Creek ground station in Alaska. The functions of the ground system are to command and control the Landsat 8 observatory in orbit as well as to manage the data transmitted from the observatory (Ridwan, RAdzi, Ahmad, Mustafa, Din, Jalil, Isa, Othman & Zaki, 2019). Landsat 8 was launched from Vandenberg Air Force Base, California, on an Atlas-V 401 rocket. It carried on board two sensors which are Operational Land Imager (OLI) and Thermal Infrared Sensor (TIRS) as opposed from prior Landsat where the thermal and reflective band images were acquired with the same sensor. OLI is

a sensor equipped with a four-mirror telescope and a quantization of 12 bits (USGS, 2015).

Aggarwal, 2004 has revealed other common types of remote sensors, which are radiometers, multispectral scanners, spectrometers, and film cameras, and these systems can either be in analog (e.g., hardcopy aerial photography) or digital format (e.g. a matrix of "brightness values" corresponding to the average radiance measured within an image pixel). Digital remote sensing images may be input directly into a GIS for use; analog data also can be used in GIS through an analog-to-digital conversion or by scanning (Gao, 2009). These sensors are mounted on moving platforms (e.g. aircrafts and satellites) operating in or above the earth's atmosphere, the principal sensing regions are in the visible, reflected near- infrared, thermal infrared, and microwave radar regions of the EM spectrum (Abdulrahman, 2010).

2.2.3. Airborne Radiometric Method

Ademila, Akingboye & Ojamomi (2018) opined that radioactivity in geoscience is based on knowledge of the physical properties of radiation sources and the ability to detect these sources through the analysis of remotely sensed data. Radiometric surveys detect and map natural radiometric emanations, called gamma rays, from rocks and soils. Because of radioactivity of minerals, demand for nuclear fuels and detection of associated non-radioactive deposits, the utility of airborne radiometric is very useful (Alhumimidi, Aboud, Alquahtani, Al-Battahien, Saud, R., Alquahtani, Aljuhani, Alyousif, & Alyousef, 2021 and Day-Stirrat, Hiller, Nikitin, Hofmann, Mahood & Mertens, 2021). The standard unit of gamma radiation is the Roentgen (R) expressed in μR per hour, which corresponds to the quantity of radiation that would produce 2.083×10^{15} pairs of ions per cubic metre at standard temperature and pressure (Milsom, 2003 and Keary, Brooks & Hill, 2002). Carlson & Boyet, 2009 and Keary et al., 2002, have revealed that some elements have isotopes whose nuclei contain an unstable number of neutrons and protons. The instability is most often balanced by ejection of material from the nucleus. Alpha decay involves the ejection of two protons and two neutrons; 4-Helium (4He) nucleus or alpha particle. Beta

decay occurs through loss of an electron from the nucleus, turning a neutron into a proton. Another form of radioactive decay involves electron capture from those surrounding the nucleus, turning a proton into a neutron. The radioactive emissions have very different penetrating properties. Gamma rays are only stopped by several centimetres of lead and can travel several hundreds of metres in air and so only gamma rays can be detected in airborne surveys via gammar ray spectometry (McCay, Harley, Younger, Sanderson & Cresswell, 2014).

At least 20 naturally occurring elements are known to be radioactive, all detectable gamma radiation from earth materials come from natural decay products of only three elements, i.e. uranium, thorium, and potassium (Nwobodo, Ikeri & Chikeleze, 2020; Magill & Jean, 2005 and Telford *et al.*, 1990). Airborne radiometrics has extensive use for geological mapping and exploration of economic minerals through detection of potassic alteration zones associated with hydrothermal alteration (Ghoneim, El Nabi, Yehia, & Salem, 2021); geochemical and environmental monitoring and in several fields of sciences (IAEA, 2007, 2003 & 1991) via information on characteristics of soil and its parent rocks, including surface texture, weathering, leaching, soil depth, moisture, and clay mineralogy (Bierwirth, 1997), provided by radiometric data sets. This is because, most geologic processes such as; Continental Drift, Continental Rifts which have initiated formation of mineral veins within the Trough, Geodynamics, Paleomagnetism, Magnetostratigraphy, Paleoseismology, Plate Tectonics, e.t.c however, occur on time scales beyond human experience as much as thousands, millions, and even billions of years. For these, the chronometer of choice is radiometric dating, where the decay of naturally occurring radioactive elements is translated into time. (Dickin, 2005; Faure & Mensing, 2005). The gamma-ray spectrometry method is widely used in diverse fields. Initially developed as uranium exploration tool, the application of the method now includes geological mapping (Anderson & Nash, 1997; Graham & Bonham-carter, 1993; Jaques, Wellman, Whitaker & Wyborn 1997; Charbonneau, Holman & Hetu, 1997), mineral exploration (Grasty

& Shives, 1997; Lo & Pitcher, 1996), soil mapping (Cook, Corner, Groves, & Grealish, 1996; Wilford *et al*., 1997), and environmental radiation monitoring. Wilford, Bierwirth, & Craig (1997) demonstrated that airborne gamma-ray spectrometry patterns provided important information for soil, regolith, and geomorphology studies used for land management and mineral exploration decisions.

2.2.4. Electrical Resistivity Method

Riwayat, Nazri & Abidin, 2018 have stated that electrical resistivity method of geophysical prospecting, has over a decade, been in use, to study vertical and horizontal discontinuities in electrical properties of the earth. The method depends on the property of resistivity of earth's material, in which for instance, it is the resistance in ohms (Ω) between two opposite faces of a unit cube of material. Because of distinct resistivity contrast of earth materials, electrical resistivity method of prospecting makes it a worthy tool for mineral exploration (Egbelehulu, Mallam, Abdulsalam & Adewumi, 2021). Detected resistivities of materials in the earth's subsurface are primarily influenced by; ions in pore fluids which influence response to electricity, making porosity and fluid saturation a determinant to electrical resistivity measurements. Fluid-filled fractures within crystalline rocks and oxidation reduce resistivities, increase induration with depth, and heightens resistivity (Patnode & Willie, 1950; Keller & Frischknecht, 1966, Barker, 1975 & Reynolds, 1997). Several geological processes are associated with mineralization such as supergene enrichments, clay and wall rock alterations, fracturing/shearing, porosity, salt water intrusions, weathering and dissolution (Guo, Sun, Jia, Jiang, Jiang, Wang, Xu, Wang, Tian, & Wu, 2020; Ward, 1990) explained that these geological processes decrease electrical resistivities of earth materials while other processes also associated with mineralization such as induration, carbonate precipitation and silicification increase the electrical resistivity of earth materials. Some other factors which control the resistivity of earth materials include porosity and intergranular permeability**,** temperature and pressure**,** rock type, age, texture and mineralization (Olorunfemi, 2014; Reynolds, 1997).

This geophysical method is a non-invasive type which utilizes direct or low frequency alternating currents introduced into the ground through current electrodes (C_1 and C_2) from an artificial source to reveal electrical properties of sub-surface rocks from resulting potential difference between two potential electrodes (P_1 and P_2), this 1D or 2D resistivity cross-section, images the geological subsurface (Keary *et al.*, 2002; Leborgne, Rivett, Wanangwa, Sentenac & Kalin, 2021).

2.3. Empirical Framework

Mohamed, Al- Naimi, Mgbeojedo & Agoha (2021) used remote sensing and geographic information system (GIS) techniques for geological mapping and prospecting for gold mineralization along the Red Sea hills in parts of Hamissana, Northeast Sudan, in order to elucidate the geological maps and evaluate mineral potentials. Different digital image processing techniques such as; Image sharpening, contrast stretching were applied to Landsat 8 Operational Land Imager image in order to increase discrimination between various lithological units, delineate wall rock alterations for target zones of gold mineralization, and enhance spatial resolution of the images for more detailed information. The principal component analysis transformation yielded saturated and interpretable images than the original data. Several ratio and composite ratio images revealed the existence of alteration zones from northeast to southwest in acid meta-volcanic and silica barite rocks and X-ray fluorescence analyses corroborated selected samples from wall rock alteration zones, as gold-bearing.

Eldosouky, Pour, Hamed, Taha, Gamal, Mahmoud & Pham (2021) interpreted Remote sensing (RS) and aeromagnetic data to reveal information for mineralization potentiality detection of ore deposits within Al-Allaqi region of the southeastern desert of Egypt. Several data processing approaches were implemented and integrated and results of band ratios (BR) and Principal Component Analysis (PCA) from Landsat-8 processing, imaged the hydrothermally altered zones and the structures outlined by lithologic contacts, faults, and porphyry features (dyke-like structures). Lineaments were well extracted

from airborne magnetic datasets while CET system method was applied for generating a heat map of structural complexity, likewise CET Porphyry Analysis system, which was used to extract likely near-circular porphyry features that revealing probable site of mineralization and to validate the remote sensing observations. Integrated outcomes showed that areas of highly complex structures, density (fractures/faults) are consistent with the detected hydrothermally altered areas that are rivaled with mining zones in Al-Allaqi region of the Southeastern Desert of Egypt.

Githenya, Mathu, Kariuki &Waita (2021) interpreted Landsat 8/OLI of the study area to map hydrothermally altered zones by integrating geology with remote sensing techniques to validate results by establishing geological structures and their associated economic mineralization in the rocks of Mwitika-Makongo area. Band combinations, band ratios and lineament extraction methods, field mapping and geochemical analysis, were all integrated techniques whose results were used in lithological discrimination of hydrothermally altered zones. Results showed some iron mineralizations in hydrothermally altered zones, especially around Kalima Kathei, they concluded that lineaments control drainage patterns in the area. Chemical analysis using X-Ray fluorescence, for mineralized samples, Pearson correction matrix of the chemical data gave a strong correlation between Fe2O3, TiO2 and P2O5 indicating that their mode of delivery in the area could be similar, with a likely source from hydrothermal fluids in the area. The results confirmed the findings from remote sensing studies on hydrothermal alteration, hence the integration of research methods, provided a tool for delineating economic mineralization in the Neoproterozoic rocks.

Franto, Pramumijoyo & Setijadji (2021) interpretated scenes of Landsat 8 satellite remote sensing images to map hydrothermal alteration minerals and to identify primary tin in Gadung village, Toboali sub-district, South Bangka District. They identified the distribution of primary tin based on types and

alteration mineralogy in the research area by using Landsat 8 images by employing a defoliant method for each mineral: 4/3;2/1 band ratio for quartz identification, 4/3;6/5 band ratio for illite identification, 4/2;7/6 band ratio for chlorite identification, and 4/3;7/6 band ratio for iron oxide. Further, the observations of morphology, lithology and geological structures were made, using 5/4; 6/3; 4/2 and 5/3; 6/4; 5/4 composite image combinations respectively. Petrography, X-Ray Diffraction (XRD) and XRF confirmed for the result of the satellite image interpretation. Results revealed that the primary tin mineralization in the area, is an oxide mineral characterized by the presence of wolframite, pyrite, arsenopyrite, and cassiterite, and deposited in big polymetallic veins, as well as allegedly influenced by NNW-SSE-trending main geological structure and associated to iron oxide mineral in form of goethite and hematite. They discovered that the type of tin mineralization within the area is the mineralization in ironstone or gossan units, from supergene process, conveyed by cassiterite, and associated with iron oxide minerals.

Osinowo, Gomy & Isseini (2021) analyzed Landsat 8 OLI satellite image data to map geological features and spatial distribution of hydrothermal alteration zones, known to be in association with gold mineralization in the Pala, Mayo Kebbi region of southwestern Chad. Radiometric calibrated, noise filtered and image enhanced Landsat 8 OLI data were subjected to colour composite, band rationing and crosta analyses in order to enhance spectral reflectance and compositional information, create colourful multispectral images to map desired spectral bands into principal component images for the purpose of accentuating salient information needful to delineate hydrothermal alteration zones. The results from composite ratios 4/2-6/7-6/5 indicated relative spatial distribution of iron-oxide in the southeast, clays and hydroxyl minerals, in the west and northwestern part of the study area. The eigenvectors and eigenvalues for hydroxyl minerals and iron-oxides showed highest loading of opposite signs which delineated hydrothermal alteration zones. Field control revealed that some areas delineated by band rationing as hydrothermal alteration zones appear to be the result of intense weathering, hence remote sensing was recommended for

delineation of hydrothermal alteration zones, followed up with a relevant ground-observation based control procedure.

Rockwell, Gnesda & Hofstra (2021) analyzed multispectral remote sensing data acquired by the Landsat 8 Operational Land Imager (OLI) sensor using new, automated techniques and GIS software packages, to generate a map of exposed mineral and vegetation groups in the western San Juan Mountains, Colo., and the Four Corners Region of the United States. Band ratio results were combined into displayed mineral and vegetation groups using Boolean algebra with view of using new analysis logic to exploit the coastal aerosol band in Landsat 8 OLI data and identify concentrations of iron sulfate minerals. Results indicated the presence of near-surface pyrite as a likely potential nonpoint source of acid rock drainage. It also revealed zoned occurrences of iron sulfate minerals in the area and known sources of pyrite. Results show high correlation with occurrences of jarosite-bearing mineral assemblages from airborne imaging spectrometer data and supporting field verification surveys.

Tompolidi, Sykioti, Koutroumbas & Parcharidis (2020) interpreted Sentinel-2, Landsat-8/OLI, and ASTER satellite multispectral datasets over south part of Lakki plain inside the Nisyros volcano caldera (Greece), in order to give a detailed description of argillic zone of a hydrothermal field. They developed a procedure of spectral unmixing by representing hydroxyl-bearing alteration with a single endmember (clays) and three nearly non-altered primary volcanic lithologies which are basic and acidic compositions and loose materials of alluvial/beach deposits, scree, pyroclastic deposits, etc.. Elemental sulfur in fumarolic vents hosted by active hydrothermal craters was represented as well. Results from ombination of spectral unmixing and geological map, provided quantitative estimations of the primary volcanic and loose material areas affected by alteration. Results from pixels with high abundance values of hydroxyl-bearing alteration corresponded to mapped areas with strong hydrothermal alteration. They concluded that the developed methodology is superior to conventional approaches such as alteration spectral index

because it could go a step further to describe overall pattern of hydrothermal fields, hence the most accurate results were taken when applied to ASTER or Sentinel-2 MSI data.

Kumar, Veeraswamy, Raghubabu & Balaji (2020) interpreted Landsat 8 OLI satellite data to investigate geochemical analysis of iron ore and iron-enriched mineralised zones and their source identification by understanding lithological, structural and geomorphological units of Veerapunayunipalle and Pendlimarri of YSR Kadapa District, AP, India. Subsequently, geochemical analysis was performed in the mineralised zones to know the type and grade of the iron ore. The study revealed that the iron ore in the study area is of haematite (Fe_2O_3) type, and its mineralization is confined to lineaments trending in E-W direction and arederived from ferruginous quartzites and shales belonging to the Cuddapah Supergroup. Based on the geochemical investigation, the overall grade of iron ore in respect of a Fe % in the study area is 39.04 which is commercially considered as lower grade and is useful for cement industry except for some villages like Chabali (56.76% Fe), Tummaluru (55.53% Fe), Animala (54.19% Fe) which is used for the steel industry.

Okeke, Ibrahim & Echeonwu (2020) interpreted Landsat 8 OLI over the Lower Benue Trough, Nigeria, adopting the Techniques of band rationing, Principal Component Analysis (PCA) and Crosta, to map coal seam area distribution. Composite image of the three was rendered in RGB format, and Spectral Angle Mapper (SAM) classification was conducted, the machine learning techniques were adopted alongside remote sensing method, to map ferric iron and hydroxyl oxide mineral locations amenable to coal formations. Results were best obtained from Crosta method out of the three, and results from PCA and band rationing, showed two ferric iron and hydroxyl oxide image maps which were combined to form a new image. Machine learning method such as Support Vector Machine, Ensemble (AdaBoost and Gradient Descent) and Neural Network (mlp) were engaged to predict areas likely to contain coal seams

based on surface feature characteristics. Surface coal mine areas were successfully mapped with SAM classification of the Crosta technique, while other areas suggestive of coal presence were successfully mapped with Machine learning predictive method.

Ourhzif *et al*. (2019) exploited the multispectral Advanced Spaceborne Thermal Emission and Reflection Radiometer (ASTER) and Landsat 8 Operational Land Imager (OLI) data in order to map lithological units and structural map in the south High Atlas of Marrakech. They employed the use principal component analysis (PCA), band ratios (BR), Minimum noise fraction (MNF) transformation in their analysis, performed a Support Vector Machine (SVM) classification for joint use of geomorphic features, textures and multispectral data of the Advanced Space-borne Thermal Emission and Reflection radiometer (ASTER) satellite. Results from SVM , PCA, BR and ground truthing showed a good correlation with existing geological map of the study area. Result from high potential of ASTER and Landsat 8 OLI data show good discrimination of lithologic units. SVM methods on ASTER and Landsat satellite data best reveals that these are powerful tools used in exploring and improving lithological mapping in mountainous semi-arid. They concluded that the overall classification accuracy of Landsat8 OLI data is 97.28% and the Kappa Coefficient is 0.97. The overall classification accuracy of ASTER using nine bands (VNIR-SWIR) is 74.88% and the Kappa Coefficient is 0.71.

Okeke, Ukaegbu, & Egesi (2019) interpreted four spectral bands from Landsat ETM namely; thermal infra-red band (Band 11), 11.5 to 12.51 μm; Short-wave infrared (Band 6), 1.57– 1.65 μm; near Infrared (Band 5) 0.85 to 0.88 μm and Red (Band 4) 0.64 – 0.67 μm, for the purpose of structural mapping in Afikpo environs. They delineated a total of 116 lineaments, which were extracted from the digital satellite scene, and they were seen to be concentrated mostly on the sandstone belt in the Northeast, around Amasiri environs. Thematic maps, digital elevation model (DEM), enhanced colour composites of bands

7, 5 and 2, were used to create surface feature maps, shaded relief and slope image, extraction and delineation of geological structures. Results revealed major NE-SW to minor E-W orientation of lineaments, of which they concluded that lineament density from regional lineaments were of great importance as indexes for groundwater exploration, mineralization targets, rocks quarrying and structural interpretation.

Onwubuariri, Mgbeojedo, Al-Naimi & Agoha (2018) carried out geophysical studies in some gully erosion sites within Orlu and environs to identify tectonic and neo-tectonic features, delineate their trends and evaluate their effect in gully development and propagation.Detailed geological field mapping was carried out to estimate the strikes and directional trends of the gullies, characterize the gullies and thereby revealing that the gullies in the area trend approximately in the NW-SE and NE-SW directions with the NE-SW being preponderant. The interpreted Landsat-ETM imageries helped to determine the lineaments and their trends, from which Rose diagrams generated from strikes and lengths of the interpreted lineaments, revealed two structural trends of NW-SE and NE-SW with NW-SE being dominant.

Ijeh *et.al.* (2018) used a digital format of aeromagnetic data and remotely sensed (Landsat ETM+7) for structural interpretation of the Awgu area in Enugu State, Southeastern part of Nigeria. Aeromagnetic data were analyzed and interpreted using vertical and horizontal gradients, analytical signal, reduction to pole, tilt depth as well as Euler deconvolution, and the 3D Euler solution of the study area showed a structural index of 1.0 with dyke/fault as the shape of the inferred geological structure.Analysis and interpretation of the Landsat ETM+7 revealed lineament trends and density across the area. Aeromagnetic and Landsat lineament maps of the study area were summarized from the rose diagrams revealing NE-SW as the major trend with some secondary trends in NW-SE, E-W and N-S directions. Conclusion was derived that a NE-SW trend reflects the younger tectonic events, because the younger events are more

pronounced and tends to obliterate the older events. Comparison of the aeromagnetic and Landsat lineament extraction of the study area in terms of number of lineaments, directions and total length oflineaments, the Landsat imagery were found to be more than the number, directions and total length of the aeromagnetic data.

Amin & Mazlan (2015) presented the applicability of Landsat-8 data for hydrothermal alteration and lithological mapping of Sar Cheshmeh copper mining district in the southeastern part of the Urumieh-Dokhtar volcanic belt, SE Iran by developing several Red-green-Blue (RGB) color combination images and specialized band ratios. Band ratios were derived from image spectra (4/2, 6/7, 5 and 10 in RGB) which allowed proper identification of altered rocks, lithological units and vegetation with supportive fieldwork and laboratory analysis verifying the image processed results. Well suited lithological mapping was achieved through thermal infrared bands of Landsat 8 significantly improving the quality of geological mapping from which geologists were encouraged to utilize Landsat-8 OLI/TIRS data forgeological purposes in the future.

Pour & Hashim (2014) analyzed Landsat-8 data, to show the applicability of the technique in delineating hydrothermal alterations and for the purpose of lithological mapping, for porphyry copper exploration in arid and semi-arid regions, with Sar Cheshmeh copper mining district of southeastern Urumieh-Dokhtar volcanic belt, Southeast of Iran, selected as a case study. They developed Red-green-Blue (RGB) color combination images and specialized band ratios from image spectra (4/2, 6/7, 5 and 10 in RGB) of the satellite image.This was to allow the identification of altered rocks, delineate lithological units and vegetation at a regional scale. They used nalytical imaging and geophysics developed hyperspectral analysis processing methods on Landsat-8 bands and Mixture Tuned Matched Filtering (MTMF) methods to identify alteration zone associated with known porphyry copper deposits in the study area. They

concluded that Landsat-8 bands bands 2 and 4 in visible and near-infrared, 6 and 7 in shortwave infrared, and 10 in thermal infrared, contain useful spectral information for porphyry copper exploration purposes.

Onyewuchi, Opara, Ahiarakwem & Oko (2012) made structural and geological interpretations of Nkalagu area, Southeastern Nigeria using Airborne Magnetic and Landsat data. This study revealed lineaments with trend directions in N-S, NE-SW, NW-SE and E-W directions with NE-SW trends being dominant. A strong relationship between lineaments and mineralization in the area was deciphered.

Opara, Ekwe, Okereke, Oha & Nnosiri (2012) carried out structural and tectonic analysis of Okposi and environs, Lower Benue Trough using Landsat-TM data with the aim of revealing a detailed structural interpretation of the study area by identifying associated lineaments, inferring their effect on the economic potentials of the area and also determining whether the Okposi Brine lake of the study area is structurally controlled. Trend analysis revealed structural trends in the E-W, N-S, NW-SE and NE-SW directions with the NW-SE and NE-SW directions as the dominant trends. It was further revealed that numerous lineaments in the study area make the region viable for mineral prospecting and that presence of a lineament zone around Okposi area may be responsible for the formation of the Okposi Brine Lake because it is believed that a linear feature must have cut through the basinal brine of the Asu River group of the Benue Trough.

Okereke, Onu, Ibe, Selemo, Opara, Ikoro, Ibeneme & Oha (2012) used Landsat and Aeromagnetic data to identify and delineate structures associated with Yola area of the Upper Benue Trough, trends/patterns of such structures and also infer their relationships with basin formation and dynamics.The study also determined the thickness of the basement, basement topography, hydrocarbon potential and groundwater availability of the study area. Magnetic results revealed a shallow layer of magnetizationwith an average depth of 0.546km and a deeper layer of magnetization with an average depth of 2.788km. The depths proved the basin viable enoughfor mineral

prospecting and unfavourable for hydrocarbon exploration and the dominant trend from magnetic data is towards the NE-SW direction which the Landsat data corroborates.

Away from the study area, Okereke *et al* (2012) integrated both airborne magnetic and Landsat data and made their analysis in order to map linear structures around Yobe Area of the Upper Benue Trough. Ologun (2004) also generated and developed filtered images and clusters in order to obtain structural and geologic map of the Jos Plateau.

Ananaba & Ajakaiye (1987) made a lineament density map of Nigeria using 30 Landsat frames. This work was done to show evidence of tectonic control on mineralization in Nigeria from lineament density. They corroborated that mineral occurrences in the country are closely related to the lineaments that are linked to offshore trans-oceanic fracture zones. The lineament density map was compared with primary mineral occurrence map and results showed good correlation between the areas of high lineament density and occurrences of most primary minerals. This correlation suggests that primary mineralization is tectonically controlled.

Lawal, Omar, Salami, Adewumi, Sunday & Fawale (2021) interpreted magnetic data of parts of Osun State and its environs, Southwestern Nigeria. They applied enhancement techniques such as analytic signal, Euler deconvolution, center for exploration targeting and porphyry analysis, with the aim of identifying structures concealing mineral deposits. Results delineated edges and distribution of magnetic sources equivalent to concealed mineral deposits, various depths to magnetic source geometries were estimated using prescribed structural indices of 0.0, 1.0 and 2.0 from Euler deconvolution. Results from CET (center for exploration targeting) grid and porphyry revealed magnetic lineaments and porphrytic intrusives which they classified as structures likely concealing mineral deposits.

Lawal, Sunday, Fawale, Salami & Adewumi. (2021) updated knowledge about the metallic source location, subsurface structures and depth information responsible for mineralization in Lafiaji and its environs, North-central Nigeria, by interpreting and analyzing airborne magnetic data, using techniques such as Total Horizontal Derivatives (THD), Tilt Derivatives (TD) and CET grid analysis, Euler Deconvolution (ED), and Fourier technique. Reduction to equator (RTE) Results revealed various striking subsurface structures in NE, SW, NW-SE, EW directions. The ED solutions revealed various structures as well from best index with the average depth values of various metallic sources. Result from the spectral analysis ranges from 1.40 km - 3.50 km. They concluded that the study did not only demonstrate the usefulness of HRAM data in revealing the nature and extent of subsurface structural features and depth information but also showed intense tectonic deformation of the basement structures responsible for mineral exploration.

Ekwok, Akpan, Ebong & Eze (2021) processed high resolution airborne magnetic data, using standard euler deconvolution (SED), source parameter imaging (SPI), spectral depth analysis (SDA) and 2D forward modelling data to determine depth to shallow and deep magnetic sources in some parts of the Lower Benue Trough and adjoining areas. Their results revealed that the Abakaliki Anticlinorium (AA) and Ikom-Mamfe Rift regions are dominated by short wavelength magnetic anomalies caused by extensive tectonic events. SED shows that shallow depths between 16.6-338.3 m and deep-seated at 394.3-5748. 1 m respectively. SPI showed shallow depths between 147.1 -554.2 m and deep-seated depths between 644.2-6141.6 m. Results from SDA shows deep magnetic basement in the range of 769 to 6666 m with an average of 3449.

Ishola, Oluwaseyi, Akerele & Adeogun (2020) interpreted and analyzed high resolution airborne magnetic data in order to map subsurface geological structures in Ewekoro, SW Nigeria. RTP image enhancement routine was applied to the data in order to map subsurface geological structures in Ewekoro,

Southwestern Nigeria. Results showed a good number of delineated lineaments in the NE-SW direction, which indicated fault and fractured zones, from tectonic episodes. Presence of shallow and deep magnetic sources at depth of 0.02-0.75 km respectively, were identified. They concluded that the deep sources were indicative of basement rocks underlying the sedimentary cover in the area.

Abdullahi & Kumar (2020) estimated Curie depths from power spectra of 25 equal window sizes with 50% overlap, extracted from high-resolution aeromagnetic anomalies of parts of lower and middle Benue Trough, Nigeria. Results revealed that Curie depths calculated from the region of study were between 11 ± 2 and 27 ± 2 km and that the shallowest depth (11 ± 2) km was obtained from Abakaliki environs while the deepest depth was calculated around Otukpa area of Anambra basin. They suggested that different geological structures and magnetic anomalies (i.e. high or low magnetic anomaly) influenced the calculated Curie depth results. They recorded curie depths (14–18 km) over basement rocks and Curie depths between 18 and 22 km within zones of volcanoes and hypothesized presence of underplating in the crust and possibly mantle plume as a result of the Mesozoic–Cenozoic volcanic magmatism (magmatic centers) mostly basalts distributed and scattered in the region.

Okpoli (2019) used high resolution aeromagnetic data set of Abakaliki (sheet 303 S) to characterize subsurface lithostructural features in parts of the Lower Benue Trough. Results of the second vertical derivative (SVD), tilt angle derivative (TDR) and analytical signal (AS) revealed three major faults: F1, F2, and F3 in NE-SW, ENE-WSW and NW-SE directions respectively. Radially averaged power spectrum and Euler deconvolution revaled depths to the top of magnetic sources as 27 m and 2.46 km for shallow and deeper sources respectively. He concluded that the structures revealed are very useful in hosting important minerals.

Abraham, Itumoh, Chukwu & Onwe (2019) interpreted high resolution airborne magnetic and gravity data, with the aim of locating and mapping regions of shallow Curie point depths (CPDs), crustal thicknesses, and geologic structures supportive of a geothermal system. Spectral analysis of magnetic field anomalies and analysis of gravity anomalies, were subjected to a series of procedures to assess geological structures. Result revealed deeper CPDs within central and southern regions of Okposi, Afikpo and Biase towns in an approximate range of 18.4 to 19.3 km. Shallow CPDs (9.8–17.4 km) were also obtained within Obubra and Abakaliki regions and estimated crustal thickness (Moho) ranged between 26.5 and 35.8 km. They discovered that part of the region with shallow CPD correlated with regions of shallow Moho depths, particularly in Abakaliki, and deeper Moho depths coincide with deeper CPD estimates at Afikpo environs. The estimated geothermal gradient and heat flow values range between 29.0 and 45.0°C/km and 52.2–101.5 mW/m^2, respectively, and fall within values evaluated from deep wells drilled for oil exploration within the adjoining Anambra Basin region. Gravity data evaluations also revealed significant subsurface intrusions within Ugbodo, Obubra and Abakaliki locations. They recommended that regions with shallow depths be explored for possible geothermal power plant location.

Adewumi & Salako (2018) made qualitative analysis of aeromagnetic data of parts of Nasarawa State with the aim of delineating mineral potential zone. Results show that the range of magnetic intensities vary between 51.2 nT to 110.4 nT, with the highs depicting the basements in the Northeast and Akwanga, Wamba and Nasarawa Eggon regions of the Northwest, with promising solid minerals of economic potentials like, gold at Wamba, Tin, Columbite, Tantalite at Akwanga and granite rocks of high radioactive elements, abundant at Nasarawa Eggon. The low magnetic values were denotative of the South's sedimentary environment at Lafia, Doma and Keana, which host some industrial minerals like clay, glass, sands and the Salt Brines at Keana. They revealed that the major high magnetic signatures trend E-W. Lineaments in NE-SW that could host minerals in the study area were delineated using first

and second vertical derivatives. Basement structures were revealed from tilt derivative and analytic signal resultsnand mineral exploration targets which agreed largely that most magnetic minerals are structurally controlled.

Eze, Mamah, Madu, & Onuba (2017) made geological and structural interpretation of possible mineralization zones of parts of Anambra Basin and Southern Benue Trough using airborne geophysical data. Nine (9) high resolution aeromagnetic and radiometric data sets of the Southern Benue Trough and the adjacent Anambra basin were used to reveal subsurface geological structure of that area, magnetic lineaments, shear zones and shallow faults in NE-SW, E-W and NW-SE trends. The ternary image from the evaluated radiometric data shows an improved version of the geological map of that area by delineating the lithology of the ASU River Group, Ezeaku formation, Awgu shale, Nkporo shale, Nsukka formation.

Ikeh, Ugwu & Asielue (2017) made structural interpretation of aeromagnetic data o ver Nkalagu-Igumale of the the Lower Benue Trough. Using 2D spectral analysis, he revealed two depth source models with D_1revealing deep magnetic source bodies of intrabasement discontinuities and faults ranging from 2.15 to 5.25 km while D_2 were shallow magnetic source bodies in the range of 0.35to 99 km. Results delineate possible mineralization and existence of a reasonable cretaceous sedimentary thickness of 3.75 km in the area.

Oha *et al*. (2016) digitally processed and analyzed high resolution airborne magnetic data of parts of the southern Benue Trough. Results from these procedures show that at least 40% of the sedimentary basin contain shallow (<200 m) magmatic bodies, which in most cases are intermediate to mafic intrusive and hyperbysal rocks, and may occur as sills, dikes or batholiths. Magnetic lineaments with a predominant NE–SW trend appear to be more densely distributed around the basement rocks of the Oban Hills and

metamorphosed rocks around the Workum Hills. 3D standard Euler deconvolution and Source Parameter Imaging (SPI^{TM}) techniqueswere employed for depth estimation. Results from the two methods show similar depth estimates. Themaximum depth to basement values for 3D Euler and SPI are 4.40 and 4.85 km with mean depths of0.42 and 0.37 km, respectively.

Onyewuchi & Ugwu (2016) did a geological interpretation of the high resolution aeromagnetic data over Okigwe-Udi area, Southeastern Nigeria which was carried out using 2-D spectral inversion and 3-D Standard Euler Deconvolution methods. Results of the 2-D spectral analysis revealed a two layer depth model with the shallower magnetic sourcedepth varying from 0.223 to 1.048 km (d_1) with an average depth of 0.641 km while the deepermagnetic source bodies (d_2) depth varies from 2.659 km to 3.748 km with an average depth of 3.088 km and predominance of NE-SW trendingstructures within the study area.

Mirianrita, Obiora, Ossai & Okwoli (2015) quantitatively and qualitatively interpreted the aeromagnetic data of Nsukka area, a part of South Eastern Nigeria. Standard Euler deconvolution, Source Parameter Imaging (SPI), Forward and inverse modeling estimated depths and mangnetic susceptibility values which indicated dominance of iron rich minerals like limonite, hematite, pyrrhotite and pyrite, and forms lateritic caps on sandstones. Outcrops of shallow and deep lying magnetic bodies resulting from lateritic bodies in the outcrops within the study area were estimated by Euler depths for four different structural indices (SI = 0.5, 1, 2, 3). Theye resolved that 35 to 150 m depth are good potential water reservoirs for Nsukka and environs and that depths of 1644 to 3082.7 m showed sufficiently thick sediments suitable for hydrocarbon accumulation.

Opara, Onyewuchi, Onyekuru, Okonkwo, Nwosu, Embarga & Nosiri (2014) made structural interpretation of Afikpo sub-basin using evidences from integration of airborne magnetic and Landsat ETM data to provide quick, fast and cost-effective reconnaissance survey of the area. The aeromagnetic and Landsat data were subjected to various image and data enhancement and transformation routines.

Results of the study revealed that the dominant structural trend direction of the study area is in the NE-SW direction. Other lineament trend directions are in the N-S and E-W directions. Presence of high density fracture zone around Afikpo and Ezi-Alayi, 8km SW of Afikpo from lineament density map and two layer depth models from spectral analysis were observed. The shallower magnetic source with average depth of 1.195km as a result of basement rocks intruding into the sedimentary rocks and deeper magnetic source bodies with average depth of 2.660km were delineated, which were associated with intra-basement discontinuities like faults. They concluded that the average sedimentary thickness of 2.660km estimated in the study area is unfavourable for hydrocarbon generation and favourable for quarrying and Pb/Zn exploration based on presence of dolerite Sill which has galena as an associated ore, estimated in the study area.

Anyanwu & Mamah (2013) made structural Interpretation of Abakiliki-Ugep using airbornemagnetic and Landsat Thematic Mapper (TM) Data.Results of the 2-D spectral analysis revealed a two depth models; the shallower magnetic source bodies range in depth (d_1) from 0.035km to 1.285km with an average of 0.656km while the deeper magnetic source bodies range in depth (d_2) from 1.585km to 4.136km with an average depth of 3.096km. A conclusion was drawn on shallower magnetic anomalies resulting due to basement rocks which intruded into the sedimentary rocks while the deeper magnetic anomalies are associated with intra-basement discontinuities associated with faults, and that the average sedimentary thickness of 3.096km estimated in the study area may favor hydrocarbon generation. Results from the study revealed lineaments with trend directions in the N-S, NE-SW, NW-SE and E-W directions, with the NE-SW trends being dominant. The dominant trend of the magnetic data is the NE-SW which agrees with the fault orientation within the Benue Trough.

Onuba *et al.* (2013) reviewed the hydrocarbon prospects on the Lower Benue Trough aeromagnetic data of Afikpo-Ogoja. Geothermal gradients of three zones were delineated. Gradients identified are 16-28˚C/1km for low geothermal gradient, 28-42˚C /km for intermediate geothermal gradient and 42-58˚/km for zones of high geothermal gradients. They revealed that the ASU river group, Ezeaku, Awgu and Nkporo formations which are within intermediate geothermal gradients.

Ugwu *et al.* (2013) interpreted aeromagnetic data over Okigwe and Afikpo areas of the Lower Benue Trough, Nigeria by forward and inverse modelling techniques. Anomalies over their study area were modelled by spherical or dyke-like bodies emplaced at various depths, ranging from 3.0km to 12.7km, either in the sediment or in the metamorphic basement. Results from the magnetic susceptibilities of most of these bodies indicated that they are igneous intrusions with large lateral extents, occurring more at Afikpo than Okigwe area which accounts for more mineralization in Afikpo than Okigwe. The hydrocarbon potential of the area was inferred from the fact that high temperature that prevailed at the time of formation of these minerals is an indicator that the area might not hold any significance of hydrocarbon potentials.

Onuba, Anudu, Chiaghanam, & Anakwuba (2011) evaluated total field aeromagnetic anomalies over Okigwe area. The Regional-Residual and slope methods were applied to delineate lineaments and estimate depth to basement (sedimentary thicknesses). They discovered on the average that deeper magnetic sources ranged from 2 to 4.99km while shallower magnetic sources range from 0.4 to 1.99 km depicting depth to pre-cambrian basement and depth to magnetized bodies respectively.

Obi, Okereke, Obei & George **(**2009) interpreted aeromagnetic data over the Lower Benue Trough to detect the presence of subsurface intrusives and their implications on hydrocarbon evaluation. Thirteen (13) intrusives were revealed from subsurface modeling and they were mainly Rhyolites and Basalts. The

close proximity of the study area to adjacent outcropping Oban massif (basement) influences the emplacement of this intrusives, and areas with greater sediment thickness had an increase in the number of intrusive emplacement. They observed that sediment thickness increased from 1.0km-2.7km and the number of intrusives were more around Nkalagu, Abakaliki, Ikot Ekpene and Uwet areas while regions with lower sediment thickness of 0.5km-1.7km around Udi, Afikpo, and Ugep had few intrusives and low probability stands in producing thermally mature source rocks, making these areas unfavorable for further hydrocarbon investigation.

Onyedim, Awoyemi, Ariyibi & Arubayi (2006) studied the morphology of the basement beneath accumulated sediments in parts of the Middle Benue Trough, Nigeria. Their work resulted in the delineation of the twelve major fault segments which divide the basement rocks into discrete blocks. Thus, they interpreted the boundaries between the segmented basement blocks, as high angle faults, some of which may be shear zone. They formed Source Parameter Imaging from aeromagnetic data of basement rocks and showed that the basement is segmented by faults or blocks whose depths range between 1.0 - 4.5 km. Two major grabens or sub-basins were identified with depths from 2.5 -3 km and 2.5 - 4 km. Computed susceptibilities showed that the basement is not homogeneous but consists of three major magnetic domains within the range of 0.0 to 0.02; 0.02 to 0.04 and 0.04 to 0.06 SI Units respectively.

Bukola, Abbass, Rafiu, Adewuyia, Ejepu, & Adewumi (2021) interpreted airborne magnetic and radiometric datasets over Bida and Zungeru, Niger State, Nigeria, to delineate geological structures such as faults, fracture, folds, joints and geological boundaries that serve as host to gold and associated minerals within the area. They engaged mathematical algorithms such as Reduce to the Equator (RTE), Analytical signal (AS), First Vertical Derivative (FVD) and Centre for Exploration Targeting (CET) in magnetic data processing and Ternary imaging for radiometric data analysis. The result of the 1VD showed

structural features labeled F1 to F8. Linear structures in NE-SW direction were delineated in the Northwestern axis of the study area within contacts of mylonites and amphibolites and the belt-type meta-sediments located around Katakwo, Gindei, Kwange, Gabas and Akusu villages. E-W lineament trends were also delieneated across the mid-region of the study area in Kata-eregi, Sabon-Dagan, Kakaki Minkwoigi, Sunbwagi, Kakagi, Sabon dagga, and Bobo-shiri environs, where the authors suspect majority of volcanic activities to have taken place. Airborne radiometric results displayed mobilization of the immobile thorium Th, synonymous to hydrothermally altered zones. It delineated increase in potassium concentration and decrease in K/Th relation, diagnostic of hydrothermal activities within the area. They concluded that gold mineralisations are found within veins and in the adjacent, highly deformed host rock located below the Federal University of Technology Minna Campus.

Shah, Ryan, Taylor, Gregory, Walsh & Phillips (2021) analyzed aeromagnetic, aeroradiometric, ground gravity, and sample petrophysical and geochemical data of the eastern Adirondack Highlands of northern New York to image and understand these deposits and the geologic framework that hosts dozens of iron oxide-apatite (IOA) deposits containing magnetite and rare earth element (REE)-bearing apatite. Results from aeromagnetic total field data revealed magnetic leucogranite host rock and major structures that likely served as fluid conduits for the hydrothermal system. Band-pass filtering and 3D inversion of magnetic susceptibility data revealed images of these deposits at depth, allowing the inference of plunge directions and relative size. Variations in the surface geology, IOA deposits and several large tailing piles containing REE-bearing apatite were revealed from variable eTh (equivalent Th), K, and t eTh/K data sets. Bouguer gravity anomalies showed limited correspondence to the surface geology, radiometric data, or magnetic data, but showed approximately 10 km wide highs in areas where deposits are observed. 2D forward models of gravity and magnetic data show that deeper, dense material beneath the leucogranite.

The study concluded that geophysical modeling thus suggests that deposits form in structural, thermal, and chemical traps near the distal ends of the hydrothermal system.

Akinsunmade, Dinh, Wojas & Tomecka- Suchoń (2020) interpreted gridded aero-magnetic and radiometric datasets of Isanlu sheet 225 in order to map geological structures and delineate characteristic lithology and potential mineral ore zones in the area. The Reduced to Equator (RTE) routine and Analytic Signal procedures were performed on the the gridded RTE and both enhancement and statistical operations were performed on the aeroradiometric data. Results from the data sets identified lithologic zones, such as metasedimentary rock units, migmatites and igneous rock units occupying varying proportions within the entire area, some localized potential radioactive and precious metal ore zones, major NW-SE deep-seated and surface structures. They recommended the obtained information as serving as a valuable database for further prospective research and mineral exploration in the region.

Suleiman, Okeke, Obiora, & Sani (2020) evaluated and reviewed the magnetic and radiometric geophysical data of the country and results of the investigation prompted some recommendations. From the review, the author revealed maximum deeper depths of 2 km, 4.85 km and 7 km in the Southeastern part of the country, while the north central part of the country revealed maximum deeper depth ranges between 0.5 km, 5.66 km, 3.24 km and 2.4 km. Also, maximum depths of 2.11 km and 1.5 km were revealed in the Northwest as against 2.8 km and 3.6 km in the southwestern part of the country. They discovered from the radiometric method that radiogenic heat production values in most parts of Nigeria fall within the range of 0.01 μWm^{-3} to 5.43 μWm^{-3}. Based on the overall results obtained from the mean concentration, internal and external hazards from the Southsouth and southwest of the country, it was concluded that the soils in the areas were safe for use in constructing dwelling places in the regions but the coverage of the study area was by no means its entirety for the country, hence the authors

recommended the need to carry out more of geophysical surveys on radiometric method in the northwestern part of the country, especially Sokoto Basin. The authors recommended that the paper serve as a reference and stimulate interests in having more geophysical investigations in integrating the two methods with a view to cover some gaps in the field and pay attention to areas uncovered.

Nwobodo *et al.* (2020) interpreted high resolution aeroradiometric data of Wukari and Donga Middle Benue Trough. The analysis of radiometric data revealed concentrations and distribution pattern of primary radioelements such as potassium (K), thorium (Th) and uranium (U). The count rate range of K (0.11 - 2.75%), Th (6.79 - 27.71 ppm) and U (1.69 - 6.21 ppm) were observed within the study area. Results revealed that the relative lower values of Uranium abundances in Wukari area are roughly related to the presence of sedimentary rocks such as carbonates and sandstones while higher values of Uranium abundances in Donga area are roughly related to the presence of metamorphic rock eg: schist. Concentration of potassium was classified dominant around southern and northwestern part of Donga and Wukari areas respectively, which is of great advantage to agriculture in the area, as shown from statistics and map analysis. The authors proved that it was possible to map out areas of radiometric mineralization, viz-a-viz statistical determination of threshold values of U, Th and K%. The threshold value for the total count was estimated as 51 cps and sources of radiation with anomaly > 51 cps were found dominant in southern part of Donga area which proves the area viable for radioelement mineralization. The identified area was thus considered and recommended for further detailed ground spectrometric survey, to determine the radiometric mineralization potentials of the area.

Elkhateeb, Abdellatif, & Elkhateeb (2018) studied the localization of probable gold mineralization zones in a selected part of the central Eastern Desert of Egypt interpreting both aeromagnetic and aeroradiometric data using some enhancement techniques such as first vertical derivative, analytic signal

ratio and ternary radiometric maps, and both Center for Exploration Targeting (CET) grid and porphyry. The results were used to validate the lithology, structures and hydrothermal alteration zones of the area. Rsults indicated dominant NW, NNW, NNE, WNW, NE, E-W and N-S structural directions with the NW-SE trend considered most important and preferred orientation of ore deposits. Favorable regions of ore deposits were mapped and correlated well with known gold occurrences in the study area, known lithological units based on the concentration of radioelements and ratios and hydrothermal alteration zones mapped within younger granites. Known locations of gold mineralization were investigated and also new sites were delineated from the results, as favorable locations for mineralization emplacement.

Olorunsola & Aigbogun (2017) prospected for radiogenic heat production in Southern Anambra basin by assessing aeroradiometric data. High aeroradiometric data from three radio-elements (Uranium, Potassium and Thorium) were used. The lithology was delineated while processing elements in each rock to evaluate radiogenic heat production values. The highest heat produced came from the sedimentary rocks (shale) of 5.43μWm^{-3} around Aimeke and Ogobia. The total airborne radiometric count of radioelements and radiogenic heat maps were produced.

Olorunsola & Aigbogun (2017) interpreted twelve sheets of aeromagnetic and aeroradiometric while correlating and mapping the geothermal and radioactive heat production from Anambra Basin, Nigeria. The data were used to investigate heat sources using the combination of aeromagnetic data to form a composite map-totalmagnetic intensity (TMI) anomaly map and radioelement maps. Curie point depth, geothermal heat flow and magnetic trends were determined from Fourier transformed residual maps. Radioelement ratios were used to estimate the radioactive heat values and surface geology of the study area. Aeromagnetic data results show that shallow magnetic source ranges from 0.59 to 3.86 km and deeper ones between 8.03 to 19.85 km; Curie point depth values range from 14.64 to 38.62 km and

geothermal heat flow values range between 37.54 and 99.02 mWm^{-2} and results of the analysis of the radioactive heat production of the study area range between 0.01 and 5.43 μWm-3. The highest heat produced was from the Shale withradioactive heat production as high as 5.43 μWm-3. He concluded that high geothermal heat flow and radioactive heat values are dominant in Aimeke and Ogobia.

Adepelumia & Falade (2017) interpreted integrated High Resolution Aeromagnetic Data (HRAD) and Radiometric Data to delineate geological lineaments, depths to the basement, uranium concentrations, and remobilizations in parts of the Upper Benue Trough, Northeastern Nigeria. This was with a view to identifying potential zones of uranium occurrence in the area. Anomalies of interest were accentuated and delineated depths estimates were obtained between 150–1941 m from SPI results. The results from the superposition of the horizontal gradient magnitude, analytical signal amplitude, first vertical derivative, and 3D Euler solutions of the HRAD revealed that the study area was dissected by linear structures that trend ENE–WSW, NE– SW, E–W, NNE–SSW, WNW–ESE, and NW–SE; among which the ENE–WSW and NE–SW trends dominated. Analyses of radiometric data showed that uranium ores in the study area were possibly remobilized epigenetically from the granitic rocks, and were later deposited into sedimentary rocks (Bima formation). Burashika group (Bongna hills) and Wawa area of the study area showed vein-type deposits, while the anatectic migmatite in the northeastern region and the uranium rich Bima formation showed both fault/fracture and contact types of deposition. It was also observed the northwesterly and southeasterly, dominant dip direction, dipping faults dip in the same direction as the paleocurrent direction (direction of depositions of sediments), and trend in a direction perpendicular to the hypothetical direction of uranium deposition. The study concluded that the studied area is dissected by several linear structures and the studied area possibly contains deposits of uranium ore, which are likely to be found in the Bima Sandstones of Wade, Shinga, Bima hill, Wuyo, Teli, Bryel, Dali, Barkan,

Gasi, Kunkun, Boragara, Deba, and Gberundi localities; the anatectic migmatite at Kubuku, Whada, and Hyama; and the Bongna hills and agglomerates around Burashika, Kawaba, and Galu.

Coker, Mustapha, Makinde & Adesodun (2013) used sodium iodide (NaI) detector crystal and Canberra series 10 plus multichannel analyser (MCA) to analyse soil samples from Sagamu (Sedimentary terrain) and Abeokuta (Basement complex) in South Western Nigeria. This was done with view to determine activity concentrations due to radium, thorium and potassium so as to delineate between two terrains using radiometric survey. From the result of the activity concentrations of the radionuclides, the mean value of the activity concentrations of 40k (72±48) in sedimentary terrain read higher than 226Ra (35± 20) and 232Thorium (43 ±26) respectively. In the basement complex, the average value of the activity concentration of 40k (80 ±46) read higher also in 226Ra (44±18) and 232Thorium (53 ± 25) respectively. The relatively high value 40k radionuclide was attributed to perceived variations in the environment resulting from past activities. The results showed that the activity concentration of the radionuclides is higher in basement complex than in sedimentary terrain thus, it was concluded that in basement complexes, granites contain high concentrations of uranium, thorium and potassium.

Youssef & Shadia (2013) utilized airborne gamma ray spectrometric data to refine surface geology of igneous, metamorphic and sedimentary rocks, detect radioactive mineralization and monitor environment at southeastern Aswan city, South Eastern Desert, Egypt. Apparent surface concentrations of the naturally occurring radioactive elements; potassium (K), equivalent uranium (eU) and equivalent thorium (eTh) were delineated from the radiometric data because they vary measurably and significantly reveals geology The composite image technique was used to display simultaneously three parameters of the three radioelement concentrations and their three binary ratios on one image which had the efficiency in defining different lithofacies within areas mapped as one continuous lithology. The integration between

surface geological information and geophysical data led to detailing the surface geology and the contacts between different rock units. Significant locations or favourable areas for uranium exploration were defined, where the measurements exceeded (X + 2S), taking X as the arithmetic mean of eU, eU/eTh and eU/K measurements and S as the standard deviation corresponding to each variables. The study area showed the presence of four relatively high uraniferous zones which cannot be ignored and need further ground follow-up as recommended by the authours. They also concluded that most of the well-developed structural lineaments have NW, NE and ENE trends and that the average radiation dose rates in the study area, range from 0.57 to 1.3mSv yr^{-1} average, which are calculated from the exposure rate of each rock unit and whose levels still remain in the safe side to individuals and less than the maximum permissible from the natural gamma radiation sources, except younger granites and ring complex.

Olugbenga (2009) did a preliminary survey of the Kufena Ring Complex, Northern Nigeria, with a view of determining radioelement potentials of the area and for detailed follow-up ground investigation. The study revealed significant albite-riebeckite rocks to radioactive mineralization within the area. Areas with such granite rocks with high counts were recommended for ground-truthing. Results revealed uranium and thorium enrichments in the albite granites between latitudes 10°50'N and longitudes 10o51' and longitude 8°14' and 8°15'E which characterizes the area as a 20% part of possible uranium mineralization. The area's atmospheric and cosmic ray backgrounds have very little effect on the total background activities measured in the survey area as indicated by the author.

Mbah, Onwuemesi, Aniwetalu & Emmanuel (2015) used the VLF-EM technique to explore over Ishiagu area of Abakaliki Basin to determine Pb-Zn mineralization in the sedimentary bedrock. Conductivity contrast between the conductive mineralized veins and host rock generated by induction was used to delineate potential Pb-Zn mineralization. High in-phase and quadrature readings from strong EM

induction were detected in the survey. They discovered that the deep source responses range 4.7% to about 7.6% while shallower source response range from 8.8-17.1%, indicating Pb-Zn mineralized bodies with thich overburden at the Northern part. Current density mineralization also showed the Pb-Zn veins in NW-SE directions and their subordinates in the N-S direction. They discovered very sharp VLF tipper responses at the Central part of the area uncovering shallow depths and broad VLF tipper response at the Northern area, displaying deeper sources. The tipper responses correlate with depth values over Pb-Zn mineralized veins in the range of 10-13 m in the central and 16-22 m in the Northern part. They concluded that the high VLF anomalies delineated from Ishiagu area, SW of Abakaliki basin yielded high conductivity contrast to Pb-Zn mineralization and geologic information of the area.

Okoyeh, Akpan, Egboka, Okolo & Okeke (2015) did geophysical delineation of subsurface fracture associated with Okposi-Uburu Salt Lake Southeastern, Nigeria using 10 Vertical Electrical Sounding (VES) and 2 electrical resistivity tomography (ERT) which were conducted around the vicinity of Okposi and Uburu salt lakes to delineate the depth of salty groundwater and the fracture zone that serve as conduits recharging the salt lakes. 4 to 5 geoelectric layers were delineated from the computer interpreted VES data and theresistivity of the first to the fifth layer range from 82.3 to 397.3 Ωm, 1.7 to 97.9 Ωm, 17.3 to 244.1 Ωm, 5.9 to 71.9 Ωm, 42.7 to 95.8 Ωm and were interpreted as shalely sand, fractured shale, shalestone, fracture shale, shalestone respectively. The thickness of the first layer is approximately 3m while the second layer ranges from 5 m to 25 m and an anomalous low resistivity region was observed from the ERT image at a depth of 5 m confirming the VES results. The low resistivity unit interpreted as fractured shale is an indication of salt water reservoir which also forms significant conduits at the base of the lakes for recharge.

Ugwu & Ezema (2014) used resistivity imaging and induced polarization (IP) technique to locate buried iron slag and furnaces at Lejja, Nsukka, southeastern, Nigeria. The inverse resistivity models revealed the presence of relatively high resistivity materials of about 1090-2600 Ωm buried at depths of 2.55 to 3.70 m at different locations of the survey area. He discovered that inverse chargeability models were consistent with inverse resistivity models in terms of spatial locations of the buried materials and that materials of relatively high chargeability values of 2.09 – 3.09 ms were buried at depth of 2.55 – 3.70 m. They interpreted high resistivity materials as iron slag or burnt bricks used for furnace by iron smelting workers many years ago. He discovered that determination of spatial distribution of buried iron slag and furnaces helped to identify most suitable locations outside the region of the buried materials where hand dug wells can be sited.

Kaura & Mohammed (2017) utilized forty-five (45) Vertical Electrical Soundings (VES) in Awe brine, Nasarawa State, with aim of providing valuable information on the geology of the area, and delineating the brine deposits and their subsurface configuration. The VES result (curves) obtained showed a dominant trend of decreasing resistivity with depth which indicates increase in salinity with depth. The result also revealed four distinct geoelectric layers; top soil with resistivity values between 4.2 Ωm and 282.5 Ωm and thickness of 0.276 m to 19m, the second layer with resistivity values between 11 Ωm and 650Ωm and thickness of 0.502m to 22.47m, third geoelectric layer interpreted of brine zone with low resistivity between 0.12Ωm to 97Ωm and thickness of 0.210 m to 21.56 m at most locations which confirmed the presence of brine deposits in them. The geoelectric section revealed the occurrence of brine deposit between the depth interval of 4 and 38 m in the study area. The fourth layer show resistivity values which vary between 15 Ωm and 34568 Ωm and thickness between 5.34 m to 44.78m. The work concluded that the layer revealed very high resistivity in most VES locations however, and some points showed low resistivity which may be because of infiltration of brine from the upper layer.

Okonkwo & Ezeh (2012) used an integrated ground geophysical exploration for sulphide ore deposits at EPL A40 mine field about 5 km^2, Lower Benue Trough, Nigeria which is underlain by two main geologic units, Abakaliki Shale and the Ezeaku Formation. Self Potential, Resistivity and Electromagnetic methods were utilized. Data was interpreted using surfer 8 computer software and Ms Excel tool Kits. Iso-contour maps of Self Potential, Resistivity and Electromagnetic (EM-VLF) values and profile plots for anomaly variations were constructed. Results showed good anomaly match across Self Potential and Electromagnetic data sets with a corresponding high apparent resistivity values indicative of sulphide ore deposits and trend orientations of anomaly peaks occurring roughly NW – SE and NE – SW in a cross-cutting stress pattern.

Odoh, Utom & Obini (2012) identified EM 34-3 electromagnetic anomalies to determine location and lateral continuity of fractures and to identify hydraulic properties of transmissive fractures in the region of 180-300 meters (highest electrically conductive anomaly) and he also used three (3)Vertical Electrical Soundings (VES) using Schlumberger configuration with AB/2 spacing from 3.5 m to 165 m to determine the formation resistivities and depths to the aquifer. Azimuthal Resistivity Survey (ARS) from graphical interpretation of Survey data was used to map fracture trends generally in the Northwest-Southeast direction at depths of28.3, 40.0 and 50.0 m with the coefficient of anisotropy ranging from 1.15 to 1.55. Because of how valuable ground water remains around the environs of the study area, Kpiri-Kpiri and Ebonyi State at large owing to lack of surface water reservoir supply facilities maintenance culture and inconsistencies attributed to various limiting factors, the integrated suite of surface-geophysical methods was used to characterize the hydrogeology of fractured shale aquifer, study groundwater potential and conditions in details. The investigation showed effectiveness in the use of combined suites for

identification and evaluation of electrically conductive fracture zones from low resistivity values associated with fracture zones inferring high secondary porosity.

Chukwu, Ekine & Ebeniro (2008) used the self-potential method to investigate the zones of mineralization within the Abakaliki High. The survey was done at the left flank of the Enugu-Abakaliki expressway using the one fixed-one movable electrode technique on a grid measuring 2.6km by 2.0km. Seventy-five observations were made within the grid. It was discovered that more than 70% of the study area recorded high negative SP values (-500mv -800mv) indicating a zone of mineralization while some other parts showed zones of little or no mineralization due to their low SP values. The iso-potential map obtained shows a number of elongated centers with maxima between -0.5v and -0.9v.

Olowofela, Ajani & Oladunjoye (2007) used Ground Induced Polarization (GIP) survey alongside dipole-dipole array which consisted of three 600 m lines with dipole separations of 30 m in the E-W direction, covering an area approximately $1km^2$ to investigate sulphide ores in Osina area of Benue. Chargeability measurements were taken in time domain and Percentage Frequency Effect (PFE) in frequency domain from 150 data points. The data sets were inverted and plotted as pseudo-sections were used to get estimated depth of ore deposit from the surface. The result revealed eight (8) anomalous zones of mineralization having attributes of galena, sphalerite and pyrite with resistivity between 100 -300Ωm at an estimated depth of 50 m. Plots of chargeability along three traverse lines showed consistent 20-90mV/V over distance of 90-100 m along the lines. Bulk resistivity of disseminated body investigated yielded high anomalies from inverse resistivity models and showed overburden thickness to the basement sulphide to be about 30 m. Conclusion was reached based on this that the sulphide ore in this area is not economically viable and can be best mined through shafts and tunnels based on various dipping shapes of deposits.

CHAPTER THREE

3.0 METHODOLOGY

This study is all encompassing of various geophysical methods, both airborne and ground techniques. The aerial geophysical techniques include the aeromagnetic and aero-radiometric methods while surface (ground) method include resistivity type and secondary data of re-digitized geologic map of the study area.

3.1 Airborne Data Acquisition

The need to re-invigorate solid mineral sector necessitated Federal Government of Nigeria to embark on provision of quality geosciences through airborne geophysical program. FUGRO Airborne Surveys was awarded contract to carry out survey in 'Phase 1' program representing 44% national coverage of the Benue Trough, parts of South West, Middle Belt up to parts of North Western regions of the country. This project was carried out under the supervision of Nigerian Geological Survey Agency (NGSA), a parastatal of Ministry of Mines and Steel Development (Reford, 2010). After this, World Bank through Sustainable Management of Mineral Resources Project (SMMRP) also commissioned FUGRO for phase II airborne survey to cover 55% Nigeria's landmass. The data were in magnetic, radiometric, gravity and electromagnetic domain which were flown at 500 m line spacing, 80 m terrain clearance generating a total of about 2 million line-km (2000 m) data in a NE-SW direction recorded at 0.1s interval, making it a high

resolution airborne data. These data belong to the phase 1 survey conducted from 2005 to 2007 which was also interpreted by FUGRO. The International Geomagnetic Reference Field model of 2015 referenced to 1984's world geodetic system was used to remove the geomagnetic gradient. The aeromagnetic data was geo-referenced to the Universal Transverse Mercator coordinate system, to make effective comparison with the geological map of the area. Airborne Radiometric and Magnetic data of the area were sourced from the Nigerian Geological Survey Agency (NGSA). Twelve (12) data sheets of aeromagnetic data (Fig.3.1); Nsukka 287, Igumale 288, Ejekwe 289, Ogoja 290, Udi 301, Nkalagu 302,

.

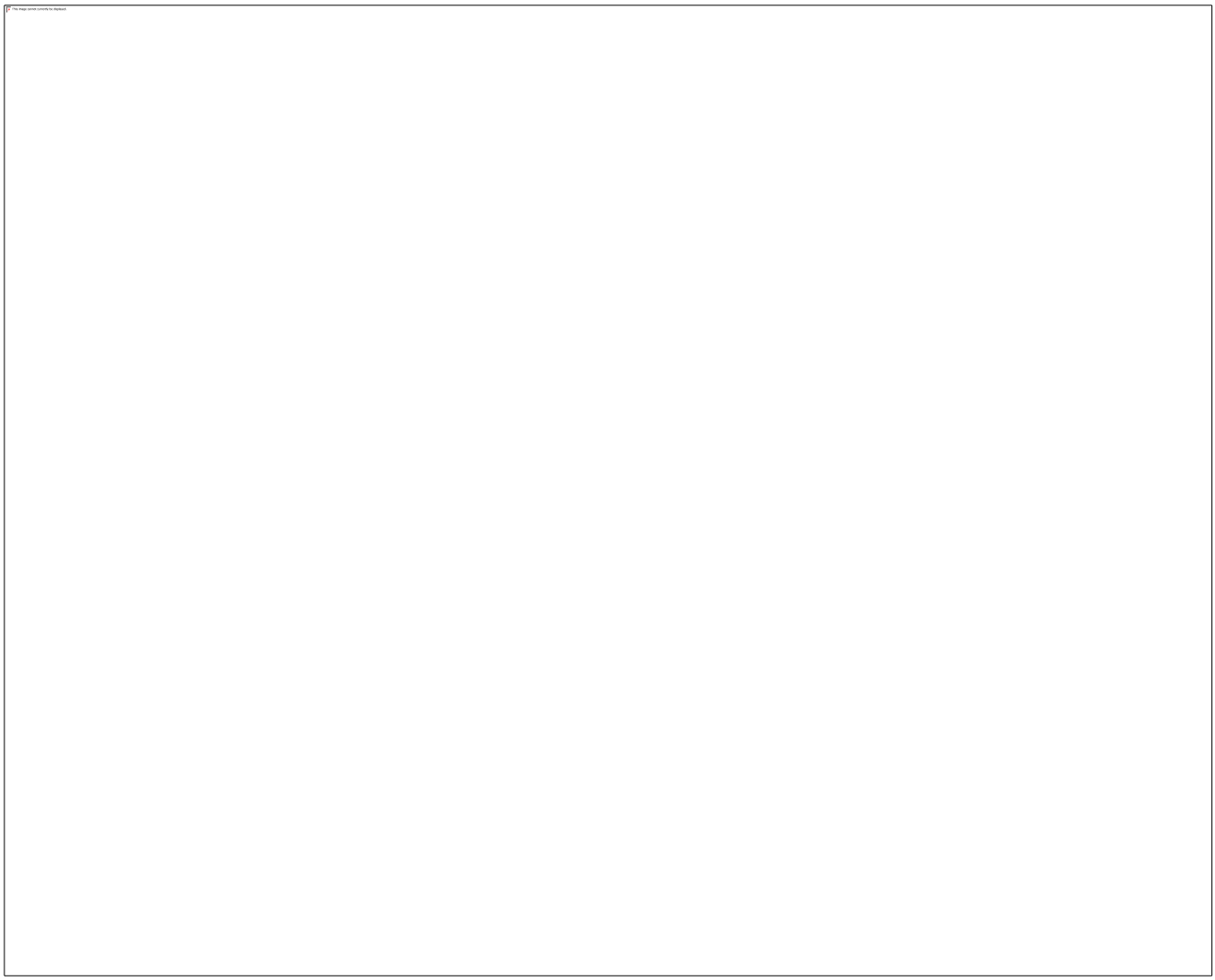

Figure 3.1: Data Sheets for Airborne Magnetic and Radiometric Data of Respective Locations.

Abakaliki 303, Bansara 304, Okigwe 312, Afikpo 313, Ugep 314, and Ikom 315, as contained in Figure 3.1 below, were used. The gridded radioelement counts (total counts) were obtained from NGSA as well, all in grid format.

1. Analysis of Airborne Magnetic Data

There were several reductions made on the magnetic data for easy and straight forward interpretation, These reduction methods employed include filtering, reduction to equator, regional-residual separation, vertical derivatives, estimation of depth of anomalies, analytical signal analysis e.t.c.

1. Filtering

This was conducted on the aeromagnetic anomaly to separate signals of different wavelength so as to isolate and consequently enhance anomalous features with a certain wavelength (Geosoft Oasis Montaj) using high pass, low pass, band pass, non-linear filters, convolution filters, Butterworth filter, Gaussian filter, Susceptibility filter, FFT Multi filter).

2. Reduction To Equator (RTE)

The RTE map was achieved by reducing the residual aeromagnetic anomalies to the equator and performing a low-pass filtering procedure on the final output. This was done on magnetic data because of Nigeria's nearness to the equator than the poles (N and S poles), to minimize polarity effects, because there could be complications while reducing to the pole especially at magnetic latitudes >13°. For this reduction, parameters of longitude, latitude, inclination, declination and IGRF model were applied. RTE correction with magnetic declination of -2.15 and inclination of -13.91 was conducted on the study area utilizing the fast Fourier transform operator. The RTE data were subjected to low pass filtering using a cutoff wavenumber of 0.98-1 km, to remove the effects of topography on the aeromagnetic anomalies. The point of change of short and long wavenumber segments of the power spectrum of the whole data was adopted. RTE was used to center anomaly peaks over their sources, and simplify interpretation.

Anomalies produced depend on the inclination and declination of the local earth field and alignment of the body to the magnetic North. North-South alignment of the anomalies of the magnetic data occurs in the Fast Fourier Transform domain making it unstable.

3. Gridding and obtaining derivatives

The magnetic data in grid format was loaded in a new database and gridded, with the coordinates extracted. Following the gridding, the x-y-z- derivative grids were computed. The first and second vertical derivatives (FVD and SVD) were generated from FFT1D and section tools menu of montaj environment using the MAGMAP.GX environment. The 1D-FFT enabled the application of varieties of fourier domain filters to one –dimensional (line) potential field and other data. Lineament structures were extracted from and superimposed on the FVD map as well (see appendix IV). The VD was done using the FFTVDRV. GX while the HD was performed using the FFTHZDRV.GX.

$$L(\omega) = \omega^n \qquad (3.1)$$

Equation 3.1 guides the VD and HD processes. The whole deconvolution procedure computes for x-y- and z-derivative grids and the system derivative grids displayed as grid images from the grid menu.

4. Analytic Signal

The Analytic signal was calculated (eqn 3.2) from the MAGMAP menu using the parameters of input

$$\text{Asig} = \sqrt{(\partial x)^2 + (\partial y)^2 + (\partial z)^2} \quad \text{(Roest } et\ al.\text{,1992)} \qquad (3.2)$$

where dx = horizontal derivative and dz = vertical derivative, both in (profile units/fid). grid, output analytic signal grid, the default Z-derivative method which is FFT. Large grid sizes were used alongside the convolution method, to save a lot of processing memory and time. The intermediate derivative grids of dx.grd, dy.grd and dz.grd were used to speed up subsequent runs of this process and thus, at the defined location, the analytic signal grids were created. The analytic signal is formed through a combination of horizontal and vertical gradients of a magnetic anomaly. It is independent on directions of magnetization but on the location of the body.

5. Standard Euler Deconvolution

This algorithm emplaced on the menu tool box of oasis montaj software was used to model contacts, dykes cylindrical pipes and spheres, using Euler's homogeneity equation:

$$(x - x_0)\square + (y - y_0)\square(z - z_0)\square = N(B - T) \quad \text{(Thompson, 1982)} \qquad (3.3)$$

Where (x_0, y_0, z_0) = the position of the magnetic source whose total field (T) is detected at (x,y,z).

The Euler 3D menu shows a dialog box which presents parameters of magnetic grid, x-derivative grid dx.grd (GRD), y-derivative grid dy.grd (GRD) and z-derivative grid dz.grd (GRD), solution data base, solution list, structural indices between 0-2, default maximum depth tolerance of 15 %, window size ≥ 3, maximum distance offset from the centre of the search window to the location of the source solution, flight height/survey elevation (depth values). These parameters create new group/line in the Standard_Euler.gdb or the data base of Euler solutions with the channels. In a magnetic field, contacts have structural index of N=0, narrow 2D dyke/sill has a structural index of N=1, a vertical pipe, line, thin bed fault or horizontal cylinder gives N=2 (Thompson, 1982 & Reid, 2007).

6. The Tilt Derivatives

From the MAGMAP menu, the tilt derivative was selected and from the dialog, the parameters of the input grid, output tilt derivative grid (TDR), output horizontal derivative of the TDR (HD-TDR) and the default z-derivative, were used to create the tilt derivative of a grid. The default z-derivative method was done in the FFT using large grids in the convolution process. Equation 3.4 calculates tilt derivative of the grid and optionally, it calculates the total horizontal derivative of the tilt derivative

$$\text{TDR} = \tan^{-1}\left[\frac{\text{FVDR}}{\text{THDR}}\right] = \tan^{-1}\left(\frac{\frac{\partial f}{\partial z}}{\sqrt{(\frac{\partial f}{\partial x})^2+(\frac{\partial f}{\partial y})^2}}\right) \quad \text{(Fairhead } \textit{et al.}\text{, 2019)} \qquad (3.4)$$

It calculates the total horizontal derivative of the analytic signal for ETilt and the analytic signal with tilt derivative for the NTilt. NTilt is an advanced edge detection filter adopted for the delineation of shallow and deep-seated structures, it is the tilt angle of the vertical gradient normalized by the total horizontal gradient of the analytical signal of the same gradient.

N_n Tilt = $\tan^{-1}\left(K^n \frac{\frac{\partial^2 f}{\partial z^2}}{\sqrt{(\frac{\partial AS_0}{\partial x})^2+(\frac{\partial AS_0}{\partial y})^2}} \right)$ (Arisoy & Dikman, 2013). (3.5)

7. Spectral Analysis

The procedures of Okubo, Graf, Hansen, and Ogawa & Tsu (1985) and Tanaka, Okubo & Matsubayashi (1999) were used for spectral analysis. 35 Windows of 55 x 55 km and 110 x 110 km dimensions, with 50% overlap and respective uncertainties for each window were evaluated for spectral analysis procedure. The radial average spectrum was performed using the Oasis FFT routine in frequency domain which converts the data from spatial to frequency domain. For each of the window size/dimension taken, just half of the window gets probed. Shuey, Schellinger, Tripp & Alley**,** 1997 and Ravat, Pignatelli, Nicolosi & Chiappini**,** 2007 gives depth of the spectra as;

Depth of Spectra = $\frac{L}{2\pi}$ (3.6)

Where L = Length of the window

The region of probe is usually the centre of the window and assuming it was a rectangular window,

to probe the centre, the diagonals of the rectangle have to be taken alongside actual points of intersection. The coordinates of those points are taken for Cartesian but numbers are taken for linear plots. Windows around regions of mixed/active anomaly regions were zeroed in and restricted so as to obtain results. A depth solution was calculated for the power spectrum derived from each grid sub-set, located at the centre of the window. Overlapping the windows creates a regular, comprehensive set of depth estimates which can be automated, with the limitation of having least squares best-fit straight line segment always

calculated over the same points of the power spectrum, which if performed manually would not necessarily be the case.

The slope of the spectral plots for the windows taken were used to calculate depth to the top boundary (Z_t) and the centroid of magnetic sources (Z_o) which in turn was used to estimate the bottom depth/Curie point depth (Z_b) of the magnetic source, from the assumptions that 1) the layer extends infinitely far in all horizontal directions, 2) the depth to the top bound of a magnetic source is small compared with the horizontal scale of a magnetic source, and 3) magnetization M(x; y) is a random function of x and y, the power density spectra of the total field anomaly using the relations (Blakely, 1995 and Tanaka, Okubo, & Matsubayashi, 1999).

$$\emptyset_{\Delta T}(|k|) = Ae^{-2|k|Z_t}\left(1 - e^{-|k|(Z_b - Z_t)}\right)^2 \quad (3.7)$$

A = constant and k = wavenumber. For wavelengths less than about twice the thickness of the layer:

$$\ln\left[\emptyset_{\Delta T}(|k|)^{\frac{1}{2}}\right] = \ln B - |k|Z_t \quad (3.8)$$

If B = constant, the upper boundary of a magnetic source Z_t by line of best fit through high wavenumber part of a radially averaged power spectrum $\ln\left[\emptyset_{\Delta T}(|k|)^{\frac{1}{2}}\right]$.

$$\emptyset_{\Delta T}(|k|)^{\frac{1}{2}} = Ce^{-|k|Z_0}\left(e^{-|k|(Z_t - Z_0)} - e^{-|k|(Z_b - Z_0)}\right) \quad (3.9)$$

where C = constant. At long wavelengths;

$$\emptyset_{\Delta T}(|k|)^{\frac{1}{2}} = Ce^{-|k|Z_0}\left(e^{-|k|(-d)} - e^{-|k|(d)}\right) \approx Ce^{-|k|Z_0}\ 2|k|d \quad (3.10)$$

For 2d thickness of the magnetic source, it can be concluded that:

$$\ln\left[\frac{\emptyset_{\Delta T}(|k|)^{\frac{1}{2}}}{\lceil k \rceil}\right] = \ln D - |k|Z_0 \quad (3.11)$$

D = constant. The centroid of the magnetic source Z_0 was estimated by fitting a straight line through the low-wavenumber part of the radially averaged frequency-scaled power spectrum, $\ln\left[\frac{\emptyset_{\Delta T}(|k|)^{\frac{1}{2}}}{\lceil k \rceil}\right]$. The geothermal gradient and heat flow were estimated using the equations as given:

GG $= \frac{dT}{dZ} = \frac{\Theta_c}{Z_b}$ (Tanaka *et al*. (1999); Stampolidis, Kane, Tsokas & Tsourlos**,** 2005; Maden, 2010) (3.12)

where Θ = 580ºC (Curie Temperature). Estimating heat flow (mW/m^2) using the relation;

$q = K(\frac{dT}{dZ}) = \lambda\frac{\Theta_c}{Z_b}$ (Turcotte & Schubert, 1982; Tanaka *et al.*,1999) (3.13)

where k = 2.5 $Wm^{-1}c^{-1}$ and λ = coefficient of thermal conductivity.

8. DSIM3D (3-D MVI)

The magnetic data was used as input to the DSIM3D routine in OASIS MONTAJ software and the parameters of: input grid file, output voxel model file, output residuals grid, output voxel Z cell size (m), output Voxel model depth in cells, distance from observation plane to the top of the model (m), maximum number of main iterations, maximum iterations to solve linear system of equations, RMS error limit to terminate iterations, maximum iterations to solve linear system of equations, RMS error limit to terminate iterations (nT), grid pre-conditioning, initial susceptibility (SI) for all output cells and data noise level (nT), ambient magnetic field strength (nT), ambient magnetic field inclination (degrees), ambient magnetic field declination (degrees), magnetization inclination (degrees), magnetization declination (degrees) were used to obtain the model image. MVI borders on magnetization distribution which is dependent on both direction and magnitude

$\Delta T(\vec{r}) = \frac{\mu_0}{4\pi}\iiint_v^v J(\vec{r}')\hat{j}(\vec{r}').\ \nabla^T\nabla\frac{1}{|\vec{r}-\vec{r}'|}.\hat{B}_0\ dv'$ (Li, 2017) (3.14)

where $J(\vec{r})$ = magnitude and $\hat{j}$ = direction are unknown and $\hat{J} = \hat{B}_0$ when weak magnetization is assumed for susceptibility magnetization.3D magnitude and its direction of magnetization, are

recovered through magnetic inversion in 3D.

The DSIM3D is a Geosoft GX implementation of an inversion approach (Pilkington, 2009) that determines a 3D susceptibility distribution from input magnetic anomaly data. The GX accepts gridded magnetic data as input and produces a subsurface 3D model of the magnetic susceptibilities of an equally spaced array of dipoles. DSIM3D provides a rapid, unconstrained 3D inversion of gridded magnetic data. The original inversion software DSIM3D was written as a FORTRAN code (Pilkington & Bardossy, 2015).

9. Source Parameter Imaging (SPI)

SPI involved an automatic calculation of the source depths from gridded magnetic data and the depth solutions were saved in a database. These depth results are independent of magnetic inclination and declination, so it is not necessary to use a pole/equator-reduced input grid. It used the grids of the: horizontal derivative in the X-direction, the horizontal derivative in the Y-direction, first vertical derivative, tilt derivative, local wavenumber, K, horizontal gradient of the tilt derivative and number of passes of Hanning smoothing filter. SPI assumes a step-type source model (GEOSOFT Inc., 2010).

Depth = 1/Kmax, (3.15)

where Kmax = peak value of the local wavenumber, K, over the step source.

$$K = \sqrt{\left(\frac{dM}{dx}\right)^2 + \left(\frac{dM}{dy}\right)^2} \quad (3.16)$$

The regular and improved source parameter imaging results were gotten using;

$$SPI = \tan^{-1}\left\{\left(\frac{\frac{dM}{dz}}{\sqrt{\frac{dM}{dx}}}\right)^2 + \left\{\frac{dM}{dy}\right\}^2\right\} \text{ (GEOSOFT Inc., 2010 \& Smith } \textit{et.al.}\text{, 1998)} \quad (3.17)$$

M = the total magnetic field anomaly grid, (x,y,z) are three orthogonal gradients of the total magnetic field. SPI.GX first computes Tilt and K. Then it finds peak values Kmax using the Blakely Test (same as SED.GX. These peak values are used to compute depth solutions, which are saved to a database. (GEOSOFT Inc., 2010).

10. Magnetic lineament Extraction

The magnetic lineaments were automatically extracted from the RTE-TMI data in OASIS MONTAJ environment. The CET Grid Analysis system analyzes the filtered texture of the RTE-TMI image to detect lineament along ridges and edges as well as regions of complex structures. The equator reduced data were loaded on MAGMAP and CET (Centre for Exploration Targeting) Grid Analysis menus. Texture analysis of lineations and measurement of their randomness were determined using the Standard deviation;

$\sigma = \sqrt{\left[\frac{1}{N}\sum(X_i - \mu)^2\right]}$(Oasis montaj guide, 2012). (3.18)

For a window with N cells, whose mean value is μ, the standard deviation, σ, of cell values, X_1,is given in eqn 3.18. This overcomes inherent noise in the data and enhances lineation detection and smooth representation of degree of randomness. The lineations were vectorized and skeletonized using a scaled filter wavelength and scales and symmetry of robustness.

The OASIS MONTAJ V. 7.1 was very key in robust airborne magnetic data processing

1. Analysis of Airborne Radiometric Data

The montaj™ 256-Channel Radiometrics Processing extension was used to process and visualize 256 channel spectrometer data. This extension is designed specifically for processing raw airborne radiometric data collected from airborne surveys. In addition to these processing capabilities, this extension provides 1D nonlinear filters to locate and remove data that is recognized as noise. Sophisticated vector postscript drivers were exported to common graphics applications such as Adobe Illustrator and Corel draw for a colourful output and easy selection and editing. Other output formats occur as Geosoft plot files. The 1D non-linear spike-rejection filter was used to remove very short wavelengths but high amplitude features from data. Short wavelengths from geological and other surficial features were removed using this filter. The algorithm is nonlinear because it looks at each data point and decides if that data is noise or a valid signal. If the point is noise, it is simply removed and replaced by an estimate based on surrounding data points. Parts of the data that are not considered noise are not modified, the processing extension imports raw 256-channel data into an array channel, windows full spectrum data to create channels for K, U, TH, and TC. The processing corrects raw data for instrument dead time, applies filters to average data and improve statistics, and corrects survey altitude to Standard Temperature and Pressure (STP), removes

background contributions from aircraft radioactivity, cosmic radiation and atmospheric radon, corrects data by removing spectral overlapping (stripping) and height attenuation effects and converting data to apparent radioelement concentrations calculates radioelement concentration ratios. Results yield maps of radioelement composites and ratios, ternary maps, total count and radioelement concentration ratio maps. MONTAJ 256-CHANNEL RADIOMETRICS in OASIS MONTAJ was employed in radiometric data processing.

3.2. Landsat Data Acquisition

Five Scenes of Landsat 8 data which are Landsat_8_Path_187_ROW_55_2019, Landsat_8_Path_187_56_2019,Landsat_8_Path_189_ROW_55_2019,Landsat_8_Path_187_ROW_56_2019andLandsat_8_Path_188_ROW_55_2019 were downloaded from USGS (United State Geological Services) GoogleEarth Explorer and opened in an environment for visualizing images (ENVI 5.1).

3.2.1 Analysis of Landsat Data

A. Production of the Surface Reflectance Data

Files were transported from ENVI to ArcGIS in order to assign bearings because ENVI 5.1 doesn't make provisions for such. Atmospheric correction was done on the digitized remote sensing data because some reflections didn't eventually get to the earth's surface (atmospheric reflection), this fast line-in-sight atmospheric analysis for spectral hypercube (FLAASH) and subsequent post FLAASH band maths were applied to generate the surface reflectance dat/true colour composite of the study area. There was no need for radiometric correction in Landsat 8 because corrections have been done on the sensors. All the individual scenes making up the extent of the study area were mosaicked together to produce a single dataset from which the exact perimeter of the study area was resized and all unwanted parts were filtered off. This was done by clicking and subjecting the required mosaic to some process involving export of the mosaic as a TIF file of the study area to ENVI environment. The ENVI environment has an existing

algorithm to compute calculations unlike ArcMap which needs input of formula and computation, hence, atmospheric correction involving radiometric calibration and dark subtraction was done to obtain a mosaic picture. The sun angle correction was also conducted on the mosaic:

$$\text{Sun angle correction} = \frac{[(0.0002 \times \text{band}) - 0.1]}{\text{Sin}(\text{Sun Elevation})} \quad (3.19)$$

The Surface Reflectance Data/True Colour Composite of the study area gives reflection of earth's surface material (aggregate of top 15cm of the earth). The Red Green Blue (RGB) bands of spectra has 4, 3, 2 assigned respectively to the EM spectra because the Landsat scene must be represented in these three (3) colours (RGB). Other steps undertaken for data processing were embedded in the atmospheric corrected data where transformations like edge enhancement, high pass filtering, creation of drainage pattern and lineament maps, NDVIs e.t.c were done.

B. Production of Band Ratios and Combinations

Imputation of bands for band rationing was done in ENVI environment where numerator and denominator values were inputted and exported to ARCMap environment for embellishment or fine-tuning of finalized maps, this process was used in the creation of the NDVIusing the Raster calculator.

$$\text{NDVI} = \frac{(NIR - VIS)}{(NIR + VIS)} \quad (3.20)$$

Colour combination is a typical way for displaying multi-spectral imagery by attributing the three primary colours (red-green-blue) to three chosen bands that are simultaneously combined (Prost, 2014). Band rationing therefore raccentuated spectral characteristics of certain materials or minerals by rationing their reflectance band over their absorption band.

C. Landsat Lineament Extraction

Lineament extraction in this study is automatic. It involved contrast stretching of mosaicked scenes of surface reflectance data, followed by image analysis in MVI and Rockwork environments. While creating the lineament map, PC-1 image (in 8-bit grey scale with partial resolution of 15 m) were inputted into the PCI software with lineament map, lineament density map, rosette diagram, gotten as output. PC1 was created using ENVI 5.1 from the Gran Schmidt Pan-Sharpened multispectral image. Automatic extraction was performed using the PC1 lines on the the Geomatica 2018. While working on the extracted lineaments, the compound lines are split into simple lines, lineament attributes are edited and exported as CAD files using ArcMap 10.7. Lineament processing was done in Rockwork_17 to know the trend in the Rose diagram which was further expanded in frequency or in length. The Rose Diagram was imported to ArcMap 10.7 during embellishment of the lineament map and lineament density map. The whole processes undertaken in the Landsat analysis procedure are represented in Figure 3.2 below.

11. PCA Analysis

The PCA uses the listings of image statistics, eigenvalues which give an indication decreasing variance in successive principal coponents and eigen vector loadings which are linear combinations of weighted input images in the principal components. For a principal component transformation using the covariance matrix on reflective bands. The transformation is applied to stretched data where each band has been given a Gaussian-type stretch, to give all bands approximately equal mean and standard deviation values prior to the transformation. The PCA was used to examine eigen vector loadings to decide which of the PC images will concentrate information related directly to theoretical spectral signatures of specific target materials. According to the magnitude and sign of eigenvectors, the technique predicts if the target material is represented by bright yellow or dark red pixels. The PCA was applied to Landsat 8 imagery to identify iron and clay materials and map alteration zones by integrating with geographic information system-based image classification. Spectral reflectance used on the surface alteration is based on the

speactral bands from $\frac{6}{7}$ and $\frac{4}{2}$ which occur between 2-7 and are used to identify surface materials of alteration.

The Software packages used for LANDSAT 8 data processing are ENVI 5.1, PCI GEOMATICA 2018, ROCK WORKS_17, ARCMAP 10.7 and ARCGIS, 10.7. The ENVI 5.1 software package was used to process the Landsat-8 data during the filtering, composite and band ratio stages. The program is efficient in exporting editable files into other grid-readable software programs. ArcMAP software was used to map the Landsat-8 data by providing co-ordinate boundaries and map scales. The digital processing of the Landsat-8 scene and the preliminary lineament mapping were executed using ArcGIS and Geomatica® software. The PCI Geomatica software helped to extract lineaments from the Landsat-8 data and it possesses both manual and automatic lineament extraction tools and ArcMap/ArcGIS V.10.7 was used

Figure 3.2: Summary of Landsat Analysis Procedure

for processed data integration.

3.3. Resistivity Data Acquisition

3.3.1. VES Data Acquisition and Processing

The ohmega **(Ω**) terrameter by Allied Associates Geophysical Ltd was used for taking voltage readings from all sites visited. It has features of: Mode for selecting Resistivity, IP or SP parameters; mA for selecting level of current to be sent to the electrodes and the Go button used to send the desired level of current into the soil. Other tools used were cutlasses for bush clearing of the traverse paths, Compass and GPS for location and hammer for driving electrodes into the ground (see plate 3.3 a-c). The Schlumberger array was used for 2D imaging from two 500 meters perpendicular traverses from areas of high geothermal gradient at Nnam Alok and Amagunze. The current electrode spacings AB/2, were done at 2, 3, 6, 9, 15, 25, 40, 50, 75, 100, 150, 200, 300, 400, 500 meters at both sides from the centre point making a total of 1 km along both traverses and the potential electrodes spacings (AB/2) were expanded at both sides from the centre point as well at 0.5, 2.0, 10 and 20 meters. Repeated readings were done at same current electrode spacings of 9, 75, 300 meters where the potential electrodes were expanded to 2, 10 and 20 meters respectively to allow an increased potential difference to be measured. Figure 3.4 below shows the arrangement of the potential electrodes in between current electrodes while adopting the configuration of Schlumberger. The geometric factor (G) is calculated for Schlumberger array:

$$G = \left[\frac{2\pi}{\frac{1}{r_1} - \frac{1}{r_2} - \frac{1}{r_3} + \frac{1}{r_4}}\right] \quad (3.21)$$

From fig.3.4:

$r_1 = d_1 = s = l\text{-}b$ (3.22)

$r_2 = d_2 = l+b$ (3.23)

$r_3 = d_3 = l+b$ (3.24)

$r_4 = d_4 = l\text{-}b$ (3.25)

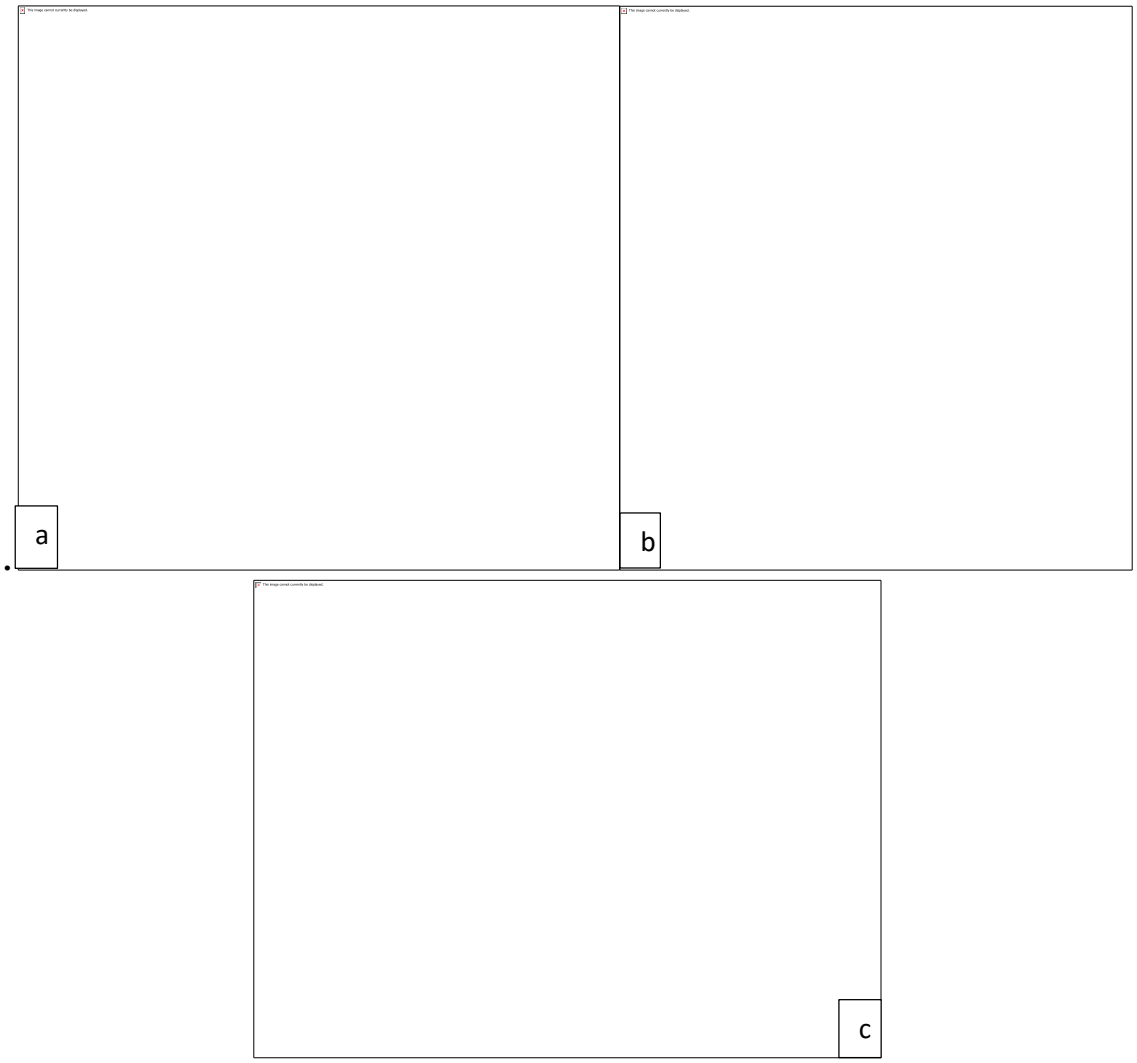

Plates 3.3 (a&b). Instrumentation (c). Features of the ohmega terrameter

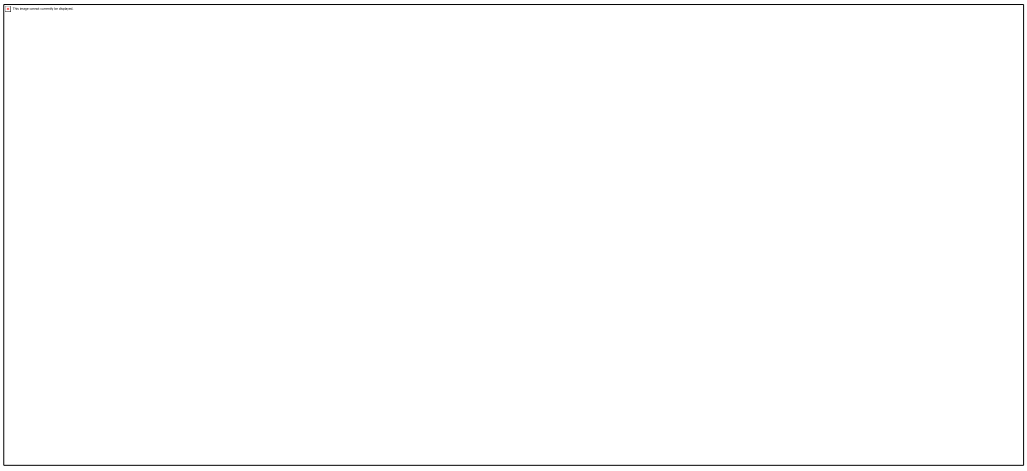

Figure 3.4: Electrical configuration of Schlumberger array (Modified after Telford, Geldart, Sheriff & Keys, 1990)

$$G = 2\pi \left[\frac{1}{\frac{1}{l-b} - \frac{1}{l+b} - \frac{1}{l+b} + \frac{1}{l-b}} \right] \quad (3.26)$$

$$G = 2\pi \left[\frac{1}{l-b} - \frac{1}{l+b} - \frac{1}{l+b} + \frac{1}{l-b} \right]^{-1}$$

$$G = 2\pi \left[\frac{2}{l-b} - \frac{2}{l+b} \right]^{-1}$$

$$G = 2\pi \left[\frac{2l+2b-2l+2b}{(l-b)(l+b)} \right]^{-1}$$

$$G = 2\pi \left[\frac{4b}{l^2-b^2} \right]^{-1}$$

$$G = \frac{2\pi[l^2-b^2]}{4b}$$

$$G = \frac{\pi[l^2-b^2]}{2b} \quad (3.27)$$

Equation 3.27 is the geometric factor for Schlumberger array and a product of the G factor and true resistance gives the apparent resistivity as displayed in the following Chapter 4. Resistivities were derived by multiplying resistance with derived geometric factors and plotting the apparent resistivity values against electrode separation AB/2 (m) on a log-log graph sheet with a resultant field curve produced. Curve filtering and smoothing were done and tentative modelling for determination of resistivity of suspected layers with their corresponding depths (m) pari passu curve matching rules. Resistivity and thickness parameters from each layer of the field curve were obtained from severally re-iterations on the model software. Semi-qualitative/quantitative approach involves computer assisted processes such as forward modelling for plotting of VES curves and 2-D inversion for generation of subsurface images. Resistivity and thickness values of the geoelectric layers gotten from direct and automated iteration of the resistivity curves, yielded the image of the subsurface.

3.3.2. Spontaneous Potential (SP) Data Acquisition and Processing

The mode on the terrameter was used for taking SP readings on site and the cycles for averaging SP readings obtained (plate 3.3c). The millivoltmeter was preferably used because of small voltage and its

preferred requirements of 1 mV resolution, ±10 volts, high input impedance of 10mega ohms and low pass filter greater than 10hertz with a maximum of 10hertz frequency allowance. The SP survey adopted the gradient array and the total field/fixed base and leap frog configurations were both used. For the total field array, measurement of voltage difference between the non-polarizing electrodes on the earth's surface was done by connecting the positive voltmeter lead to the leading electrode, to maintain proper polarity with fixed based. The base station electrode was fixed permanently and only the lead electrode was moved (Figure 3.5a). Spacing was increased by 10 m as movement was made along 35 points of each traverse within the location, causing an increased potential over a total of 350 m traverse. The fixed base array however obtained high quality data having high signal to noise ratio because of higher potentials from large electrode spacing which had already eliminated every susceptibility to soil-electrode contact, electrode polarization and telluric current. The only challenge was the entanglement of wire in the woods of the rainforest vegetation. This array was used in Nsude and Umuobom. The leap frog/gradient array was also used in Umuobom. The lagging and lead electrodes were simultaneously moved at a constant spacing of 10 m all through the 35 points occupied (see fig. 3.5b). The station of measurement is midway between P_1 & P_2 and when negative was changed to positive, the terminals were changed as well, to avoid the alteration of polarity. Areas of mineralization are depicted by very negative amplitude peaks from total field array curves and at amplitude crossover points (figs. 3.6 a&b) at origins from gradient array curves (Olorunfemi. 2014, Adeyemi; Idornigie & Olorunfemi, 2006).

The electrical resistivity technique is very useful in groundwater and mineral exploration and in subsurface mapping through surface measurements. The 2D subsurface imaging of the areas of high geothermal gradient was done using Vertical Electrical Sounding. The formations of the subsurface determine the distribution of electric potential because interstitial water containing dissolves ions, contribute to the conduction of electricity. Since this technique is very efficient at probing greater depths

by increasing the current electrode spread, it was used to check for underlying materials which could have contributed significantly in increased geothermal gradients.

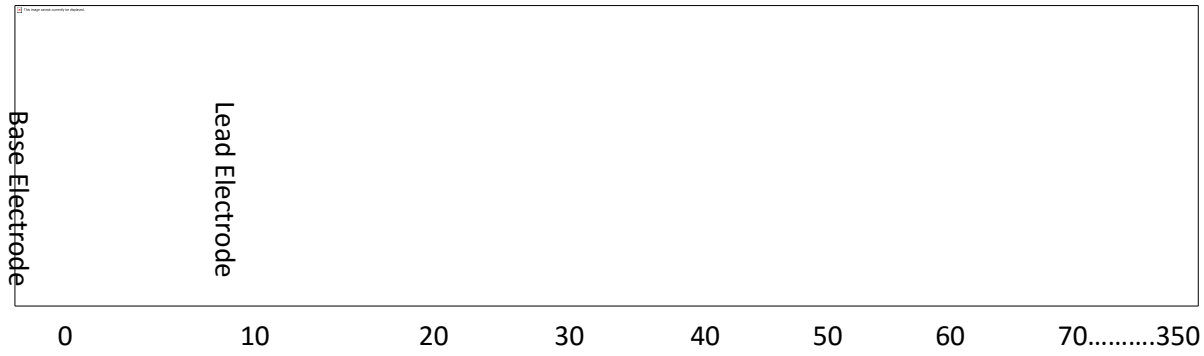

Figure 3.5a: Total field electrode configuration used during the SP Survey

$$0\text{-}10 = \Delta V_{10}$$

$$0\text{-}20 = \Delta V_{10} + \Delta V_{20}$$

$$0\text{-}30 = \Delta V_{10} + \Delta V_{20} + \Delta V_{30}$$

$$0\text{-}40 = \Delta V_{10} + \Delta V_{20} + \Delta V_{30} + \Delta V_{40}$$

$$0\text{-}350 = \Delta V_{10} + \Delta V_{20} + \Delta V_{30} + \Delta V_{40} + \Delta V_{50} + \text{----------} \Delta V_{350}$$

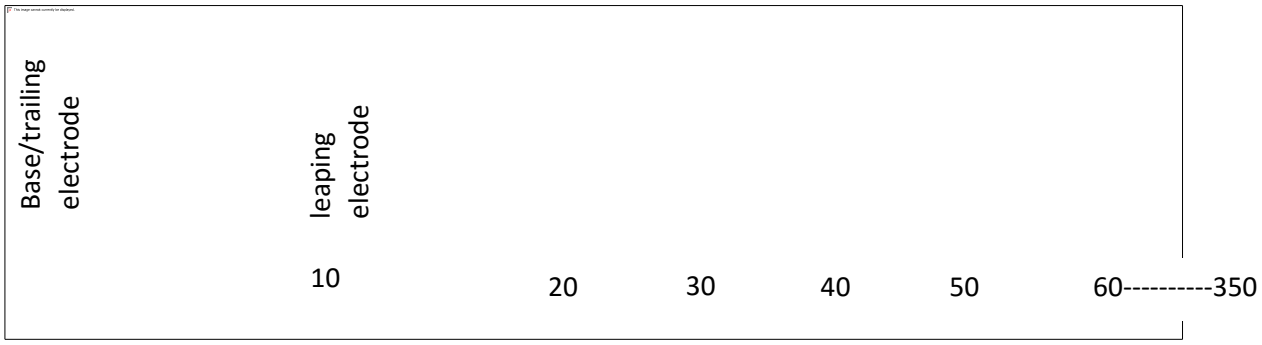

$$\Delta V_{10} = 0\text{ -}10$$

$$\Delta V_{20} = 10\text{-}20$$

$$\Delta V_{30} = 20\text{ -}30$$

$$\Delta V_{350} = 340\text{ -}350$$

Figure 3.5b: Leap frog electrode configuration used during the SP Survey

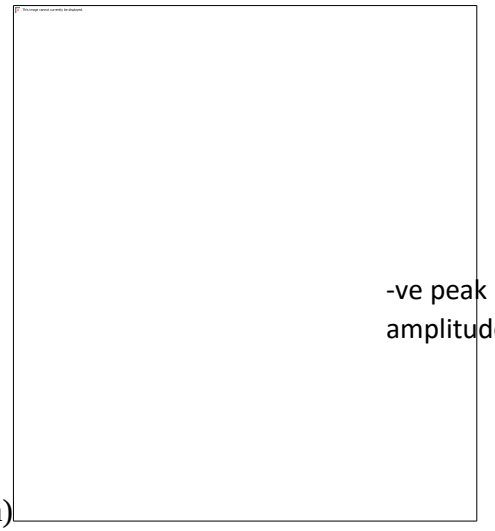

(a)

Total Field Array (TFA)/Fixed Base Array

$X_{\frac{1}{2}} = \sqrt{3}z$ (Adeyemi *et al.*, 2006)

$Z = \frac{X_{\frac{1}{2}}}{\sqrt{3}} = 0.58X_{\frac{1}{2}}$

Figure 3.6a: Generating depth to anomaly using the half width of the TFA (Adeyemi *et al.*, 2006).

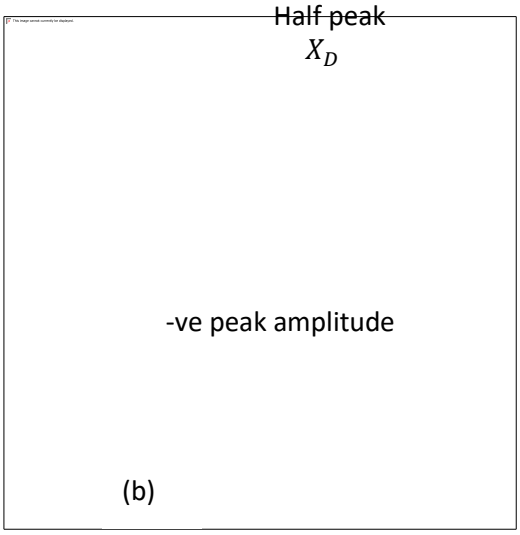

Gradient Array (GA)

$X_D = Z^2\sqrt{3}$ (Adeyemi *et al.*, 2006)

$Z^2 = \frac{X_D}{\sqrt{3}} = 0.58X_D$

$Z = \sqrt{0.58_{X_D}}$

Figure 3.6b: Generating depth to anomaly using the half width of the GA (Adeyemi *et al.*, 2006).

Having plotted apparent resistivities against half current electrode spacing on log-log graphs for each surveyed sounding stations, depths, thicknesses and apparent resistivity layers determined from curve matching techniques were used as model parameters in Res2D environment through repeated iterations on the software to produce curve models. The VES points were geo-referenced using the ARCMap or ARCGIS software. Matlab and MS Excel 2013 were used to plot the amplitude anomaly curves of SP data for delineation of mineralization potentials. Collation of the softwares and applications employed for resistivity data processing are Res2DINV/ZOHDY Software, Matlab and MS Office Excel, 2013.

CHAPTER FOUR

4.0 RESULTS AND DISCUSSION

This section presents the results of analyzed data gotten within the study area to eventually relate the influence of geothermal gradient on ore fluid migration and ore accretion and also reveal the relevance of geologic structures towards constituting the mineral bearing potential of the study area.

The Landsat 8 data obtained were subjected to several image enhancement and transformation routines. From the processed Landsat8 data, band ratios, composites, lineaments, NDVIs and PCIs were obtained. The scenes were chosen due to their near perfect quality (9/9), the virtually non-existent cloud coverage (0.33/100) and due to the relative low solar elevation (34.4◦). Solar elevation (relative to the horizon) can be an impacting factor in choosing a satellite scene. Lower solar elevations are usually preferred for structural focused studies since they enhance terrain morphology and structural features. On the contrary, higher solar elevations usually favour lithological interpretation (Wilson, 1997).

4.1.1 Results from Remote Sensing Data

1. Surface Reflectance Result

All the individual Landsat scenes that make up the extent of the study area were mosaicked together to produce a single dataset from which the exact perimeter of the study area was resized. The Surface

Reflectance Data/True Colour Composite map is a composite of Red Green Blue bands of the visible EM Spectra with 432 assigned respectively to the Spectra. This is done because the Landsat scene must be represented in three (3) colours (RGB) i.e. three (3) variable colour composites (Fig. 4.1).

B. Band Combination Result

The most common composites used in geological remote sensing include: 6-5-2, 6-5-3, 7-5-2, 7-5-3 and 7-6-5 from Landsat 8 bands (Rajesh, 2004). A typical way for displaying multi-spectral imagery by attributing three primary colours (red-green-blue) to three chosen bands that are simultaneously combined

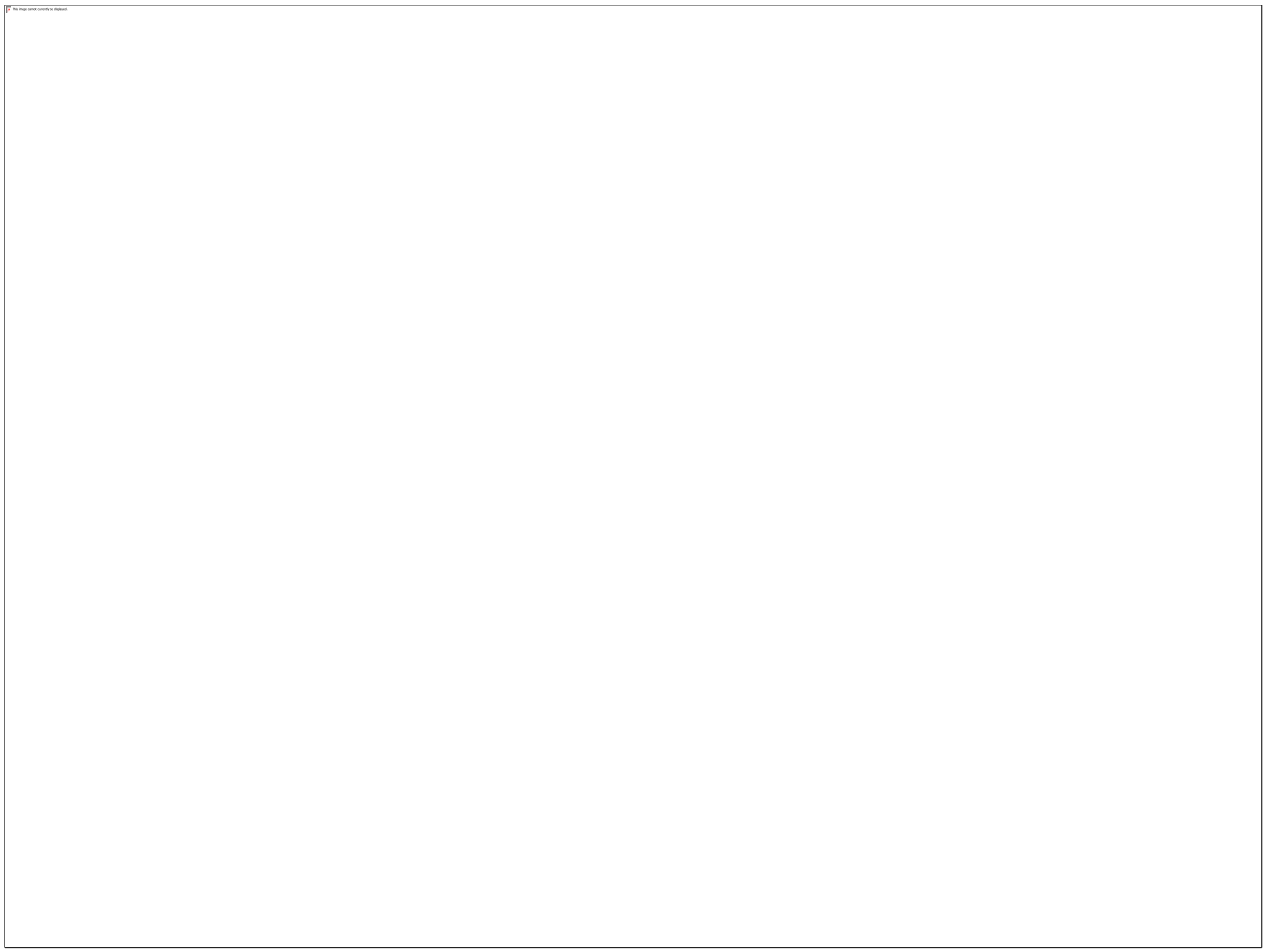

Figure 4.1: True Colour Composite Map

(Prost, 2014).While undertaking this study, several band combinations were generated such as: RGB 432, RGB 753 RGB 576, RGB 754, RGB 567, RGB 10 11 7 and NDVI composite. Drainage patterns and textures, bare rocks and vegetated areas were enhanced in single band images.

1. Composite 576

Band combination with (band 5: 0.845-0.885 μm), a Near Infra Red (NIR) band and two Short Wave Infra Red bands (band 7: 2.100-2.300 μm and band 6:1.560-1.660 μm) of Landsat-8 data was created, allowing a regional discrimination of altered rocks from varying lithologies within the areas. In this full scene image (Fig. 4.2a), altered rocks are depicted by green colour to dark green colour (Prayudi, Arrofi & Ali, 2019).

2. Composite 567

Colours were tweaked and band 567 (Fig.4.2b) was created which allowed same discrimination of altered rocks in cyan from varying lithologies just as 576. Colour variations of orange brown, bright blue and red are depictive vegetations, drainage and state boundaries respectively.

3. Composite 543

RGB 543 color combination image (Fig.4.3), was allocated to near infrared (band 5: 0.845-0.885 μm), red (band 4: 0.64 - 0.67 μm) and green (band 3: 0.53 - 0.59 μm). In this scene image, active vegetation appears red, bare soil appears as cyan or light green patches, the drainage pattern is portrayed in blue lines and crystalline units, in thick red colors.

4. Composite 753

RGB 753 (Fig. 4.4) is a natural colour combination image with an atmospheric removal (Butler,2013) allocated to short wavelength infrared bands (band 7: 2.100-2.300 μm), near infrared (band 5: 0.845-0.885

μm) and green (band 3: 0.53 – 0.59 μm). The resulting scene from image composite 753 shows vegetation in light green to dark green, bare soils in brown with taints of purple colorations, crystalline rock units in dark green lines and drainage pattern portrayed in light blue lines.

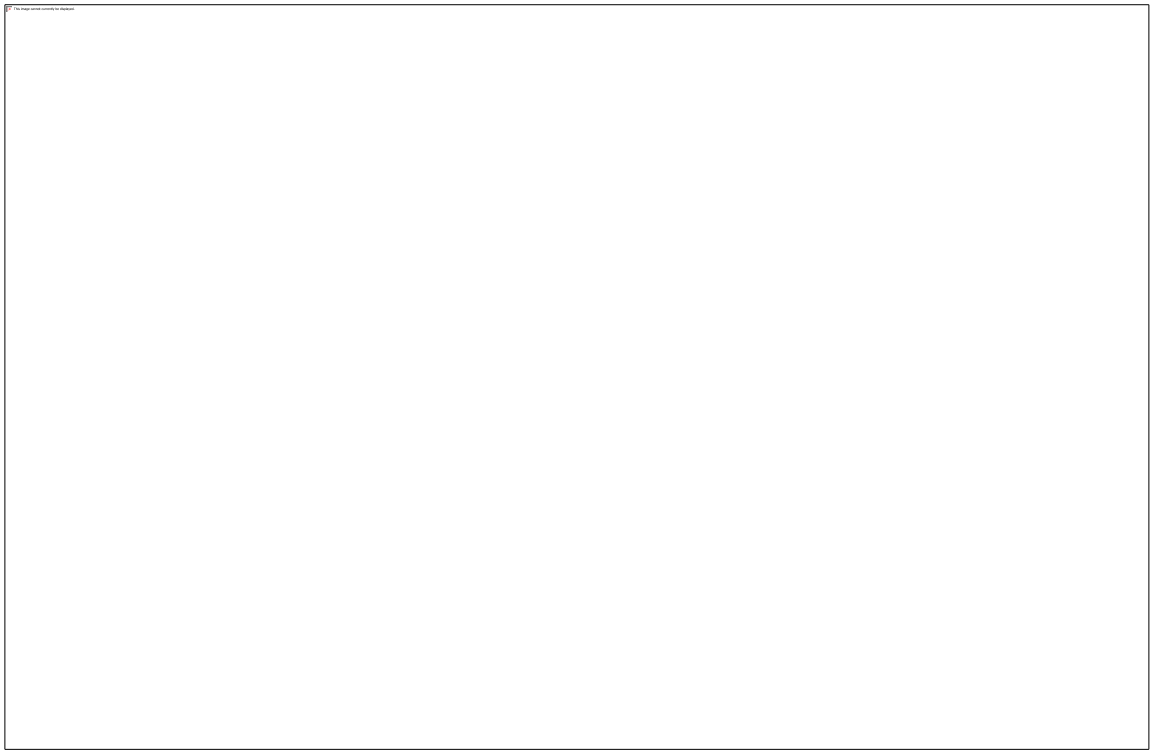

Figure 4.2a: Colour Composite (576) Map

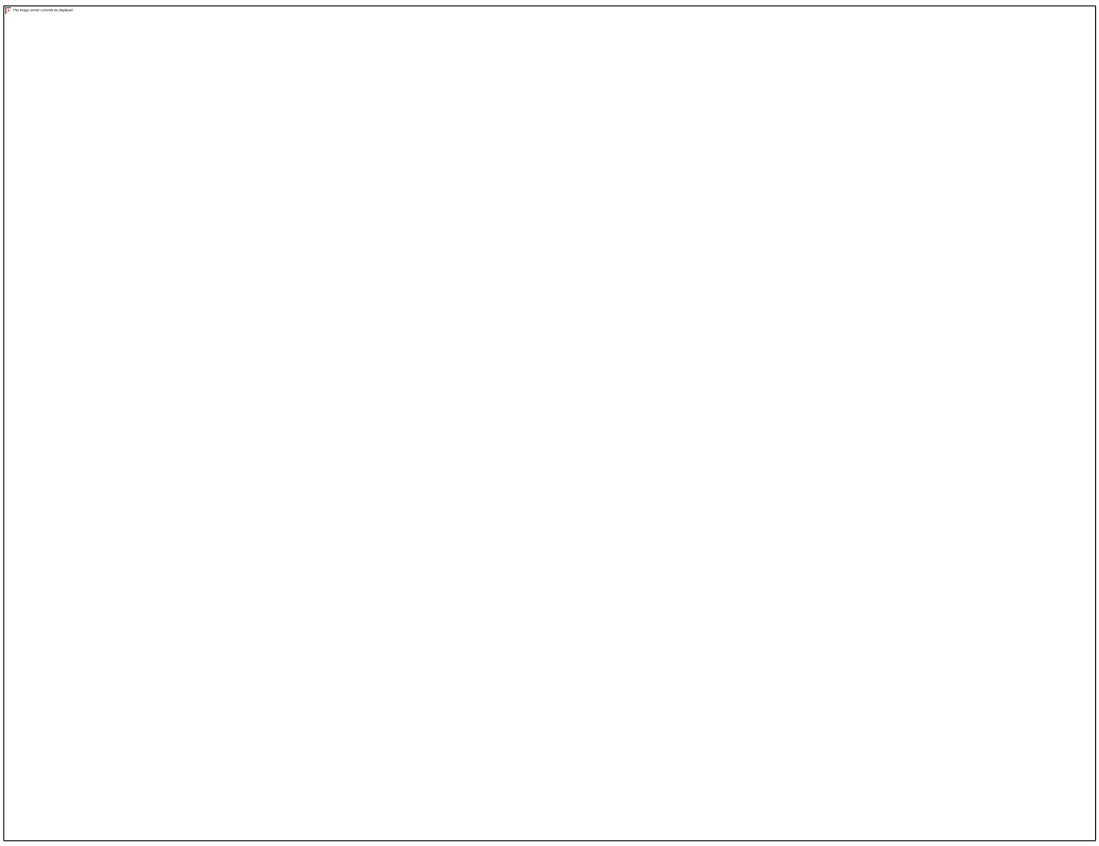

Figure 4.2b: Colour Composite (567) Map

Figure 4.3: False Colour Composite Map, RGB 543

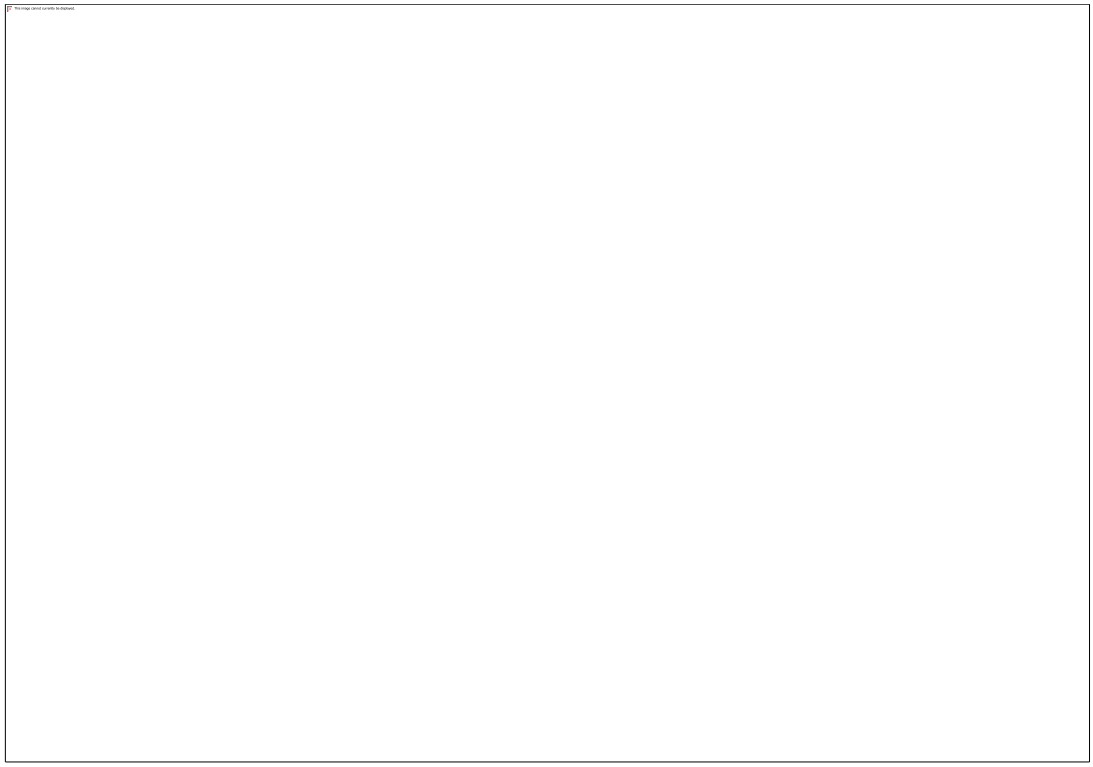

Figure 4.4: False Colour Composite Map, RGB 753

5. Composite 754

RGB 754 color combination image was allocated to short wavelength infrared bands (band 7: 2.100-2.300 μm), near infrared (band 5: 0.845-0.885 μm) and red (band 4: 0.64 – 0.67μm).The light to dark green colouration (Fig.4.5), denotes vegetation, brown with taints of purple colourations denote bare soils, deep violet and dark green colourations are denotative of varying lithologies and the drainage patterns are represented by light blue lines just as represented on the topographic map (Fig.1.2).

6. Composite 10 11 7

Figure 4.6 shows RGB colour combination image of two thermal infrared bands; band 10 (10.30-11.30 μm) and band 11 (11.50-12.50 μm) and short wave infra-red band, band 7 (2.100-2.300 μm) at a regional scale. Because energy measured by TIR bands from the Earth's surface is a function of temperature as well as emissivity of the target, dependent on its chemistry and texture, TIR bands of Landsat-8 have improved quality (Jhabvala, Choi, Waczynski, & Arun, 2011). In this scene, Silicate minerals exhibit spectral features in the TIR because silica emissivity curve shows significant variation in 8.5 μm to 9.30 μm minima in blue and 10.30 to 11.70 μm maxima in pink. (Watanabe & Matsuo, 2003).

C. Band Rationing Result

Band ratios help to accentuate spectral characteristics of certain materials or minerals by rationing their reflectance band over their absorption band (Imbroane, Melenti & Gorgan, 2007). The ratios generated were studied in detail and information extracted was attributed to the color patterns observed from the color composites. The ratios generated ($\frac{6}{7}, \frac{6}{5}, \frac{4}{2}, \frac{5}{4}, \frac{7}{5}, \frac{5}{6}$) were employed to reduce the effects of shadowing as well as to enhance the detection of certain features. Secondary features such as iron stainings and clay

rich sediments are identified in image ratios. Band rationing technique is capable of emphasizing alteration zones and it has been proven powerful in discriminating iron oxide rich rocks from host rocks (Pour & Hashim, 2015).

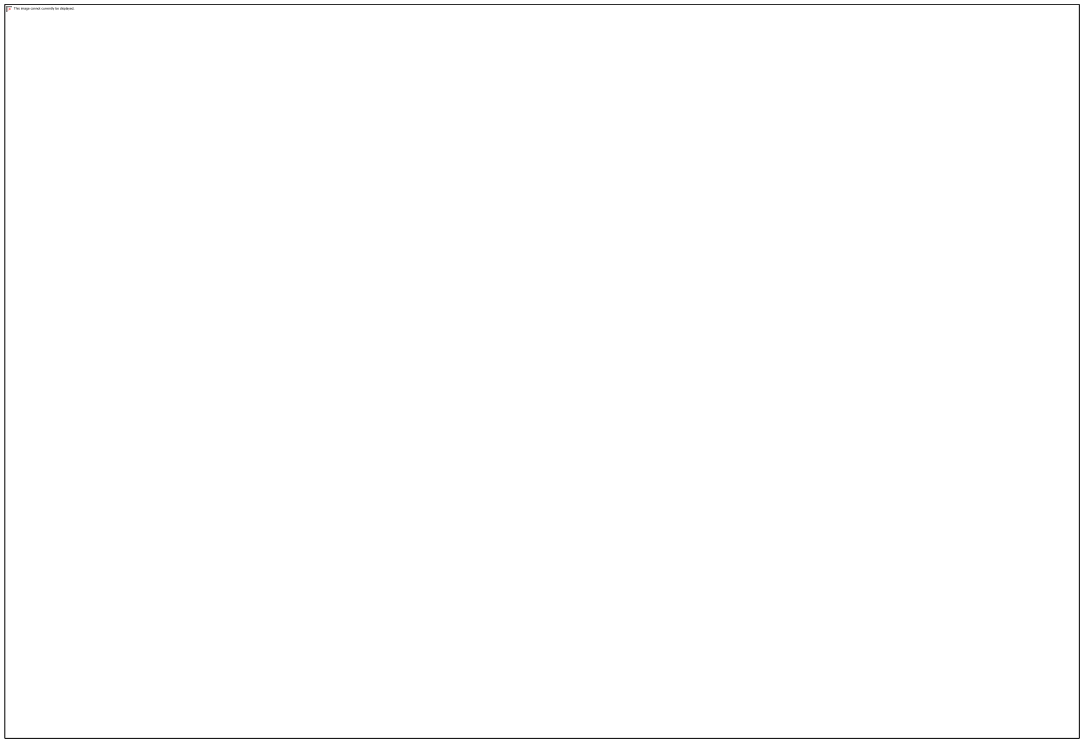

Figure 4.5: RGB 754 Composite Map

Figure 4.6: RGB 10 11 7 Composite Map

1. Ratio 4 on 2

The entire extent of iron oxide in the Landsat scene (Fig.4.7) was gotten from the standard ratio of 4/2. This is because the mapping of iron oxides is carried out using bands 2 and 4 and also because iron oxide/hydroxide minerals such as hematite, jarosite and limonite have high reflectance within 0.63 to 0.69 μm and high absorption within 0.45 to 0.52 μm. Iron Oxide comes out clearly in that band and gives it red appearance (Fig.4.7).

2. 5/6 and 5/4 Ratio Map

Both maps were used for hydroxyl mineral mapping because here, 5/6(Fig.4.8) and 5/4 in appendix, delineate hydroxyl alterations in yellow to red because band 5 reflects hydroxyl mineral in the near infrared (band 5: 0.845-0.885 μm), band 6 identifies altered rocks but highly distorted by vegetation and represents rock absorption features in Short Wave InfraRed region due to Al–OH, Fe, Mg-OH, Si-O-H

and CO_3. Iron oxide/hydroxide minerals have high reflectance in band 4 of 0.63 to 0.69 μm wavelengths and these compositions hence influence higher alterations in yellow to dark red.

3. 6/7 and 7/5 Ratio Map

Ratio image of band 6 over band 7 (Fig. 4.9) distinguishes altered rocks containing clays and alunite from unaltered rocks, where pixels are bright red. The clay minerals such as illite, kaolinite and montmorillonites are discriminated in the ratio images of bands 7 over 5 and 6 over 7. The analysis to map clay and carbonate minerals must incorporate bands 6 and 7 attributed to high reflectance in the range of 1.55 to 1.75 μm and high absorption in 2.08 to 2.35 μm that correspond with ETM+ bands 5 and 7 respectively. Areas colored yellow to red are represented Clay minerals such as illite, kaolinite, and montmorillonite and are discriminated with the ratio image of band 7 over band 5 as bright pixels. Fig.4.10).

Figure 4.7: Ratio $\frac{4}{2}$ Iron Oxide Map

Figure 4.8: Ratio $\frac{5}{6}$Hydroxyl Mineral Map

Figure 4.9: Ratio $\frac{6}{7}$Clay Bearing Mineral Map

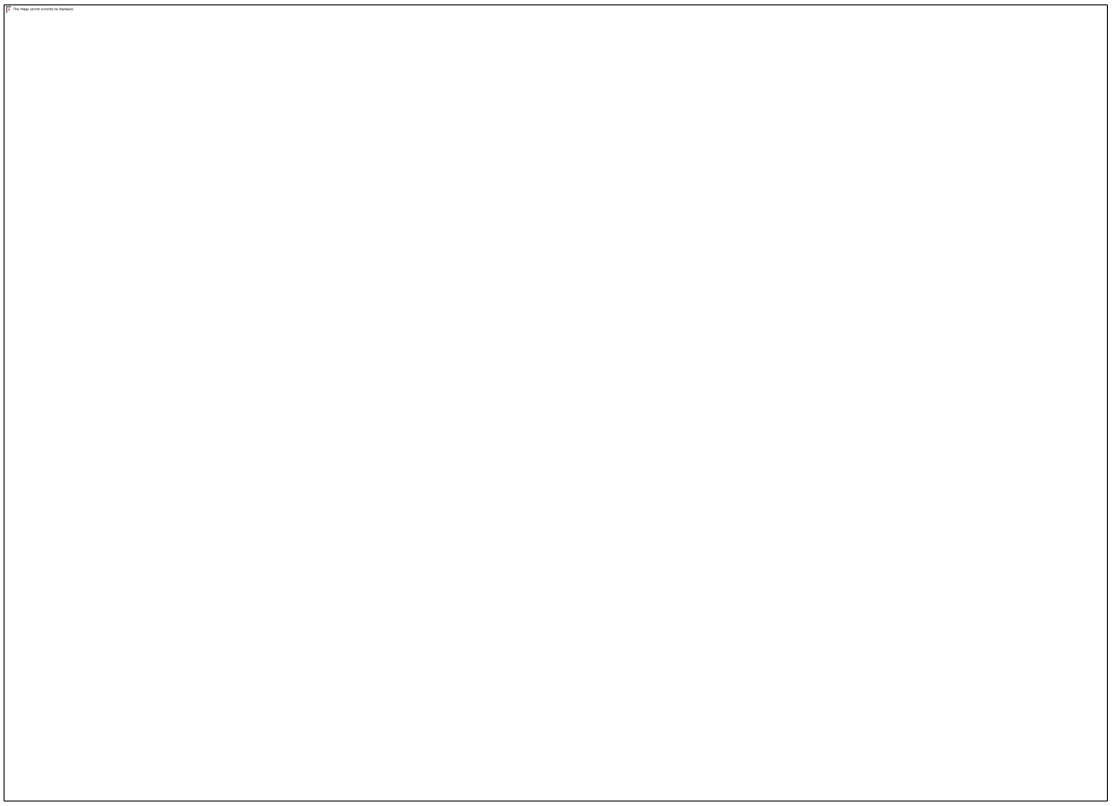

Figure 4.10: Ratio $\frac{7}{5}$Clay Bearing Mineral Map

D. Ratio Composite Results

1. Kaufmann Ratio Composite

Kaufmann band ratio composite; 7/5, 5/4 & 6/7 reveals light cyan to bright blue colours which represent basement outcrops and metasediments (Fig.4.12), their individual composites delineated, have been described above. Areas highlighted in light sea blue are also representative of dense vegetation, the red zones can be related to hydrothermally altered rocks while blue lines represent river channels.

2. Sabin's Ratio Composite

Sabin's ratio composite is established as 4/2, 6/7 and 6/5 as RGB but the designated bands were re-rationed as 4/2, 6/5 and 6/7 as RGB because of non-clarity of the map from the initial ratio. 6/5 is displayed

in Fig.4.11 where there is high reflectance in 1.55 to 1.75 μm and high absorption in 0.845-0.885 μm, it delineates iron alteration in red. Light green areas highlight possible hydrothermal alterations in outcrop rocks just same as red zones from Kauffman ratio, as delineated by Sabin's ratio composite (Fig.4.13).

1. Principal Component Analysis (PCA) Results

The PCA, as estimated from PCA statistics using the parameters in table 4.1., reveals anomalous alterations of clay and iron (Figs. 4.14 & 4.15 respectively) in red colourations in regions they occur.

F. Lineament Results

The Lineament map shows very dense linear structures in the range of 0.46 to 1.03 obtained around the study area, these dense concentrations were observed in the Central, Northeastern, Northwestern and Southwestern parts of the Study Area and in parts of Enugu, Anambra, Imo, Abia, Akwa Ibom, Ebonyi and Cross River states (Figs. 4.16a, 4.16b & 4.16c). These general trends are displayed in Fig.4.16d.

G. Normalized Difference Vegetative Index (NDVI) Results

NDVI results (Fig.4.17) yielded the chlorophyll content of vegetative zones within the study area, bare soils and rocks as well, in lighter green colorations. The higher value of NDVI depicts healthy plants because of their high reflectance of infrared (band 5) and relatively low reflectance of red (band 4) light.

Figure 4.11: Ratio $\frac{6}{5}$Ferrous Mineral Map

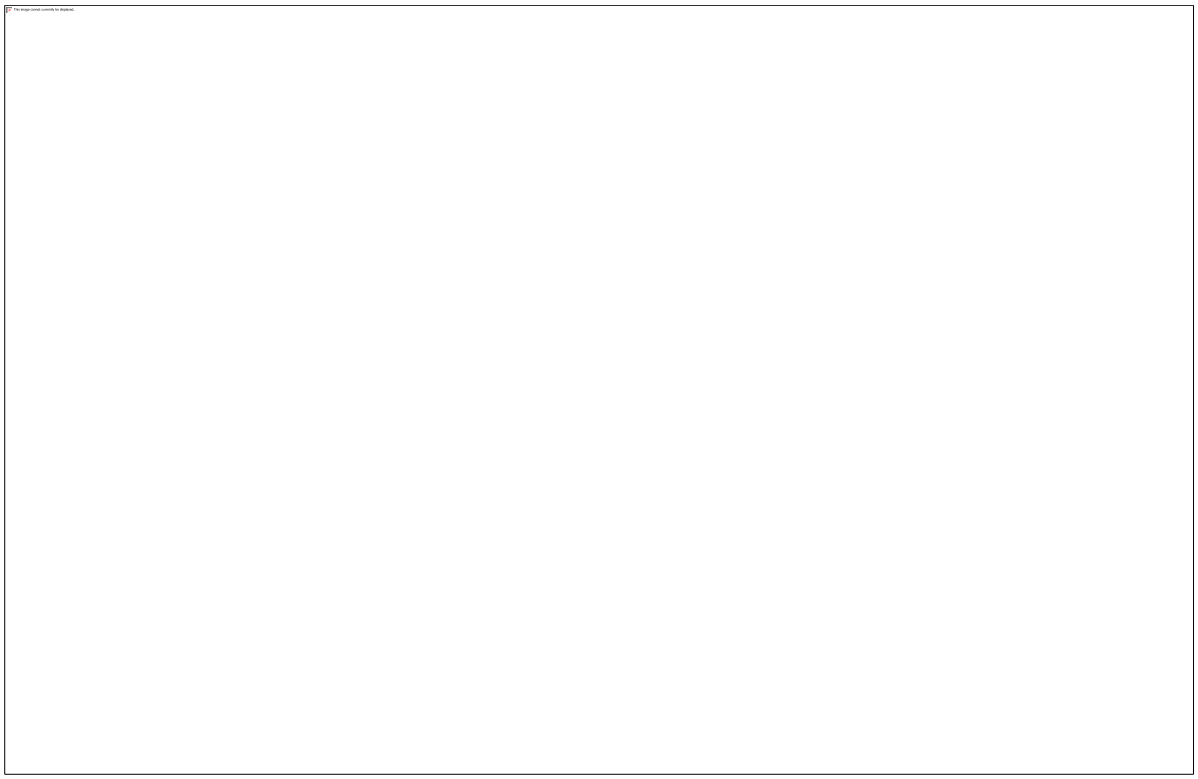

Figure 4.12: Kauffman Ratio $\frac{7}{5}, \frac{5}{4}\frac{6}{7}$Composite Map

Table 4.1a: PCA Clay Statistics

Dims: Full Scene (41,232,480 points)PCA Clay Stat						
Basic Stats	**Min**	**Max**	**Mean**	**Stddev**	**Num**	**Eigenvalue**
Band 2	8798	26399	10566.97693	420.800462	1	5909100.006
Band 5	7922	39892	14280.15298	1022.59638	2	1063581.748
Band 6	6179	65535	12414.17626	1778.897195	3	82835.98362
Band 7	5627	65535	9421.885932	1653.656758	4	66314.55236

Covariance	**Band 2**	**Band 5**	**Band 6**	**Band 7**
Band 2	177073.0292	71903.15331	583022.3176	537815.1545
Band 5	71903.15331	1045703.357	472434.0634	123745.6805
Band 6	583022.3176	472434.0634	1778.897195	2801568.203
Band 7	537815.1545	123745.6805	1653.656758	2734580.674

Correlation	**Band 2**	**Band 5**	**Band 6**	**Band 7**
Band 2	1	0.167097	0.778858	0.772879
Band 5	0.167097	1	0.259708	0.073178
Band 6	0.778858	0.259708	1	0.952368
Band 7	0.772879	0.073178	0.952368	1

Eigenvector	**Band 2**	**Band 5**	**Band 6**	**Band 7**
Band 2	0.137625	0.089561	0.726147	0.667644
Band 5	0.000424	-0.966507	-0.098693	0.236906
Band 6	0.074863	0.23861	-0.678601	0.690624
Band 7	0.987651	-0.030151	-0.049705	-0.145484

Table 4.1b: PCA Iron Statistics

Dims: Full Scene (41,232,480 points) PCA Iron Stat						
Basic Stats	**Min**	**Max**	**Mean**	**Stdev**	**Num**	**Eigenvalue**
Band 2	8798	26399	10566.97693	420.800462	1	3928952.293
Band 4	6981	32073	9356.421618	819.795962	2	984827.2078

Band 5	7922	39892	14280.15298	1022.59638	3	137538.8283
Band 6	6179	65535	12414.17626	1778.897195	4	7998.705686

Covariance	**Band 2**	**Band 4**	**Band 5**	**Band 6**
Band 2	177073.0292	323008.245	71903.15331	583022.3176
Band 4	323008.245	672065.4197	77598.89136	1318680.4
Band 5	71903.15331	77598.89136	1045703.357	472434.0634
Band 6	583022.3176	1318680.4	472434.0634	3164475.23

Correlation	**Band 2**	**Band 4**	**Band 5**	**Band 6**
Band 2	1	0.936336	0.167097	0.778858
Band 4	0.936336	1	0.092565	0.904238
Band 5	0.167097	0.092565	1	0.259708
Band 6	0.778858	0.904238	0.259708	1

Eigenvector	**Band 2**	**Band 4**	**Band 5**	**Band 6**
Band 2	0.174768	0.38266	0.16095	0.892817
Band 4	0.049662	0.182046	-0.978033	0.088566
Band 5	0.601735	0.666548	0.116189	-0.424416
Band 6	0.777757	-0.613306	-0.06361	0.122084

Figure 4.13: Sabin's Ratio $\frac{4}{2}, \frac{6}{5}\frac{6}{7}$ Composite Map

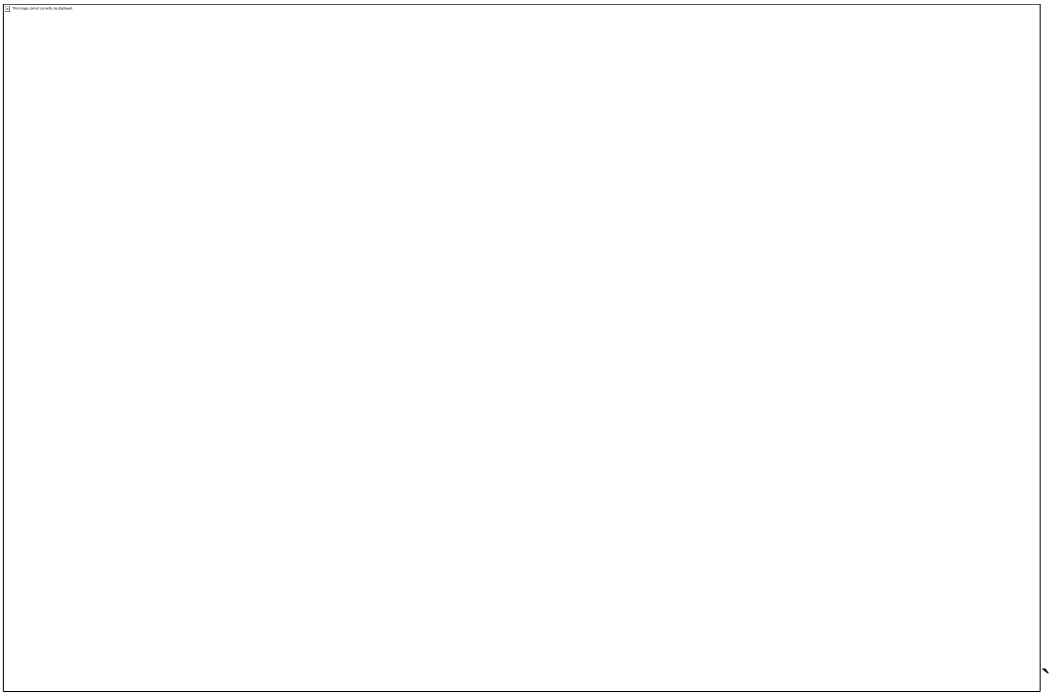

Figure 4.14: PCA Clay Plot

Figure 4.15: PCA Iron Plot

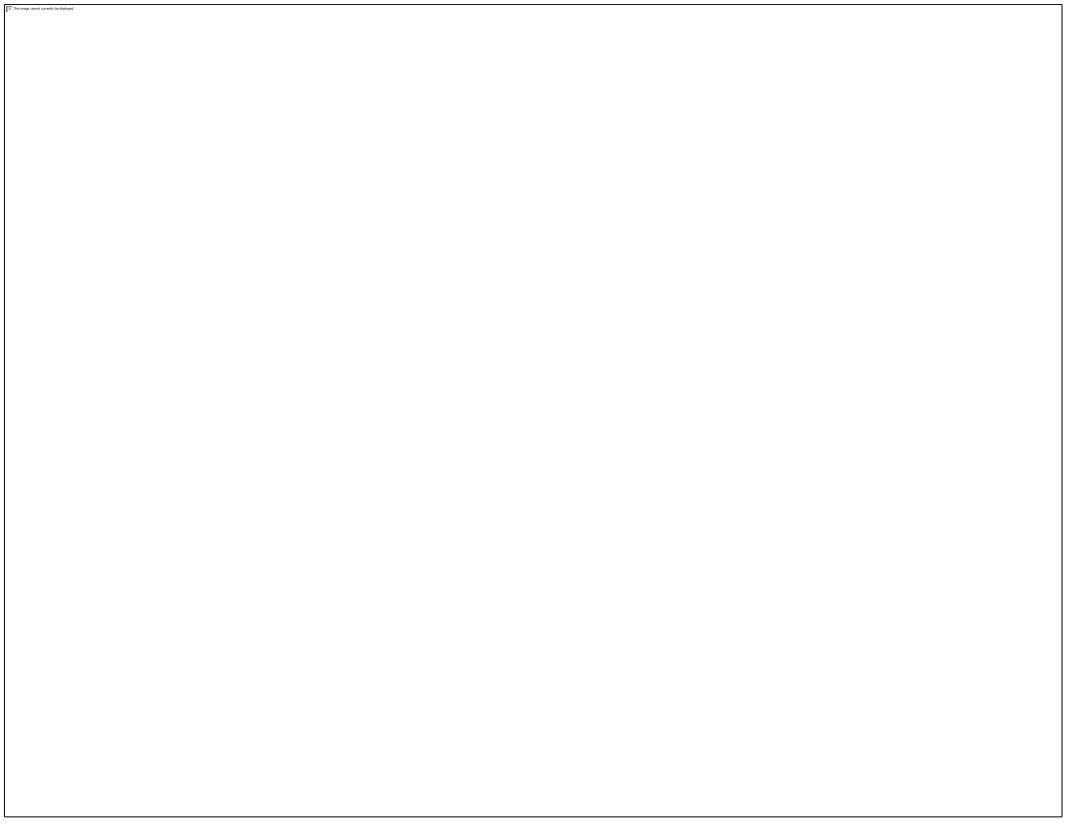

Figure 4.16a: Lineament Map of the Study Area

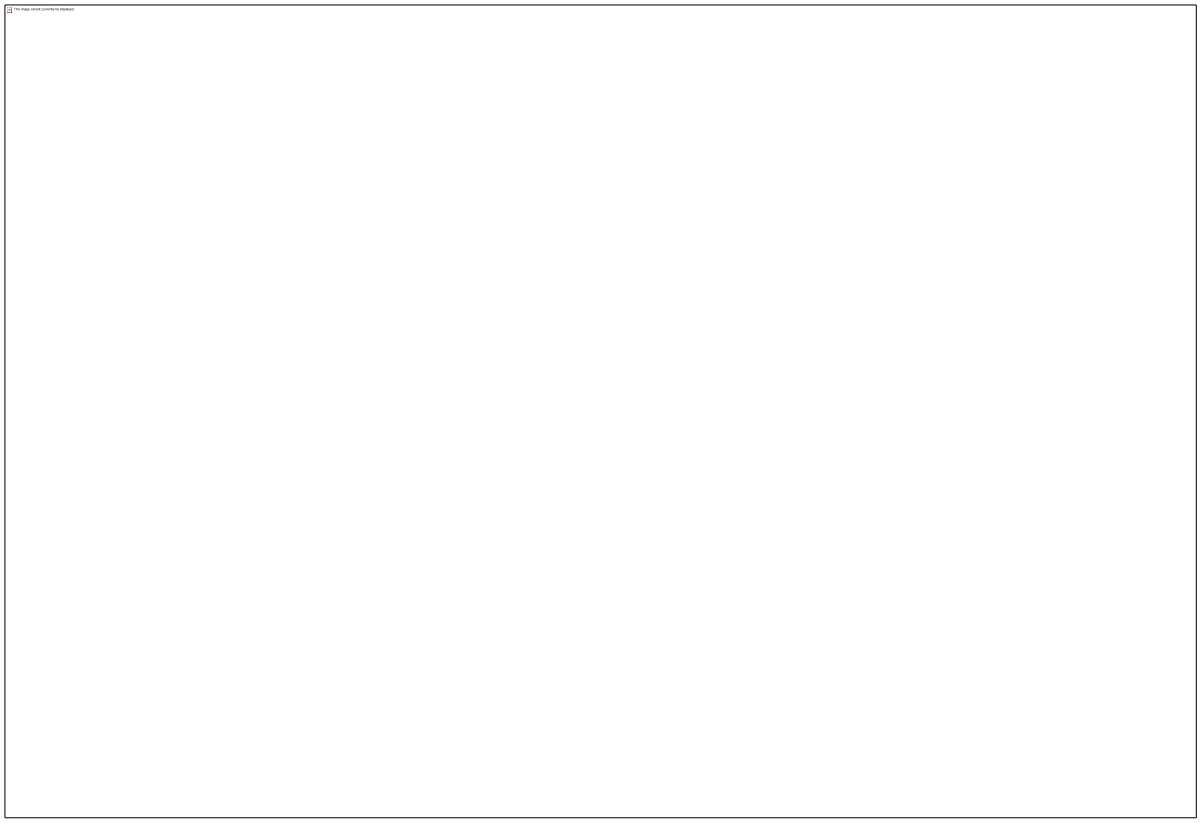

Figure 4.16b: Lineament Density Map of the Study Area

Figure 4.16c: Automatically Extracted Lineaments and Trends

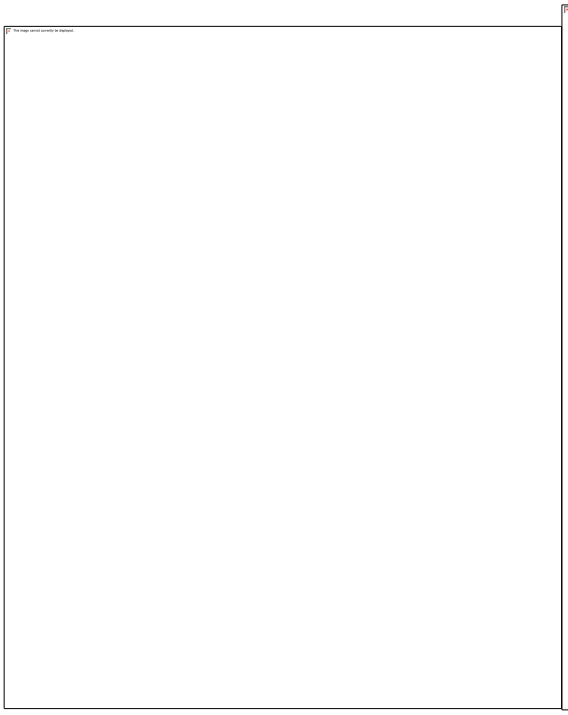

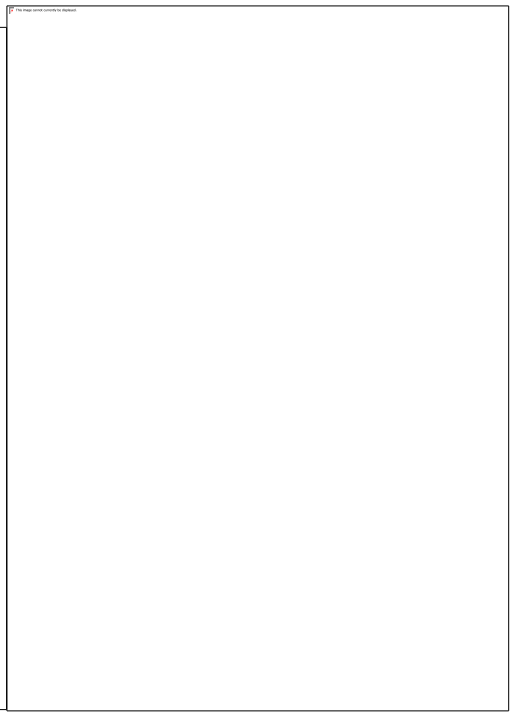

Figure 4.16d: Rossette Plot and Summary of Lineament Trend Within the Study Area

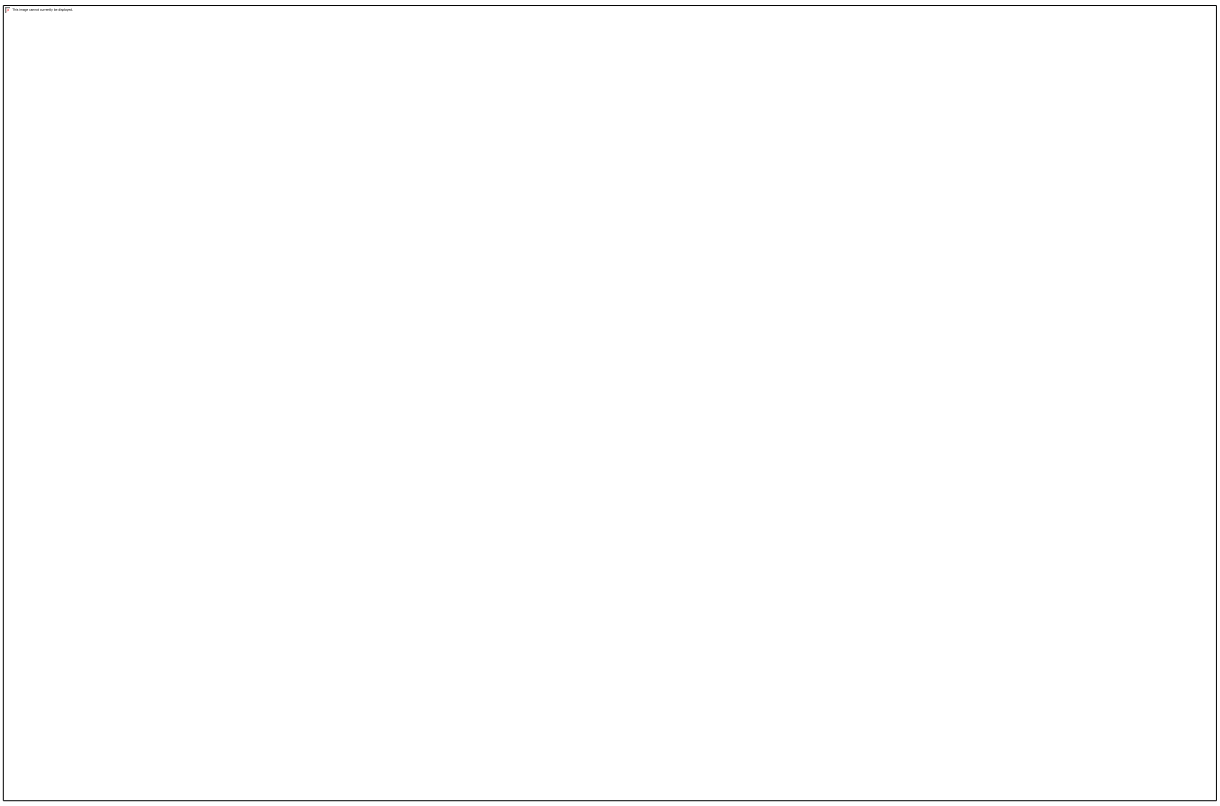

Figure 4.17: Normalized Difference Vegetative Index Maps with Varied NDVI Values

4.1.2 Results from Aeromagnetic Data

Both regional and residual magnetic values make up the Total Magnetic Field Intensity (TMFI) map which comprises both the magnitude of the earth's field plus the anomalous field. The aeromagnetic anomaly map usually given by NGSA is almost a residual data because of 32000nT or gamma subtracted from it but the actual Total magnetic field intensity data still has 32000nT or gamma (the regional) not subtracted from it. The removal of regional fields allows the TMI data easy manipulation and makes it less cumbersome to the user. The TMI reveals the magnetic susceptibility of the basement from long wavelength anomalies, localized bodies and overburden/subsurface sediments, from short wavelength anomalies which invariably estimates thickness of overlying sediments (Fig.4.18).

A. The Reduced to the Equator -Total Magnetic Intensity (RTE-TMI) Map

Jain (1988) accepted the RTE technique as being preferable at lower latitudes. This was so here since the study area occurs at lower latitudes. From the RTE-TMI map (Fig.4.19), there are various ranges and corresponding values representing varying degrees of magnetizations; -45.9 to 14.5 (nT) is denoted by blue; 14.7 to 51.35 (nT) by green; 54 to 59 (nT) by yellow; 64.5 to 87 (nT) by brown to dark orange; 94.2 to 121.7 (nT) by red and high magnetic response denoted by values > 122 nT in purple.

B. Spectral Analysis

Inserted squares (Fig. 4.19) are examples of the 55 x 55 km, 50% overlapping data windows selected for spectral analysis procedures. Spectral plots for 55 x 55 km windows were taken across the study area and the display is for the first four windows out of the 35 windows sampled. From the 55x 55 km window, a total of 7 sections were made and plots of power spectrum, Ln (power), with frequency values were made against wave number in cycles/km with their depths obtained. Figures 4.20(a), (b), (c), and (d) are spectral plots used to compute depths to the top of magnetic sources (DDT/dz) which is the depth of the second topmost layer denoting high frequency signals and long wavelength, while figs.4.20 (e), (f), (g), and (h)

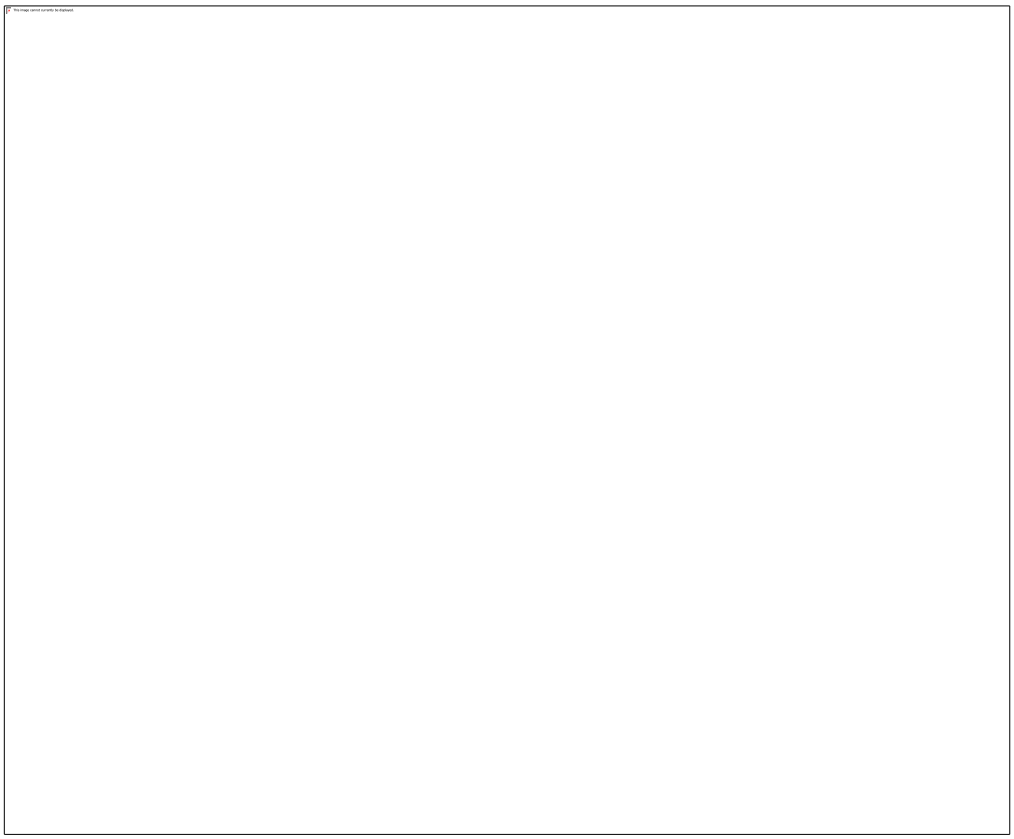

Figure 4.18: Aeromagnetic Anomaly (TMI) Map as obtained from NGSA.

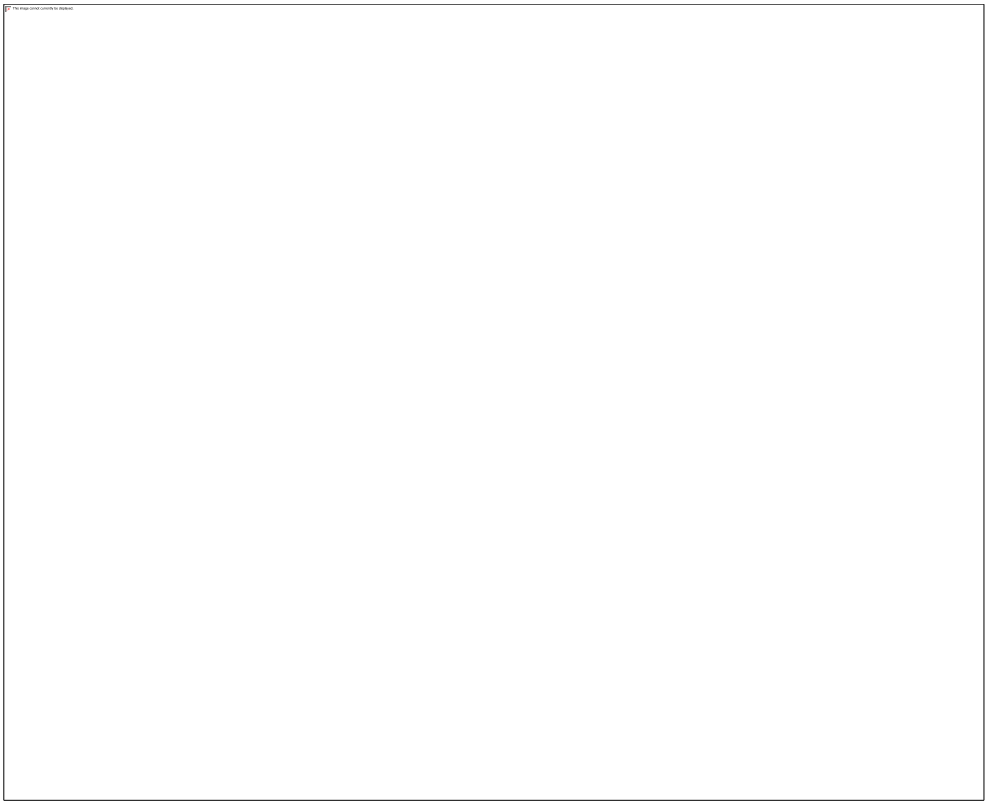

Figure 4.19: RTE Geomagnetic Anomaly Map with inserted squares of 55 x 55 km

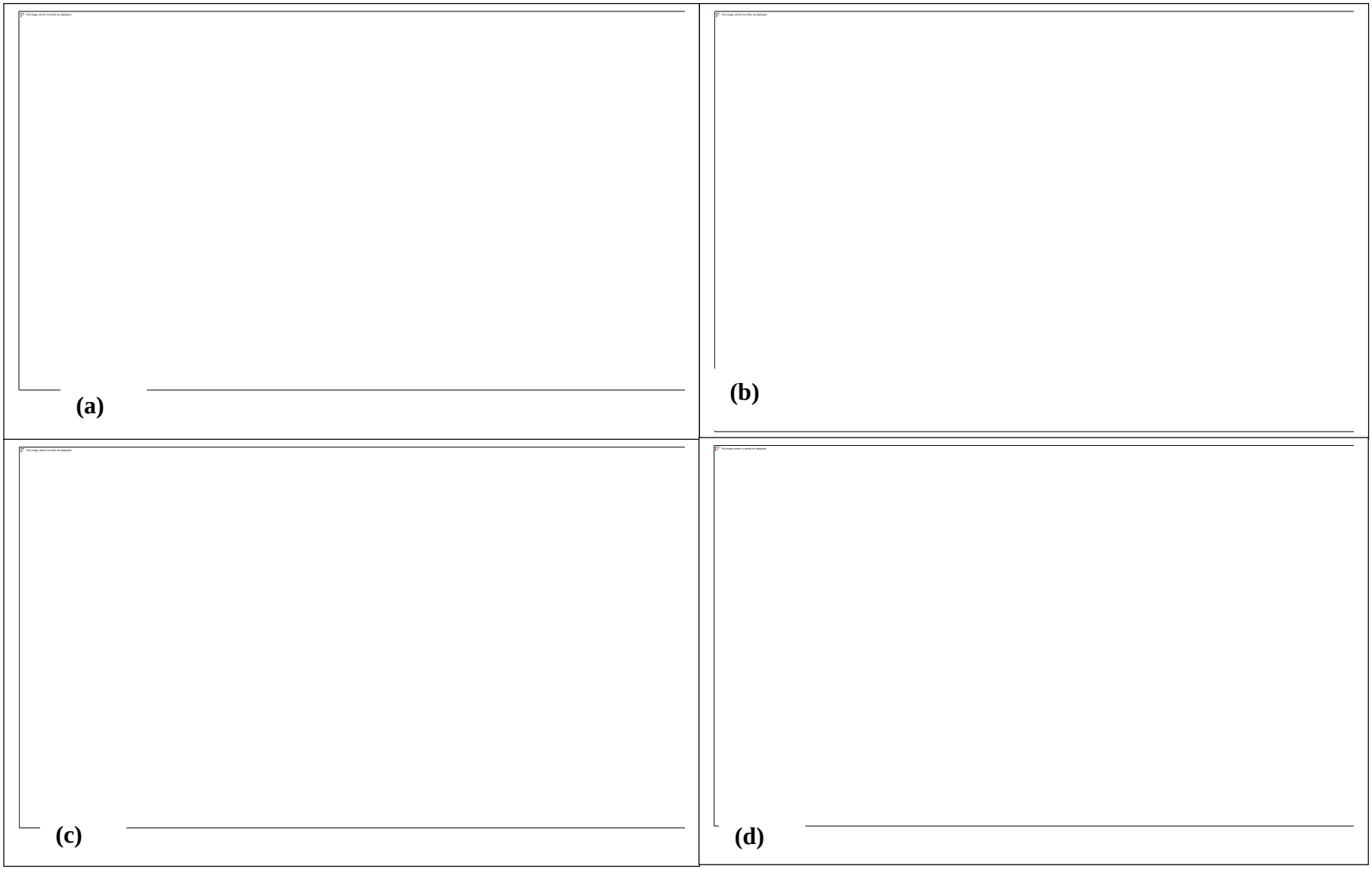

Figure 4.20 (a-d): Spectral plots for the 55 x 55 km windows taken across the study area used to compute depths to the top of magnetic sources

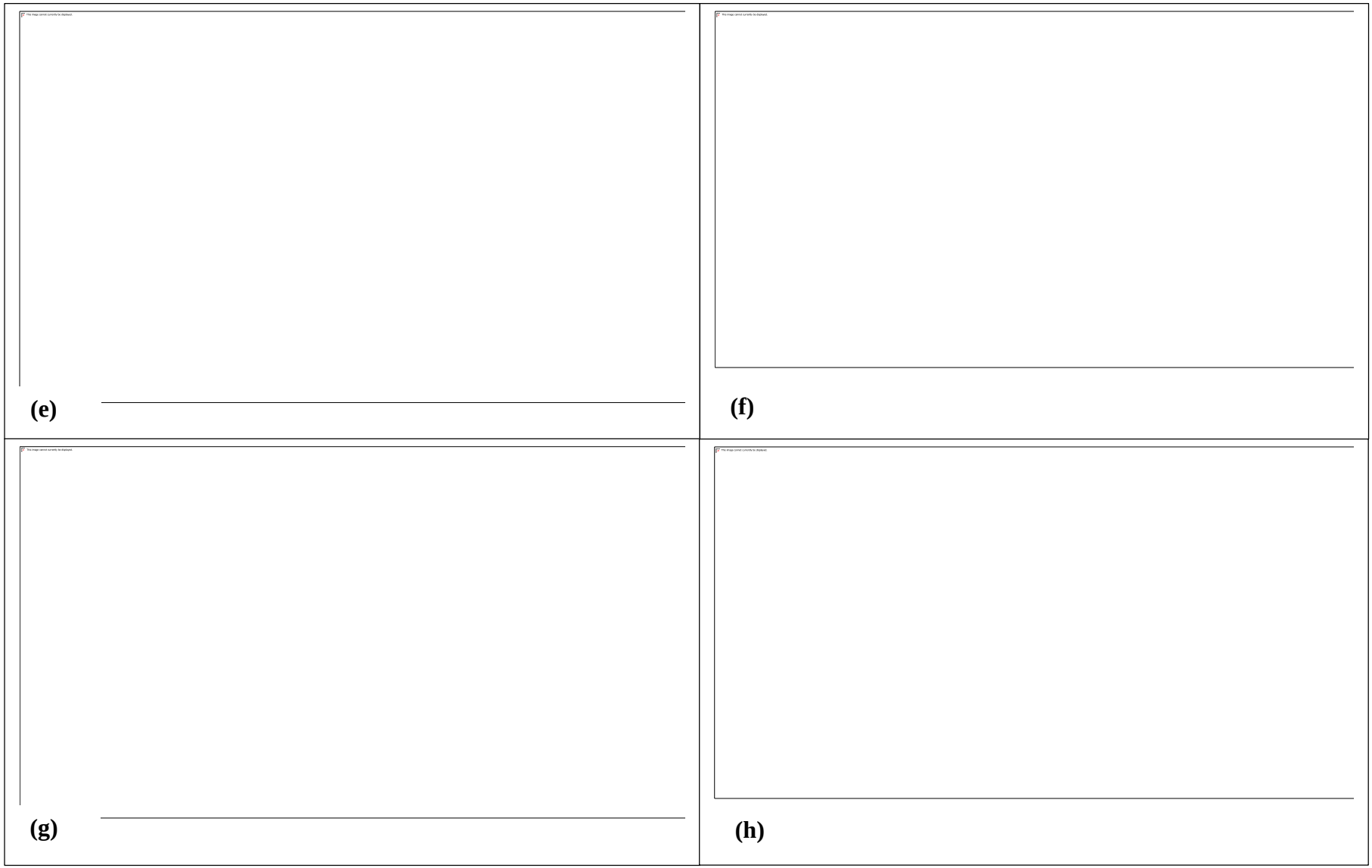

Figure 4.20 (e-h): Spectral plots utilized to compute depths to the centriod of magnetic sources in the region

are spectrum utilized to compute depths to the centriod of magnetic sources in the region (z_0). Table 4.2 provides extended details on computational results for the other 55 x 55 km windows taken across the region. Depths to the top (DTT) of Magnetic sources were computed from spectral analysis of magnetic data on a 55 x 55 km window (Fig.4.21). The Curie Point Depth (CPD) was estimated from Z_0 and Z_t computations and CPD variations are displayed in Fig 4.22. Figures 4.23 and 4.24 show the variation of geothermal gradient and heat flow values estimated from CPD. Spectral Analysis results were gotten for 6 Windows of 110 x 110 km dimension and 50% overlap as shown in Figure 4.25 and the respective uncertainty of each window was also evaluated. The display for the first four windows out of 6 windows sampled were made as seen in Figures 4.26 (a), (b), (c), and (d) as spectral plots used to compute depths to the top of magnetic sources (DDT/dz) which is the depth of the first/topmost layer denoting high frequency signals and long wavelength from subsurface magnetic sources, while Figures 4.26(e), (f), (g), and (h) spectra were utilized to compute depths to the top (Fig.4.27) and centroid of magnetic sources in the region (z_o). Table 4.3 also provides extended details on computational results for the other 110 x 110 km windows taken across the region. Here, a total of 7 sections were obtained from plots of power spectrum, Ln (power), made against wave number in cycles/km. CPD, geothermal gradient and heat flow estimations were made and represented on Figs. 4.28, 4.29 and 4.30 respectively.

C. Magnetic Lineament Result

Lineament map shows all available trends of the lineaments within the study area, obtained using CET Grid Analysis of OASIS Montaj software. Figure 4.31 shows the various available trends from magnetic data lineament extract from which is most useful in this Study. Figure 4.32 displays filtered magnetic lineaments in the dominant NE-SW trend. Dip amount of the NE-SW trends (Fig.4.33) were also recovered from the aeromagnetic data within 0 and 10 degrees. The Rose diagram showing dominant NE

– SW trending strike were also represented on the rose plots (Fig.4.34 above). On the other hand, the rose plots of the dip direction when NE-SW trending lineaments are considered were

Table 4.2. Spectral Analysis results for 35 Windows of 55 x 55 km dimension and 50% overlap. The respective uncertainty of the each window was also evaluated.

Block	Location		z_t (km)	Error z_t (± km)	z_o (km)	Error z_o (± km)	CPD (km)	Error CPD (± km)	GG(°C/km)	Heat Flow (mW/m2) GG*1.8-sed units GG*2.5-igneous unit	Geologic Formation
	Longitude (º)	Latitude (º)									
1	7.25	5.75	1.378	0.078	7.514	0.272	13.65	1.76	18.69084249	33.64351648	Agbada shales
2	7.5	5.75	1.889	0.318	7.257	0.254	12.63	3.01	22.12240697	39.82033255	Ajali Sand St.
3	7.75	5.75	1.558	0.095	7.874	0.256	14.19	1.79	17.07385483	30.73293869	Mamu Fm
4	8	5.75	1.108	0.024	6.531	0.27	11.95	1.24	24.73556485	44.52401673	Amaseri Sand St.
5	8.25	5.75	0.69	0.073	5.974	0.253	11.26	2.14	27.70976909	46.72710623	Migmatite gneiss
6	8.5	5.75	0.94	0.107	5.568	0.238	10.2	2.03	33.0627451	55.30601743	Granite gneiss
7	8.75	5.75	0.441	0.052	4.259	0.014	8.08	1.01	47.98217822	86.3679208	New netim marl
8	8.75	6	0.824	0.081	5.708	0.225	10.59	1.88	30.96864967	55.74356941	Awgu shale
9	8.5	6	0.578	0.026	6.597	0.281	12.62	1.64	22.15879556	39.88583201	Awgu shale
10	8.25	6	0.451	0.034	4.864	0.022	9.28	0.79	38.7	69.66	Nkporo shale
11	8	6	1.377	0.069	5.271	0.014	9.17	0.51	39.44972737	71.00950927	Awgu shale
12	7.75	6	1.51	0.067	4.747	0.019	7.98	0.42	48.88170426	87.98706767	Asu River G
13	7.5	6	1.28	0.018	5.499	0.012	9.72	0.18	35.87078189	64.5674074	Asu River G
14	7.25	6	1.257	0.062	6.334	0.274	11.41	1.55	27.03260298	48.65868536	Imo shale
15	7.25	6.25	1.158	0.138	5.106	0.021	9.06	1.15	40.21766004	72.39178807	Imo shale
16	7.5	6.25	1.185	0.088	5.199	0.018	9.21	0.75	39.17502714	70.51504885	Awgu shale
17	7.75	6.25	1.529	0.015	4.296	0.092	7.06	0.37	49.3529745	88.83535	Ezeaku Shale
18	8	6.25	1.124	0.034	5.233	0.133	9.34	0.76	38.29850107	68.93730193	Asu River G
19	8.25	6.25	0.997	0.017	7.554	0.277	14.11	1.27	17.30559887	31.15007797	Asu River G
20	8.5	6.25	1.102	0.063	3.626	0.091	6.15	0.66	49.50894309	89.1161	Ezeaku Shale
21	8.75	6.25	1.122	0.089	4.482	0.199	7.84	1.32	49.17959184	122.949	Banded gneiss
22	8.75	6.5	0.712	0.027	4.464	0.113	8.22	0.73	46.75961071	84.16729928	Ezeaku Shale
23	8.5	6.5	0.654	0.016	5.609	0.029	10.57	0.36	31.07228004	55.93010407	Ezeaku Shale

24	8.25	6.5	0.657	0.028	4.611	0.026	8.56	0.46	43.95700935	79.12261683	Asu River G
25	8	6.5	0.584	0.037	4.528	0.016	8.47	0.59	44.67697757	80.41855963	Asu River G
26	7.75	6.5	0.682	0.018	4.001	0.175	7.32	0.83	49.43497268	88.98295	Awgu shale
27	7.5	6.5	1.502	0.062	5.118	0.141	8.73	0.84	42.63757159	76.74762886	Nkporo shale
28	7.25	6.5	1.849	0.118	5.873	0.033	9.89	0.74	34.84509606	62.72117291	Nsukka Fm
29	7.25	6.75	1.372	0.128	7.137	0.073	12.9	1.47	21.16124031	38.09023256	Nsukka Fm
30	7.5	6.75	1.604	0.135	7.134	0.08	12.66	1.35	22.0135861	39.62445498	Maamu Fm
31	7.75	6.75	1.098	0.022	6.649	0.081	12.2	0.54	23.74098361	42.7337705	Nkporo shale
32	8	6.75	0.628	0.024	5.466	0.037	10.3	0.53	32.51067961	58.5192233	Awgu shale
33	8.25	6.75	0.68	0.029	5.587	0.027	10.49	0.56	31.4907531	56.68335558	Awgu shale
34	8.5	6.75	0.698	0.023	5.857	0.039	11.02	0.52	28.83157895	51.89684211	Ezeaku Shale
35	8.75	6.75	0.797	0.034	5.079	0.026	9.36	0.5	38.16581197	68.69846155	Ezeaku Shale

Figure 4.21: Depths to the top (DTT) of Magnetic sources computed from spectral analysis of magnetic data on a 55 x 55 km window.

Figure 4.22. Map representation of the omputed Curie Point Depths (CPDs)

Figure 4.23: Geothermal Gradient (GG) map computed from derived CPD data.

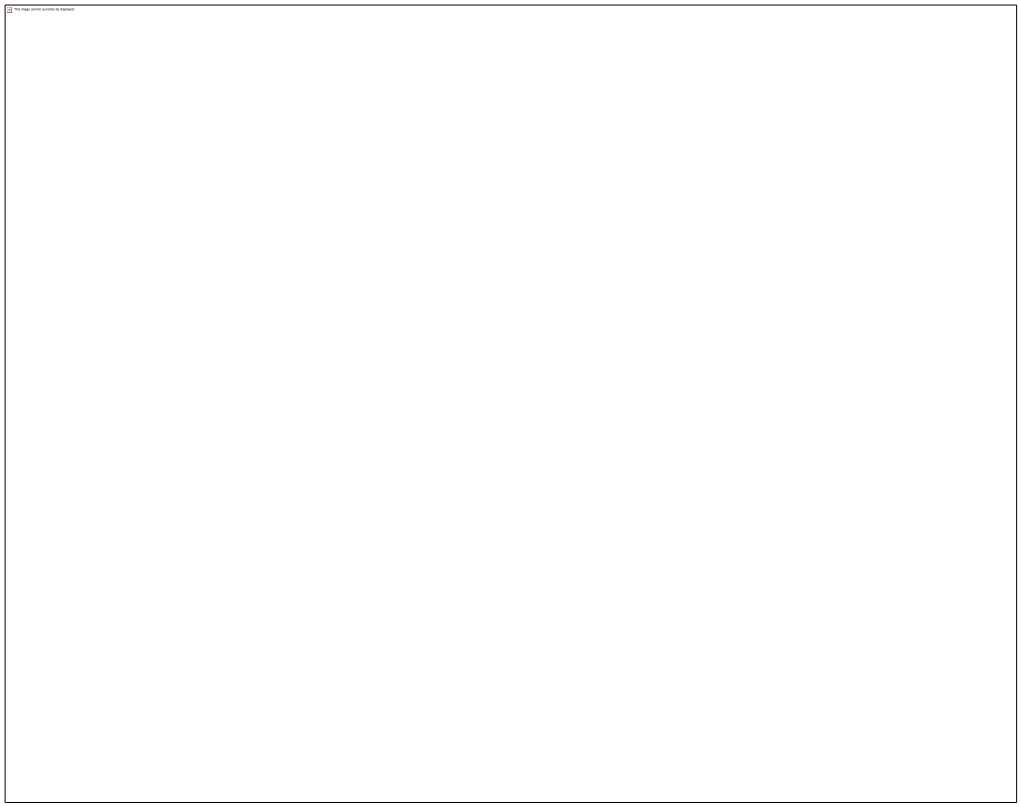

Figure 4.24: Heat Flow map computed from derived results.

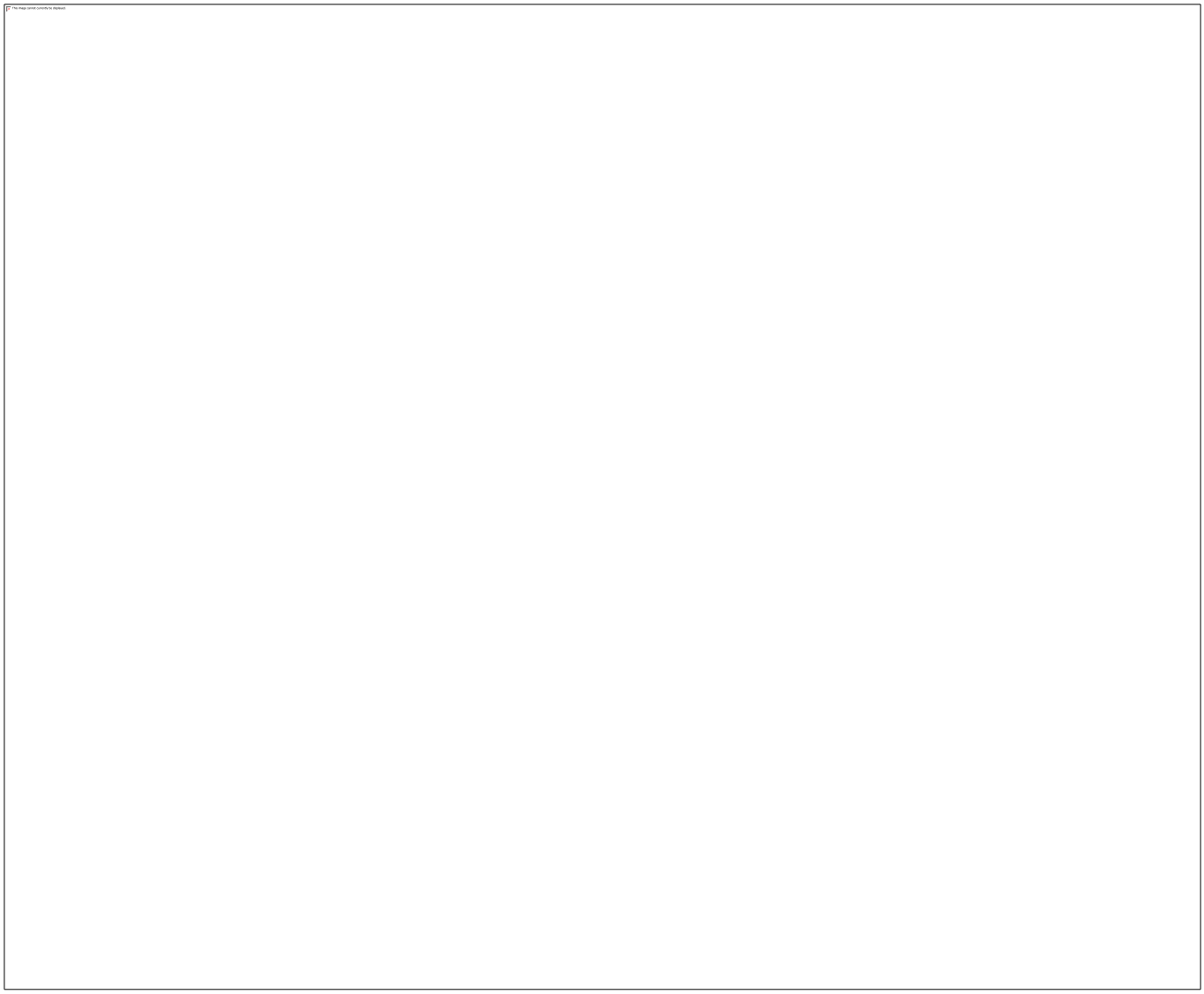

Figure 4.25: RTE Geomagnetic anomaly map.Map (Inserted squares of 110 x 110 km, 50% over lapping data windows selected for the spectral analysis procedures.

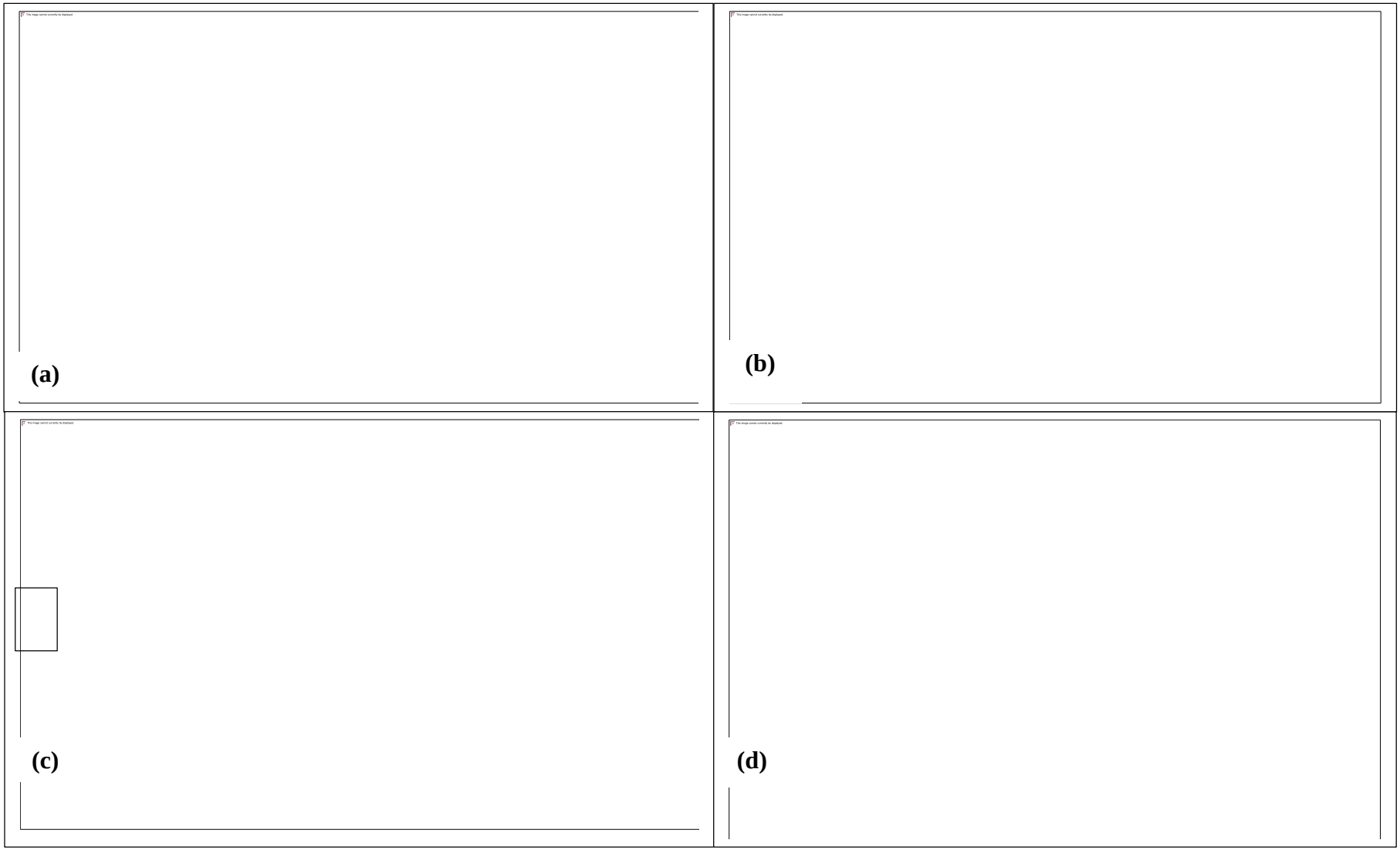

Figure 4.26 (a-d): Spectral plots for the 110 x 110 km windows taken across the study area used to compute depths to the top of magnetic sources

(e)

(f)

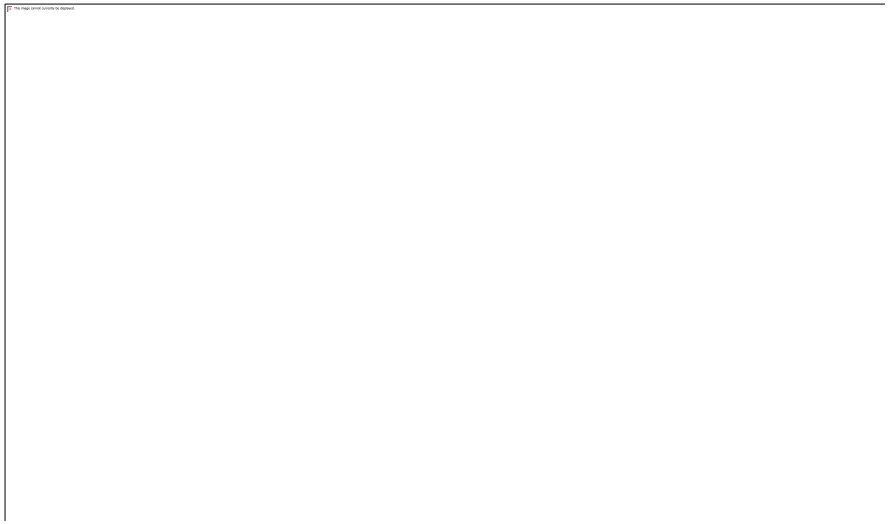

(g)

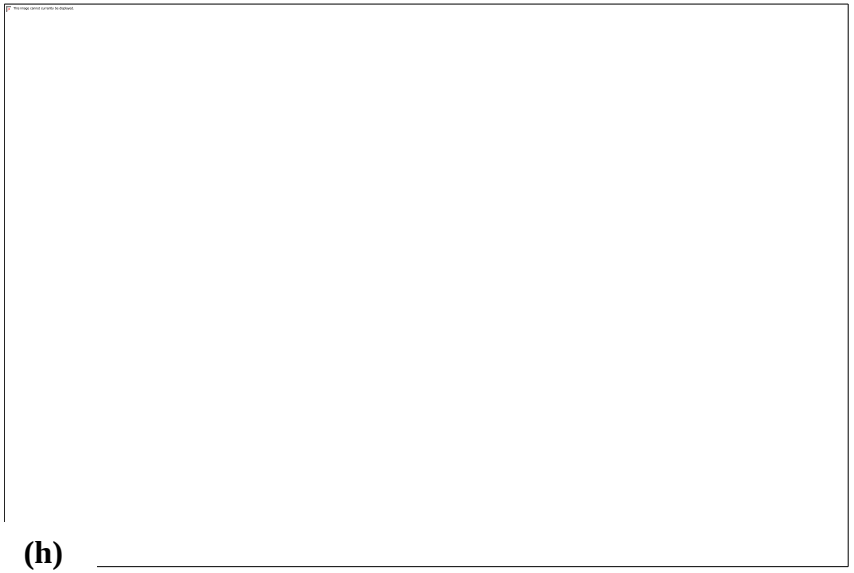

(h)

Figure 4.26 (e-h): Spectral plots for the 110 x 110 km windows taken across the study area were utilized to compute depths to the centriod of magnetic sources in the region

Table 4.3: Spectral Analysis results for 6 Windows of 110 x 110 km dimension and 50% overlap as shown in Figure4.21. The respective uncertainty of the each window was also evaluated.

Block	**Location**		z_t **(km)**	**Error** z_t **(± km)**	z_o **(km)**	**Error** z_o**(± km)**	**CPD (km)**	**Error CPD (± km)**	**Heat Flow GG(degC/km)**	**(mW/m^2)**	Formations
	Longitude (º)	**Latitude (º)**									
1	7.5	6	0.658	0.043	8.324	0.024	15.99	1.15	36.27267042	65.29080676	Asu River G
2	8	6	0.517	0.009	8.975	0.283	17.43	1.41	33.27596099	59.89672978	Awgu
3	8.5	6	0.395	0.026	7.386	0.196	14.38	1.72	40.33379694	72.60083449	Awgu
4	8.5	6.5	0.585	0.04	7.019	0.13	13.45	1.41	43.12267658	77.62081784	Ezeaku formation
5	8	6.5	0.432	0.017	6.984	0.053	13.54	0.74	42.83604136	77.10487445	Asu River G
6	7.5	6.5	0.562	0.019	5.208	0.167	9.85	0.96	58.88324873	105.9898477	Nkporo Shale

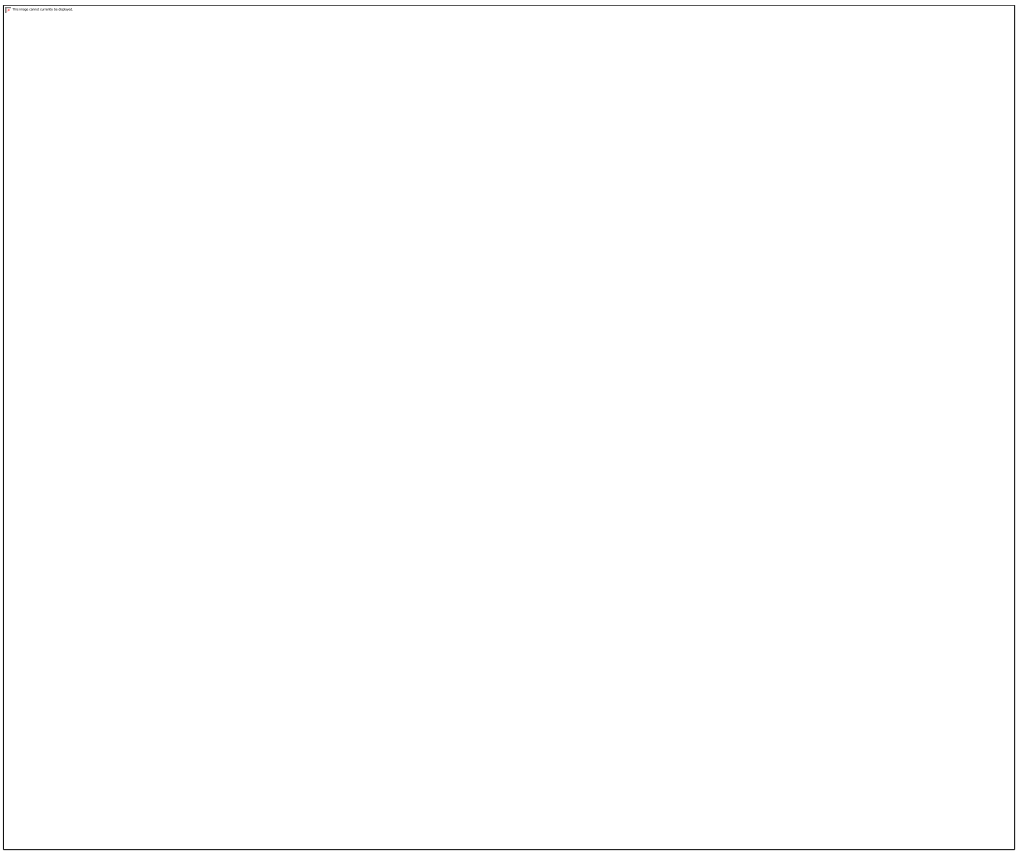

Figure 4.27. Map representation of depths to the top (DTT) of magnetic sources using the 110 x 110 km data window.

Figure 4.28. Map representation of the computed Curie Point Depths (CPDs) obtained from computations using windows of 110 x 110 km dimension as represented in Table 4.2.

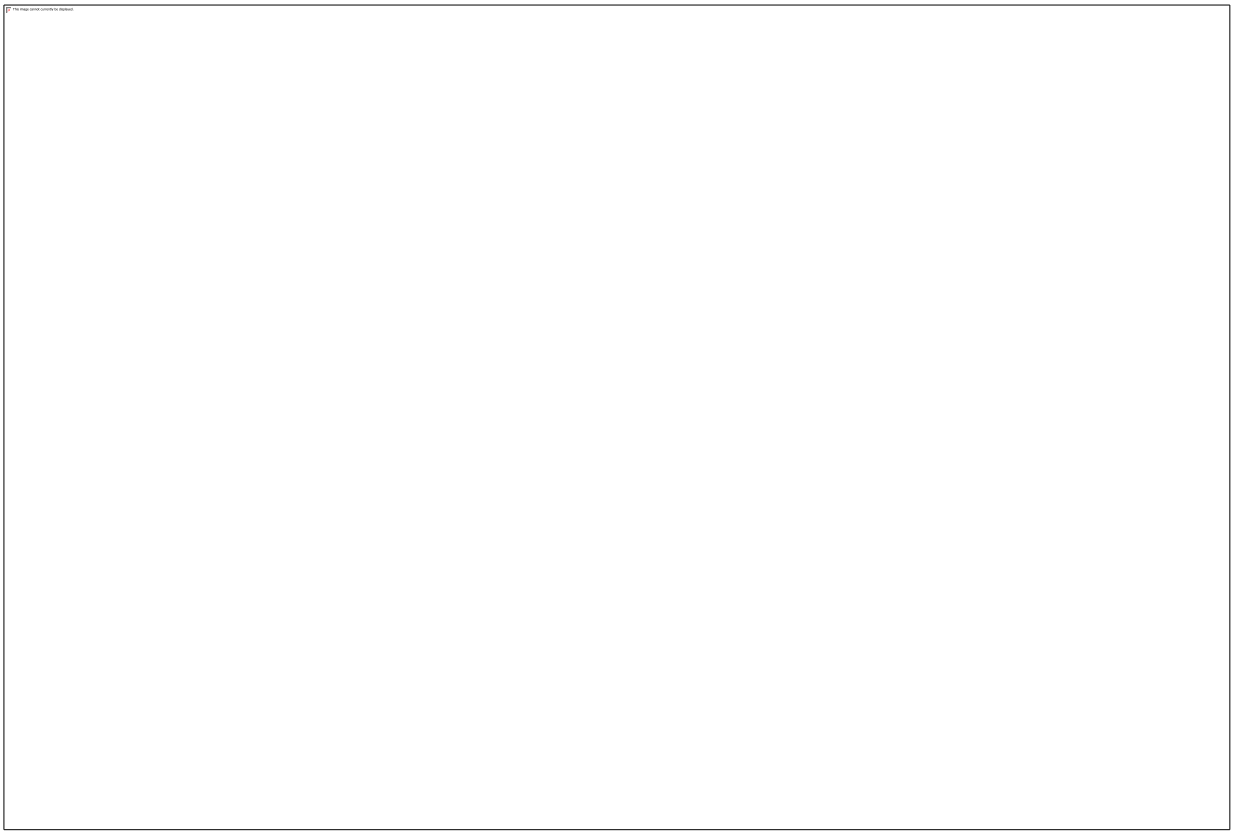

Figure 4.29. Geothermal Gradient (GG) map computed from derived CPD data.

Figure 4.30. Heat Flow map of the region computed from GG data from the 110 x 110 km window computations

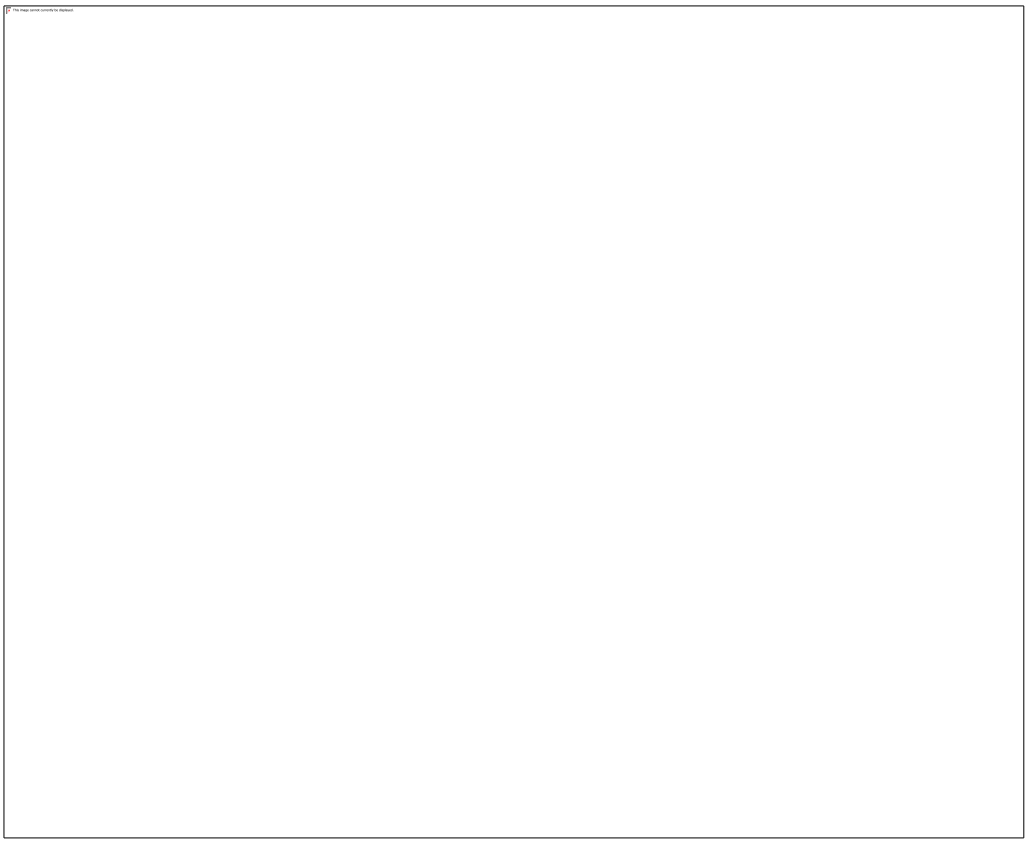

Figure 4.31. Lineament map extracted from magnetic data showing available trends in all directions.

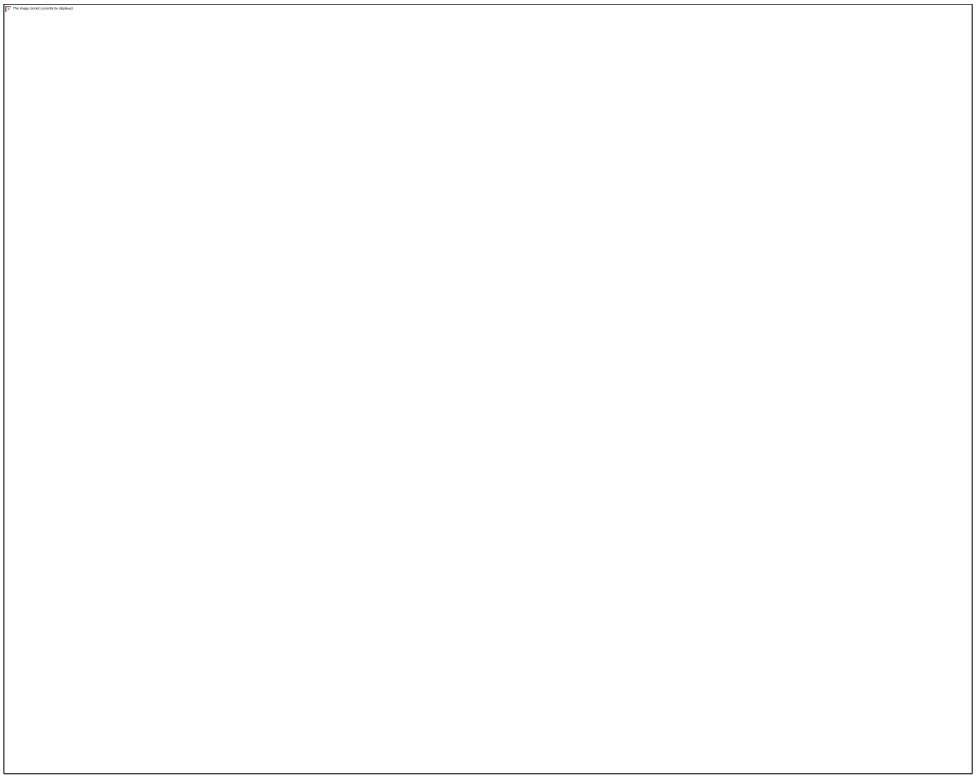

Figure 4.32: Lineament map extracted from magnetic data showing dominant NE – SW trends.

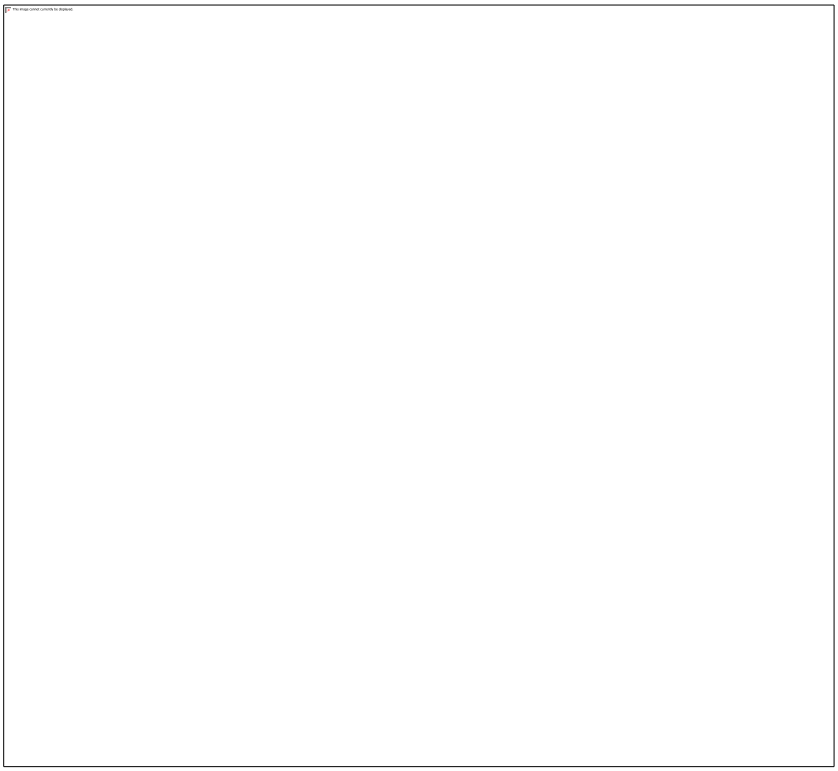

Figure 4.33: Dip amount in NE – SW trends recovered from aeromagnetic data within 0 and 10 degrees.

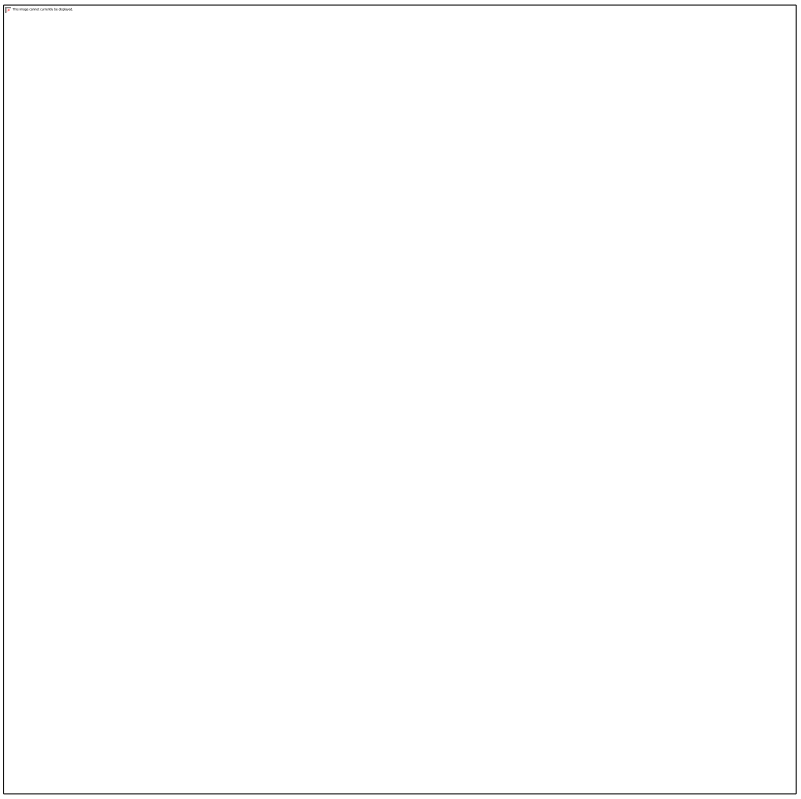

Figure 4.34: Rose diagram showing dominant NE – SW trending strike extracted from the aeromagnetic data.

made on figure 4.35. Figure 4.36 shows available lineament map of the study region in a NW-SE trend and this trend was computed and extracted from the aeromagnetic data as well. The same regions where NE-SW dominant trends occur have the same occurrence of NW-SE trends. The NW-SE trends are displayed in rose plots in figure 4.37. The resulting dip amounts computed from NW-SE lineament trends in the aeromagnetic data fall within 0 and 10 degrees as shown in Fig.4.38 and the resulting dip directions were as well made on a rose plot (Fig.4.39). The rose plot in Figure 4.40 displays the various dip directions of subsurface geologic structures in the study region. The dip, dip direction, and strike were all computed directly from the geomagnetic anomaly data of figure 4.18 and figure 4.41 makes a representation of all the strike components derived directly from the same geomagnetic anomaly data.The dip azimuth from figure 4.42 was computed directly from geomagnetic anomaly data of Figure 4.18 and it can be seen clearly that the structures dips within 0 and 10°. From the geomagnetic anomaly map, there was extraction of lineament map which shows dominant E – W trends as seen in Figures 4.43. The dip amount of the E – W trends recovered from Figure 4.43, are displayed in figures 4.44 and from the plot, it can be seen that the dip amount falls within 0 and 10 degrees. The resulting dip direction when E-W lineaments in Figure 4.43 are considered, plotted and displayed in figure 4.45. The rose plots of figure 4.46 also represents the dominant E-W trending strike as displayed in Figure 4.43.

D. 3-D Standard Euler Results

The structural indices of 3D Standard Euler De-convolution of aeromagnetic data are established from past literature for contacts, sills and dykes, horizontal cylinders and pipes and spheres, based on certain criteria or attributes. Figure 4.47-4.50 show various solution clusters for contacts and sills, cluster solutions with maximum depth range of >2444.2 m were obtained, however, best solution clusters for contacts with maximum depth range of >2444.2 m were obtained with the index of 0. Solutions were

obtained with 0-1 structural indices with the rest of 2-3 showing very poor solution clusters and hence 3 was overlooked.

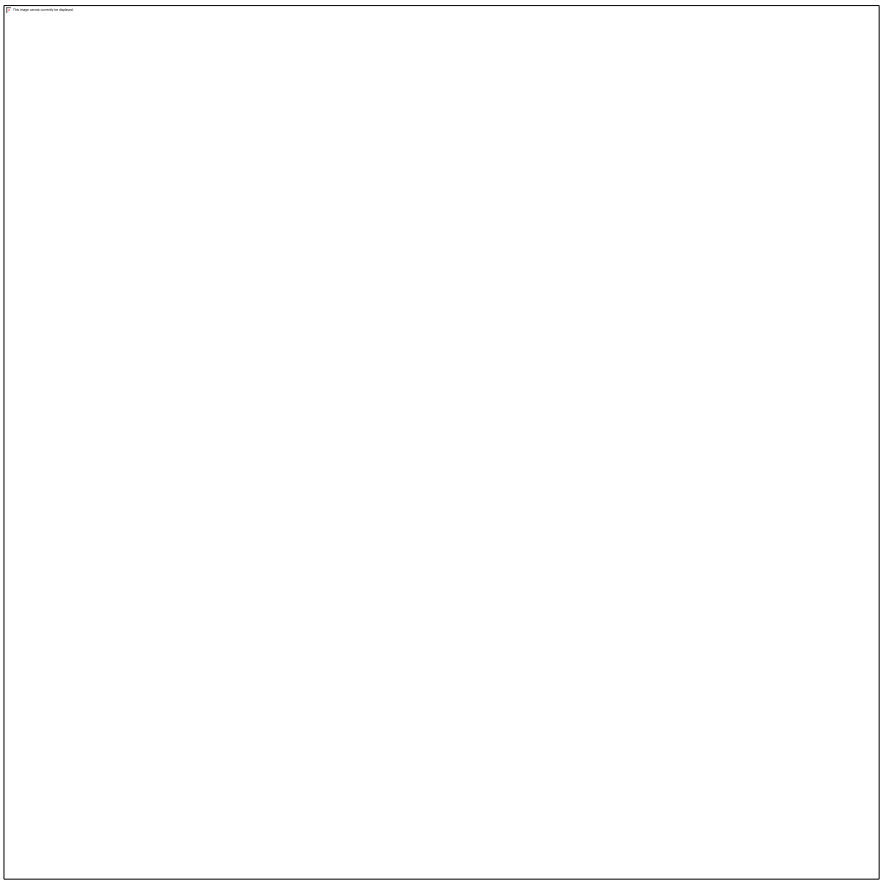

Figure 4.35: Dip direction when NE – SW lineaments are considered

Figure 4.36: Lineament map of the study region showing available NW – SE trends in the region

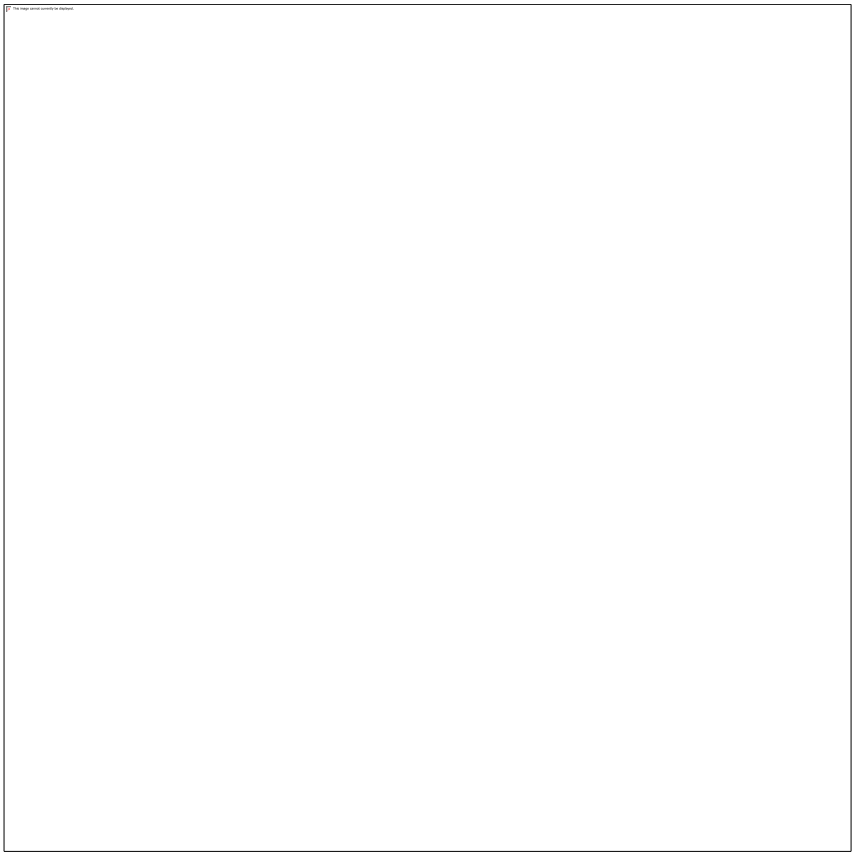

Figure 4.37: Rose plot displaying NW-SE Strike trends

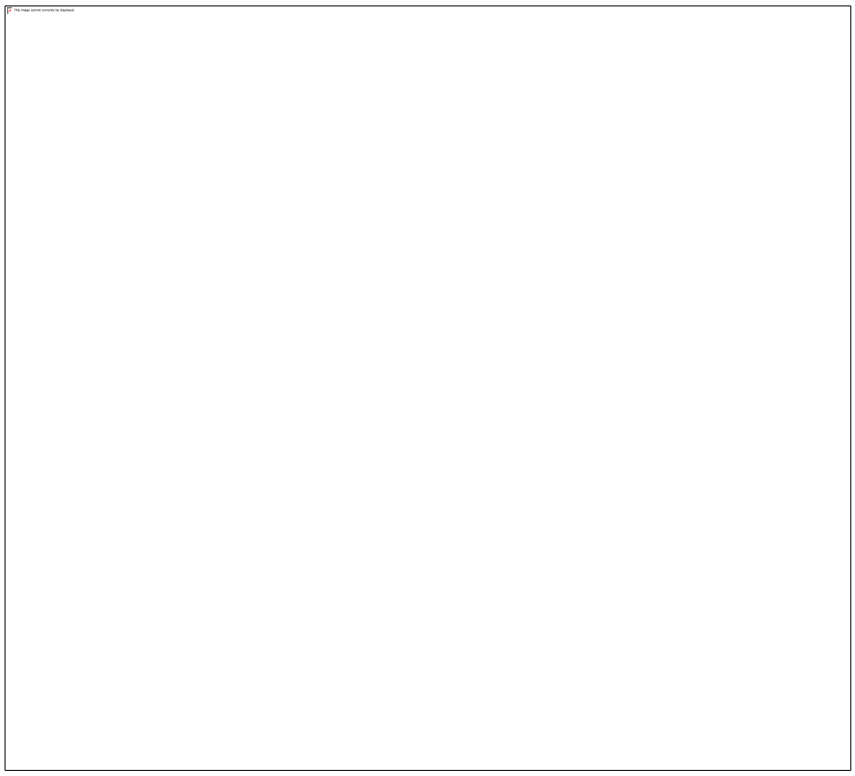

Figure 4.38: Dip amount computed from NW –SE lineament trends in the aeromagnetic data.

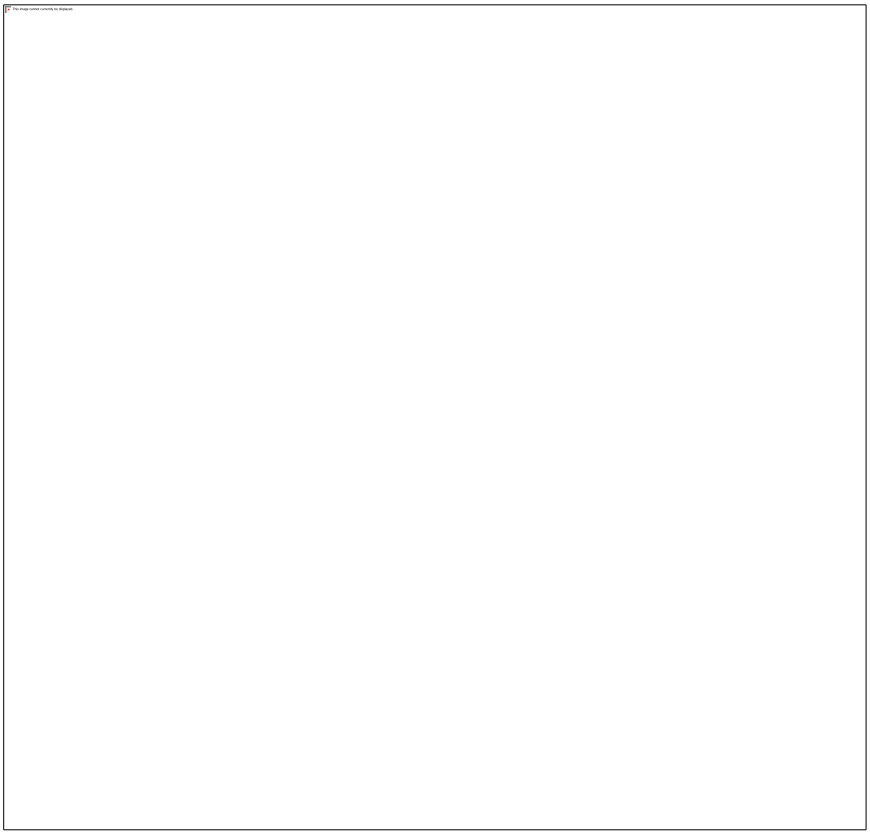

Figure 4.39: Dip direction when NW – SE lineaments are considered

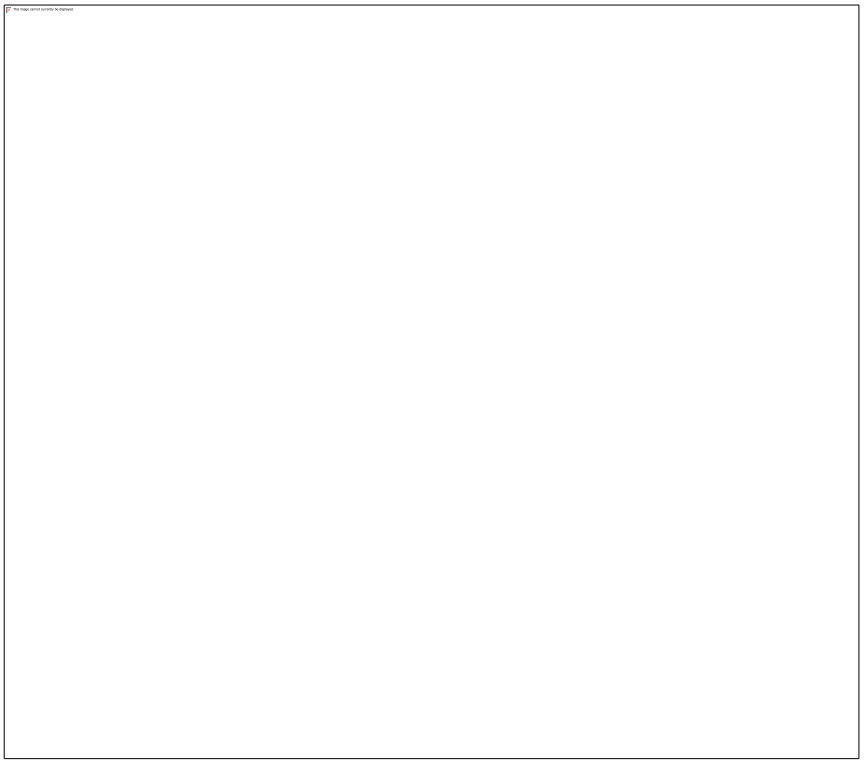

Figure 4.40: Rose Plot displaying the various dip directions of subsurface geologic structures in the Study Region.

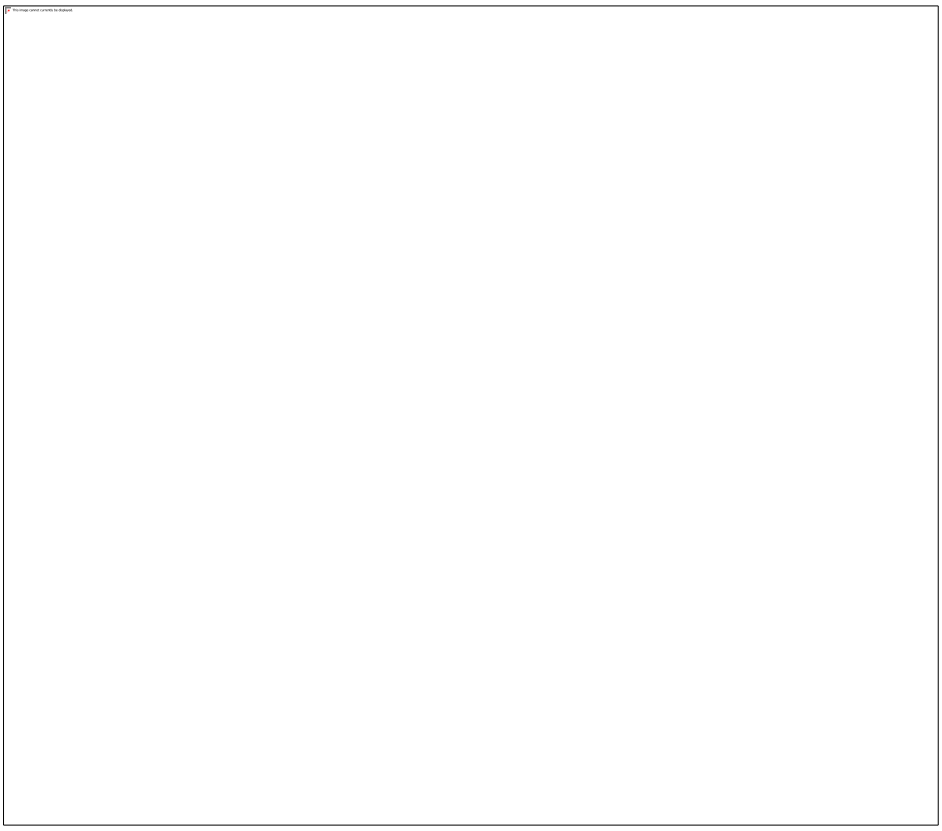

Figure 4.41: Strike component derived directly from the geomagnetic anomaly data of Figure 4.18

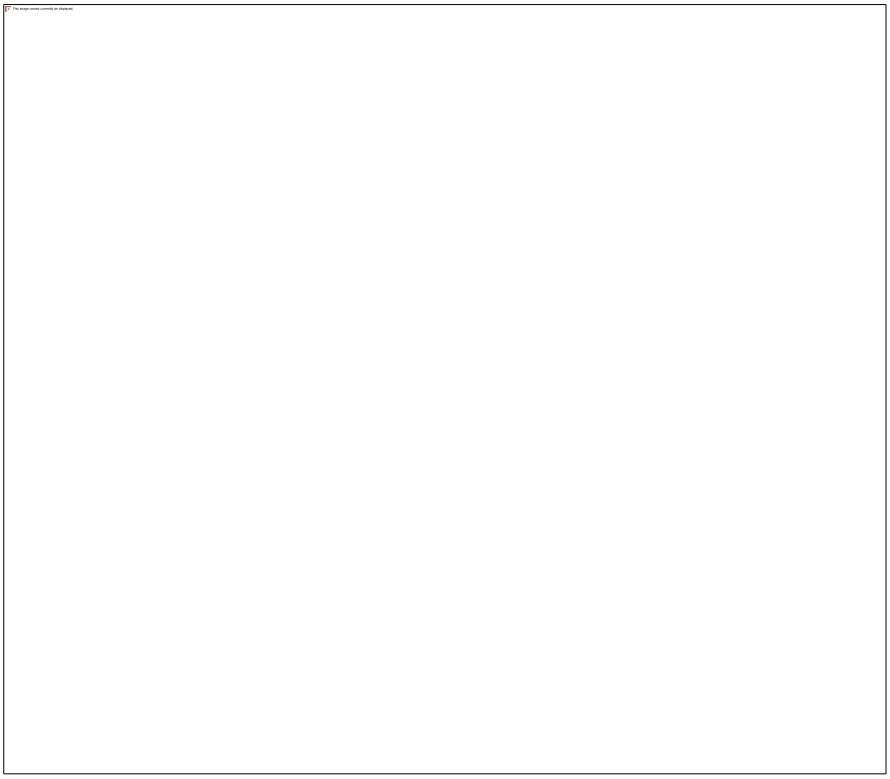

Figure 4.42: Dip azimuth computed directly from the geomagnetic anomaly data of Figure 4.18. It could be seen clearly that the structures dips within 0 and 10º .

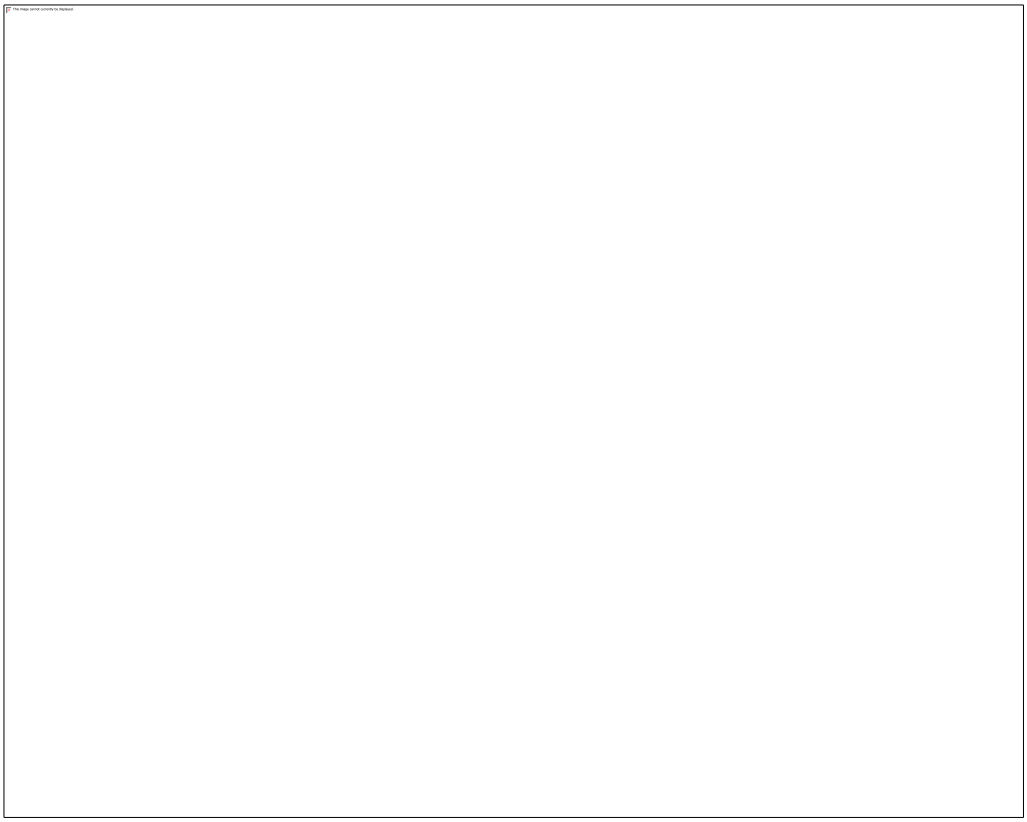

Figure 4.43: Lineament map extracted from magnetic data showing dominant E-W trends.

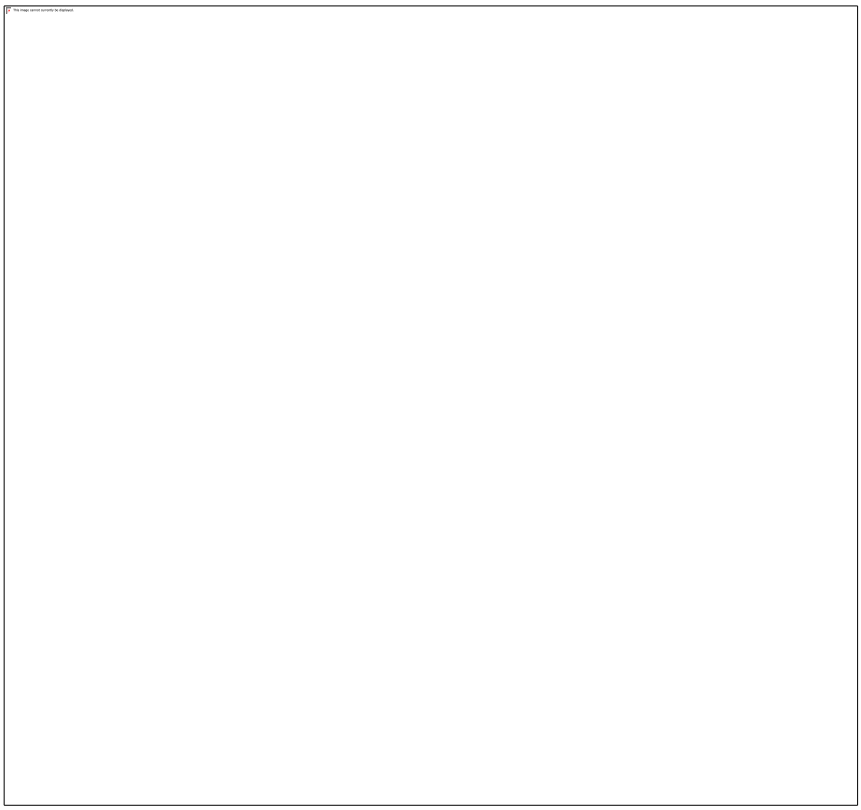

Figure 4.44. Dip amount of the E – W trends of Figure 4.43

Figure 4.45. Dip direction when E-W lineaments are considered as displayed in Figure 4.43

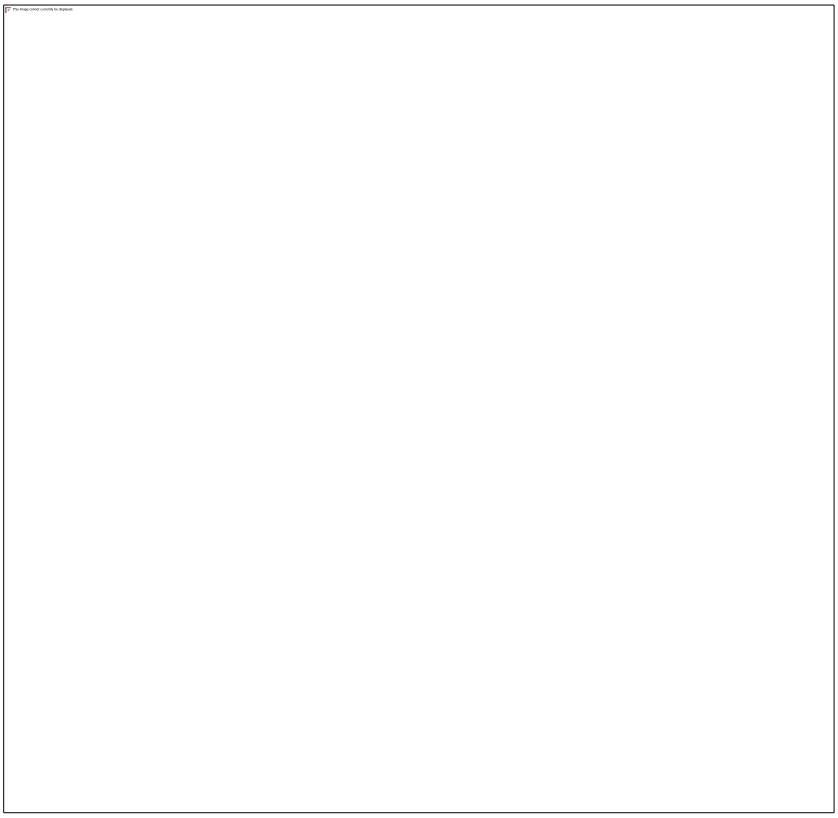

Figure 4.46: Rose diagram showing dominant E – W trending strike as displayed in Figure 4.43.

Figure 4.47: Euler Solutions from processing magnetic anomaly data using a structural index (SI =0).

Figure 4.48: 3D Euler depths solutions of Figure 4.47 overlain on magnetic anomaly field data

Figure 4.49: 3D Euler depth solution for SI = 1.

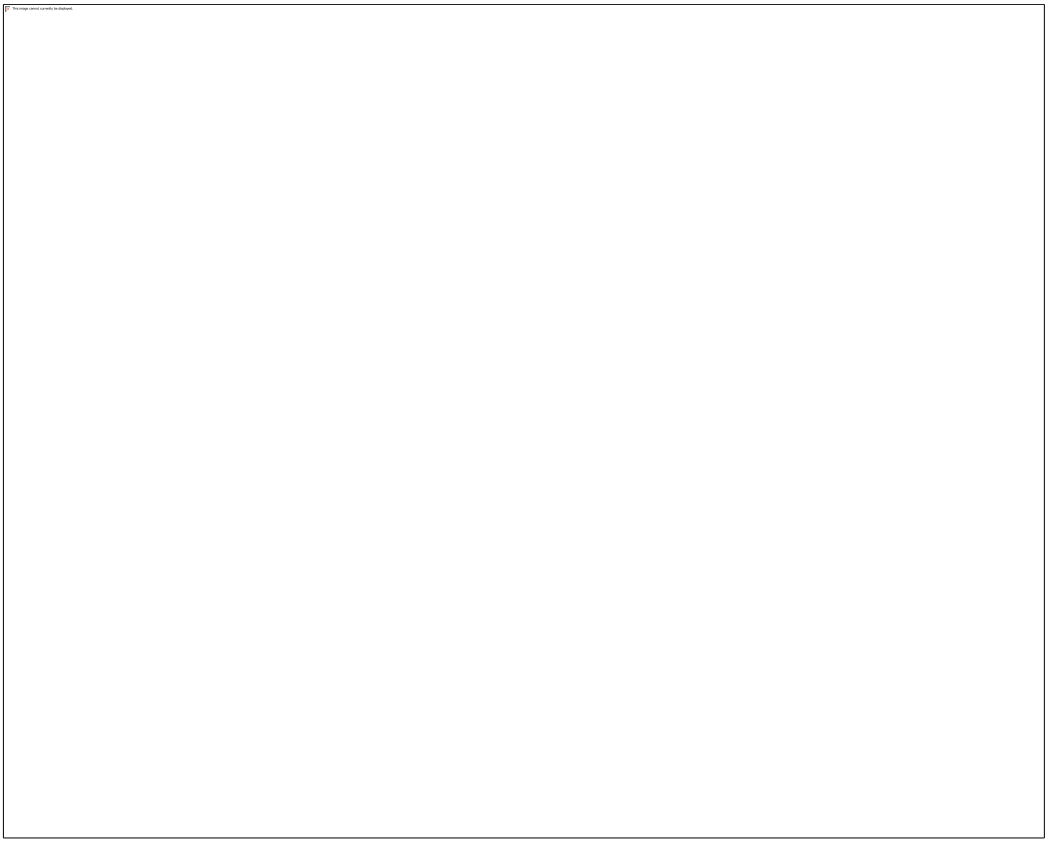

Figure 4.50: Magnetic field anomaly data with superposed Euler solutions (SI=1).

E. Source Parameter Imaging Results

The SPI and ISPI (Figs. 4.51 & 4.52) were achieved through best structural index of 0.5. It is observed in figure 4.51 that 55–65% of the study area contains sources that are averagely deep-seated to about a maximum depth >2.4 km and <2.5 km.

F. Vertical Derivative Result

The vertical derivative maps are represented in Figs. 4.53 and 4.54 a&b. The first vertical derivative result as shown in Figure 4.53 reveals most shallow geological structures in the data by enhancing high wavenumber components of the spectra using additional low-pass filter to remove high wave number noise. The changes in values depict subtle transitions in lithologic changes within different lithologies.

G. Horizontal Derivative Results

This approach estimates various contacts of magnetic materials at depth and being an edge-enhancing technique as well. The horizontal derivatives in x- and y- direction (Figs. 4.55a & 4.55b) which are first two order horizontal derivatives of the magnetic field, are not sensitive to noise. The horizontal gradient magnitude of the TMI-RTE in Fig.4.55c has varying amplitude gradients > 0.067 nT/m and as high as 0.093 nT/m.

H. Analytic Signal Results

Fig.4.56 shows the second order of the analytic signal which will eventually be used in the production of the NTilt map. There are similarities between the HG map (Fig. 4.55c) and the AS map (fig.4.56), the locations of the major shown ENE-WSW directions on the HG map are represented also on the AS map with high maximum amplitude of > 0.067 nT/m (> 67 nT/km). It exhibits maxima over magnetization contrasts, independent of ambient magnetic field and source magnetization directions.

I. NTilt Results

The very first phase filter before the production of the N-tilt derivative filter is the tilt derivative.

Figure 4.51: Source Parameter Imaging result achieved through the best structural index of 0.5

Figure 4.52: Improved Source Parameter Imaging (SPI). with SI of 0.5

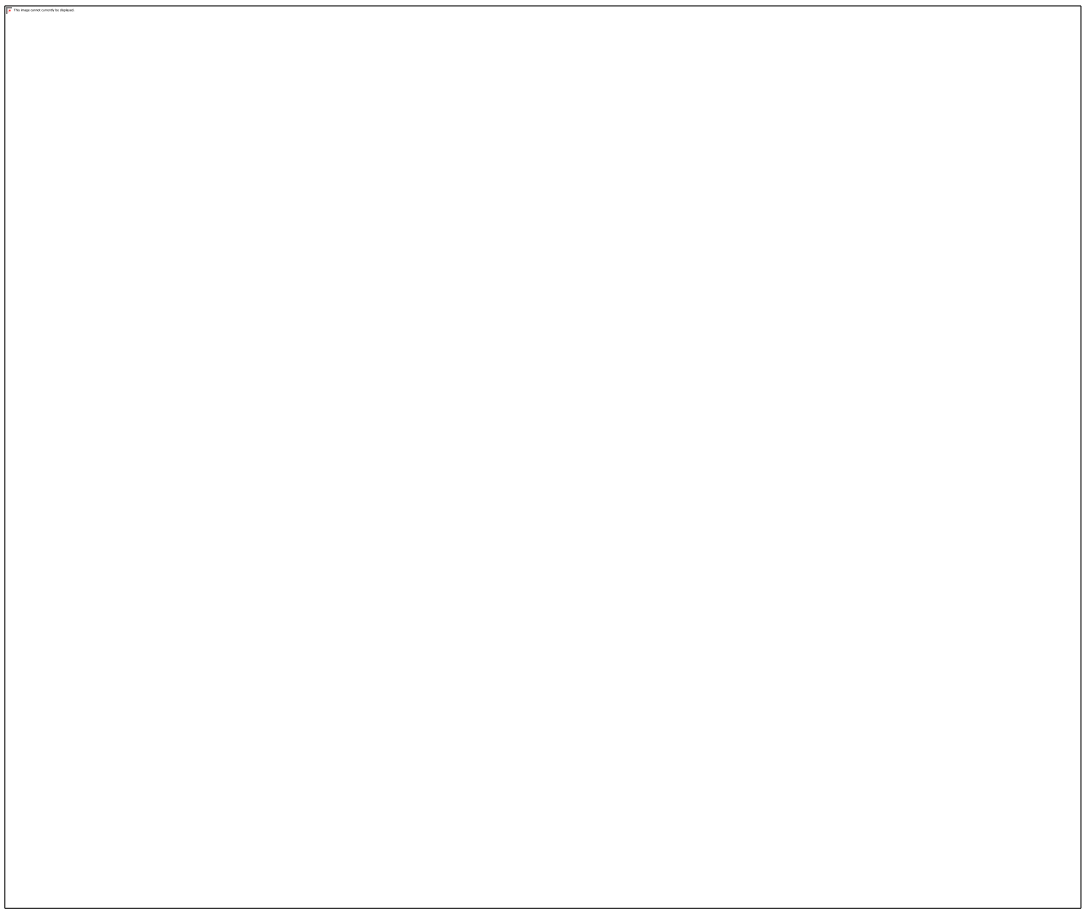

Figure 4.53: First Vertical Derivative of the geomagnetic anomaly data

Figure 4.54a: Second Vertical Derivative of the geomagnetic anomaly data

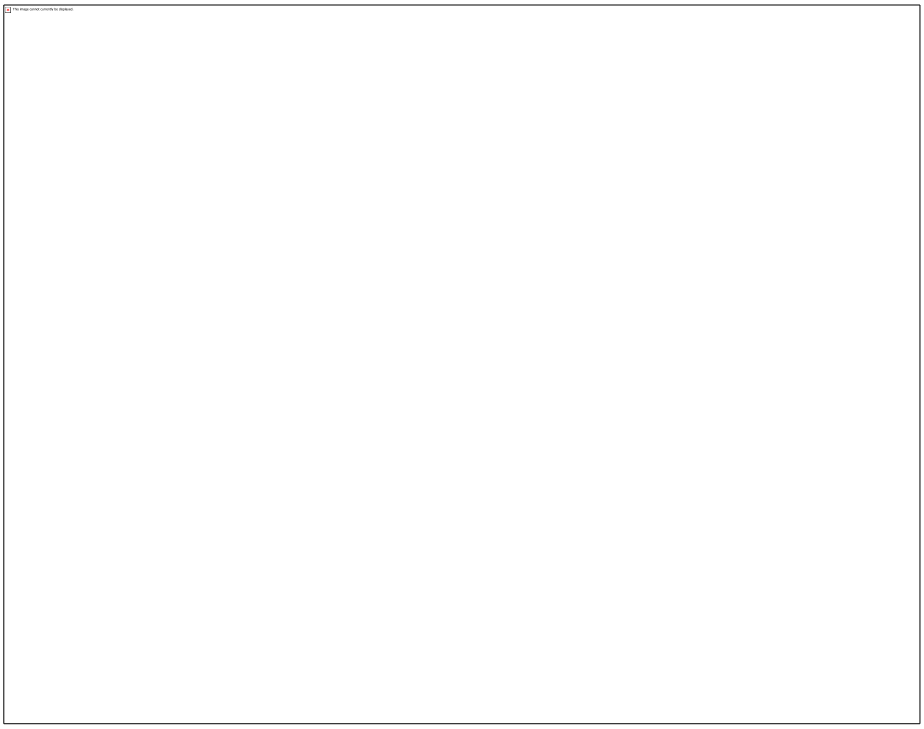

Figure 4.54b: Second vertical derivative results revealing clearly the different geologic formations: A-surface outcrops of Oban hill basement rocks; B-mafics (basaltic/doleritic rocks) outcropping around Obubra; C-mafics (basaltic rocks); D-mafic to ultramafic rocks of outcropping Obudu basement rocks; E_1, E_2 and E_3-parts of Abakaliki-Ishiagu and Arufu-Akwana-Azara mineral districts; F-near surface intrusives characterizing Igumale;

G-surficial Campanian-Maastrichtian-Paleocene carbonaceous shales and ferruginized iron stone cappings; H-Okigwe-Ishiagu mineral districts and I-ferruginized Imo-Aimeke formations

Figure 4.55a: Horizontal derivatives of the geomagnetic anomaly data with x-directional magnitude gradient

Figure 4.55b: Horizontal derivatives of the geomagnetic anomaly data with y- directional magnitude gradient

The second phase filter is the production of the analytic signal or total gradient as seen in Figs. 4.55c and 4.56 and represented in equations 3.2 & 3.4 respectively. The third phase filter which is the horizontal tilt angle (TDX) and a balanced horizontal derivative (Fig. 4.58), has a much sharper gradient over the edges compared to the original tilt derivative of the function of magnetized bodies and it comes to be by having the tilt angle introduced to it. It is arctan inverse of the normalized vertical derivative. The analytical signal is not able to enhance deep and shallow anomalous sources simultaneously and also enhance weak magnetic anomaly adjacent to a strong magnetic body, hence an enhanced analytical signal (AS), i.e. the second order derivative of the AS as represented in Figure 4.56, thus introduces the fourth phase filter. The fifth phase filter, i.e. the ETilt filter was used to produce the ETilt map in Fig.4.59. It is the ratio of the vertical derivative to the total horizontal derivative of the analytic signal (AS). The ETilt shows a clear resolution and advantage over the original tilt derivative, not only in delineating shallow bodies but

also deeper anomalies. NTilt map (Fig. 4.60) from the final Ntilt filter as represented in equation 3.5, shows edges of anomalous bodies.

J. Magnetic Vector Inversion Modeling Results

Geothermal gradient map of Figure 4.23 shows divisions of two parts A and B as represented in figure 4.61. The window dimensions of A and B were extracted from the geomagnetic anomaly map presented earlier and used for the Magnetic Vector Inversion modeling procedures. Part A of the Geomagnetic Anomaly Field data covered in the 55 x 55 km window shows sub-surface imaging results in figure 4.62a below which is an inversion result. This inversion result of this window dimension is further displayed with superimposed aeromagnetic data in figure 4.62b. The plot was done using a 10000m offset with relief scaled at 50. The inversion result from Part A of the window covered in the 55 x 55 km window was also superimposed with 3D computed geothermal gradient data as represented in Figure 4.62c, and the plot was done using a 15000m offset and the relief scaled at 550.34.

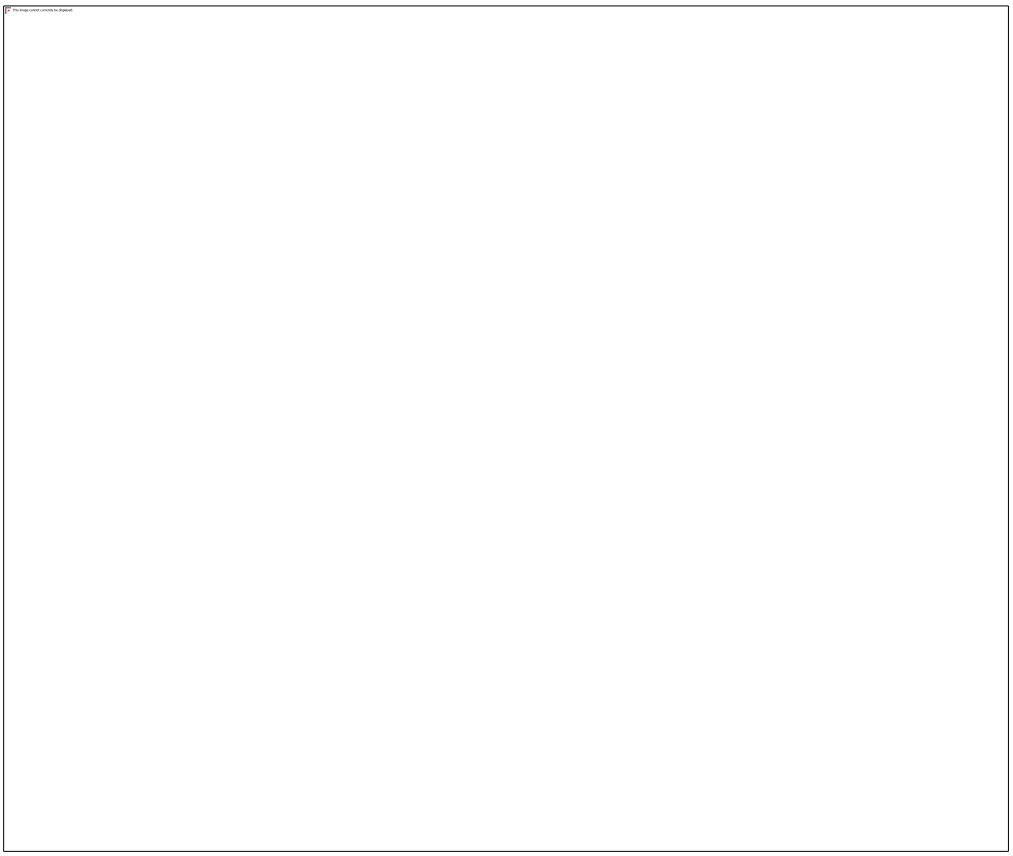

Figure 4.55c: Horizontal derivatives of the geomagnetic anomaly data with total magnitude gradient.

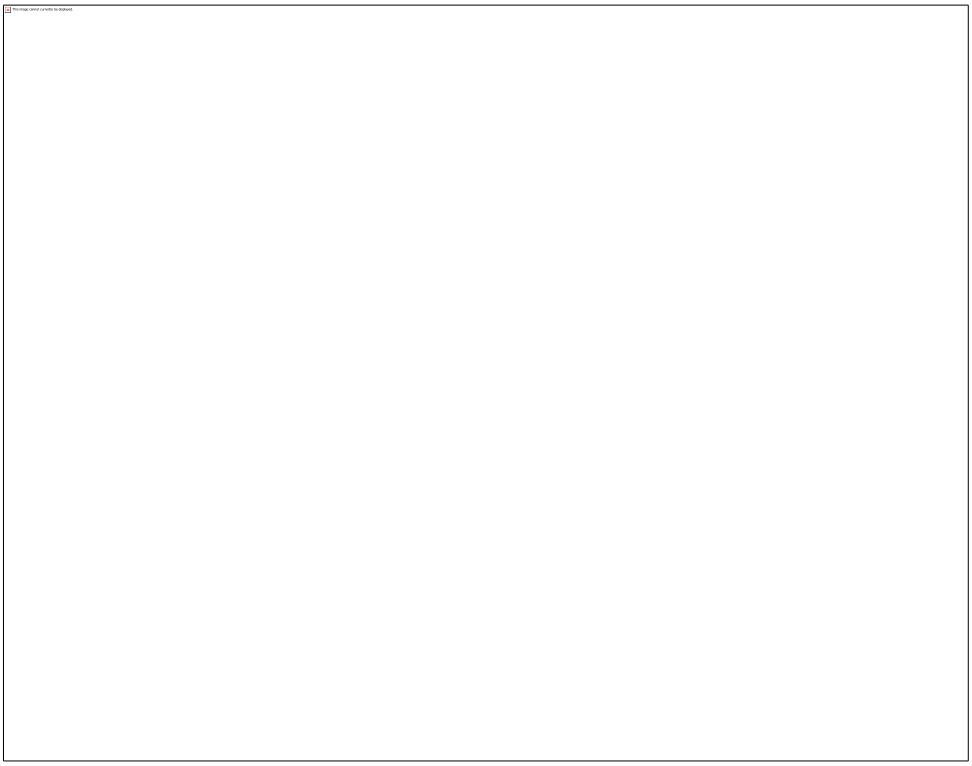

Figure 4.56: Analytic Signal of the TMI-RTE Map with higher order derivative

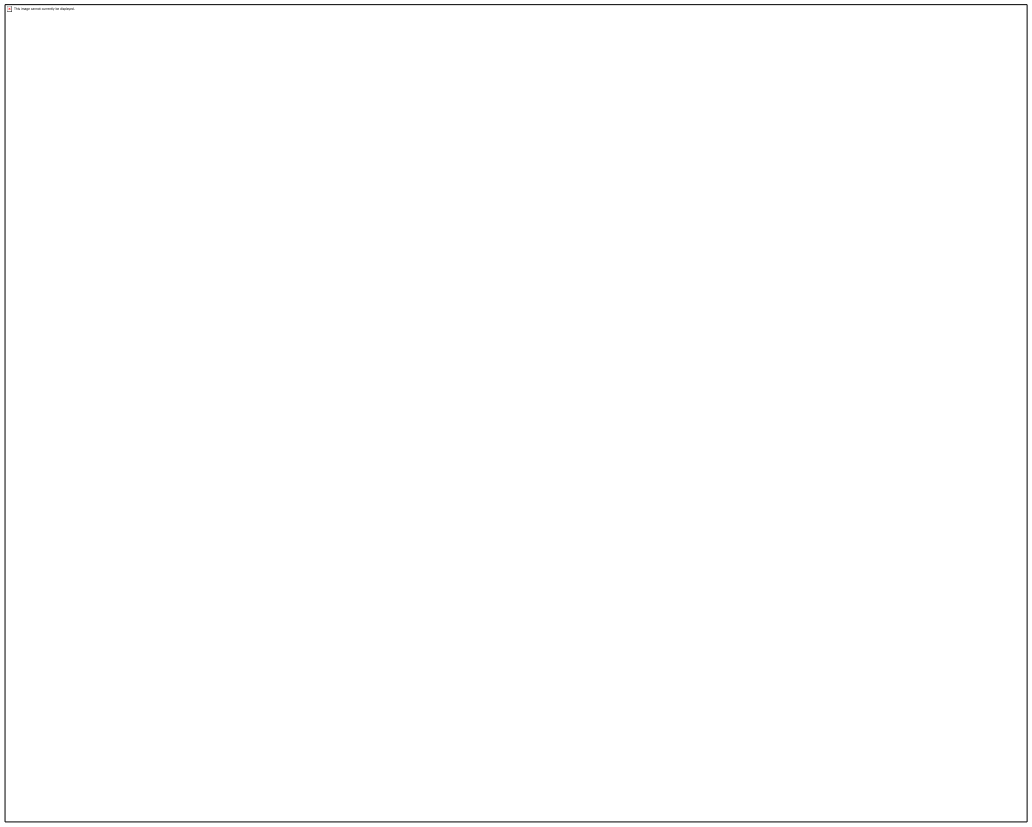

Figure 4.57: Tilt Derivative/ TDR Map of the Study Area

Figure 4.58: Horizontal Tilt Angle/ TDX Map of the Study Area

Figure 4.59: ETilt Map of the Study Area

Figure 4.60a: NTilt Map of the Study Area Showing Viable Ore Zones

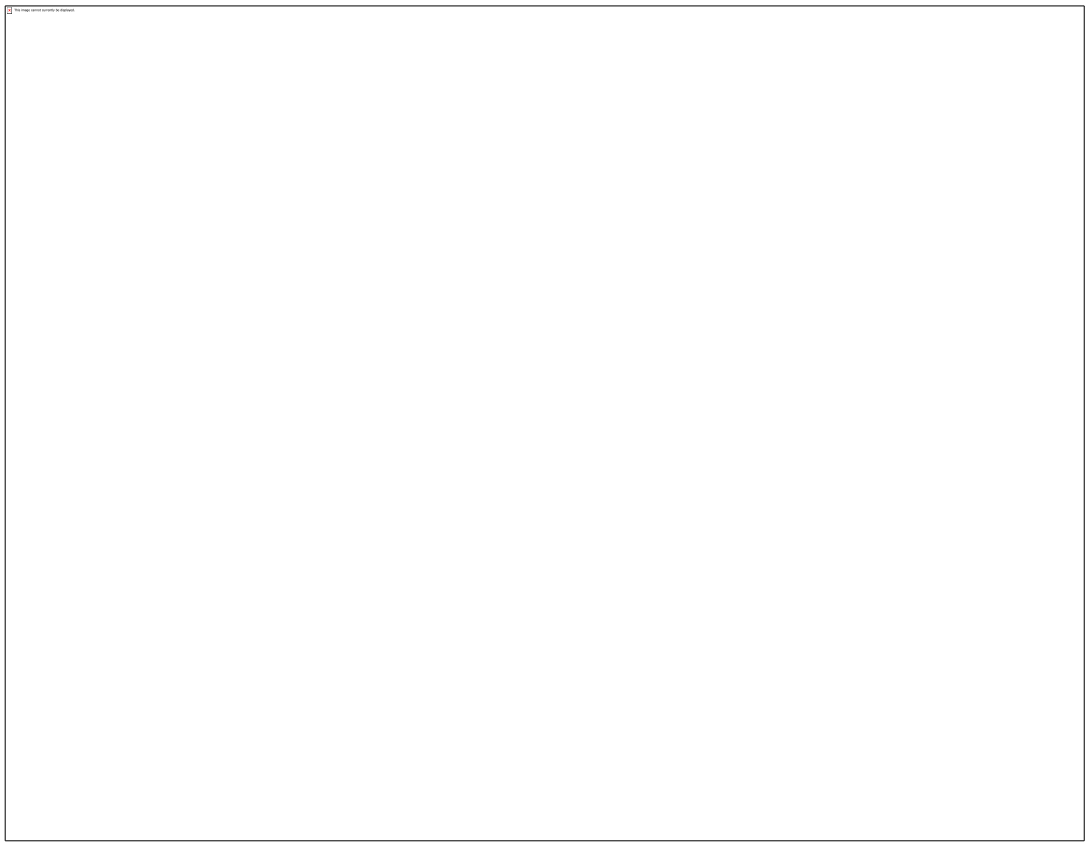

Figure 4.60b: NTilt Map of the Study Area

Figure 4.61: Geothermal gradient map Obtained from figure 4.23 showing divisions into two parts (A and B).

Figure 4.62a: Subsurface imaging results from part A of the Geomagnetic Anomaly Field data covered in the 55 x 55 km result window.

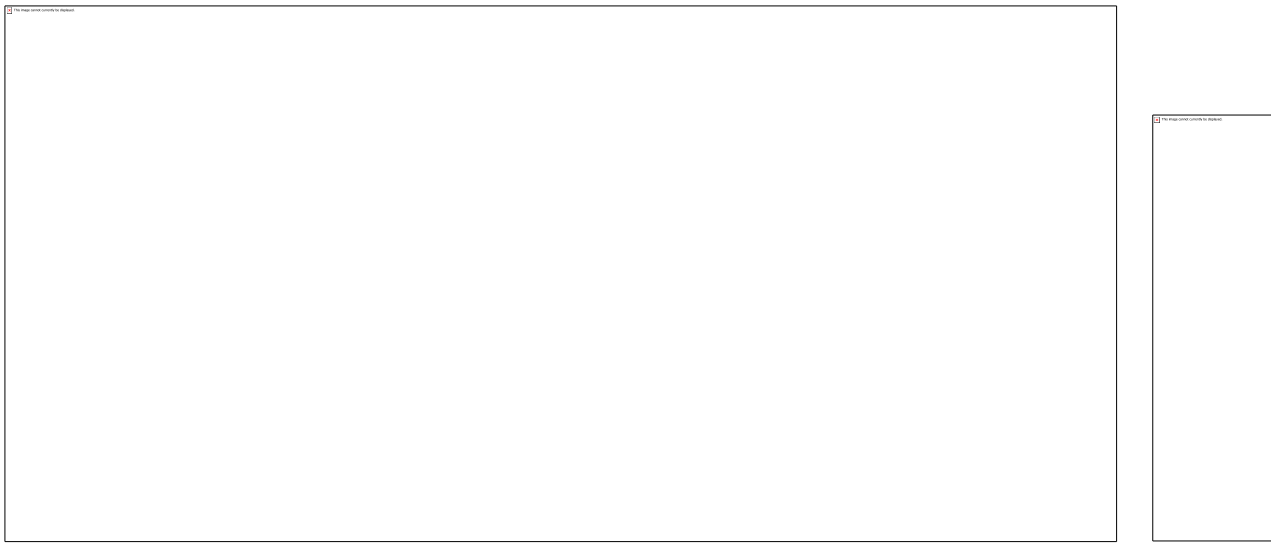

Figure 4.62b: Inversion results from Part A of the window covered in the 55 x 55 km window with superimposed aeromagnetic data. The plot was done using a 10000m offset and the relief scaled at 50.

Figure 4.62c: Inversion results from Part A of the window covered in the 55 x 55 km window with superimposed 3D computed geothermal gradient data. The plot was done using a 15000m offset and the relief scaled at 550.34.

Figure 4.63a shows subsurface imaging or inversion result from Part B of the geomagnetic anomaly field data covered in 55 x 55 km result window. The inversion result was further displayed with superposed aeromagnetic data in figure 4.63b exaggerated to a height of 19202.65 m in order to accommodate both plots and this plot was done using an 8000m offset and a relief scaled at 329. The inversion results from Part B of the window covered in 55 x 55 km window further had 3D computed geothermal gradient data as well superposed on it. This plot represented in figure 4.63c was done using an 8000m offset and relief scaled at 328.

Figure 4.64a shows subsurface inversion imaging results of Parts A&B from the 110 x 110 km dimension window which probes also from 100m ASL to 9000 m depth BSL. The Inversion results from Parts A&B of the window covered in 110 x 110 km was superimposed with aeromagnetic data and this plot was done using 0 offset and the relief scaled at 89. There is superposition of aeromagnetic data on inversion results from Part B and from the result displayed in Fig.4.64b. Inversion results from 110 x 110 km window probed in the computation of CPD using a 110 x 110 km window size was superposed with 3D computed geothermal gradient data represented in Fig.4.64c.

Based on the varying susceptibility contrasts, prominent anomaly windows P-Y in Fig.4.65 were captured on the geomagnetic anomaly map for wider and more detailed probe using the Magnetic Vector Inversion modeling. Modelling result from window P in Fig. 4.66a(i), shows models revealed from the magnetic vector inversion technique. Figure 4.66 a(ii) shows the aeromagnetic anomaly data superimposed on 4.66 a(i).

Q window represented in Figures 4.66 b(i) captures varying shapes of models. Fig. 4.66b(ii) shows superimposed aeromagnetic anomaly data on the modelling result from Q window.Modelling result from

window R in Fig. 4.66c(i), shows models revealed from magnetic vector inversion technique as well and the aeromagnetic anomaly data superimposed on the modelling result is shown in Fig. 4.66 c(ii).

Figure 4.63a: Subsurface imaging results from Part B of the Geomagnetic Anomaly Field data covered in the 55 x 55 km result window.

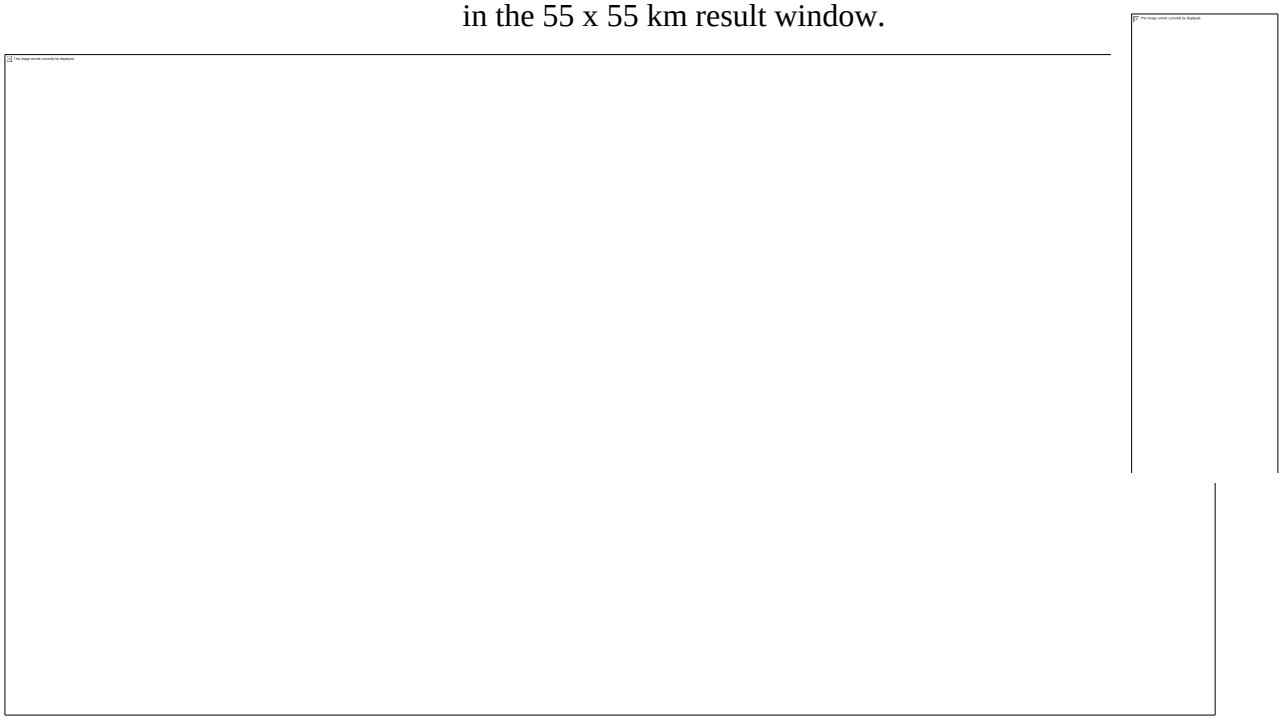

Figure 4.63b: Inversion results from Part B of the window covered in the 55 x 55 km window with superimposed aeromagnetic data. The plot was done using an 8000m offset and the relief scaled at 329.

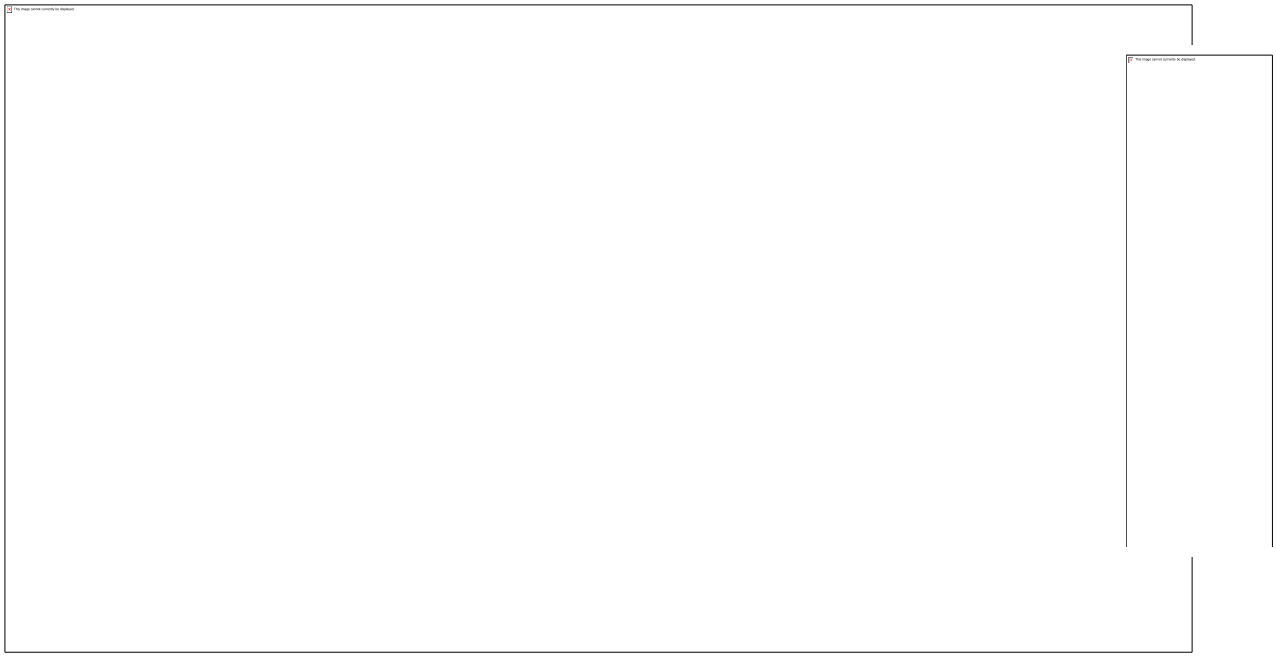

Figure 4.63c: Inversion results from Part B of the window covered in the 55 x 55 km window with superposed 3D computed geothermal gradient data. The plot was done using an 8000m offset and the relief scaled at 328.

Figure 4.64a: Subsurface Inversion imaging results from Parts A& B from 110 x 110 km dimension window

Figure 4.64 b: Inversion results from Part B of the window covered in the 110 x 110 km window with superposed aeromagnetic data. The plot was done using 0 offset and the relief scaled at 89.

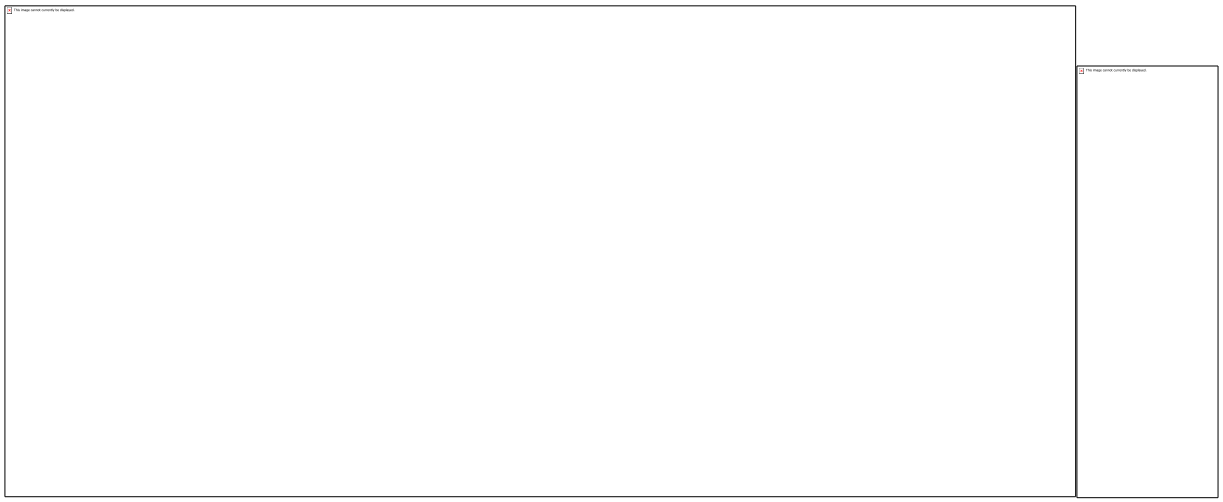

Figure 4.64c: Inversion results from 110 x 110 km window probed in the computation of CPD using a 110 x 110 km window size. The result has been superposed with 3D computed geothermal gradient data. The plot was done using a 2000m offset and the relief scaled at 500.

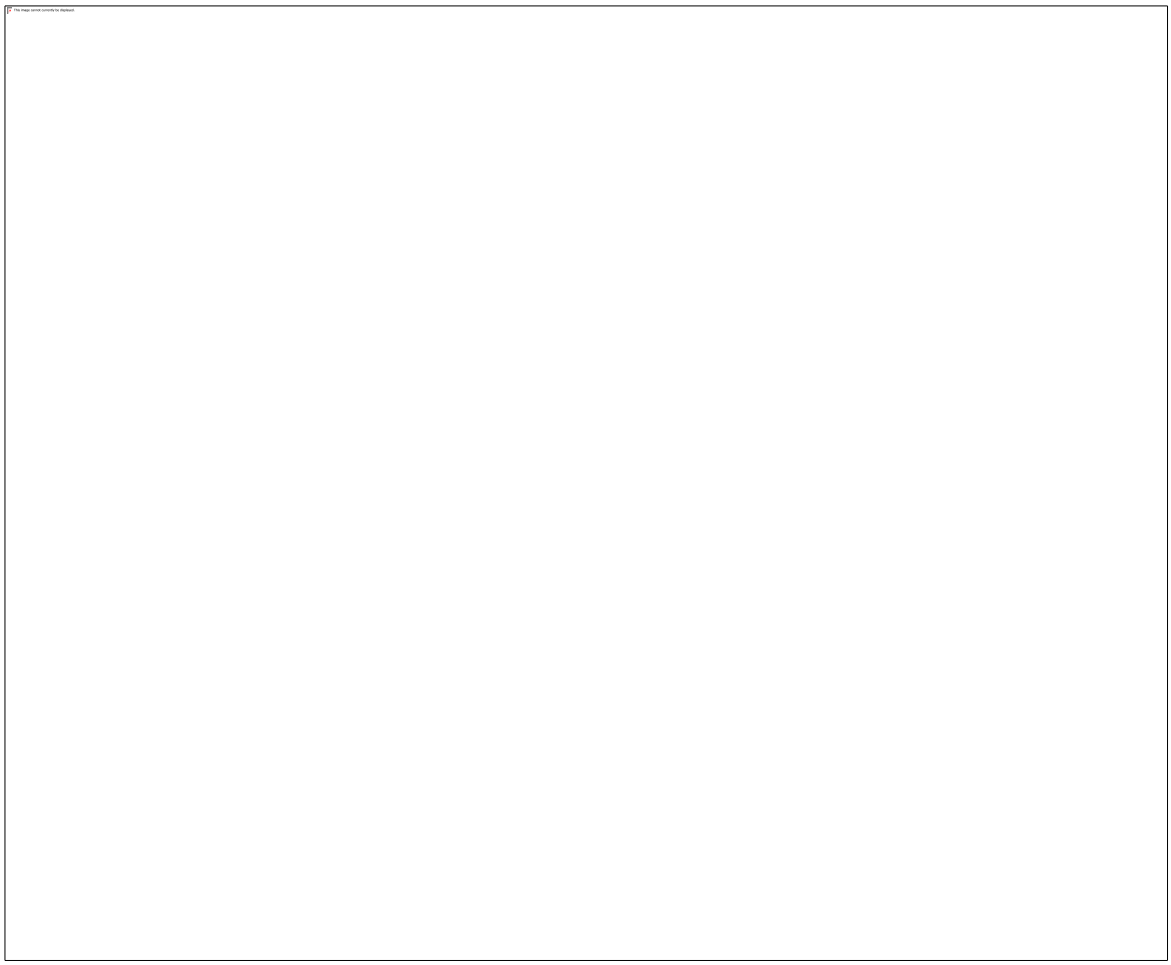

Figure 4.65. Geomagnetic anomaly map showing prominent anomaly windows captured for wider and more detailed probe using the Magnetic Vector Inversion modeling. Windows are labelled from P – Y.

Figure 4.66a(i): Inversion modeling results from window P of Figure 4.65

Figure 4.66a (ii):. Magnetic inversion result of window P with overlaid aeromagnetic anomaly data

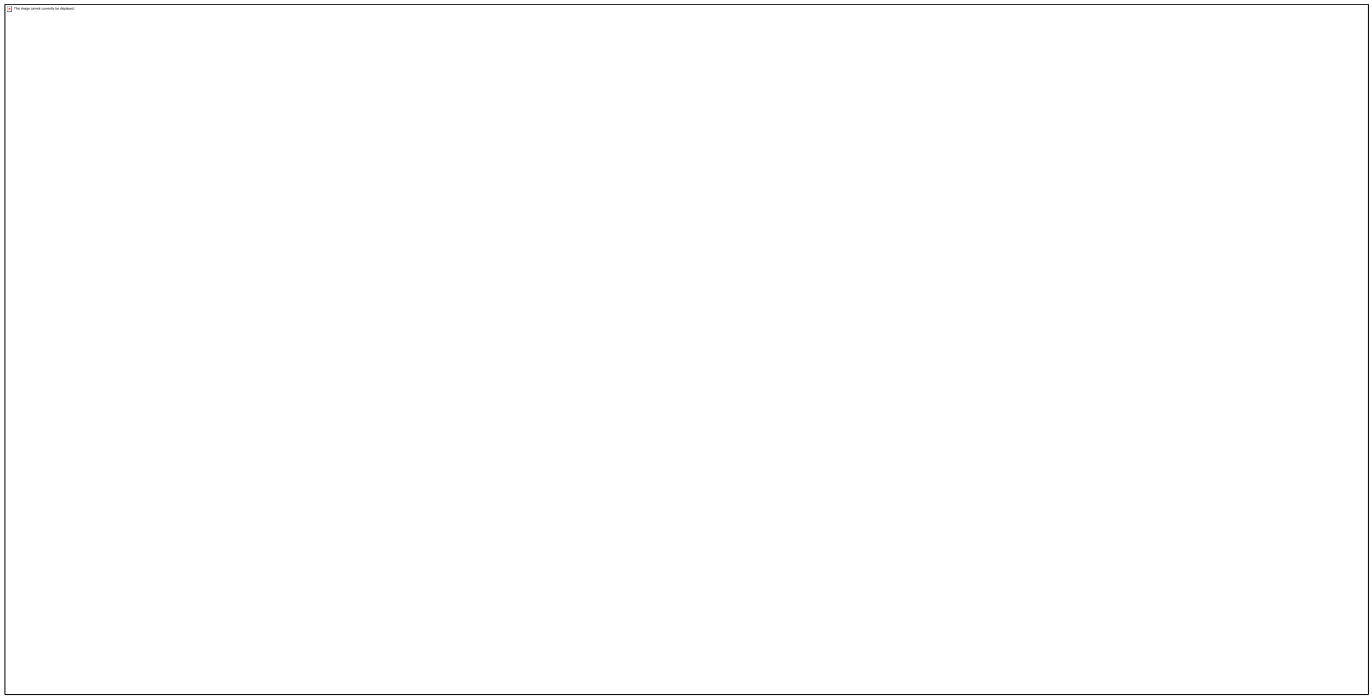

Figure 4.66b (i): Inversion modelling results from window Q of Figure 4.65

Figure 4.66b (ii): Magnetic inversion result of window Q with overlaid aeromagnetic anomaly data

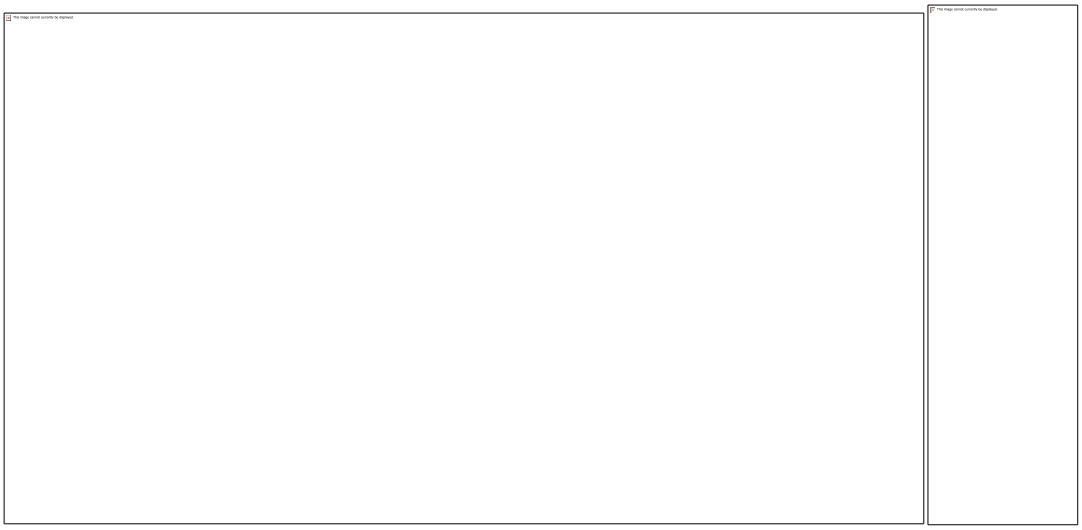

Figure 4.66c (i): Inversion modelling results from window R of Figure 4.65

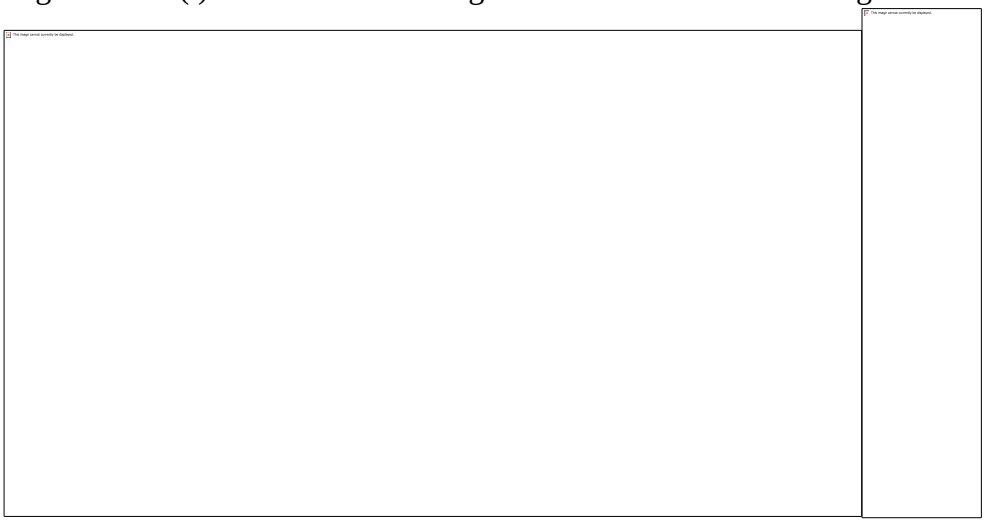

Figure 4.66c (ii):. Magnetic inversion result of window R with overlaid aeromagnetic anomaly data

S window in Figures 4.66 d(i) reveals horizontal models with varying MVI values. The aeromagnetic anomaly data was also superimposed on the inversion modelling result of the window. Corresponding high magnetic intensity anomalies on the aeromagnetic anomaly map were revealed over the rows of N-S trending horizontal deposits with varying MVI values in Fig.4.66d(ii).

T window represented in Figures 4.66 e (i) reveals a lot of nucleated but concentrated clusters on the subsurface. The aeromagnetic anomaly data directly overlies the models from this window, as revealed in Fig. 4.66e(ii).

U window is represented in Figures 4.66f(i) which captures models delineated with varying range of MVI values. Overlying these models in Fig. 4.66f (ii), is the aeromagnetic anomaly data whose variegated short wavelength anomalies correspond with the underlying model.

V is represented in Fig. 4.66g(i) which captures inclined to spherical models with varying low MVI values between 0.00031 and 0.00032. The near-spherical model has a range of MVI values between 0.00034 to 0.00049. Figure 4.66g(ii) shows superposition of aeromagnetic anomaly data on inversion modeling results.

Figure 4.66h(i) shows window W which captures models of higher intensity and MVI values within the range of 0.00031 and 0.00053. The inversion models were overlain with the aeromagnetic data as shown Fig.4.66 h(ii).

Window X captures models with high MVI values > 0.00038 which overlie those of lower MVI values <0.00024. in Fig. 4.66I(i). There are various magnetic intensities of the models at the evident from the varying MVI values of surface outcropping models between 0.00015 to 0.00031 MVI. The aeromagnetic anomaly data superposed on the inversion modeling results, is represented in Fig. 4.66I(ii).

Figure 4.66j(i) shows window Y which captures basically, sub-surface deposits revealed in this

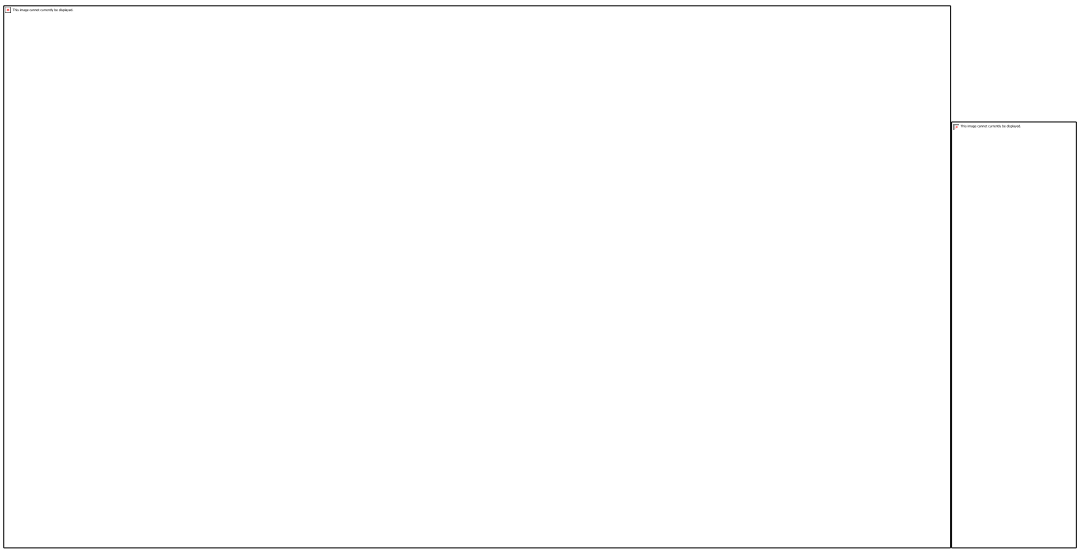

Figure 4.66d (i): Inversion modeling results from window S of Figure 4.65

Figure 4.66d (ii): Magnetic inversion result of window S with overlaid aeromagnetic anomaly data

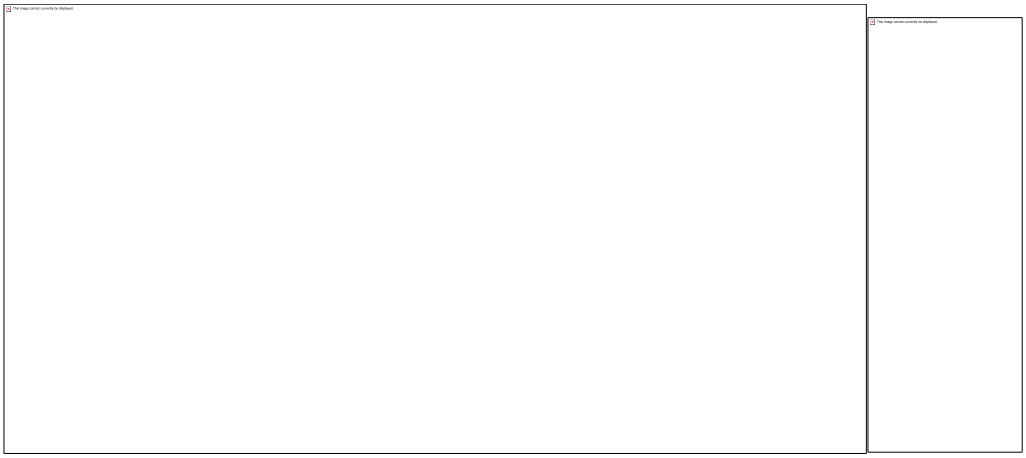

Figure 4.66e (i): Inversion modeling results from window T of Figure 4.65

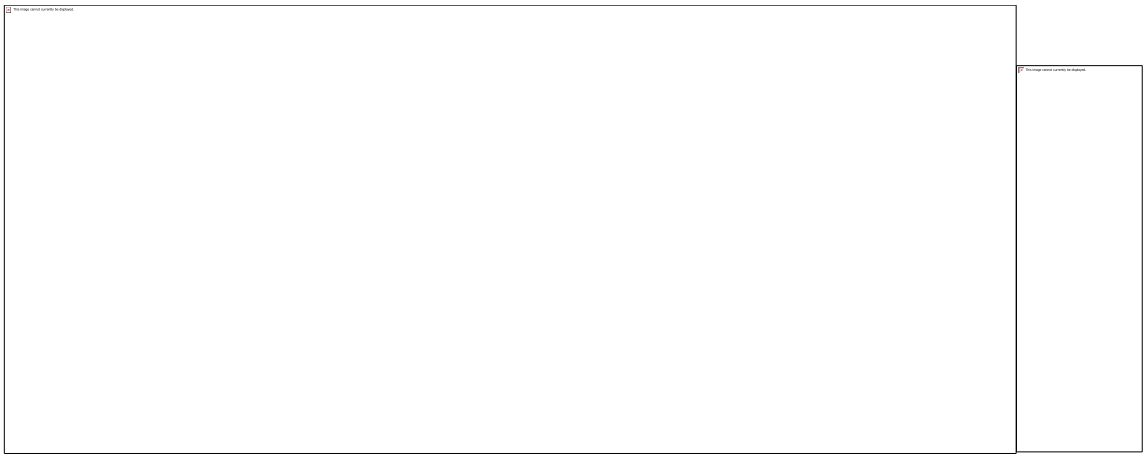

Figure 4.66e (ii): Magnetic inversion result of window T with overlaid aeromagnetic anomaly data

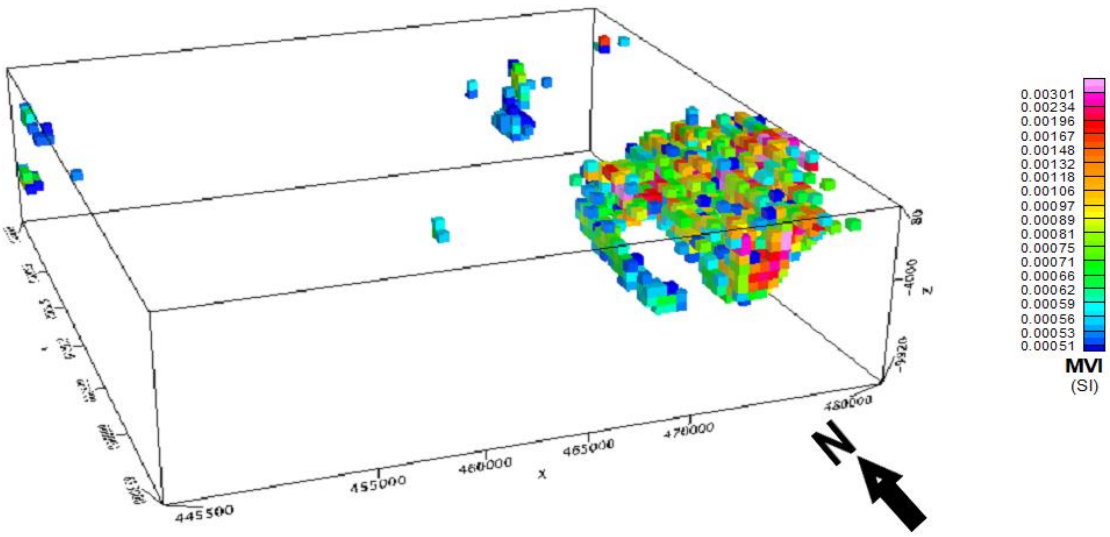

Figure 4.66f (i): Inversion modeling results from window U of Figure 4.65

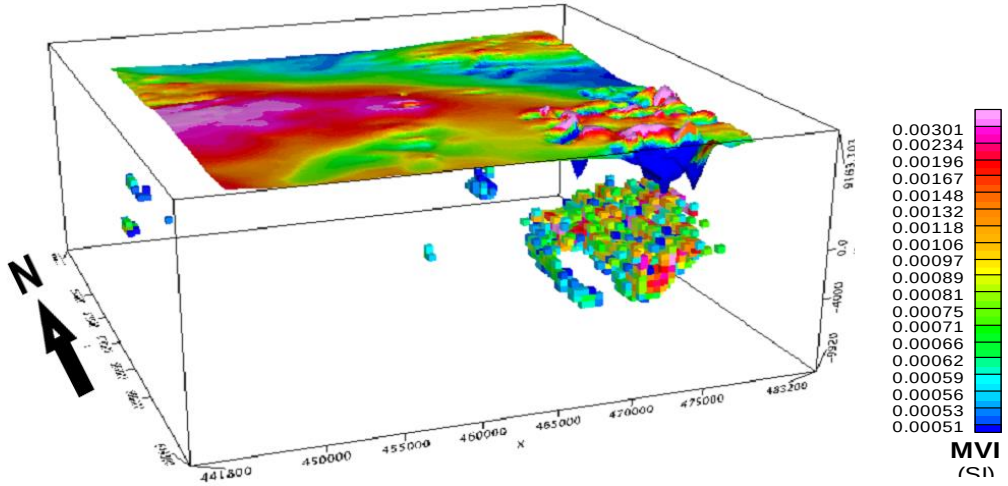

Figure 4.66f (ii): Magnetic inversion result of window U with overlaid aeromagnetic anomaly data

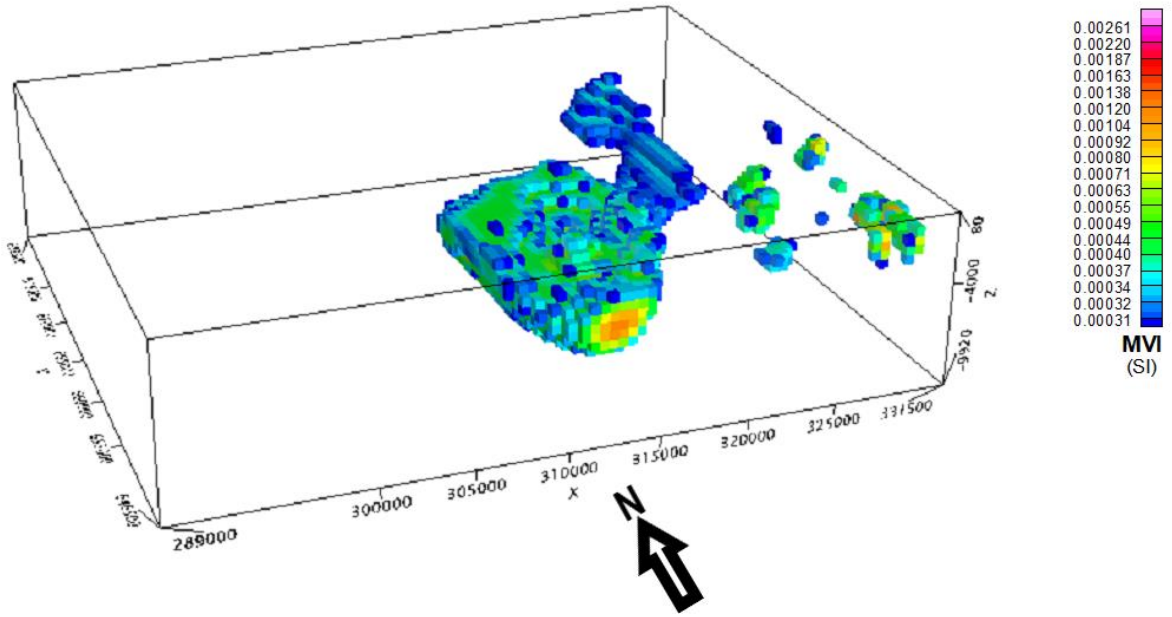

Figure 4.66g (i): Inversion modeling results from window V of Figure 4.65

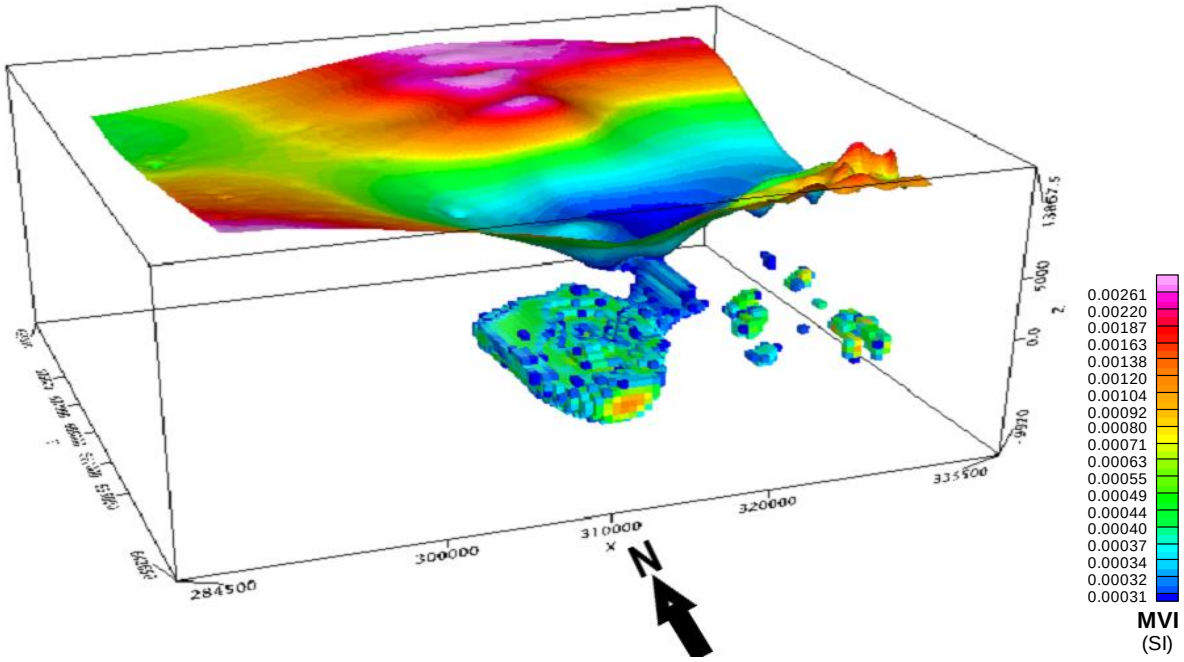

Figure 4.66g (ii): Magnetic inversion result of window V with overlaid aeromagnetic anomaly data

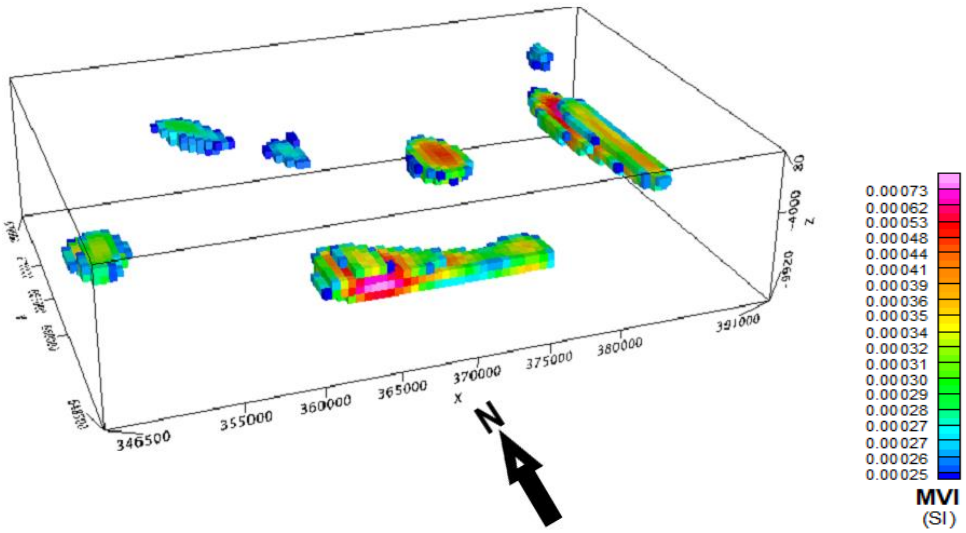

Figure 4.66h (i): Inversion modeling results from window W of Figure 4.65

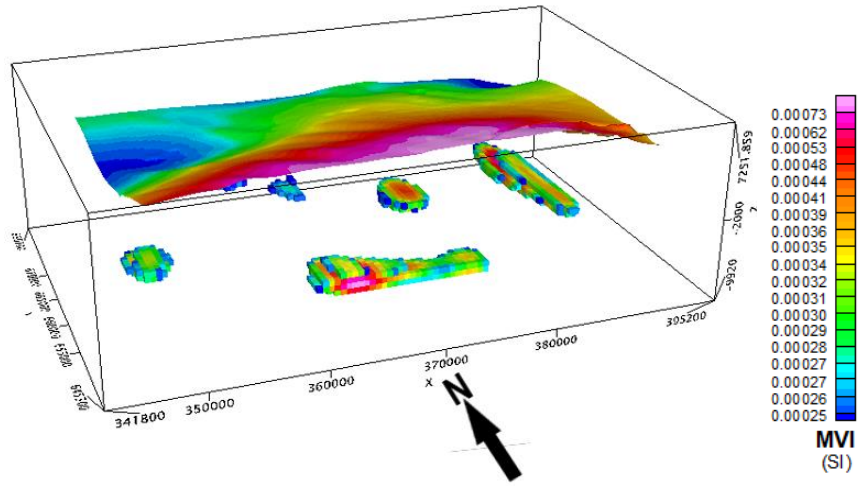

Figure 4.66h (ii): Magnetic inversion result of window W with overlaid aeromagnetic anomaly data

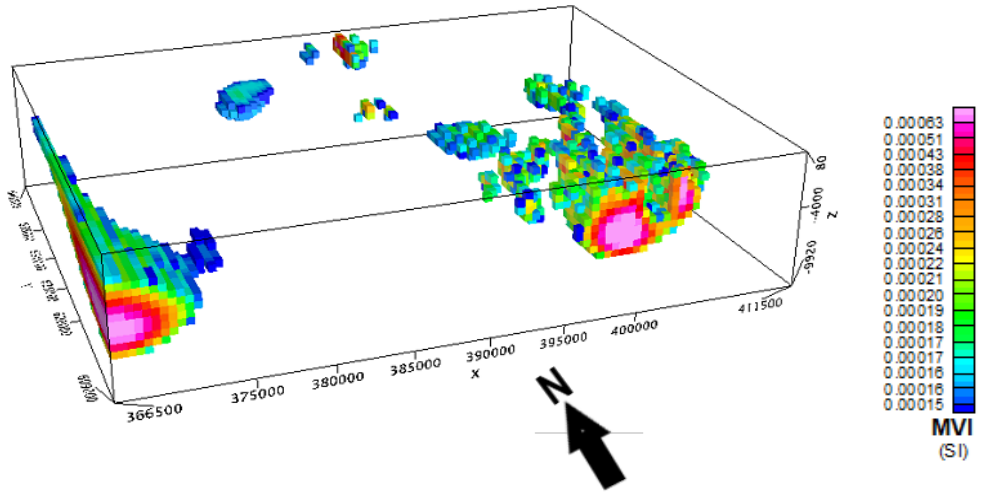

Figure 4.66I (i): Inversion modeling results from window X of Figure 4.65

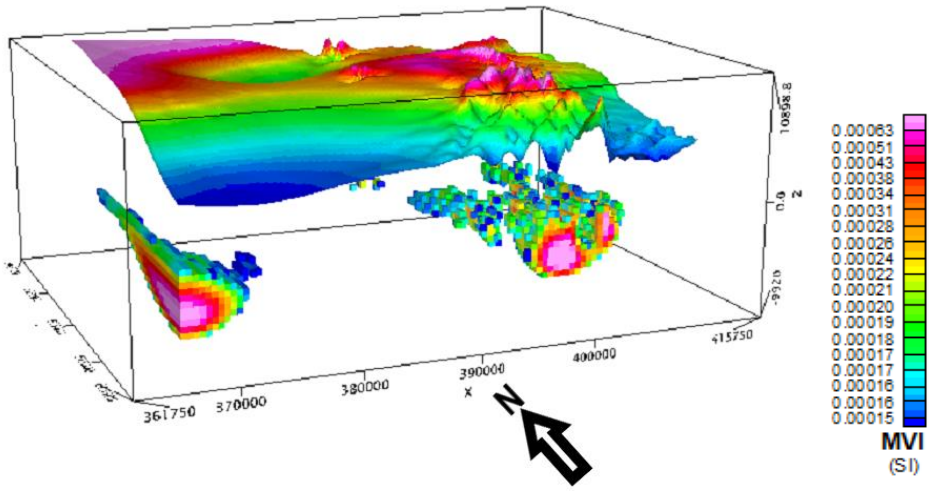

Figure 4.66I (ii): Magnetic inversion result of window X with overlaid aeromagnetic anomaly data

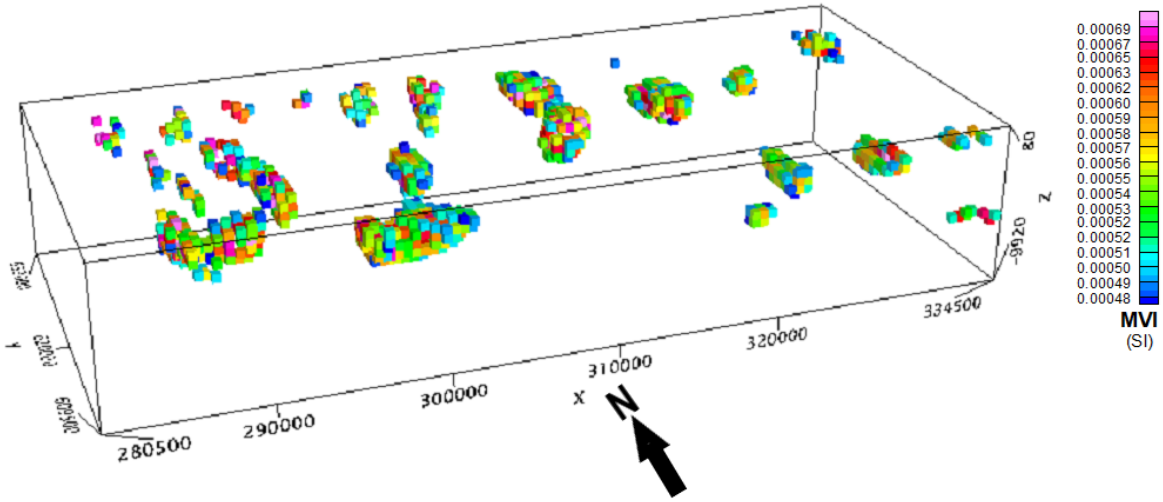

Figure 4.66j (i): Inversion modeling results from window Y of Figure 4.65

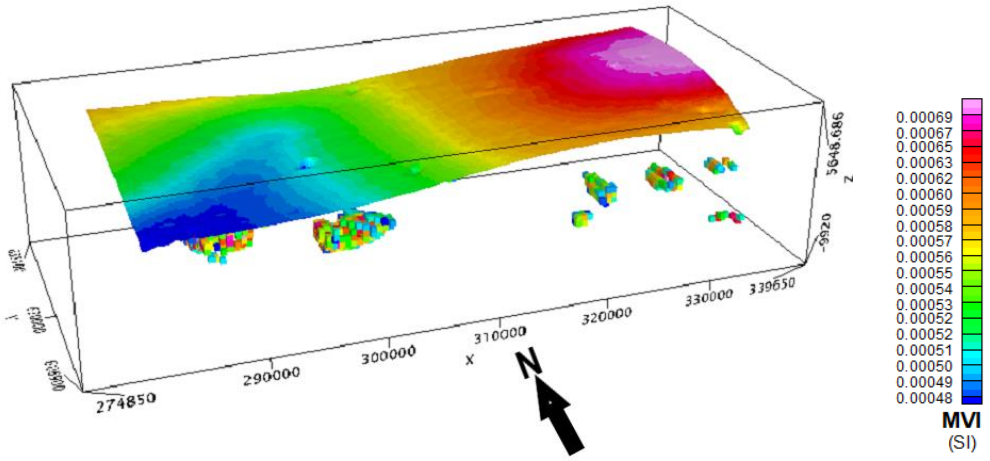

Figure 4.66j (ii): Magnetic inversion result of window Y with overlaid aeromagnetic data

window. The deposits are almost spherical and nodular and dispersed all through the window area and the models have equally varying MVI values between 0.00048 to 0.00069. The superimposition of aeromagnetic anomaly data over the revealed deposits is shown in Figure 4.66j(ii).

4.1.3 Result from Airborne Radiometric Data

Information on naturally occurring K, eU, and eTh were collected through a spectrometer. The e(U) and e(Th) are designated to represent Uranium and Thorium counts indirectly from their decay products not more than 30 cm for shallow surface layer of high density and consolidation and a bit more for unconsolidated sediments.

A. Results from Radioelement Concentrations

The radioelement composite image combines data of K in cyan, eTh in magenta, and eU in yellow (Fig.4.69). The various radioelement concentrations are represented in Figures 4.67(a) - 4.67(c) and the total count concentrations in Fig. 4.67(d).

B. Results from Radioelement Ratio Composites

The radioelement ratio composite image map shows overall spatial distribution of relative radioelement concentrations. These concentrations reveal lithologic colonies as they distinguish between different rock type units in the study area which are sedimentary and igneous. The Potassium ratio composites in the

forms of K/eTh and K/eU are represented in Figures 4.68(a) and 4.68(b) respectively. Uranium ratio composites of eU/eTh and eU/K are represented in Figures 4.68(c) and 4.68(d) respectively. Uranium plots are displayed in Figures 4.68h and 4.68i, while Thorium ratio composites; eTh/eU and eTh/K are represented in Figures 4.68(e) and 4.68(f) respectively. Figure 4.68g shows combination of radioactive results which was established from combination of each of the three radioelement ratio composites for three radioactive elements (combination of three radiometric ratios), eU/eTh, eU/K and eTh/K.

C. Results from Ternary Image

Figure 4.69 reveals the ternary radioelement map which is a colour composite image usually

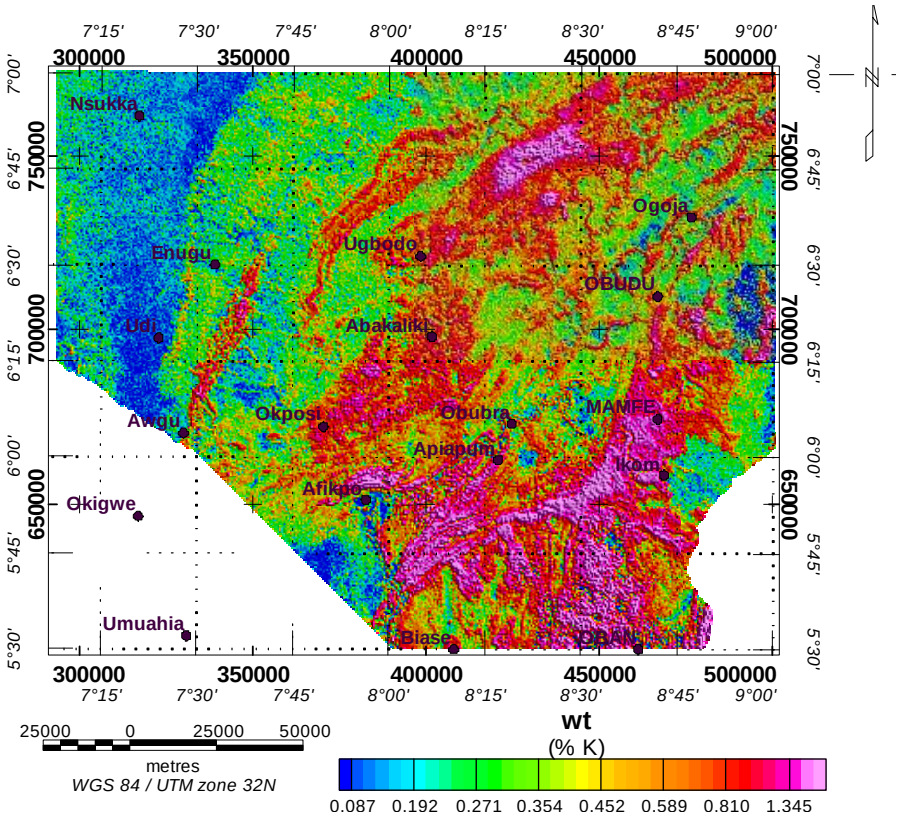

Figure 4.67a: Potassium (K) Concentration Map of the Radiometric Data

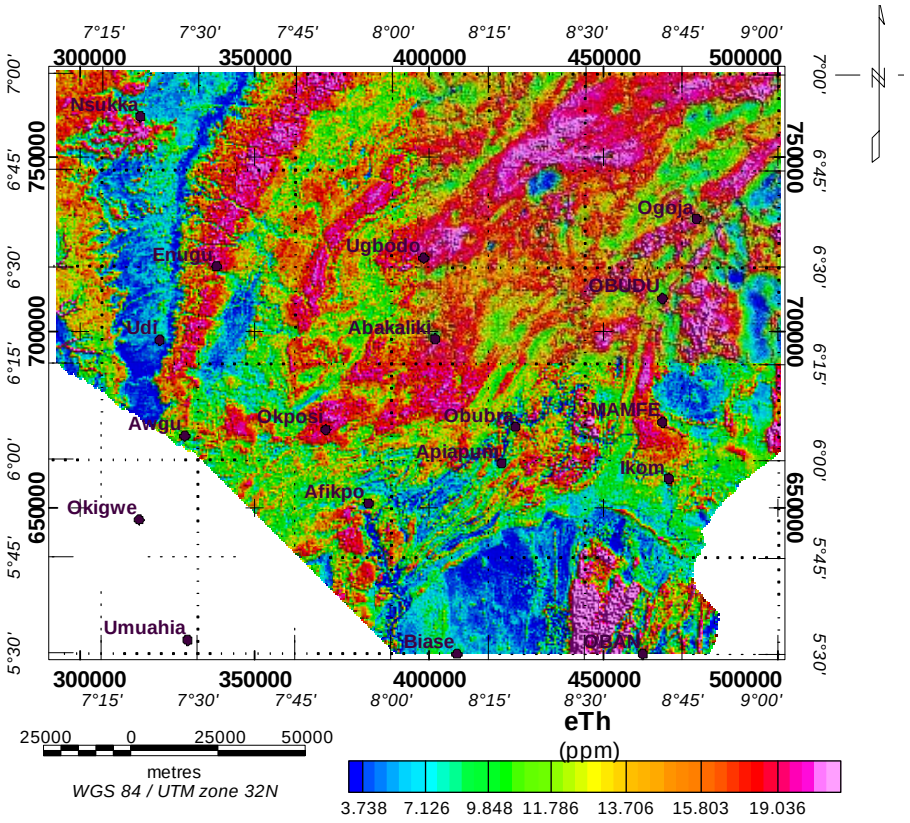

Figure 4.67b: Thorium (Th) Concentration Map of the Radiometric Data

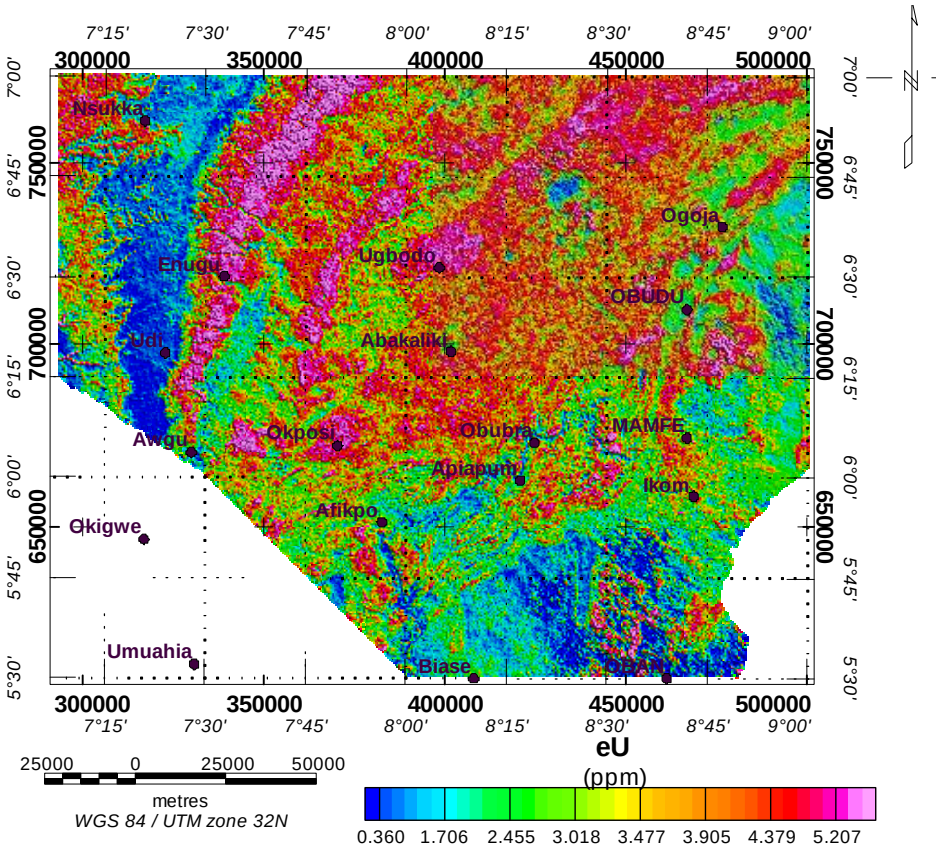

Figure 4.67c: Uranium (U) Concentration Map of the Radiometric Data

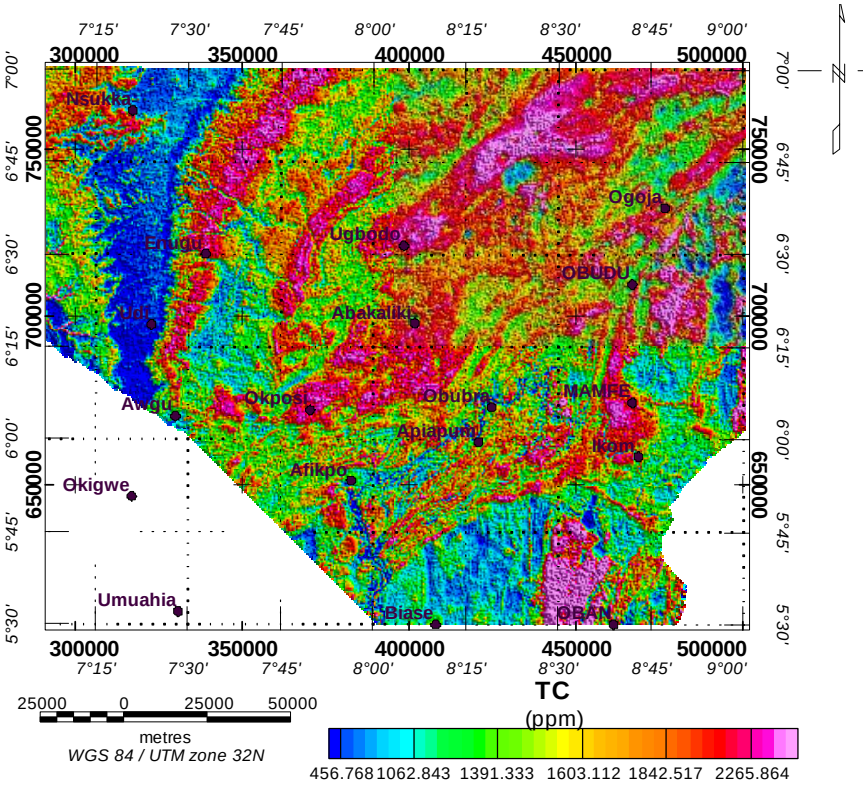

Figure 4.67d: Total Count (TC) Concentration Map of the Radiometric Data

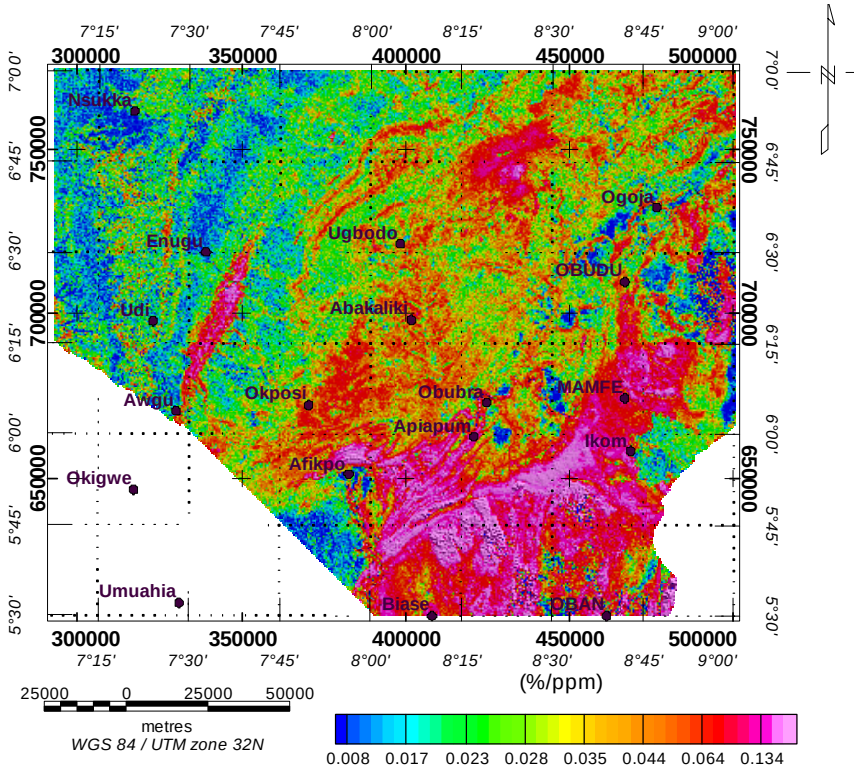

Figure 4.68a: Potassium Composite Image per Thorium Concentration (K/eTh).

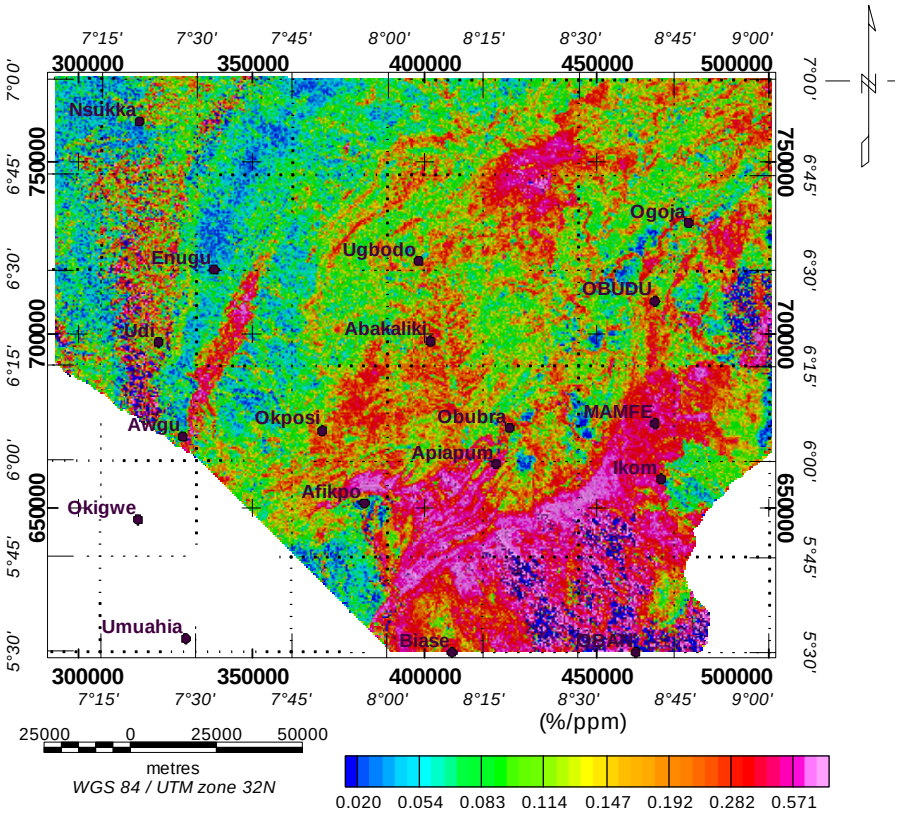

Figure 4.68b: Potassium Composite Image per Uranium Concentration (K/eU).

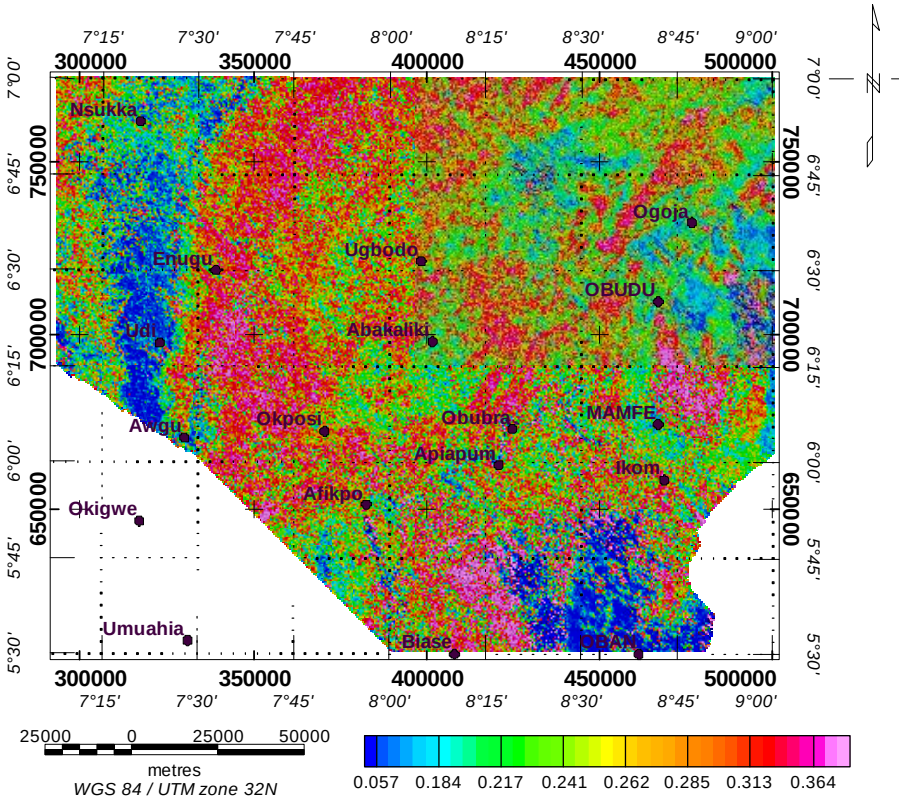

Figure 4.68c: eU/eTh concentration map of the region.

Figure 4.68d: eU/K concentration map of the region.

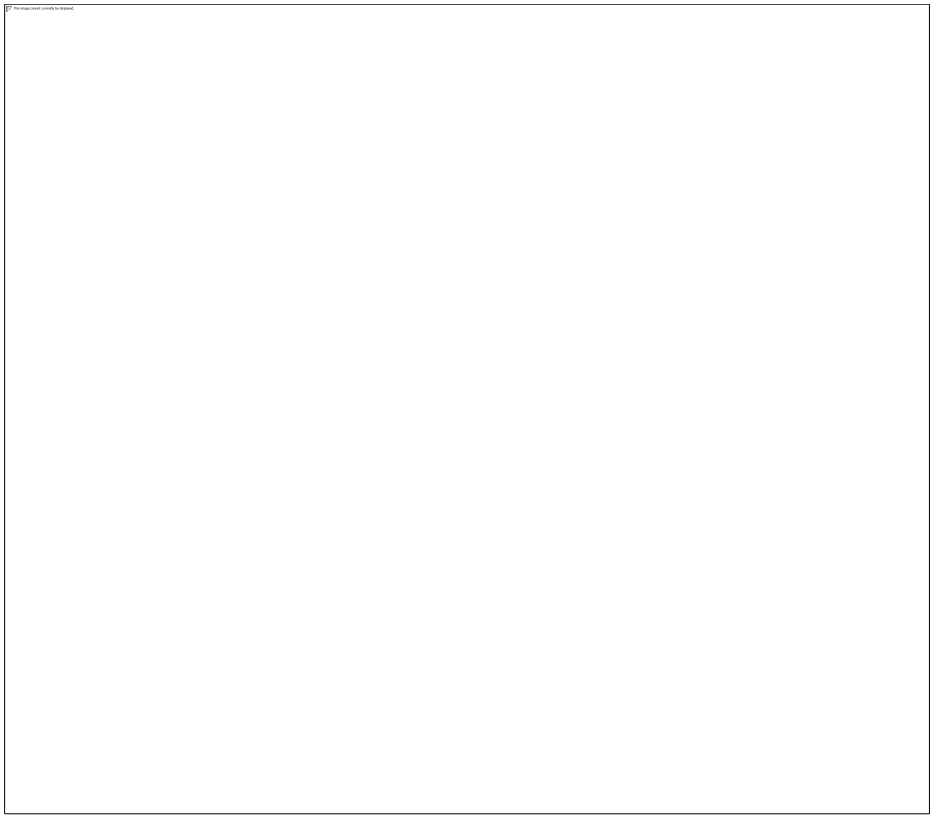

Figure 4.68e: eTh/eU concentration map of the region.

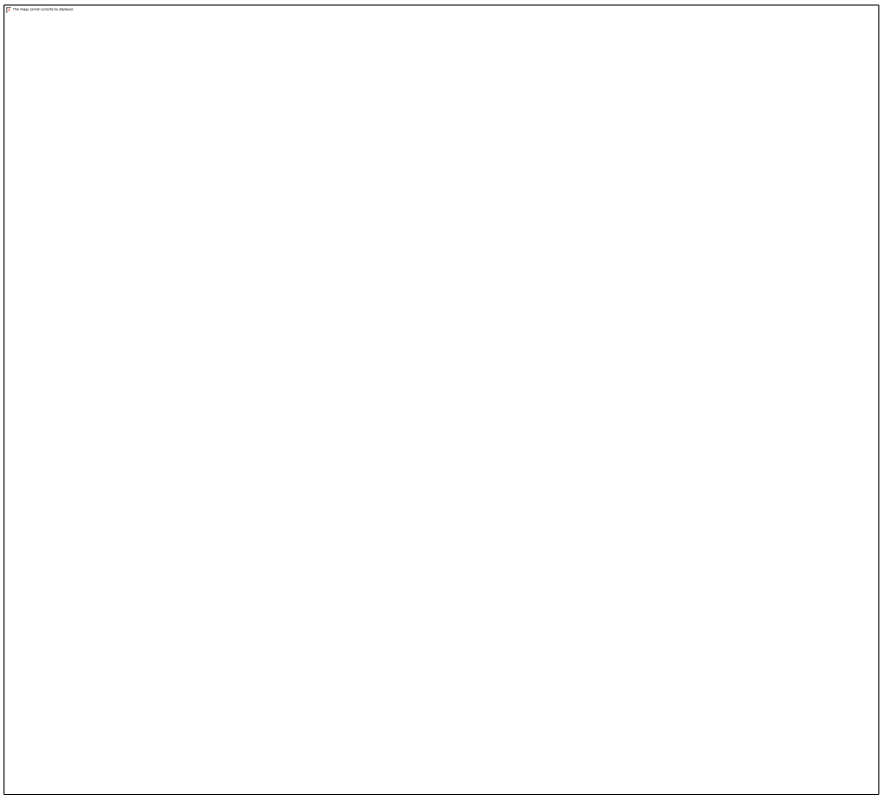

Figure 4.68f: eTh/K concentration map of the region.

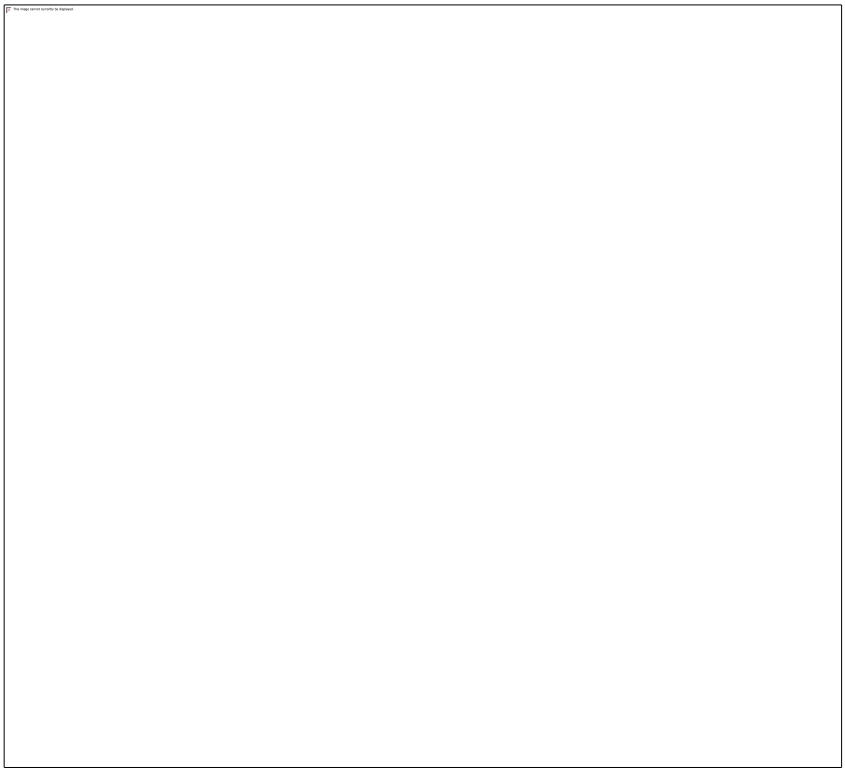

Figure 4.68g: Combination of radioactive results of radioelement ratios (eU/eTh + eTh/K + eU/Kconcentration map of the region).

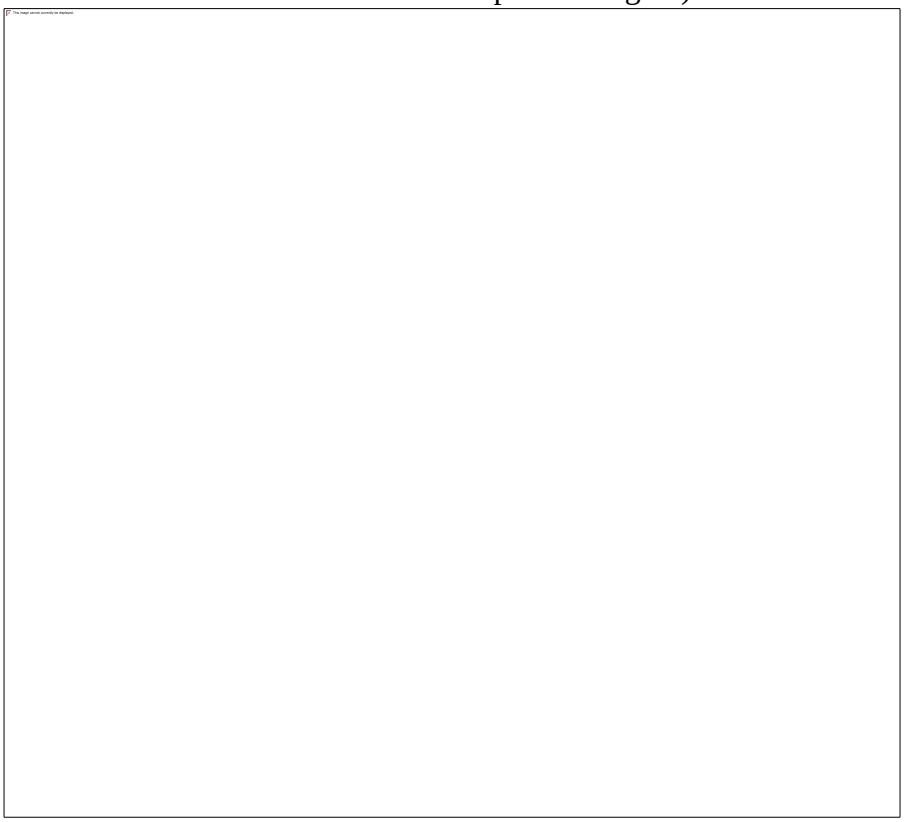

Figure 4.68h: $\frac{eU^2}{eTh}$ concentration map of the region.

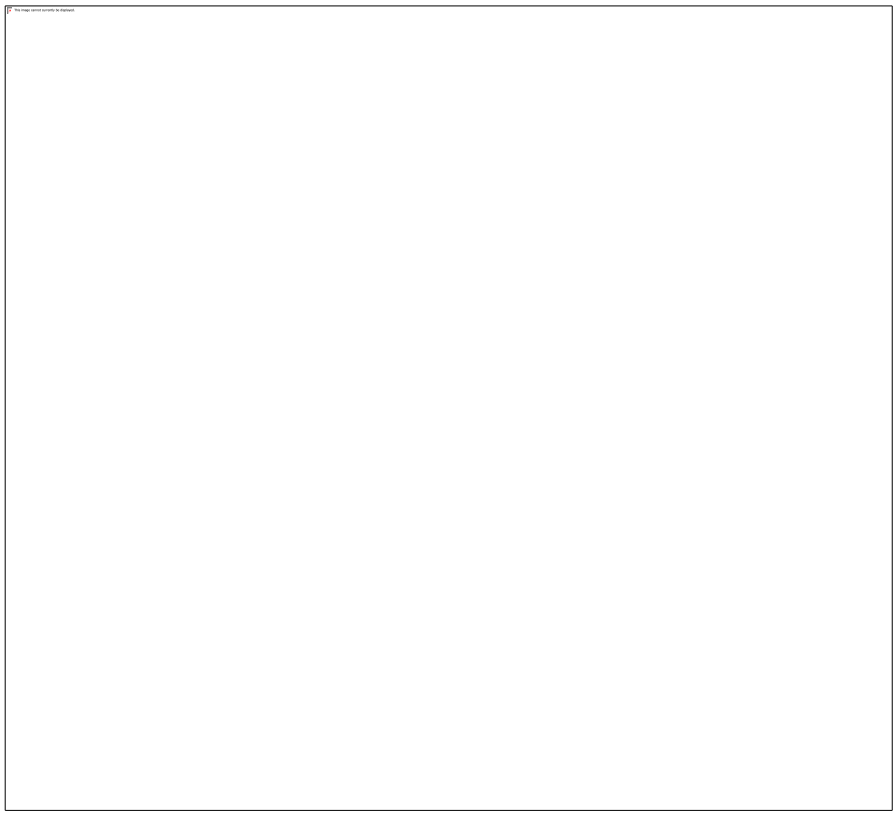

Figure 4.68i: eU–(eTh/3.5) concentration map of the region.

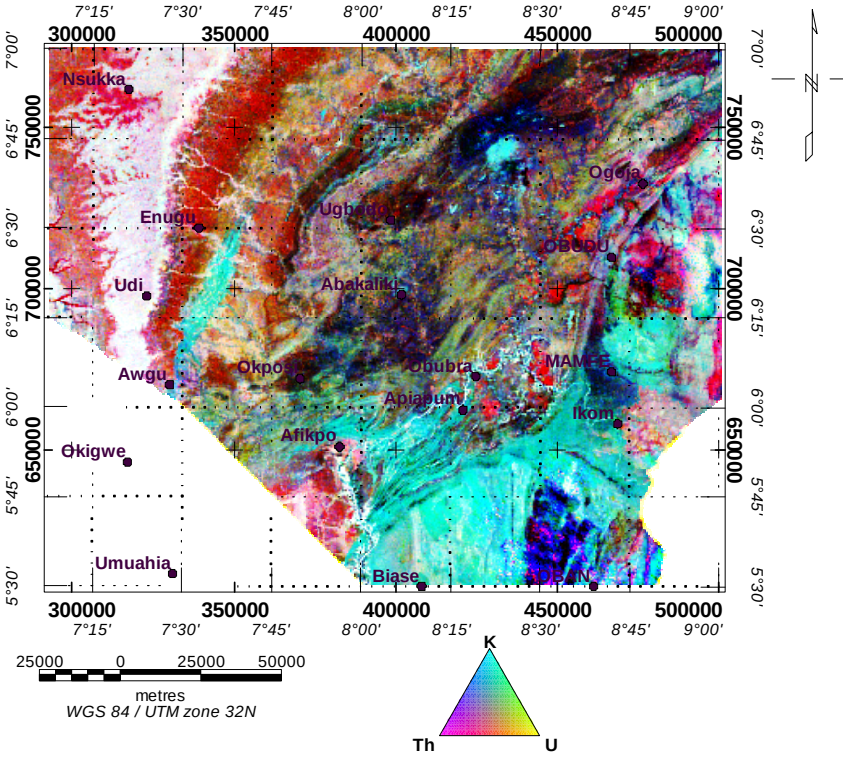

Figure 4.69: Ternary image map constructed from combination of the Radio-elements (K (%), eTh, and eU).

generated by modulating red, green and blue phosphors of the display device in proportion to the radioelement concentration values of the K, Th, U and TC grids. The use of red, green and blue for K, eTh and eU respectively is usually the standard for displaying gamma ray spectrometric data but cyan, magenta and yellow were used for K, eTh and eU respectively based on colour variation choice.

4.1.4. Results of Re-appraising the Trend of Mineral Occurrence Pattern viz-a-viz Map Composites

Two to three maps were merged or compared in the course of having a broader picture about mineralized areas.

A. Results from Clay Alteration on Magnetic Lineament Map

Ratio 6 on 7 which delineates clay alteration regions was superimposed on extracted magnetic lineament map (Fig.4.70) to show areas likely viable for ore accretions. The encircled zones are considered likely viable for ore deposits because they are contact zones where both surface and deep-seated lineaments coincide with areas in green to blue denoting rich clay mineral regions.

B. Results from Magnetic and Landsat Lineament Maps on Iron Oxide Map

Magnetic and Landsat lineament maps were both superimposed on the iron oxide (4 on 2) map (Figs. 4.71a & 4.71b respectively).

C. Results from Magnetic and Landsat Lineament Maps on Mineral Map

The superimposition of the magnetic and Landsat lineaments (Fig. 4.72) show dense lineation of the study area which serves as good conduits for hydrothermal fluid migration, wall rock alteration and ore precipitation. Mineral map of the study area which was digitized from updated 2019 mineral map of Nigeria (Falade, 2016) was superimposed on Figure 4.72 and most minerals correlated with areas of dense lineations, thus the map gives a prediction of prospective mineral occurrences of the study area.

D. Results from Evaluation of Zones Viable for Ore Deposits

Minerals on NTilt Map (Fig. 4.73) and on geothermal gradient map (Fig.4.75) were used to evaluate the effect of structures and temperatures on mineral distribution within the area. Figure 4.74 which is

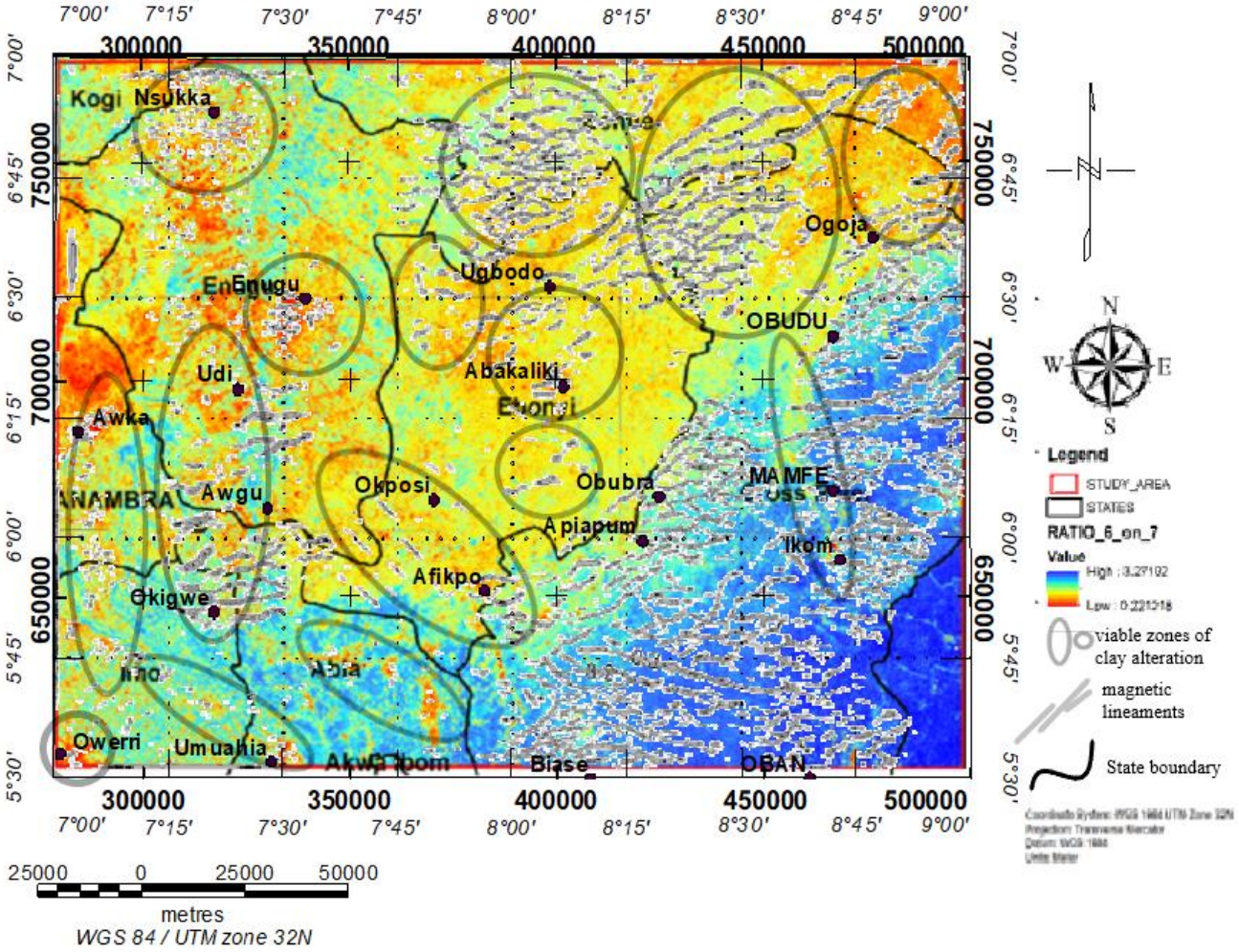

Figure 4.70: Magnetic Lineament Superimposed on Clay Alteration (6 on 7 Ratio) Map

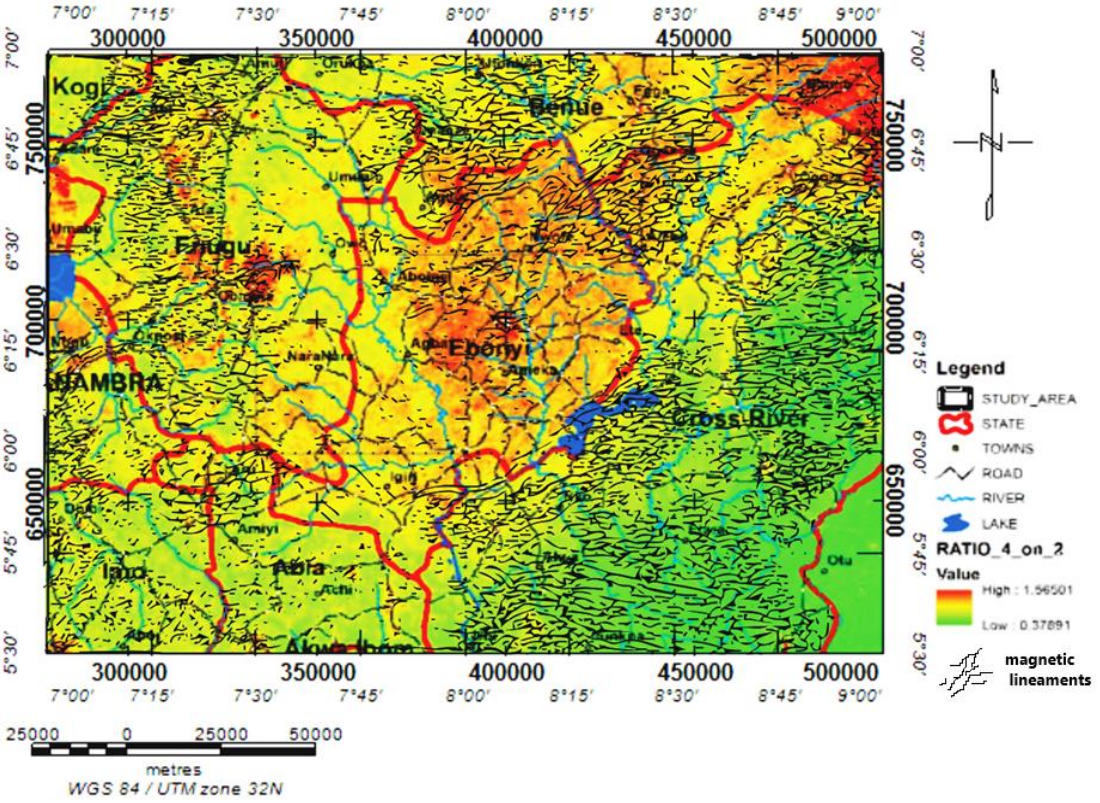

Figure 4.71a: Magnetic lineament map superimposed on 4 on 2 ratio map

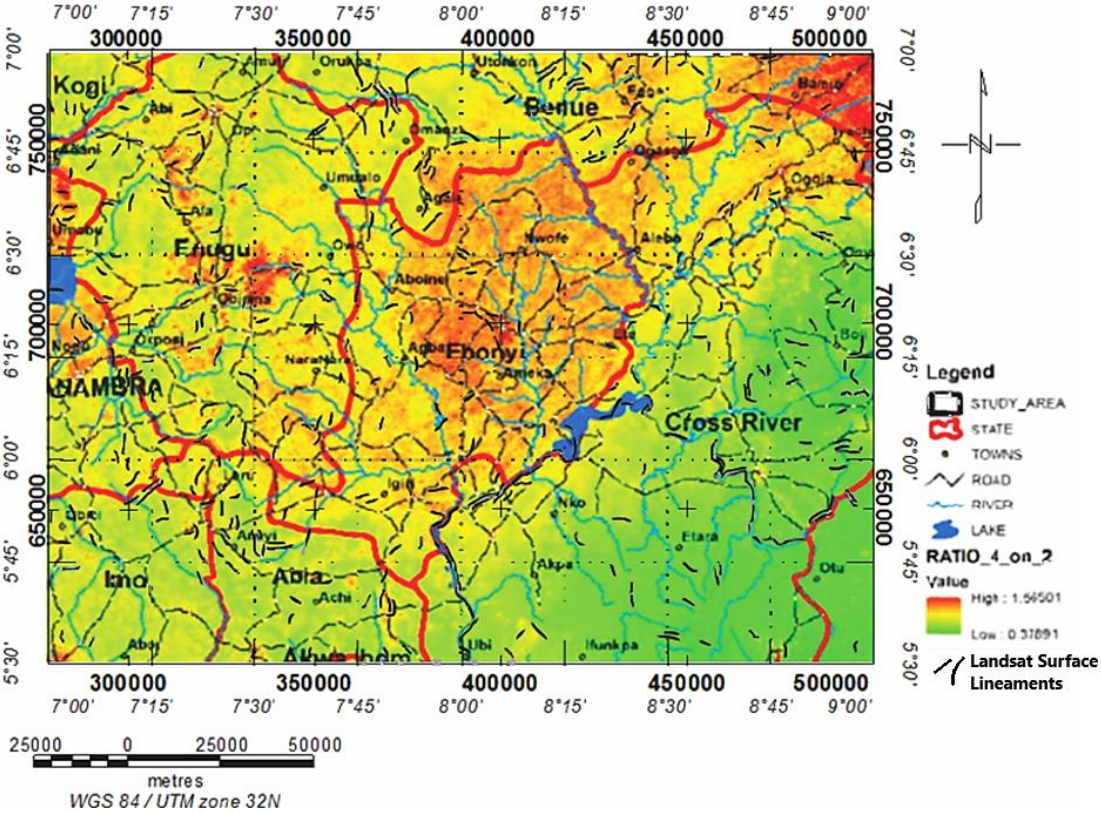

Figure 4.71b: Landsat lineament Map superimposed on 4 on 2 ratio map

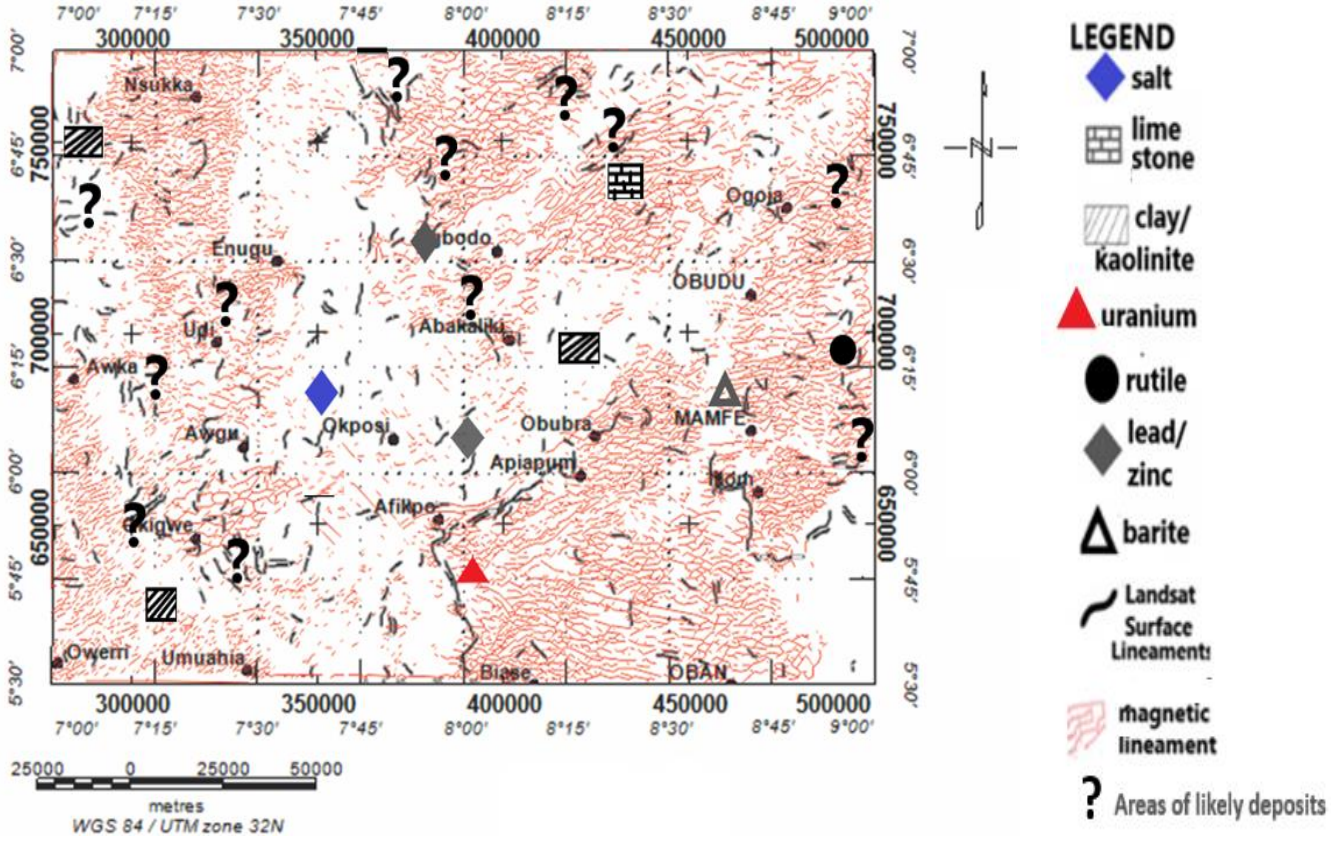

Figure 4.72: Predictive mineral potential map of the study area

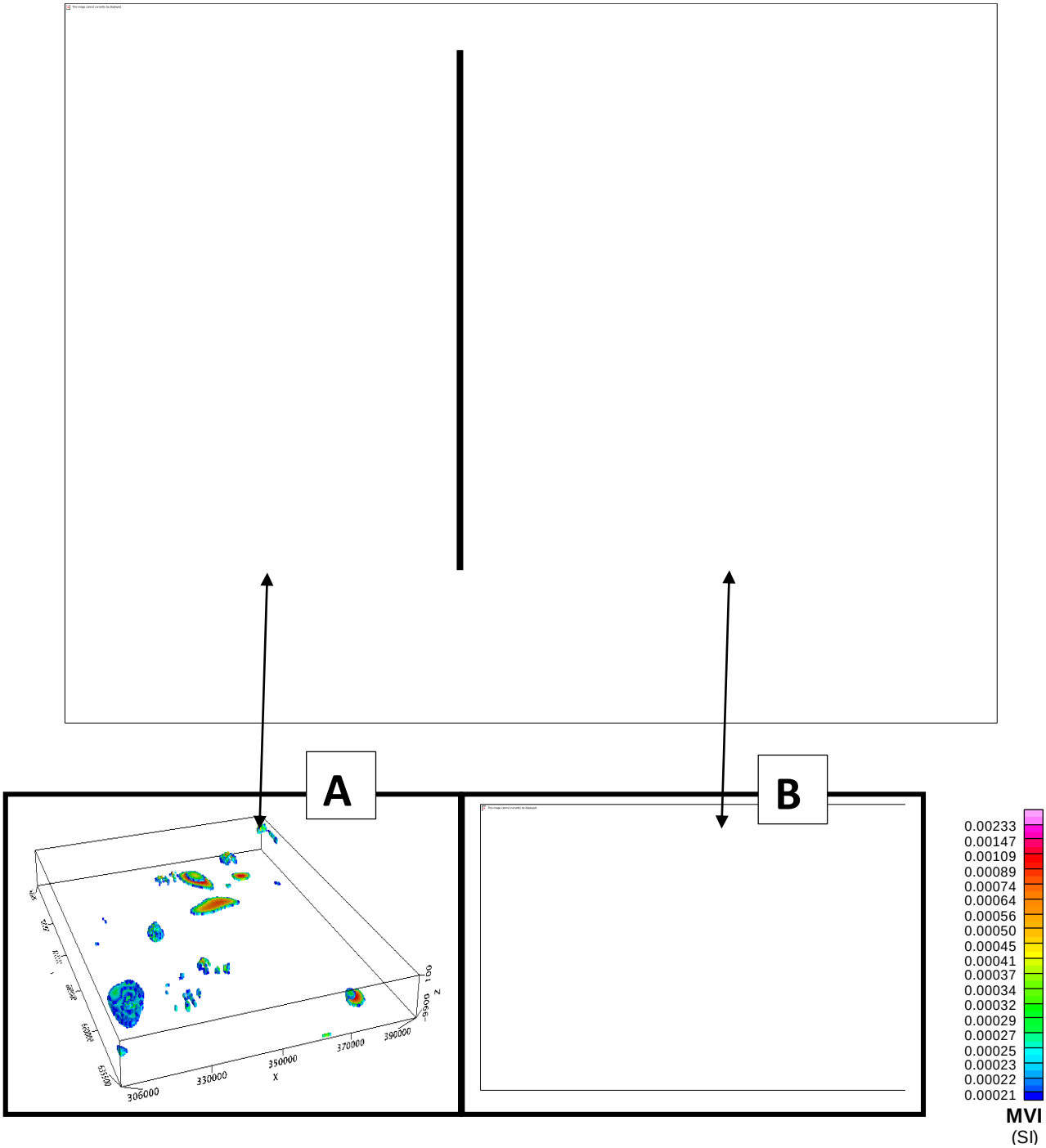

Figure 4.73: Comparison of inversion model results to NTilt results

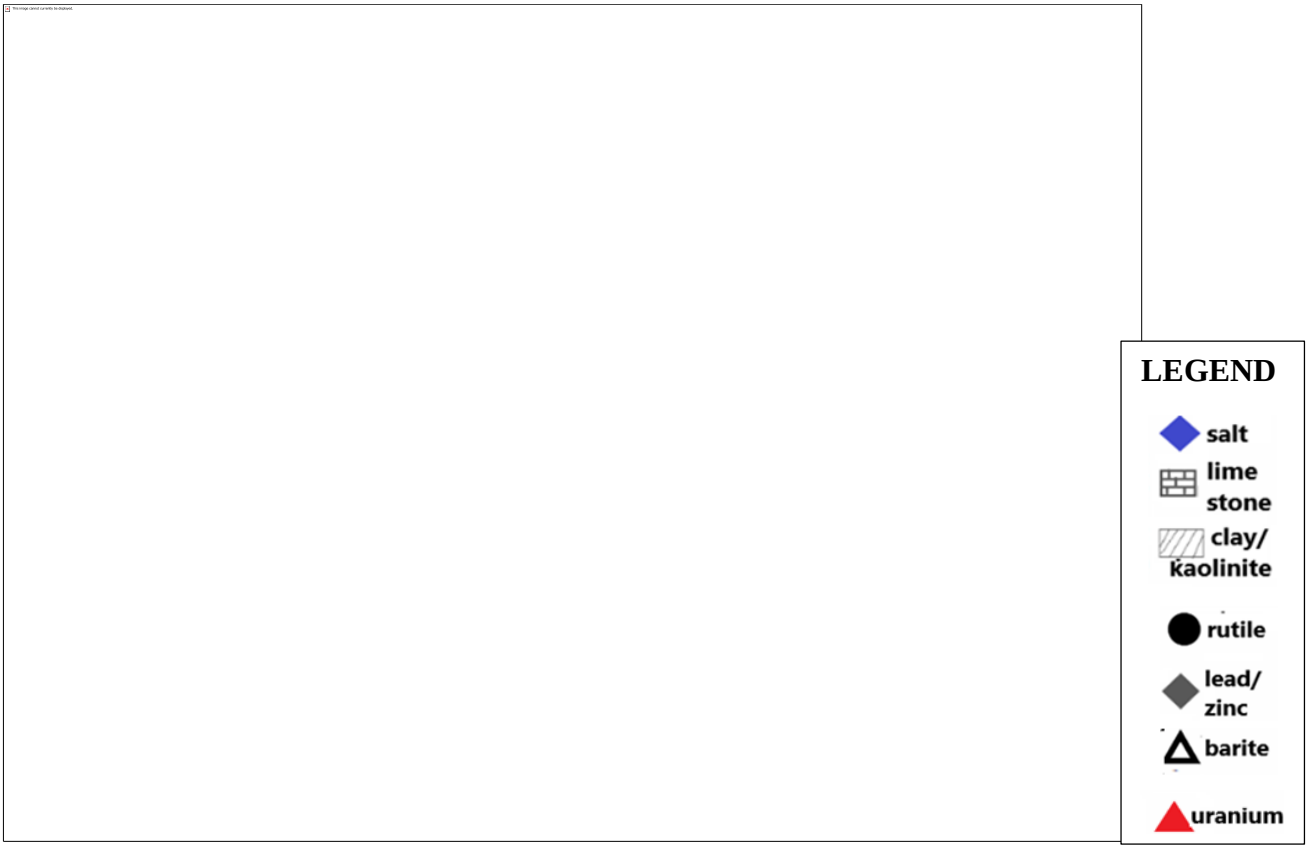

FIG.4.74: NTILT on Mineral Map

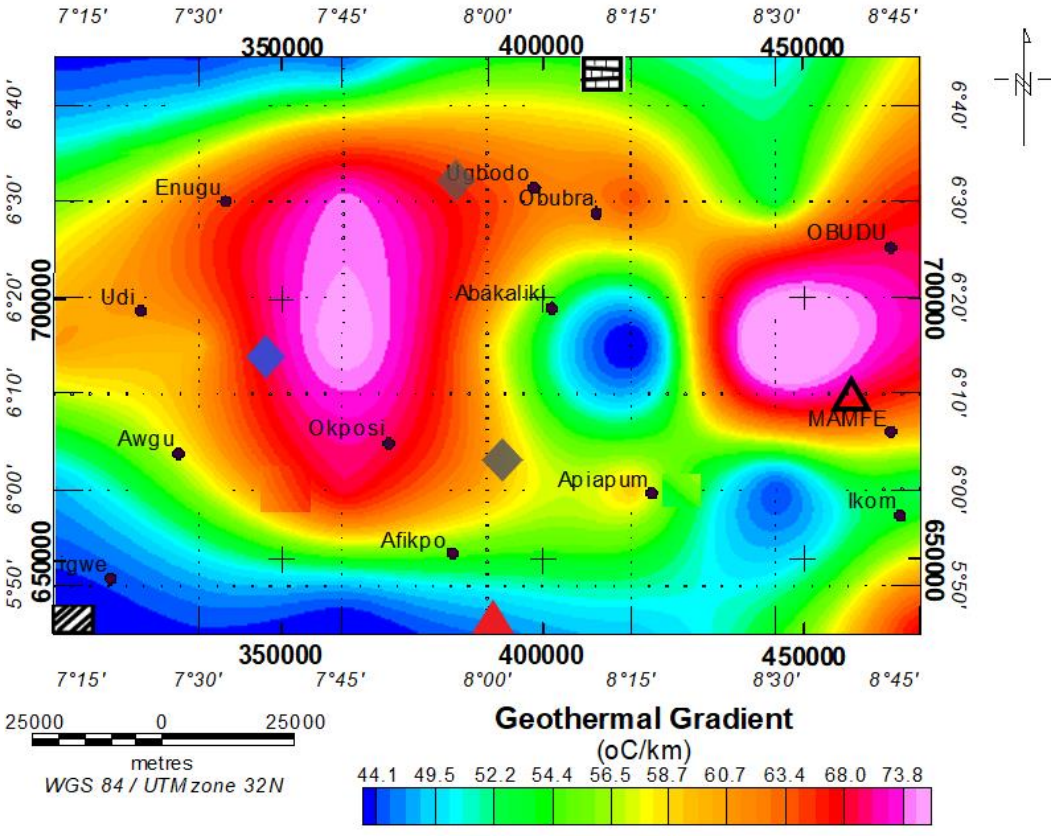

FIG.4.75: Geothermal Gradient on Mineral Map

the part B modelled results from the geomagnetic anomaly field data were compared with NTilt map in order to compare shallow and deep structures delineated by the two techniques. Structures from inferred fault zones compare well with occurrence trend of delineated minerals as displayed in Figure 4.76 b. Varying degree of occurrence of these parameters such as radiometric total count, landast and magnetic lineaments, geothermal gradient, heatflow, hydrothermal alteration from ratio composites and magnetic intensities were evaluated in Table 4.5 to detect coinciding anomalous spots as potential zones of mineral deposits. Based on this afore-mentioned evaluation, a comprehensive catalogue was deduced from study results of Table 4.5, model results from Fig.4.65, results from Figs. 4.70 and 4.72b and inferences from Fig.4.72a. Table 4.6 was developed to infer regions of potential ore deposits.

4.1.5. Results of Electrical Data

Exploration for geothermal energy often involves geological (including remote sensing), geophysical and geochemical investigations (El-Qady, 2006; Kana *et al*., 2015; Shah *et al.,* 2015; Chabaane *et al.*,2017; Azaiez *et al.,* 2020). Geophysical investigation is either direct, involving methods that measure parameters (e.g. temperature, fluid content, resistivity/conductivity) directly influenced by geothermal activity such as the thermal, electrical resistivity, magnetotelluric (electromagnetic) and self-potential methods or indirect with methods that explore physical parameters of the host rock (e.g. magnetic property, density, seismic velocity) enabling mapping of subsurface structures or geological bodies including the magnetic, gravity and seismic reflection methods (Georgsson, 2013; Shah *et al*., 2015).

Regions of mineral occurrence and high geothermal gradients were ground-truthed using electrical method, in order to confirm subsurface response as delineated from anomalous points from airborne data. At two regions of mineralization, SP technique was used to ascertain mineralization potentials while Vertical Electrical Sounding was done at two zones of high geothermal gradient. Four sites in all were visited for ground-truthing as shown in Tables 4.6 & 4.7, and represented in Figure 4.76 also.

A. SP and Image Results from Umuobom

For this location, accessibility was so threatened and hence the frog leap/gradient array which

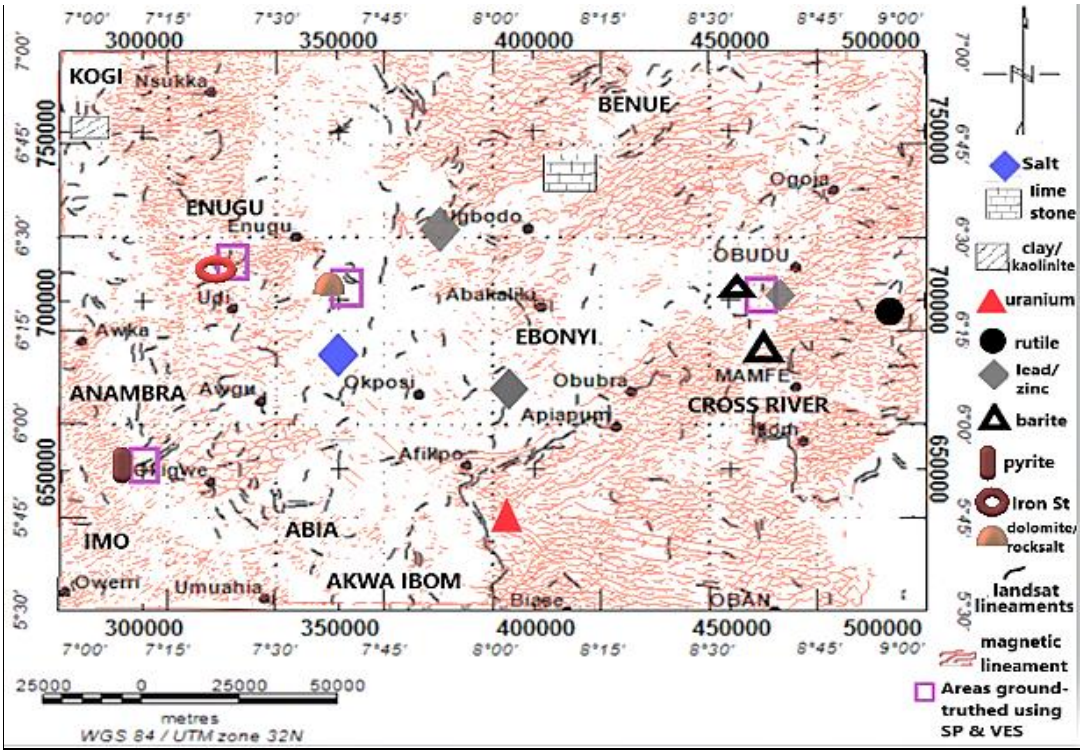

Fig. 4.76a: Mineral map of the study area wuth the ground-truthed points

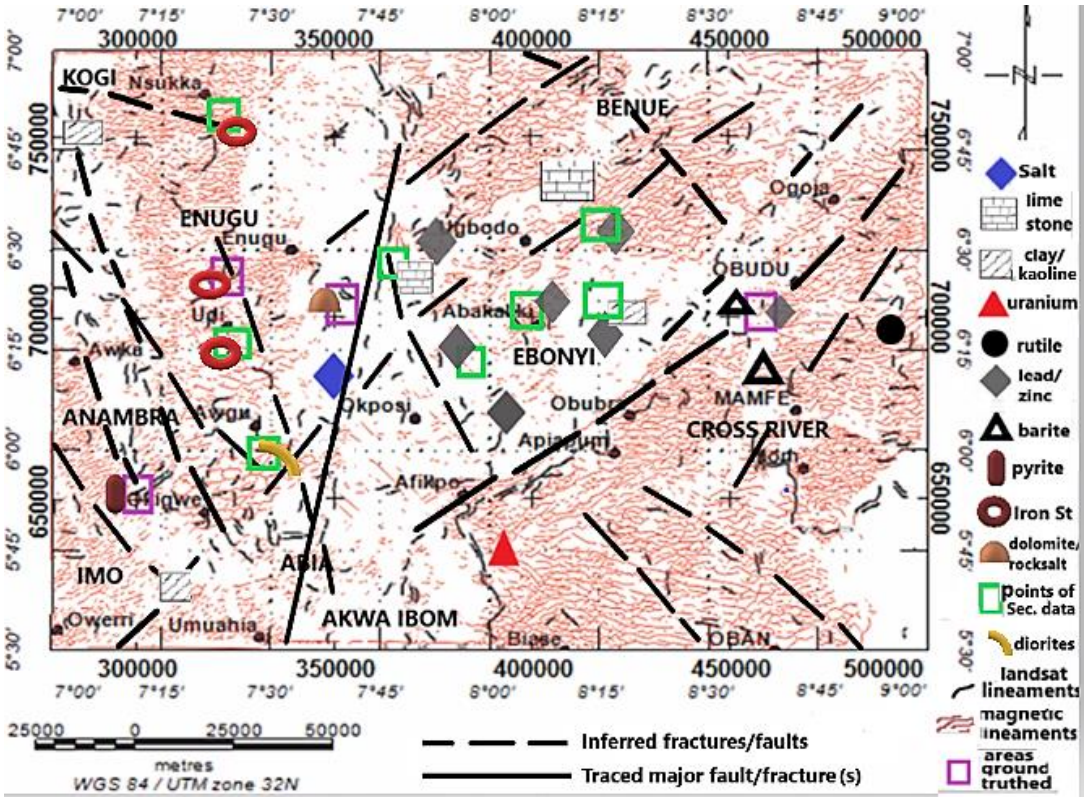

Fig. 4.76b: Improved Mineral Map with Inferred fault zones from Euler, NTilt and Lineament Density Maps

TABLE 4.5: Evaluation of Varying Parameters Within Locations of the Study Area

Table 4.6: Catalogue of potential mineralized zones developed by Evaluating table 4.5 and all mixed data sets

S/N	STATE	LGA	TOWN/ COMMUNITY	COORDINATE(S)	TYPE OF GEOLOGIC FEATURE	RESOURCE
01.	Enugu	Nkanu West	Akpugo-Ndiagu, Akpugo, Ugbowo Road, Nigeria. (Joins to Enugu-Abakaliki Rd)	N06°26'15" E007°37'30"	Awgu formation	Coal & Iron
02.	Enugu	Nsukka	Obimo	N06°49'00.0012" E007°19'00.0012"	Ajali red earth sandstones	Coal & Oolithic Iron Stones Iron
03.	Anambra	Ayamelum	Umumbo	N06°33'29.9988" E007°03'51.0012"	Imo Shales	Clay
04.	Enugu	Ezeagu	Imezi Owa II	N06°23'30.0012" E007°23'00.0024"	Ajali Sandstone	Lateritic Clay & Iron Stone
05.	Enugu	Udi	Nsude, between old Enugu-Onitsha and Udi Rd.	N06°24'26.4" E007°24'14.8"	Dark Lateritic clay with iron stone outcrops which reduces farther away from main areas of concentration.	Lateritic Clay & Iron Stone
06.	Anambra	Njikoka	Nawfia. Along Ajali-Ihube Road.	N06°02'60" E007°13'59.9988"	Ameki shales	Clay & Sulphide mineralization
07.	Anambra	Ideato North	Obodo Ukwu, off Awka-Orlu Road.	N05°55'00.0012" E007°04'59.9988"	Ameki shales	Clay & Sulphide mineralization
08.	Imo	Ideato South	Amaiyi, Umuobom.	N05°52'03.0" E007°10'16.0"	Pyrites within dark grey shale beds in anoxic environments of Ameki shale	pyrite mineralization
09.	Enugu	Igbo Etiti	Nkpologu, Ohodo Abba, Nsukka.	N07°17'00" E006°45'00"	Ajali red earth sandstones	Coal & Iron
10.	Abia	Umu Nneochi	Umuchieze III, Lekwesi-Ishiagu.	N05°57'00" E007°28'00.0012"	Awgu Shales	Clay&Dolerite veins (quarry and construction materials)
12.	Abia	Isiukwuato	Ikeagha1, Eluama, Okigwe, Nigeria, off Okigwe-Afikpo Rd.	N05°54'22.7988" E007°26'00.6"	Ajali sands and Shales of Maamu Fm	Clay&Dolerite veins (quarry and construction materials)
13.	Abia	Isiukwuato	Otampa, Alayi	N05°45'00.00" E007°30'00.00"	Maamu Shales	Clay

S/N	LOCATIONS	DENSITY SURFAECE LINEAMENTS (m)	DENSITY OF MAGNETIC LINEAMENTS	NATURE OF ALTERATION	MAGNETIC RTE-TMI VALUE(s) (nT)	GEOTHERMAL GRADIENT (°C/km)	HEAT FLOW (mW/m^2)	TOTAL COUNT (ppm)
1.	ENUGU	0.91335-1.0275 very dense lineament value	high	Iron and Clay/ Hydrothermal alterations	27.4 to 55 Low	39-45 High to very high	83.15 to 96.75 High to very high	>2265.864
2.	UDI	0.79918-0.91334 dense lineament	high	Iron and Clay/ Hydrothermal alterations	112.15 to >123.1 High	35.9-39.6 Moderate to high	73.9 to 86.2 High	<456.768
3.	UGBODO	0.4567-0.9133 Moderate to dense lineament	high	Iron and Clay/ Hydrothermal alterations	56 to 78.6 moderate	38.3-41.9 Moderate to high	83.1 to 87.7 High	>2477.538
4.	OBUBRA	0.2283-0.4567 Low to moderate	high	Iron and Clay/ Hydrothermal alterations	56 to 80 Moderate-high	27-33 Low to moderate	54.7 to 64.7 Low to moderate	450-1603.112
5.	OKPOSI	0.2283 to 0.5076 Low to moderate	low	Iron and Clay/ Hydrothermal alterations	72.45 to 100 Moderate to high	39.6- 46.5 high	86.7 to 103.7 High to very high	2100 to >2265.864
6.	OBUDU	0 to 0.3425 Very low to low	high	Iron and Clay/ Hydrothermal alterations	72.45 to 87.25 moderate to high	39.6-46.7 high	88.5 to 102.7 high	1391.333 - 2265.864
7.	OBAN	0 to 0.2283 Very low to low	moderate	hydroxyl alterations	-35.2 to 19.15 very low to low	- Low (from extrapolation)	- Low (from extrapolation)	1391.333 – 1947.517
8.	AWKA	0.3425 to 0.6850 Low to moderate	moderate	Iron and Clay/ Hydrothermal alterations	27 to 55 low to moderate	28.4 -35.2 moderate (from extrapolation)	54.7 to 74.7 Moderate (from extrapolation)	<456.768 (from extrapolation)
9.	UMUAHIA	0.4567 to 0.91334 Moderate to high	moderate	Hydroxyl alterations	58 to 110 moderate to high	10.3-18.7 Low (from extrapolation)	34.7 to 39.7 low(from extrapolation)	-------
10.	ABAKALIKI	0 to 0.343 very low to low	moderate	Iron and Clay/ Hydrothermal alterations	5 to 51 Low to moderate	28.4 to 33 moderate	54.7 to 65.7 Moderate	1391.333 - 2265.864
11.	APIAPUM	0.571 to 0.7991 Moderate to high	high	Hydroxyl alterations	56 to 86 moderate	28.2 to 34.2 moderate	54.7 to 66.7 moderate	1391.333 – 1842.517
12.	MAMFE	0 to 0.3425 Very low to low	high	Hydroxyl alterations	19-42 low	35.2 to 42.2 Moderate to high	70.7 to 87.7 Moderate to high	2265.864 – 2689.211
13.	OGOJA	0.5708-1.0275 Moderate to high	high	Iron and Clay/	9 to 46.3 low	39.6 to 46.2 high (from extrapolation)	77.7 to 93.5 high (from extrapolation)	

				Hydrothermal alterations				1391.333 - 2265.864
14.	IKOM	0 to 0.4567 low to moderate	high	Hydroxyl alterations	-35.2 to 56 Low to moderate	28.2 to 33.2 Moderate	57.7 to 63.7 Moderate	>900 -2200
15.	AWGU	0.5708 to 1.0275 Moderate to high	low	Mainly hydroxyl, but with iron and clay alterations	--35.2 to 19.15 very low to low	33.2 to 37 moderate	68.7 to 74.7 moderate	600 – 1062.843
16.	OKIGWE	0.2283 to 0.5706 Low to moderate	okigwe	Mainly hydroxyl, but with iron and clay alterations	100 to >128.4 high	18.2 to 22.2 low	32.7 to 40.7 Low	------
17.	OWERRI	0.2283 to 0.5706	moderate	hydroxyl, iron and mainly clay alterations	9 to 18.2 Very low to low	------	------	-------
18.	BIASE	0 to 0.2283 Very low to low	high	Hydroxyl alterations	--35.2 to 19.15 Very low to low	------	------	1070 – 1497.333
19.	AFIKPO	0.6850 to 1.0275 high to very high	moderate	Iron and Clay/ Hydrothermal alterations	114 to >128.4 high	28.2 to 32.2 moderate	57.7 to 64.7 Moderate	1070 – 1497.333
20.	NSUKKA	0.4567 to 0.9133 High to very high	moderate	Iron and Clay/ Hydrothermal alterations	20 to 51 Low to moderate	------	------	450 - 1400.00

14.	Abia	Bende	Uzuakoli, Okigwe-Bende Road.	N05°37'30" E007°31'59.9988"	Imo shales	Clay&Dolerite veins (quarry and construction materials)
15.	Abia	Ohafia	Ohafia, off Amauke-Mgbom Road.	N05°38'30.0012" E007°49'59.9988"	Nsukka shales and sands of Ajali	clay
16.	Ebonyi	Ohaozara	Okposi Town, Off Umuka Oshiri Rd.	N06°01'59.9988" E007°50'60"	Asu River Group shales	Salt & Pb/Zn
17.	Enugu	Udi	Akpakume/Nze, Akpakume.	N06°37'30" E007°16'00.0012"	Nsukka shales	Coal & Iron
18.	Cross River	Abi	Igbo Imabana	N05°56'12.0012" E008°04'00.0012"	Shales of Awgu	Salt & Pb/Zn
19.	Cross River	Bekwara	Abuochicie, Katsina-Ala, Calabar Rd.	N06°45'00" E008°57'29.9988"	Awgu Shales and biotite-garnet-schists of part of Obudu basements	Clay, brine, rutile & limestone
20.	Ebonyi	Ohaukwu	Ezza Ohu, Abakaliki, between Nagbo and Ezamgbo Effium Rd, Nagbo, Ishieke, Abakaliki.	N06°25'41.9988" E007°58'30"	Asu River Group shales	Pb/Zn
21	Benue	Oju	Ainu	N06°55.85'00" E008°15'00"	Shales of Awgu Fm	Limestone, precious stone, bauxite, coal, clay, zinc & salt

22.	**Benue**	**Okpokwu**	**Okpoga South between Ichama and Igumale.**	**N06°52'30" E007°49'59.9988"**	**Shales of Awgu Fm**	**Limestone, precious stone, bauxite, coal, clay, zinc & salt**
23.	**Anambra**	**Orumba North**	**Ndiukwuenu/Okpeze. Between Ajali-Ozu, Umualu Ugwuoba Rd and Akpugo**	**N06°10'00.0012" E007°10'59.9988"**	**Imo shales**	**Clay/Laterite**
24.	**Anambra**	**Orumba South**	**Ihite, Umunze. Besides Federal College of Education. Around Uga, Ekwulobia and Enugu Umunze Roads**	**N05°56'30.0012" E007°13'59.9988"**	**Ameki Shales**	**Clay**
25.	**Ebonyi**	**Ishielu**	**Umuhuali**	**N06°30'00.0012" E007°45'00"**	**Amaseri sands and shales of Awgu**	**Pb/Zn/ brine**
26.	**Ebonyi**	**Abakaliki**	**Between South of Ezzagu and Northeast of Izekwe.**	**N06°18'20.9988" E008°10'59.9988"**	**Shales of Asu River Group**	**Pb/Zn**
27.	**Ebonyi**	**Ohaukwu**	**Nagbo**	**N06°27'59.8899" E008°01'00.00"**	**Amaseri sands and Shales of Asu River Group**	**Pb/Zn**
28.	**Benue**	**Oju**	**Okpokpo**	**N06°45'00.00" E008°22'00.0012"**	**Basaltic intrusives in Awgu shale host rocks**	**Limestone, precious stone, bauxite, coal, clay, zinc & salt**
29.	**Benue**	**Igede Oju**	**Aimeke, Oju-Alebo, off Ikache-Ejekwe Road.**	**N06°45'00.00" E008°28'00.0012"**	**Basaltic intrusives in Awgu shale host rocks**	**Limestone, precious stone, bauxite, coal, clay, zinc & salt**
30.	**Cross River**	**Ikom**	**Nnam (wards: Alok, Emaghabe, Abilti, Mande/Nkleta, Akorofono, Nyarenkpo, Ogomogom)**	**N06°19'20.4" E008°38'43.0".**	**Outcrops of medium grained granites within sediments of Odukpani**	**Barites,Salt,Pb/Zn Also a region of high geothermal gradient**
31.	**Enugu**	**Nkanu East**	**Isi Ndiagu,Amagunze, Enugu-Ebonyi**	**N06°19'00.59.9988" E007°45'00"**	**Ezeaku shales**	**Illites/shales/oil shales**
32.	**Cross River**	**Ikom**	**Nta/Nselle**	**N06°10'59.9988" E008°28'00.0012"**	**Shales of Ezeaku and Nkporo**	**Barites/brine**
33.	**Cross River**	**Biase**	**Akpet/Abini**	**N05°35'60" E008°05'60"**	**Granite gneiss in host rocks of New Netim marl**	**Granites for quarry, uraninites, dolomitic limestone**
34.	**Cross River**	**Akamkpa**	**Ikpai**	**N05°37'59.9988" E008°38'30.0012"**	**Granite gneiss in host rocks of New Netim marl**	**Granites for quarry, dolomitic limestone**

35.	Cross River	Akamkpa	Iko Esai	N05°46'00.0012" E008°25'30"	Granite gneiss in host rocks of New Netim marl	Granites for quarry, dolomitic limestone
36.	Cross River	Iyala	Gabu	N06°52'30" E008°43'59.9988"	Ezeku and Awgu shales	Pb/Zn & Barites
37.	Enugu	Nsukka	Obimo	N06°49'00.0012" E007°19'00.0012"	Oolithic Iron stones	Iron
38.	Enugu	Nkanu East	Amagunze (Wards Ishielu, Ohuani, Enuvu egu, Umuokpara)	N06°19'51.5" E007°40'48.9"	Vesicular weathered outcrops of basalts/limestones within Ezeaku and Awgu shales and sandstones of Amaseri	Iron stones, Clay, rock salts, limestone/dolomite Also a region of high geothermal gradient
39.	Ebonyi		Ugbuloke, Nkaliki-Abakaliki	N06°18'05.0976" E008°05'38.292"	Baked shales of ASU River group	Pb/Zn
40.	Ebonyi	Ezza North	Ameka	N06°10'40.70" E007°57'33.4296"	Baked shales of ASU River group	Pb/Zn
41.	Ebonyi	Ishielu	Nkalagu	N06°28'38.5932" E007°46'32.2644"	Baked shales of ASU River group	Limestone
42.	Ebonyi	Ivo	Ishiagu	N05°56'32.7876" E007°32'08.0016"	Clays and Shales of Ezeaku group	Dolerite/Diorite
43.	Enugu	Igbo-Etiti	Ejuoma-Lejja	N06°48'11.9484" E007°23'25.0584"	Ajali sandstone	Ironstone
44.	Enugu	Nsukka	Obinagu	N06°17'15" E007°23'38.0004"	Ajali sandstone	IronStone
44.	Enugu	Enugu South	Ugwuaji	N06°25'00.0012" E007°32'60"	Nkporo shale group	Clay, Iron Stone
45.	Enugu	Enugu South	14 Omechi Rd, Gariki, Uwani	N06°24'00.00" E007°30'00"	Nkporo and Awgu shales	Clay, Iron Stone

-NB-

The points highlighted in red are areas whose primary data were obtained in the field (information is presented in table 4.4 below) while those in blue are secondary data.

Table 4.7: Details of the primary data acquired in the field

S/N	Date of Acquisition	Coordinates	Elevation (m)	Name(s) of Location	Type of Activity	Profile direction (°)
Ikom, Calabar-Area of high geothermal gradient						
01.	17/12/2020	N06°19’20.4” E008°38’43.0”	114	Nnam Alok Comp.Sec.Sch.	VES-TR.1	125
02.	17/12/2020	N06°19’17.7” E008°38’44.4”	118	Akorfornor-Ogomogo	VES-TR.2	035
Amagunze, Enugu-Area of high geothermal gradient						
03.	18/12/2020	N06°19’51.5” E007°40’48.9”	71	Ishielu-Ohuani	VES-TR.1	030
04.	18/12/2020	N06°19’50.9” E007°40’44.4”	71	Enuvuegu-Umuokpara	VES-TR.2	020
Nsude, Enugu-Area of iron stone mineralization						
05.	19/12/2020	N06°24’26.4” E007°24’14.8”	441	Nsude	SP-TR.1	110
06.	19/12/2020	N06°24’16.6” E007°24’20.6”	454	Nsude	SP-TR.2	020
Amaiyi Umuobom, Imo-Area of pyrite mineralization						
07.	20/12/2020	N05°52’03.0” E007°10’16.0”	63	Amaiyi, Umuobom	SP-TR.1	100
08.	20/12/2020	N05°52’03.0” E007°10’13.7”	63	Amaiyi, Umuobom	SP-TR.2	10

ensured very short cable, was used because it was easier to move the cable without having it damaged. Areas of mineralization are depicted by very negative amplitude peaks from total field array curves and at amplitude crossover points at origins from gradient array curves (Olorunfemi. 2014). Profiles from gradient configuration along traverse 2 and total field array along traverse 1 of Umuobom were developed (Figs. 4.77 b&a respectively) from SP profiling done along these

traverses. The SP results obtained were tabularized in Table 4.8a. Laminated shales and pyrite samples (plates 4.78) were picked from the shallow pit hand dug in the process of local excavation.

B. SP and Image Results from Nsude

The same SP configuration was used in acquiring data at Nsude around areas of iron stone mineralization at N06°24'26.4" E007°24'14.8" and N06°24'16.6" E007°24'20.6". The Total Field or fixed Base array was used along both traverses. The profiles (Figs. 4.79a&b) developed along the traverses were obtained from the SP data in Table 4.8b. The iron stones in plates 4.80 a&b are hosted within the red earth Ajali sands as seen in plate 4.80c

C. VES Results from Nnam Alok, Ikom

The Schlumberger array was used for 2D imaging from two 1000 meters perpendicular traverses in these regions at Nnam Alok and Amagunze. The apparent resistivity values were plotted against half current electrode spacing (Table 4.9) on log-log graph. The depths, thicknesses and apparent resistivity layers calculated from repeated iterations of the curve models (Fig.4.81a&b) in Res2DINVsoftware, were used as model parameters for 2D inverse modelling in the production of geoelectric sections (Fig.4.81a&b). The pseudo and resistivity cross-sections developed along the two perpendicular traverses are displayed in Fig. 4.82 a&b. Nshor Efor Spring (plate 4.83) at Ikom's environment of high geothermal gradient was visited to check surface manifestations of anomalous geothermal gradients within the environment.

(a)

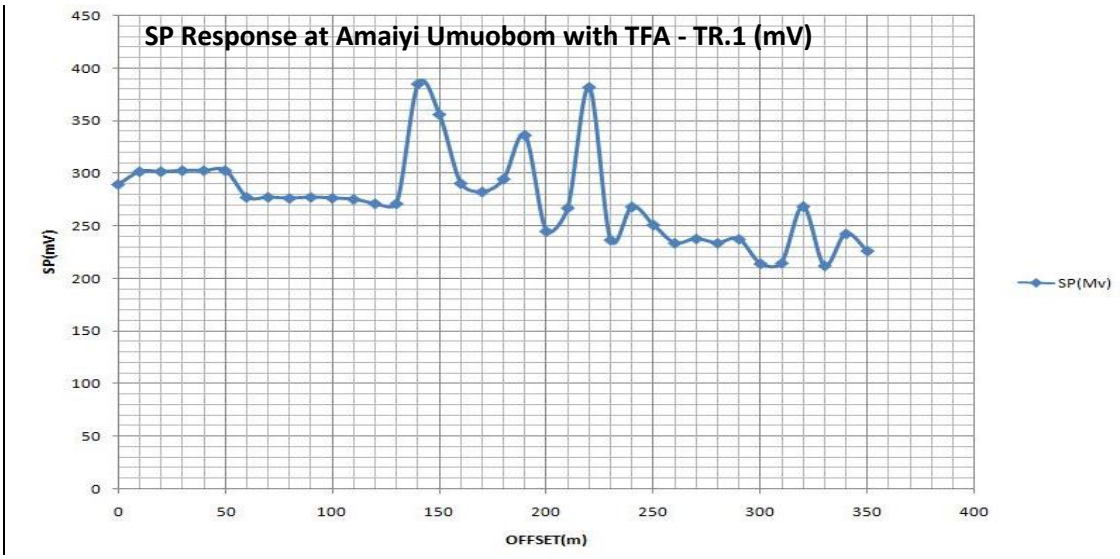

(b)

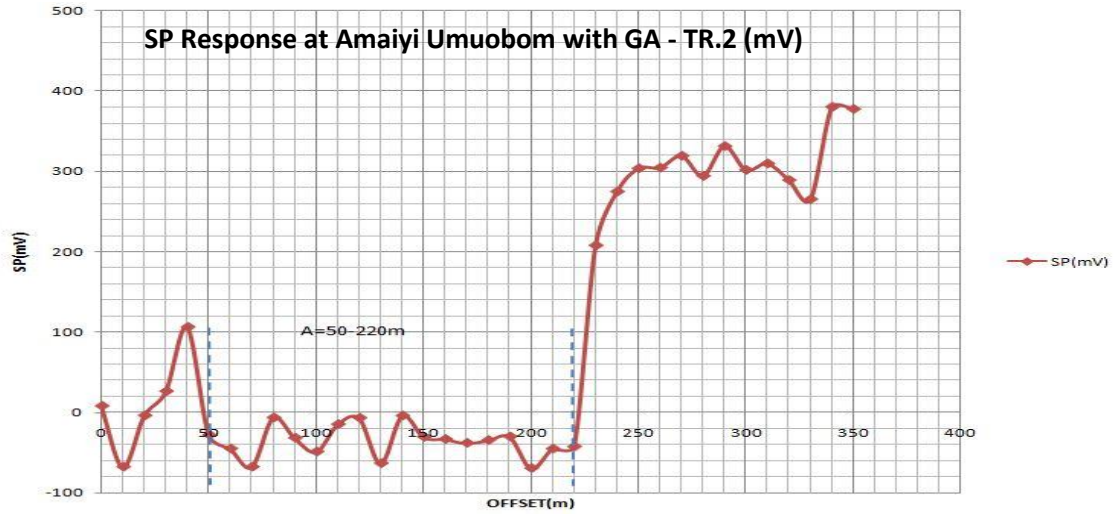

Figure 4.77(a&b): 1D profile plots from SP results along traverses 1&2 at Umuobom

Table 4.8a: Results from Spontaneous Potential (SP) Survey at Umuobom

SP-TRAVERSE 1 AT AMAIYI-UMUOBOM		SP-TRAVERSE 2 AT AMAIYI-UMUOBOM
N05°52’03.0” E007°10’16.0”		N06°52’03.0” E007°10’13.7”
Offset (m)	SP (mV)	SP (mV)
0	289.7	7.87
10	301.9	-67.95
20	301.9	-31.94
30	302.9	26.67
40	302.9	106.4
50	302.9	-28.29
60	277.5	-45.23
70	277.5	-67.95
80	276.5	-6.612
90	277.5	-31.84
100	276.6	-49.08
110	275.5	-14.90
120	271.4	-6.896
130	271.4	-63.48
140	385.3	-4.137
150	356.3	-30.62
160	290.7	-33.4
170	282.6	-38.2
180	294.8	-34.7
190	336.5	-30.2
200	245.0	-69.7
210	267.3	-45.37
220	382.2	-42.71
230	236.8	208

240	268.4	275.2
250	251.1	304.12
260	233.8	304.97
270	237.9	319.71
280	233.8	294.7
290	237.6	331.82
300	214.2	302.18
310	214.8	310.12
320	268.7	289.48
330	212.2	265.65
340	242.6	380.71
350	226.4	378.12

a.  **b.**  **c.** 

d.  e. 

Plates 4.78 (a&d). pyrite samples (b). local pitting for pyrites (c&e). laminated shale samples from shale host rocks

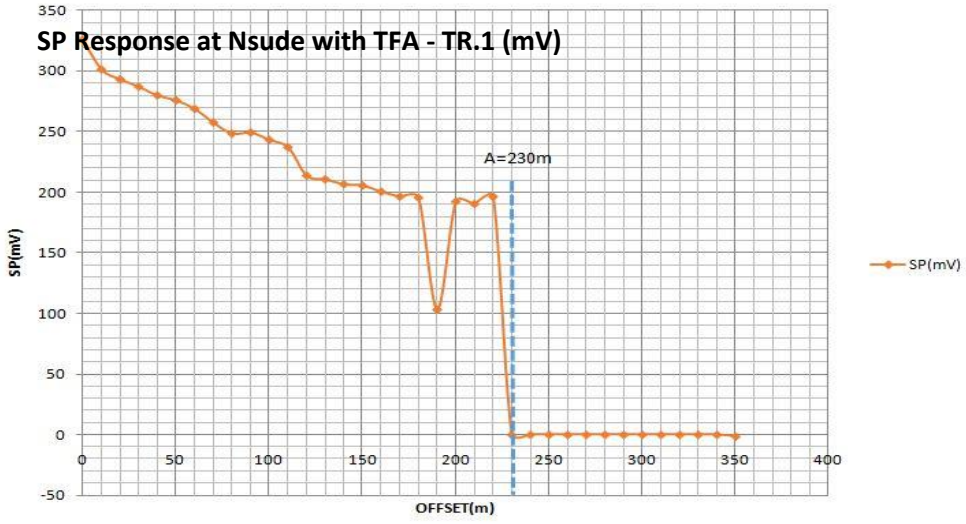

(a)

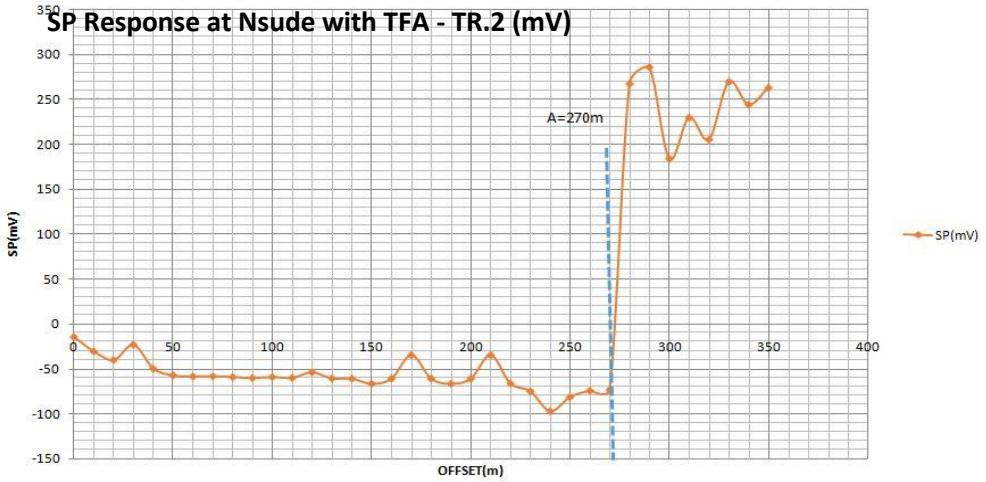

(b)

Figure 4.79(a&b): 1D profile plots from SP results along traverses 1&2 at Nsude respectively

Table 4.8b: Results from Spontaneous Potential (SP) Survey at Nsude

OFFSET(m)	SP-TRAVERSE 1 AT NSUDE N06°24'26.4" E007°24'14.8"	SP-TRAVERSE 2 AT NSUDE N06°24'16.6" E007°24'20.6"
0	325.3	-14.3
10	300.9	-30.29
20	292.8	-39.95
30	286.7	-22.92
40	279.5	-49.49
50	275.5	-56.99

60	268.4	-58.21
70	257.2	-58.01
80	248	-58.82
90	249	-59.83
100	242.9	-58.82
110	236.8	-59.63
120	213.5	-53.54
130	210.4	-60.44
140	206.3	-60.64
150	205.3	-66.32
160	200.2	-60.64
170	196.2	-34.38
180	195.2	-60.64
190	103.1	-66.32
200	192.1	-60.64
210	190.1	-34.38
220	196.2	-65.92
230	-0.001159	-74.64
240	-0.001413	-96.78
250	-0.001423	-81.13
260	0.001586	-74.03
270	-0.00342	-73.02
280	-0.001352	267.3
290	-0.001392	285.6
300	0.001423	184
310	-0.001382	229.7
320	-0.00504	205.3
330	-0.00127	269.4
340	-0.00514	244

350	-1.421	262.8

(a).  **(b).** 

(c). 

Plates 4.80 (a&b): Iron Stone samples at Nsude & (c): Thick red earth sand outcrops

Table 4.9: VES Results

pi	ab/2	ab/2sq	mn/2	mn/2sq	mn	ab-mn	ab-mn/mn	K/G $G = \frac{\pi(l^2-b^2)}{2b}$	R_1 (Alok) $R = \frac{\Delta V}{I}$ TR.1	ρa_1 (Alok) (Ωm) TR.1 $\rho_a = GR = \frac{\pi(l^2-b^2)}{2b}\frac{\Delta V}{I}$	R_2 (Alok) TR.2	ρa_2 (Alok) TR.2	R_2 (Amagunze) TR.1	ρa_1 (Amagunze) TR.1	R_2 (Amagunze) TR.2	ρa_2 (Amagunze) TR.2
3.142	2	4	0.5	0.25	1	3.75	3.75	11.7825	60.64	714.4908	34.88	410.9736	9.31	109.695075	26.02	306.58065
3.142	3	9	0.5	0.25	1	8.75	8.75	27.4925	23.32	641.1251	15.51	426.4087	2.332	64.11251	5.425	149.1468125
3.142	6	36	0.5	0.25	1	35.75	35.75	112.3265	7.616	855.4786	6.41	720.0129	0.4026	45.2226489	0.4614	51.8274471
3.142	9	81	0.5	0.25	1	80.75	80.75	253.7165	3.306	838.7867	3.803	964.8838	0.1389	35.24122185	0.1196	30.3444934
3.142	9	81	2	4	4	77	19.25	60.4835	12.98	785.0758	11.66	705.2376	-6.547	-395.9854745	24.8	1499.9908
3.142	15	225	2	4	4	221	55.25	173.5955	4.046	702.3674	4.716	818.6764	0.1311	22.75837005	-0.1474	-25.5879767
3.142	25	625	2	4	4	621	155.25	487.7955	0.851	415.114	1.075	524.3802	0.0249	12.14610795	0.0144	7.0242552

180

3.142	40	1600	2	4	4	1596	399	1253.658	0.135	169.2438	0.1713	214.7516	0.00914	11.45843412	0.01855	23.2553559
3.142	50	2500	2	4	4	2496	624	1960.608	0.0808	158.4171	-0.3255	-638.178	0.02541	49.81904928	0.4279	838.9441632
3.142	75	5625	2	4	4	5621	1405.25	4415.296	0.01064	46.97874	0.04279	188.9305	0.03324	146.7644224	12.91	57001.46491
3.142	75	5625	10	100	20	5525	276.25	867.9775	-0.06916	-60.0293	-0.09154	-79.4547	3.954	3431.983035	24.5	21265.44875
3.142	100	10000	10	100	20	9900	495	1555.29	0.1697	263.9327	-0.06906	-107.408	0.03527	54.8550783	14.23	22131.7767
3.142	150	22500	10	100	20	22400	1120	3519.04	0.1609	566.2135	-0.00644	-22.6626	0.02734	96.2105536	17.89	62955.6256
3.142	200	40000	10	100	20	39900	1995	6268.29	0.01118	70.07948	0.1085	680.1095	0.02734	171.3750486	20.43	128061.1647
3.142	300	90000	10	100	20	89900	4495	14123.29	0.1464	2067.65	0.1267	1789.421	0.03131	442.2002099	14.94	211001.9526
3.142	300	90000	20	400	40	89600	2240	7038.08	0.1632	1148.615	0.16812	1183.242	-0.02596	-182.7085568	15.55	109442.144
3.142	400	160000	20	400	40	159600	3990	12536.58	0.05679	711.9524	0.2028	2542.418	0.009371	117.4802912	9.211	115474.4384
3.142	500	250000	20	400	40	249600	6240	19606.08	0.1632	3199.712	0.2463	4828.978	0.01069	209.5889952	10.85	212725.968

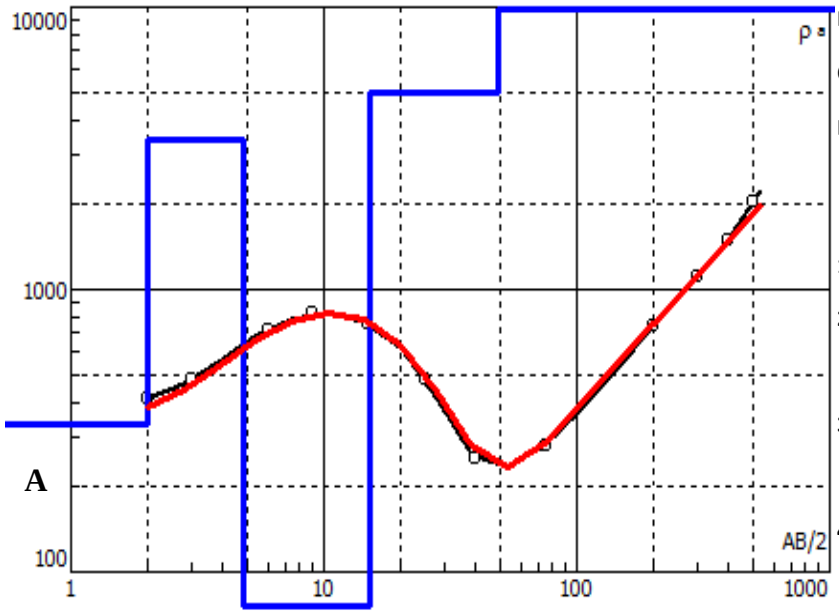

Nnam Alok: Traverse 1-Nnam Alok Comp. Sec. School

Curve type: KH Type-$\rho_1 < \rho_2 > \rho_3 < \rho_4 < \rho_5$

Layers	Lithology	ρ_a(Ωm)	Thickness(m)	Depth (m)
1.	Laterized sand	334	2.01	2.01
2.	Lateritic shale	3391	2.84	4.85
3.	Fractured clay	41.1	10.3	15.1
4.	Fractured basement	4977	33.6	48.7
5.	basement	63540	?	?

N	ρ	h	d	Alt
1	334	2.01	2.01	-2.009
2	3391	2.84	4.85	-4.847
3	41.1	10.3	15.1	-15.12
4	4977	33.6	48.7	-48.71
5	63540			

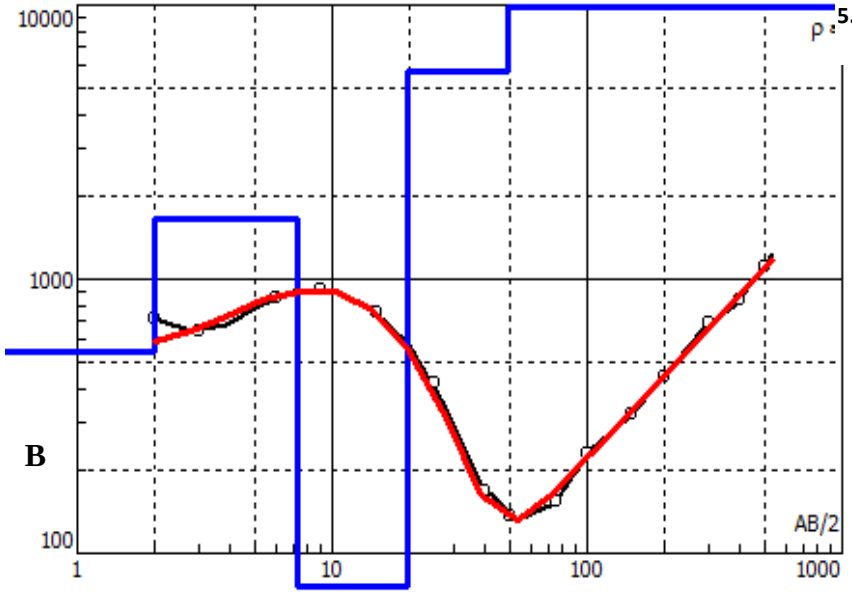

Nnam Alok: Traverse 2-Akorfornor-Ogomogo

Curve type: KH Type-$\rho_1 < \rho_2 > \rho_3 < \rho_4 < \rho_5$

Layers	Lithology	ρ_a(Ωm)	thickness	depth
1.	Weathered basement	547	2.01	2.01
2.	Lateritic shale	1659	5.36	7.36
3.	Fractured clay	27.9	12.2	19.6
4.	Fractured basement	5734	29.1	48.7
5.	basement	64316		

N	ρ	h	d	Alt
1	547	2.01	2.01	-2.007
2	1659	5.36	7.36	-7.362
3	27.9	12.2	19.6	-19.59
4	5734	29.1	48.7	-48.71
5	64316			

Figure 4.81 (a&b): The Resistivity Curves and Numbers of Layer apparent resistivity, thickness, depth and lithology from Nam Alok VES Data

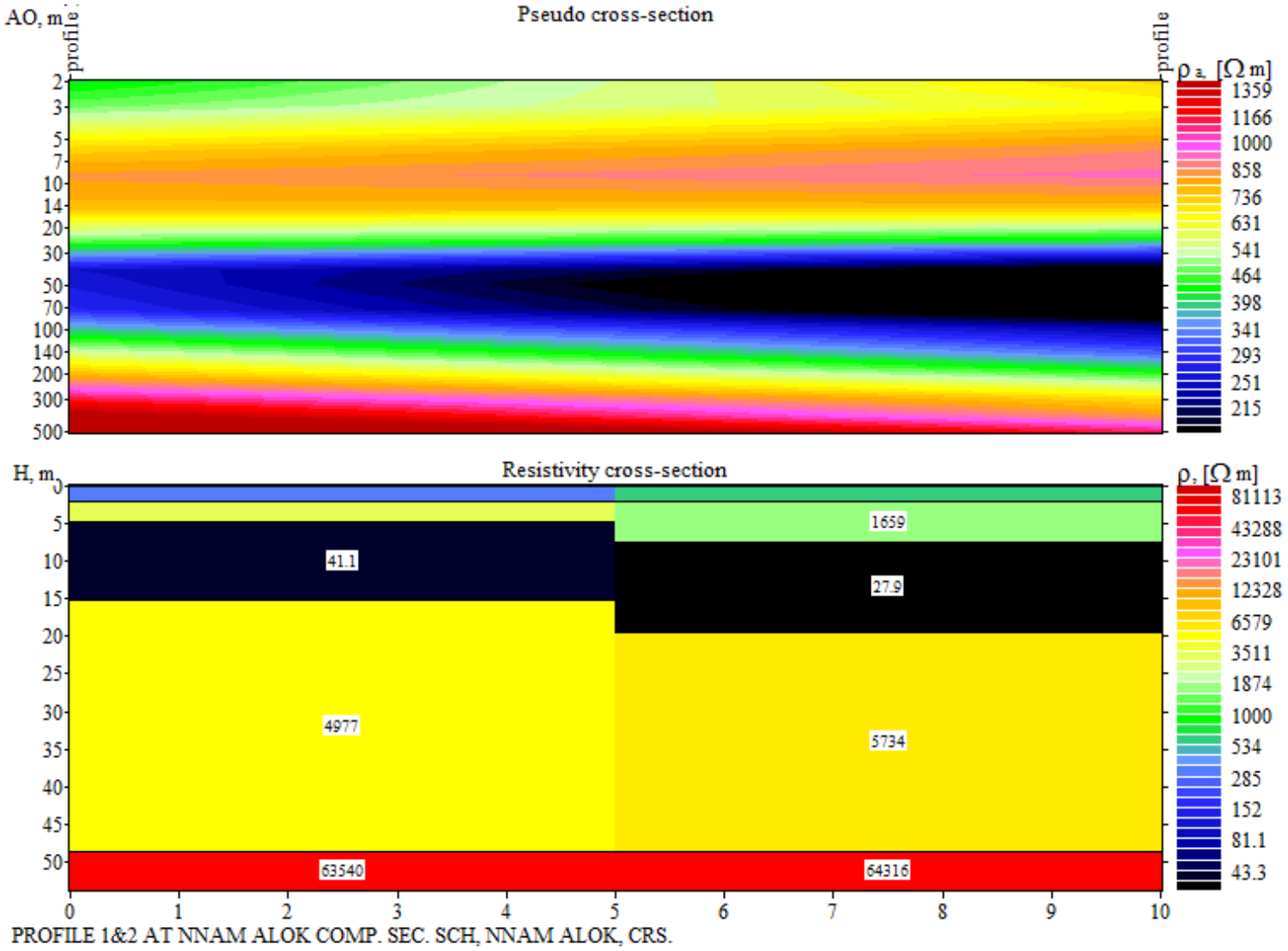

Figure 4.82 (a&b): Pseudo and Resistivity Cross-Sections Along the two traverses taken at Alok

Plate 4.83: Nshor Efor Spring at Alok

NB: Stream flow direction in red; indication of fracture/fissure by blue lines

D. VES Results from Amagunze.

The true resistance and geometric factor obtained in eqn 3.27 were used to calculate for apparent resistivity values (Table 4.9). The apparent resistivity values, plotted against half current electrode spacing were also used to generate depths, thicknesses and apparent resistivity layers from repeated iterations of the resistivity curves (Fig.4.84) in Res2DINVsoftware, and they were used as model parameters for 2D inverse modelling in the production of a 6-layer geoelectric section (Fig.4.85a). The bank of Isi Ube Spring (Plates 4.86) at Amagunze's environment of high geothermal gradient was visited to check surface manifestations of anomalous geothermal gradients within the environment.

4.1.6 Results from Field Images and Secondary Data

The image results show evidences of mineralized zones visited within the study area. These captured zones are presented in blue in tables 4.6. They encompass Obinagu in Enugu which show deposits of Iron stone, Nkalagu and Ishiagu in Ebonyi State which have mineralizations of limestone and dolerites respectively and Nkaliki and Ameka which show mineralizations of Lead/Zinc (Plates 4.87 to 4.92). Egudinego, Ebonyi State also, from double dipole results, corroborate findings of being a viable zone for mineralization as well. Figs.4.93 a&b show two subsurface layers in purple to reddish brown and yellow on the eastern flank, localized occurrences are depicted by red colourations. (Fig. 4.93b).

4.2. DISCUSSION

4.2.1. Discussion of Remote Sensing Results

A. Discussion of True Colour Composite Result

The Surface Reflectance Data/True Colour Composite of the study area gives reflection of earth's surface material (aggregate of top 15cm of the earth). Blue is positioned between 0.450-0.515 μm, Green between 0.525-0.600 μm and Red between 0.630-0.680 μm regions of the electromagnetic spectra. The RGB 432 illustrates the original colour appearance of the area.

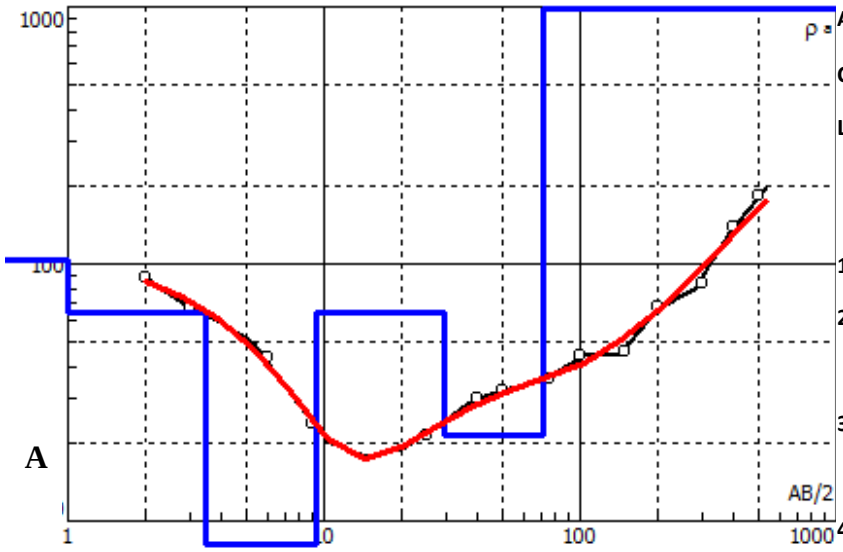

Amagunze: Traverse 1: Ishielu-Ohuani

Curve type: HA Type-$\rho_1 > \rho_2 > \rho_3 < \rho_4 > \rho_5 < \rho_6$

Layers	Lithology	ρ_a (Ωm)	Thickness(m)	Depth (m)
1.	Clayey sand	104	1	1
2.	Clay	64.8	2.44	3.44
3.	clay	8.08	5.89	9.33
4.	clay	64.2	20.3	29.7

N	ρ	h	d	Alt
1	104	1	1	-1
2	64.8	2.44	3.44	-3.443
3	8.08	5.89	9.33	-9.328
4	64.2	20.3	29.7	-29.67
5	21.5	42.2	71.8	-71.82
6	35499			

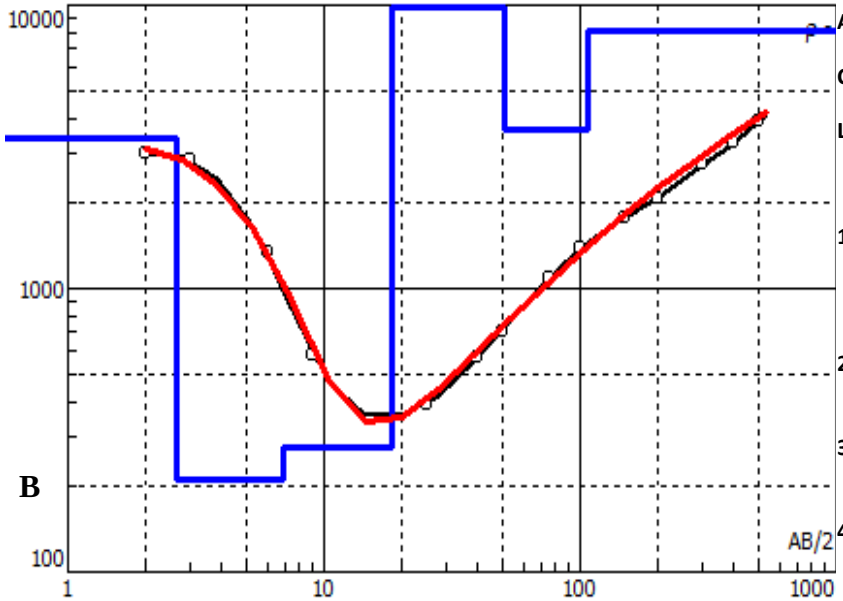

Amagunze: Traverse 2: EnuvuEgu-Umuokpara

Curve type: HA Type-$\rho_1 > \rho_2 > \rho_3 < \rho_4 > \rho_5 < \rho_6$

Layers	Lithology	ρ_a(Ωm)	Thickness (m)	Depth (m)
1.	Ferruginized vesicular massifs	3364	2.64	2.64
2.	Clayey Sand	213	4.34	6.98
3.	Dry lateritic sands	273	11.5	18.4
4.	basement	10344	32.2	50.6

N	ρ	h	d	Alt
1	3364	2.64	2.64	-2.643
2	213	4.34	6.98	-6.98
3	273	11.5	18.4	-18.44
4	10344	32.2	50.6	-50.65
5	3658	56.6	107	-107.2
6	8112			

Figure 4.84 (a&b): The Resistivity Curves and Numbers of Layer apparent resistivity, thickness, depth and lithology from Amagunze VES

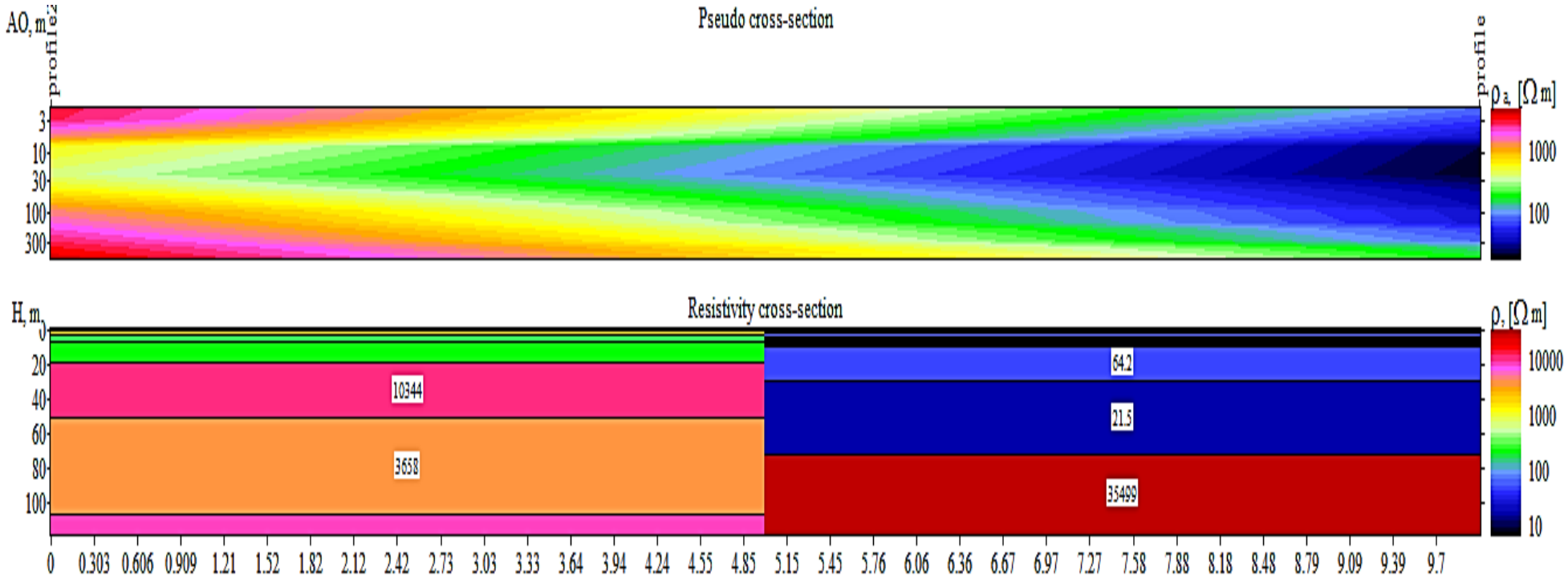

Figure 4.85(a&b): Pseudo and Resistivity Cross-Sections Along the two traverses taken at Amagunze

Plates 4.86a-b: Murky water of River Isi ube & fig.4.86c-d: Outcrops of cemented ferruginized vesicular Limestone and conglomerates (Awgu Massifs) around the river bank.

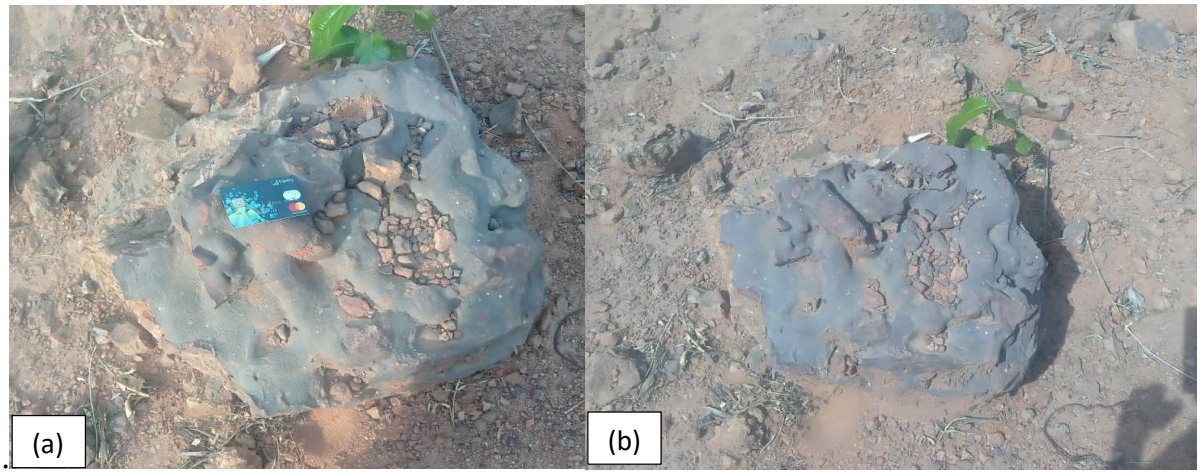

Plate(s). 4.87(a&b): Iron stone deposits at Obinagu

Plate(s). 4.88(a&b): Iron stone deposits at Ejuoma, Lejja, Nsukka

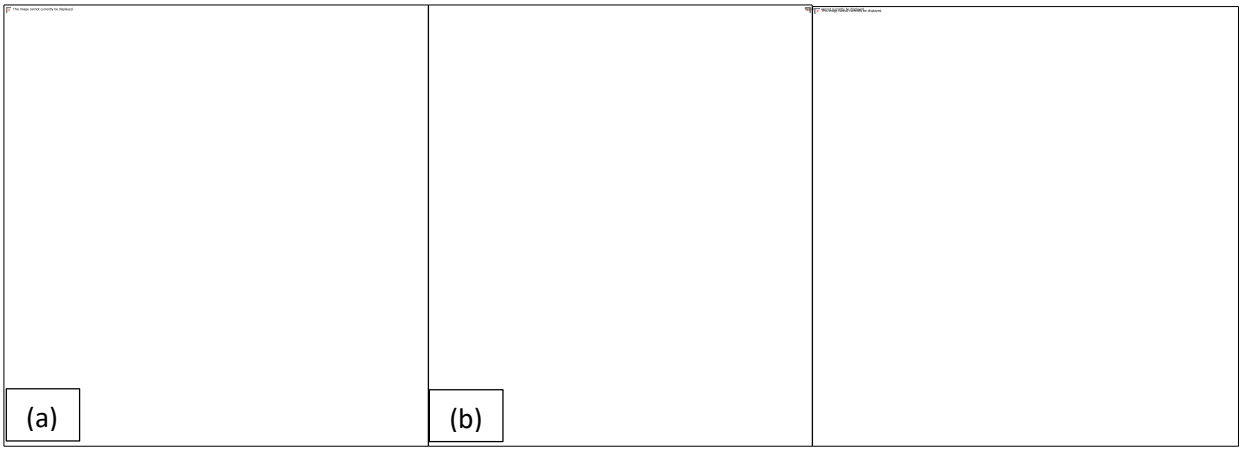

Plate(s).4.89a&b:Nkaliki-Abakaliki Pb-Zn Mine

Fig.4.90:Ameka nine Pb-Zn Mine

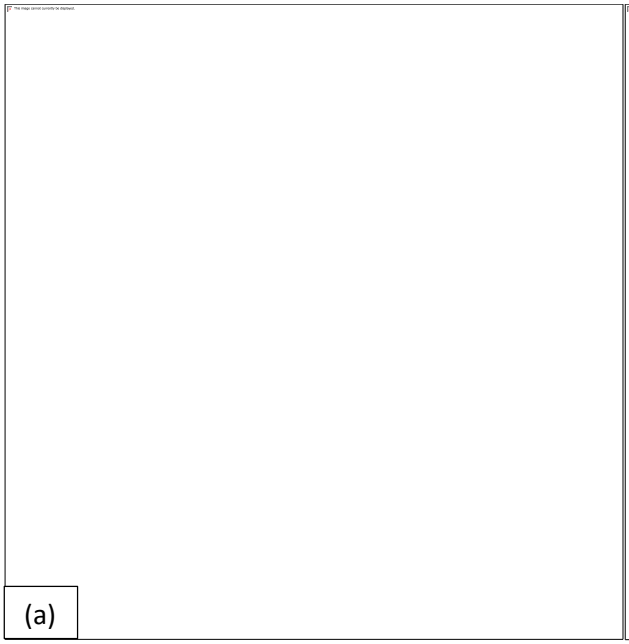

(a)

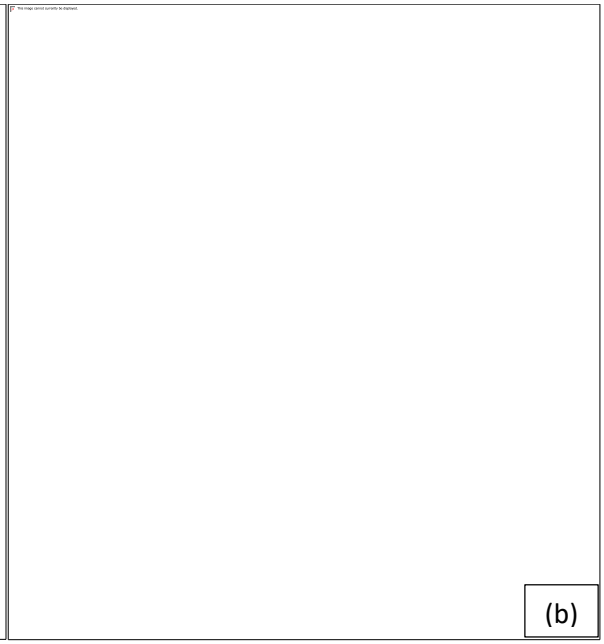

(b)

Plate 4.91: Nkalagu limestone Quarry

Plate 4.92:Ameka-Ezza north Pb-Zn Mine

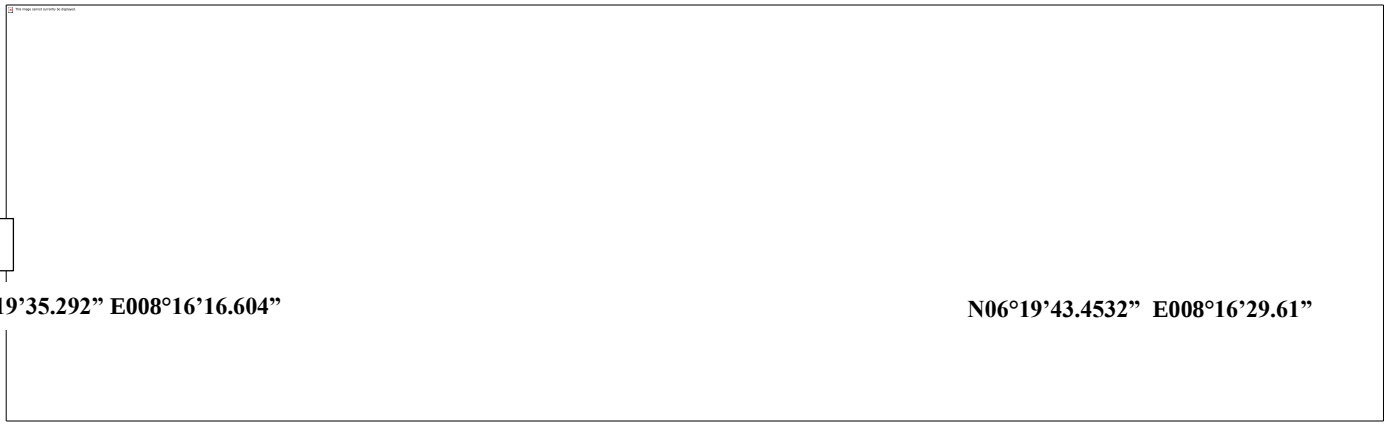

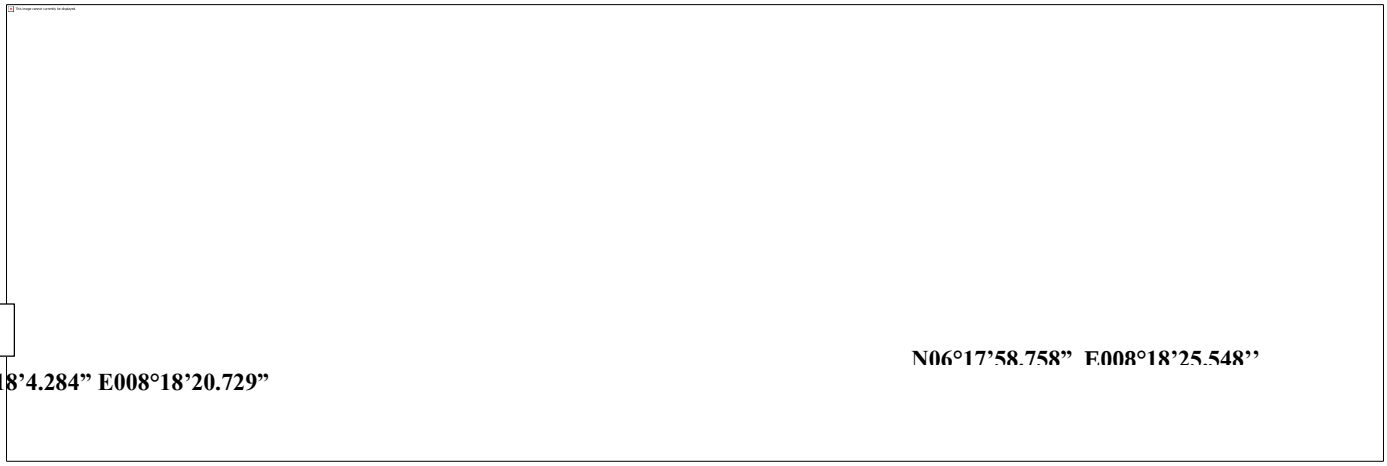

Figs.4.93a&b: 2D 250 m dipole-dipole section across Egudenego environs, Abakaliki (Modified from Okiyi, 2015.

B. Discussion of Band Combination Results

1. Composite 576 Map

The composite 576 is used to detect the presence of alteration minerals or rocks affected by hydrothermal alteration processes (Mia & Fujimitsu, 2012). These alterations are ferrous and occur on sediments of Nsukka formation within Anambra basin. Dark red colouration depicts undifferenciated igneous rocks of the late Paleozoic to Albian basement complex and black lines depict state boundaries while the dark blue lines represent Cross River. The Albian Asu River Group sediments of Abakaliki and the Turonian-Coniacian shales of the Afikpo syncline show responses in light violet colouration. Vegetated areas appear in bright red color and textural features of both igneous and sedimentary rocks are more robust in this scene than in figure 4.1 at a regional scale.The cyan/light green colour occurring within Ajali formation depicts the ferruginized sandstones, at the extreme Northeast of the study area, it depicts basalt intrusive contacts with Ezeaku formation and doleritic/basaltic intrusives within sediments of the ASU River group (ARG).

2. Composite 567 Map

In bands 567, the vegetated areas appear in orange brown, drainage in bright blue and state boundaries in red. The Albian ARG sediments of Abakaliki and the Turonian-Coniacian shales of the Afikpo syncline show responses in light blue colouration instead (Figure 4.2b). RGB 576 and 567 are very similar to the false colour composites of 543. RGB 543 has same similarity with 576, both show same images as false colour composite maps because both show same colour alterations and discriminations but the alterations are more accentuated in 576.

3. Composite 543 Map

From composite 543, active vegetation appears red, which is observed in Southwest of the study area where parts of the Anambra Basin and Niger Delta formations fall into, Southern part of the study area and Southwest of the study area around the Mamfe Basin. In bands 543 (Fig.4.3), bare soil appears as cyan or light green patches

located in the extreme top NW and NE of the map, and towards the mid part of the study area where the Abakaliki trough occurs and this also corroborates the ridges or elevated formations of the surrounding Awgu Shales, Nkporo Shales, Mamu Formation, Ajali Sandstone and Nsukka Formation on the DEM image (Fig.1.8b) and on the geological map (Fig.1.7). The crystalline units adjacent to the Mamfe basin is represented by thick red colors. The drainage pattern of the study area is portrayed in blue pattern, which corresponds to main river source, Cross River. The drainage system reveals the presence of streams which occur as thick blue lines from the main stream source and light blue. The drainage is dendritic, suggesting the presence of underlying homogenous sediments/litho-units such as clay, mudstone, shale and limestone that have undergone folding and are least resistant to erosion of rivers and streams (Nelson, 2015). The dendritic lines occur simultaneously with the red vegetation shades delineating the importance of moisture to vegetation formation. (Fig.1.2).

4. Composite 753 Map

The resulting scene from image composite 753 shows vegetation in light green to dark green, bare soils in brownish with taints of purple colourations which are the exposed surfaces of the sedimentary units described with bands 576. The adjacent crystalline units to the Mamfe Basin are dark green and the main source of drainage from Cross River is also depicted by a blue line and other smaller dendritic river channels as light blue.

5. Composite 754 Map

RGB 754 color combination image shows active vegetation in light green to dark green as well, as seen with RGB 753 while bare soils appear brownish with taints of purple colourations. Basically, the sedimentary units have a deep violet colouration especially depicting Nsukka and Imo shales and the late Maastritchian sediments.The elevated adjacent crystalline units to the Mamfe embayment and ferruginized sandstone caps of Ajali are dark green in colour. The main source of drainage from Cross River is also depicted by a blue line and other smaller dendritic river channels as light blue. (also see Fig.1.2).

6. Composite 567 Map

From RGB 10 11 7, rocks with moderate emissivity value appear as pink as well in this image. Band 7 was chosen in this colour combination because it represents rock absorption features in SWIR region due to Al–OH, Fe, Mg–OH, Si–O–H and CO3 in their compositions (Pour & Hashim, 2014). Hence in the study area, blue areas contain low silicate minerals because of ferromagnessians in outcropping igneous and metamorphic rocks of Obudu escarpment and Oban massifs and high silica emissivity in shale dominated Abakaliki trough and ferruginized sandstones of the Upper Maastrichtian sediments.

C. Discussion of Band Rationing Results

1. 4/2 Ratio Map

From the map, high value of 1.56501 in red depicts ferrous rich zones. The ferruginized zones from the $\frac{4}{2}$ map encompasses sediments of the upper Maastrichian, Asu River Group and Ezeaku shales. This corroborates the fact that the ASU River group host the ores containing iron minerals in form of pyrites,

chalcopyrites, marcasites and siderites. (Agumanu, 1989; Umeji, 2000).

2. 5/6 and 5/4 Ratio Maps

5/4 and are seen in Southwestern part of the study area where the basements occur adjacent to the Mamfe Basins (Fig. 4.8).This high response most probably stems from sandstones, limestones and shales with calcareous sandstones of Odukpani Formation resting unconformably on and in association with the Basement rocks of the Calabar flank. (see ratio 5/4 displayed at appendix).

3. Band 6/7 and 7/5 Maps

Band 6 over band 5 discriminates ferrous minerals in bright red tone (Fig.4.11) just like ratio 7 over 5, in association with sedimentary host rocks. It has high reflectance within 1.57 to 1.65 μm and high absorption within 0.85 to 0.88 μm which is because often times, mineralized veins and lodes are in close association with shale host rocks. The areas with bright red highlight regions rich in sulphide minerals materials such as pyrites, chalcopyrites, marcasites, siderites e.t.c. in association with hydrothermal deposits (ferrous minerals).

D. Discussion of Ratio Composite Results

1. Kaufmann Band Ratio Results

Kaufmann band ratio composite (7/5; 5/4; 6/7) reveals a good combination for geological purposes. In this image, light cyan to bright blue colours represent basement outcrops as seen within the Calabar flank (Fig.4.12) and metasediments of the upper Maastrichian and proto-Niger Delta. Areas highlighted in light sea blue are also representative of dense vegetation especially around the Southeastern side of the study area. The areas in red can be related to hydrothermally altered rocks while blue lines represent river channels. Just like the ratio 4 on 2, the ratio composite highlights in red, ferruginized sediments of the upper Maastrichian and Asu River Group and Ezeaku shales of Afikpo syncline and all other ratio composites highlight same region of alteration. The correctness of figures 4.7 to 4.12 was ground-truthed and ascertained true.

2. Sabin's Ratio Composite Results

The image from 4/2, 6/5 and 6/7 composite was produced for lithological mapping and hydrothermal alteration zones. As already established, the ratio 4/2 was used for mapping iron oxides as hematite, limonite and jarosite, and has high reflectance in red region. The ratio 6/7 was used to map clay minerals as kaolinite, illite and montmorillonite and the ratio 6/5 shows high reflectance in presence of ferrous minerals. In figure 4.13, light yellow colour represents metasediments and blue areas represent vegetation. Light green areas highlight possible hydrothermal alterations in outcrop rocks just same as red zones from Kauffman ratio.

E. Discussion of Principal Component Analysis (PCA) Results

PCA iron plots conspicuously projects the ferruginization of the Ajali and Nsukka formations. The clay plots as well conspicuously typifies the shales of the Afikpo syncline and depicts the occurrence of magnetic minerals to be dominant in the sediments of the ASU River Group. Combination of both clay and iron plots are displayed at appendix.

F. Discussion of NDVI Results

NDVI imagery from Fig.4.17, the light green areas with low NDVI values between -0.11 to 0.25 correspond to bare rock and soils with little vegetative zones which is observed around Ogoja, Enugu, Abakaliki and Nsukka , milk to light brown areas 0.25 to 0.39 correspond to sparse or semi-dense vegetation while 0.39 to 0.71 correspond to thick vegetation in bright green, seen in regions around Enugu, adjacent flanks of the Mamfe Basin in the Southeast, Southern to Southwestern parts of the study area as seen around Okigwe, Umuahia, Owerri e.t.c.

G. Discussion of Landsat Surface Lineament Results

These surface and subsurface lineaments are manifestations of fractures and fissures, faults, intrusions, topographic features, straight valleys, continuous scarps, straight rock boundaries, stream channels and systematic offset of rivers, sudden tonal variations and alignment of vegetation (O'Leary, 1976). The minor trends are E-W and N-S and NW-SE, majority of the lineaments trend in the ENE-WSW direction where lots of echelon fractures indicative of younger and most recent geodynamic events lie. Remnants of pre-santonian stress fields likely dominate in WNW-ESE trends and are less pronounced alongside major ENE-WSW lineaments. The establishment of linear features in this area corroborates some findings of Cratchley & Jones (1965) who observed that Cretaceous rocks were highly deformed with intrusives concealing rift structure directions. Major deformational structures such as Abakaliki Anticlinorium and Afikpo Syncline as observed by Murat (1972), display NE-SW trending faults. This stands as a prove to the dominance of magnetic minerals within sediments of ASU River Group (Agumanu, 1989), deposits of Pb-Zn ores occur in large quantities as lodes or veins in Shales of ASU River group, caused by Santonian tectonism (Benkhelil, 1989). It also agrees with findings of Umeji (1988) that the Lower Cretaceous is characterized by NE-SW oriented shear zones and fractures controlled by volcanism. Linear features equal to or greater than 1km in length are considered to have greatest potential of being more fully developed and penetrating greater depths (Opara *et al*., 2012). The lineaments corroborate some findings by Umeji in 1988 that the lower Cretaceous is characterized by NE-SW oriented shear zones and fractures controlled by volcanism and that NNE-SSW and NNW-SSE trending shear zones and fractures characterize the PAN-African Shields as well. The enhanced filtered map (Fig.4.16c) reveals a high density fracture zone basically

around the environs of the Eastern States; Enugu, Anambra, Imo, Abia, Akwa Ibom, Ebonyi and Cross River. Lineaments with lengths >1 km were automatically extracted from figure 4.16b and reproduced in Figure 4.16c with dominant trends in the E-W, N-S, NE-SW, NNE-SSW and ENE-WSW directions. High density lineaments occur in environs of Okigwe, Afikpo, Okposi, Awgu, Awka, Udi, Nsukka and Ogoja. The dense lineamentsaround the Calabar flank are created by intense tectonic activity along the Cross River channel which empties into

Mamfe Basin. The interpreted structural lineaments were represented by aon rose diagrams (Fig. 4.16d).

4.2.2. Discussion of Results from Aeromagnetic Data

A. Discussion of RTE-TMI Results

High magnetic anomaly response is characteristic of magnetic minerals/ore bodies, intrusives and localized bodies

at shallow depths while low magnetic susceptibilities typify regions of low levels of magnetic minerals. Adopting a qualitative interpretation of the TMI, high magnetic intensities are seen basically in South-and Northwestern parts of the study area. It is not to be overlooked that the lithology of the basement controls the magnetic relief observed over the Southeastern sedimentary basin.

High and positive anomalies between 90 and >128 nT are seen in regions around Okigwe, Afikpo, Udi, Awgu, Obudu, Okposi, Obubra, Apiapum e.t.c. Udensi and Akanbi, 2006 described elliptical or circular contours on magnetic anomaly maps as indicative of intrusions, and these high magnetic elliptical contours which denote sub-surface intrusives relatively strike E-W and NE-SW (The NE-SW trend is seen in the elliptical contours around Umuahia and Okigwe). These anomalies are likely influenced by the lower coal measures of the Mamu Formation. High susceptibilities >128 nT are noticeable within Okigwe and Umuahia which are areas laden with subsurface basic and intermediate intrusions. Some of these intrusives are exposed in Okigwe environs. Negative anomalies ranging from < -20 nT are observed Northwest of Obudu, Southwest of Ikom, North of Oban, Okigwe, Awgu and Biase environs and northwards of Obubra. The undifferentiated basement complex of the Obudu Hill gave

positive magnetic responses >100nT. From the RTE, high magnetic anomalies would likely occur as a result of responses of buried intrusives as seen from the isolated high magnetic structures represented by elliptical contours around Okigwe environs. The basement are represented by low magnetic relief anomalies on the RTE-TMI map which are characterized by smooth contours, areas like Ikom, Mamfe, Oban, Biase, Ogoja of the Calabar flank and Awgu, Owerri, e.t.c of the Southeastern region are marked by low relief. Reynolds, Rosenbaum, Hudson & Fishman, 1990 & Opara 2011 have also attributed a series of closed lows to depict linear trends which initiate shear/fault zones. Fault zones as well typify basement environments around sedimentary units and these contrasting lithologic and tectonic units within the Study Area, offset the varying magnetic responses (lows and highs). Around Ikom, North of Ugbodo and Northwest of Ogoja, there seems to be responses from surficial localized bodies emanating from the basement because of adjacent low magnetic reliefs, these intrusions may have been from the basement which are embodiments of aggregate economic minerals.

B. Discussion of Spectral Analysis Results

The spectral depths show varying depth information as obtained from spectral analysis result, shallow magnetic sources are located Northwards at Ugbodo and Southeastwards at Apiapum towns. Deeper depths were also obtained at Northwestern and Southwestern regions of the study area. Depths >1.3km were obtained at Okposi, Afikpo, Okigwe, Enugu, Udi. (Fig. 4.21). Computation of Curie Point Depths (CPDs) using windows of 55 x 55 km dimension as represented in Table 4.2, was obtained from Z_t and Z_0 parameters being related by equation 2.55 (Spector & Grant, 1970) and these results were plotted on the coverage area dimensional map. From the power spectra of magnetic anomalies, depth to the magnetic source was calculated and the data were transformed to frequency domain to perform this calculation. From Table 4.2, depth to the top of the magnetic source ranges between 0.451-1.899 km with an average of 1.057 km. The Centroid depth ranges between 4.001 - 7.874 km with an average value of 5.61731 km and the CPD values range from 6.15-14.19 km with an average of 10.1769 km. The estimated CPD, geothermal gradients and heat flow, were done by applying centroid method for the blocks or windows in the study area. Figure 4.22 shows CPD variations in the study area and the shallowest parts are

less than 8km in the Central and Eastern parts of the study area. These areas are around Enugu, Okposi, Awgu and Obudu and Mamfe regions of the Calabar flank. On the other hand, the maximum values are located at Abakaliki, Apiapum, Okigwe axis and the bottom depths of these magnetic sources are estimated through the CPD, which gives insight to the thermal structure of the region. Average crustal temperature from lithospheric thermal condition seem to influence Curie temperature depths. The CPD shows that high geothermal areas and volcanic environments have shallow depths <10 km. The shallow CPDs obtained around Ugbodo, Awgu, Obudu regions can be attributed to basaltic intrusives and outcropping igneous rock basements in the region. Central to the Western parts of the Study Area and extreme Eastern parts have high geothermal environments. The anticlinuous Abakaliki has a higher CPD value >10 km, Apiapum and Okigwe all have high CPDs which typify anticlinal and elevated areas especially volcanic arcs, ridges and elevated volcanics/extrusives. The geothermal gradient results were obtained utilizing the Curie-point (θ) for magnetite (580 °C) with an average thermal conductivity of 1.80 Wm^{-1} k^{-1} (Onuoha & Ekine 1999) for the sedimentary shale formation and 2.5 Wm-1 k-1 (Manea & Manea 2011) for the region with older hard rocks in the Calabar flank.The geothermal gradient values range from 20.3°C/km to 50.0°C/km with an average of 34.33°C/km and heat flow ranges from 34.9 to 105 mW/m^2 with an average of 68.85mW/m^2. Figures 4.23 and 4.24 show the variation of geothermal gradient and heat flow values. The geothermal gradient and heat flow values increase with reduction in curie point depth. There is inverse relationship between geothermal gradient and curie point depth and between heat flow and curie point depth. A prove to this, is the work of Manea and Manea 2011 which shows that shallow CPDs are generally characteristic of volcanic arcs. CPD >10 km at Abakaliki–Apiapum environs delineate possible bottom of the volcanic rocks in the region, corroborating this, Obiora & Charan (2010) identified basaltic and doloritic sill structures including volcanic intrusives at the Abakaliki region.

Heat flow is a yardstick to the measurement and occurrence of geothermal reserves because heat flow >88 mWm^{-2} imply an anomalous geothermal situation in the subsurface (Sharma 2004). The Albian volcanic regions of the Calabar flank and the upper Southern Benue Trough have high heat flow and geothermal gradient

which correspond to volcanic and metamorphic regions since these two units have high heat conductivities. Geological conditions and lithology type influence high heat flows obtained in an area. The upper Benue Trough predates the mid-Santonian deformation and magmatism in the Benue Trough because of tectonically active regions with series of deformation in the Upper Southern Benue Trough, up to the Anambra Basin. Also, the silting up of 9-12 km thick sediments of the Anambra Basin (Nwajide, 2013) significantly increases heat flow (>72mW/m^2) and geothermal gradient (>35°C/km) around these areas, such is seen in the Western and extreme Eastern part of the Study area, going by the established fact that threshold for mean heat flow at Continental and Oceanic crust are 65 mW/m^2 and 101mW/m^2 respectively within the Study area. Areas with values exceeding 35°C/km indicate anomalous geothermal conditions and high heat flow >72 mW/m^2 are seen in the Study area. Two geothermal ring zones were delineated in the study area (see fig.4.23) which reveals N-S trending ring zones, North of Okposi town in Ebonyi State and E-W trending ring zones North of Mamfe and South of Obudu towns in Cross River State. For good geothermal reservoir in the area, thresholds of CPD < 10km, GG >42°C/km and heat flow >88mW/m^2 have been earmarked. The study area reveals anomalous heat flow environs which serve as geothermal reserves especially as seen in Enugu, Udi, Okposi, Ugbodo, Obudu, Mamfe e.t.c environs and thus have prompted ground-truthing of Amagunze and Ikom precisely.

Depths to the top (DTT/Zt) of magnetic sources were computed from spectral analysis of magnetic data on a 110 x 110 km window. The depth ranges from 0.395-0.658 km with an average of 0.525km depicting same information of varying depths. This window size centralizes on the study area, locating shallow magnetic responses around Apiapum and Obubra environs. (Fig.4.27). Curie Point Depths (CPDs) of windows 110 x 110 km as computed in Table 4.3, was obtained from Z_t and Z_0 parameters being related by equation 2.55 (Spector & Grant, 1970) and these results (Fig.4.28) were plotted on the coverage area dimensional map. This window size ensured the analysis of the central blocks of the study area. The depth to the centroid from this window size, ranges from 5.208-8.975 km with an average depth of 7.316 km. CPD values range from 9.85-17.43 km with an average of 14.107 km. The estimated CPD, geothermal gradients, and heat flow maps, were gotten from centroid

method for this particular window size. North of Awgu has a minimal curie point depth 9km or less, because bottom depths of these magnetic sources are estimated through the CPD, an insight to the thermal structure of the region can be estimated mostly influenced by average crustal temperature from lithospheric thermal conditions. Utilizing the Curie-point (θ) for magnetite (580 ℃) with an average thermal conductivity of 2.5 $Wm^{-1}k^{-1}$ for rocks, the geothermal gradient results for the 110 x 110 km window size was obtained.The values range from 33.276°C/km to 58.883°C/km with an average of 42.454°C/km and heat flow ranges from 83.190 to >105 mW/m^2 with an average of 106. 135mW/m^2. The geothermal gradient and heat flow maps (Figs. 4.29 & 4.30 respectively) are same with areas of high CPD such as Okposi, having anomalous geothermal gradients and heat flow.

C. Discussion of Deep-Seated Magnetic Lineament Results

Lineaments from aeromagnetic data reveal structures more deep-seated than Landsat's surficial lineaments.Trends ranging from E-W, NW-SE, NE-SW and their corresponding dip directions were obtained and almost every part of the study area have occurrence of these lineaments. Four conspicuous tectonic events have been delineated so far in the NE-SW, NW-SE, N-S and E-W trends. The E-W lineament structures are pronounced and older within the study area but are most likely extirpated by the NE-SW younger lineaments. The NE-SW lineaments are older also but surbordinate to E-W older lineaments. They both relate to Chain and Romanche transcurrent fault systems extending from Atlantic ocean into the country (Ajakaiye *et al*., 1986) which initiated fractures within the pre-Cambrian basements overlain by cretaceous sediments. The post-PAN African fractures may have been re-activated by some major transcurrent faults within the Cretaceous sediments of the study area (Merti, 1970), the folding of the Albian basements and westward flexure of Anambra may have offset localized fractures in the N-S and NW-SE directions. The localized fractures and stress concentrations within the sediments have been induced by intruding pyroclastics, microdiorite sills and basalt dykes. (Nwachukwu, 1972; Benkhelil, 1986).

Areas of shallow CPD such as Obudu, Ugbodo, Awgu and areas of deeper CPD such as Apiapum, Abakaliki, Okigwe have varying concentrations of lineament structures and have been influenced by tectonic activities. As

afore-mentioned, some of the structures are faults and fractures which are deep-seated. The volcanicity in these regions during the Albian from magmatic intrusives, have contributed thus, in enthalpy change within the adjoining Cretaceous sedimentary units in the LBT, hence, the development of local thermal anomalies observed in the region. The fracture and fault systems creates a pathway for ore fluid migration and heat exchange in the anomalous geothermal fields. Geothermal and mineral exploration is feasible in these regions of shallow CPDs.

D. Discussion of 3D Euler De-convolution Result

The structural indices of 0, 1, 2, 3 were preferred to be used in the study, based on the assumptions that the area has a wide range of geologic models present in it. From present and improved literature of Standard 3D Euler Deconvolution, structural index of 0 reveals geologic contacts and edges of infinite depths. From Figure 4.47 when superimposed on the magnetic anomaly map, it can be deduced that Euler solutions gotten from structural index of 0, shows dense cluster solutions and also reveals various geologic structural trends such as faults/fractures in dominant NE-SW and localized NW-SE and E-W trends, developed across geologic boundaries (see direction of black arrows on Fig.4.48). At Southwestern part of the study area for example, fracture/fissure trend in the NE-SW direction may likely have been created by subsurface basic to intermediate intrusions at 1.1-2.5 km depths in Awgu shales and Okigwe-Umuahia sediments of the ARG. Figure 4.48 shows 3D Euler depth solutions of Figure 4.47 overlain on magnetic anomaly field data. The contacts are clearly mapped by the Euler model with information on their respective depths. Both the finite and infinite source contacts have been identified from good clustering of Euler solutions at locations on the map. These contacts are interpreted as geologic fractures/faults in the region and these structures have varying depth ranges between <713 m to >2444 m. Almost all around the study area, these structures have occurrences >2 km depth as seen dominantly around Afikpo, Okposi, Oban, Ogoja, Abakaliki e.t.c . They yield high magnetic anomalies that occur at shallow depths of 0.5-1.5 km around North to Northeastern parts where they have an alignment in the NW-SE direction. Okposi, Afikpo, Biase, Obudu e.t.c most likely have shallow structures, however, these structures in the environs of Biase and Obudu, may be as a result of granitic intrusions or older granites of undifferenciated basement complex from high

magnetic responses >60nT (see zones encircled by white circles in Fig.4.48). The folding of the Albian basements and westward flexure of Anambra may have offset fractures in the E-W and NE-SW, NW-SE directions (see Fig.4.48). The localized fractures and stress concentrations within the sediments have been induced by intruding pyroclastics, microdiorite sills and basalt dykes (Nwachukwu, 1972; Benkhelil, 1986). Hydrothermal fluids in association with granite extrusives of the Southeastern flanks, precipitate ores at contact zones, hence the relevance of contact zones to mineralization.

There is also a similarity of solution to the structural index of 1 representing sills and dyke structures as presented in figure 4.49 and 4.50, but fewer clusters were obtained with this index. This therefore shows that sills and dykes are less dominant geological structures in the study area as compared to contacts which have more cluster of solutions dominant in most of the Eastern sections of the study area, if not all over the map. Figure 4.50 shows magnetic field anomaly data with superposed Euler solutions (SI=1), short wavelength and low residual magnetic intensity of -35.4 match with closely spaced clusters from Euler solutions, depicting vein lodes. These clusters occur in areas of intruding basalts, Northeast of Ugbodo. There are fewer clusters of these solutions representing the dyke/sill structures and these structures occur North of Ugbodo, in the Northernmost part of the study area, Southeast of Obubra and Apiapum, South of Mamfe and East of Biase, all towards the Southeastern part and extreme Eastern parts of the study area. The shallow basaltic intrusive Northeast of Ugbodo (also trace it to Fig.1.7) and a discordant inclined spherical dyke in NW-SE, relative to the low magnetic susceptibility (-35.4nT) host rocks in the E-W trend, must have crystallized at considerable depth between 2-3 km and within Awgu shale host rocks {see Fig.4.66b(i) for the inclined body}. Such assimilation of intrusives into host shales may have resulted to mineralization along the contact zone existing as vein lodes. This is depicted by elliptical low amplitude anomalies on the magnetic field anomaly map. There seems to be a concordance of the sill trend relative to the trend of shale host rock, both strike in NE-SW direction. Such situation is also in congruence with the shallow intrusives around the outcropping igneous basements of Oban massifs.These ringlike granitic sills to inclined dykes in NE-SW and N-S directions, averagely occur at 2km depth and cuts into the ARG shales that

tongue into the Mamfe basin. The same Albian magmatism influenced the occurrence of shallow basaltic intrusives in NE-SW trend within the basin.

The lithologic contacts are significant zones for ore precipitation because the likelihood or possibility of solid minerals being deposited in contact/shear zones and other delineated geologic structures is very high. Depth estimates of some of these geologic structures range from <2226 m to >3042 m. There was little or no solution clusters for SI of 2 (see appendix) and none for S.I of 3.

E. Discussion of Source Parameter Imaging Results

These intrusives and other magnetic source ensembles in purple colour, emanate from depths >2.4 km while the rest are generally shallow deposits less than 400 m deep. The shallow parts of the study area, are in blue and attain depths lower than 0.4 km. Enugu, Nsukka, Biase, Ogoja, adjacent environs of the Mamfe basins e.t.c. reveal shallow depths of source ensembles. From Improved Source Parameter Imaging, the number assigned to the horizontal gradient of the tilt derivative, serves as an index to measure resulting depth ranges of the occurrence of the varying magnetic source ensembles. This number denoted by n_k and representing Structural Index, denotes 0 for contact; 1 for thin sheets and 2 for horizontal cylinder models (Smith, Thurston, Dai, & Macleod, 1998). From SPI map of fig.4.51, an SI of 0.5 was improved to obtain an ISPI map of Fig. 4.52 which improves the relief and the depth of occurrence of these intrusives and other magnetic sources in purple colour at great depths >2.5 km while the rest are generally shallow deposits less than 200 m deep. Okposi, Awgu, Okigwe, Afikpo, Awka all have 0.6 to 2.4 km depth occurring magnetic materials which corroborates the average depth to magnetic source of 1.057 km delineated from spectral analysis on a 55×55 km window.

F. Discussion of the Vertical Derivative Results

The first vertical derivative result in coloured scale, enhances linear features, which appear like dikes, sills, geologic contacts, faults, fractures e.t.c as seen trending from Afikpo to Apiapumand Eastern environs of the study area, gives a clearer resolution of lithologic boundaries and distinguishes hyperbasal materials from felsic rock forming minerals. Opara *et al*., 2012 pointed out that high positive second vertical derivative values denote

melanocratic rock-forming minerals while low negative second vertical derivative values denote leucocratic rock-forming minerals.

The use of second vertical derivative in revealing and estimating depths to the basement is the major backbone for aeromagnetic interpretation (Nabighian *et al.* 2005).This is because improved edge detection and depth to source estimation techniques are dependent on horizontal and vertical derivatives. Using a higher order of derivatives, leads to increased noise which is why this method is limited to the first and second order. More of the mafic rock-forming minerals and features in violet are revealed more in the 2VD map but with major interference from noisy backgrounds. There was neither upward nor downward continuation of the 2VD grid in order to avoid reduction in quality of the resolution since the aeromagnetic anomaly data were more like a residual TMI data from NGSA which needs to accommodate all anomalous responses within the area. Shallow structural details of high magmatic origin as well as conspicuous magnetic lineaments similar to the magnetic lineament structures in Fig. 4.31 are elaborated and depicted by high amplitudes on the 2VD map in Fig. 4.54a. The 2VD technique proves to be very useful when little or no regional effects are to be taken away from more of the residual TMI obtained from NGSA. Anomaly overlap due to discrepancies in delineating respective sources of magnetic anomalies are further enhanced by application of 2VD technique, near surface effects in isolation of deeper magnetic anomaly sources are obtained in preference. The difference in magnetic mineral contents as depicted from the various colourations and demarcation from base contours of the 2VD map, forms a major basis in lithology differences and lithologic boundaries. Similar to description from Oha *et al.,* 2016, the 2VD image in fig.4.54b, though not upward continued to any height, reveals some dispersions of shallow deposits demarcating lithologic outcrops. Section A are surface outcrops of Oban Hill basement rocks, B represents mafics (basaltic/doleritic rocks) outcropping around Obubra, C denotes the mafics (basaltic rocks) around Ikom. D are the mafic to ultramafic rocks of the outcropping Obudu basement rocks, E_1 represents the pyroclastics of Abakaliki and other associated mafic rocks, E_2 have more surface magnetic responses from the Workum Hills and around Wanikande and Wanakom, E_3 represents near surface intrusives associated with barite mineralization

around Gabu-Oshina (Oha, Onuoha & Dada, 2017). Some of the magmatic responses come from basically intrusives which are syn-depositional to the ore deposits of the conspicuous North-East trending shallow sub-surface deposits (see fig. 4.54b). E_1, E_2 and E_3 occur in a NE-SW structural trend falling categorically into part of the Abakaliki-Isiagu and Arufu-Akwana-Azara mineral districts. The ores of the Abakaliki-Isiagu deposits consist of massive sphalerite, galena, chalcopyrite, marcasite, siderite, calcite and quartz in descending abundance (Okafor & Uwadiale, 1997). Fluorite, quartz and minor galena disseminations are the mineral assemblages of the Arufu-Akwana-Azara mineral district. Sulphide minerals, such as sphalerite, galena and chalcopyrite are dominant in the Zurak-Wase deposits (Ogundipe & Obasi, 2016). Several concentrations of intrusive sills and dykes, bosses and stocks occur as lamprophyres, feldspathoidal syenite, leucodiorites, microdiorites gabbro and microgabbro and are essentially posterior to lead-zinc mineralizations (Olade, 1976). F has lot of near surface intrusives characterizing Igumale, G represents responses from surficial Campanian-Maastrichtian-Paleocene carbonaceous shale and ferruginized ironstone capping overlying the sediments, H represents Okigwe-Ishiagu magmatic region still part of the Abakaliki-Ishiagu mineral district, This is part of the Albian Asu River group facies which experienced two deformation (folding) phases (Nwachukwu, 1972; Amajor, 1985), offsetting magmatic activities, such as intrusion of dolerite and granitic dykes intrusions. Resultant hydrothermal ore mineralization like Pb-Zn mineralization arose as a result of this, and I represents responses from ferruginized Imo shales and Aimeke formation.

G. Discussion of Horizontal Derivative Results

This technique helped in establishing the advantage the total horizontal gradient has in centering peak anomalies over magnetic contacts because the regional field is assumed to be vertical, magnetization is vertical, contacts are assumed vertical and isolated with thick magnetic sources (Philips, 1998). The horizontal gradient magnitude of the TMI-RTE in Fig.4.55c shows ENE-WSW and NE-SW anomaly trends with presence of varying basement structural complexities as seen from the amplitudes of the gradients >0.067nT/m and as high as 0.093nT/m. Magnetic susceptibility differences are measured from the degree of varying amplitudes. From the TMG, the

contacts around Oban basement appear lenticulated and straight in NW-SE and N-S directions and the majority in the NE-SW direction at other locations.

H. Discussion of Analytic Signal Results

The analytic signal method does not make the same assumptions with the horizontal gradient, and does not result in displaced contacts. Isolated horizontal gradient contacts may likely denote contact locations. Comparing the AS and TMG map, when there is an offset of the horizontal gradient from the analytic signal contacts, the analytic signal contact represents the true contact location and the horizontal gradient further indicates a down dip direction Ndougsa-Mbarga, Meying, Bisso, Sharma, Layu & Manguella-Dicoum **(**2011). The degree of magnetization is high North and Northeast of Ugbodo, around the basements of Oban and Obudu and outcropping doleritic intrusions in Okigwe. Magnetization >0.044nT/m are diagnostic of basaltic and doleritic intrusives and low amplitude signal <0.009 are diagnostic of sedimentary environments, basically non-ferruginized sediments. Just like the derivative maps, analytic signal discriminates between basement and sedimentary environments.

I. Discussion of NTilt Derivative Result

TDR which is an arctan function of the normalized vertical derivative (Fig.4.57) and as given in equation 3.4, improves the edges and highlights potential ore fields in trends of occurrences. The directional derivatives improves the trend of occurrence of most magmatic materials as seen around Enugu, through Ugbodo up to Enugu, Umuahia, through Afikpo, Obubra up to Ikom and Obudu. There are also conspicuous E-W and Northeasterly trends in this map of sub-surface deposits from Umuahia to Obubra. e.t.c. >1 radians. The total horizontal gradient, alongside Ntilt filter, enhances the boundary of adjacent anomalies, shallow and deep structures. The maximum value shows the edges of the anomalous magnetic bodies and also enhances shallow and deep structures. From figure 4.60, most shallow subsurface to surface basement bodies occur in Eastern parts and other dispersed parts in the Western part of the study area, represented by variegation of colours in the midst of purple colours. These variegated colours likely denote less mafic surface intrusives within the study area. This is seen occurring at Ogoja, Obudu, Ikom, Oban which are around basements adjacent to the Mamfe basin. North,

South and Northeast of Ugbodo are viable regions for ore accretion as well as other places in white blocks (see Fig. 4.60b). The purple colour most likely represents deeper magnetic responses occurring within the surface area. Variegated NTilt responses delineate actual responses from edges of subsurface deposits.

J. Discussion of Magnetic Vector Inversion Results

From the subsurface imaging results of section A of the geothermal gradient map, models originally unseen and sandwiched into the magnetic anomaly maps were resolved and obtained separately as models of subsurface deposits ranging between 100 m Above Sea Level (ASL) to 9000 m Below Sea Level (BSL) as represented in figures 4.62a. There is a trend of occurrence of deposits in NE-SW trend. Regions of higher geothermal gradients >45°C/km correspond to disseminated higher magmatic deposits at >5km depths towards the NE while massive deposits at Okigwe environs with lower magmatic properties occurring at the Southwestern part of the study area at about 1.8 km correspond to areas with low geothermal gradient of 21.2°C/km.(fig.4.62b). Some deposits appear at 2.2 km around Afikpo and environs which have geothermal gradient of 30.6°C/km. From part A, environs of Ezzagu (Ogboji), Amanator-Isu, Azuinyaba, Nkalagu, Amagunze e.t.c occur in regions of high geothermal gradients >45°C/km which is within the range estimated by Onuoha & Ekine, 1999) for deep wells drilled in Anambra basin. This anomalous zone coincides with the point of conjunction of the structurally inverted Benue Trough encompassing the Afikpo syncline and parts of the depocenters within the Anambra basin. These units of Turonian to Maastrichtian age, are obviously thickest and most silted up >450 m ASL with sedimentary thickness of approximately 9 km. This sedimentation triggers increased temperature and pressure gradients across buried sediments. The Albian Afikpo sediments of the Asu River Group which is the oldest sedimentary pile with poorly bedded Abakaliki shale, lenses of sandstones and sandy limestone (Reyment, 1965), was affected by Santonian tectonic activity whch generated tectonic fractures in the form of folds, faults and fractures (Benkhelil, 1989). These structures host sulphide deposits, and create aquiferous units for groundwater occurrence (Nwajide, 2013), creates a migration pathway for plutons and hydrothermal fluids as revealed at regions with shallow intrusives from shallow CPD, and functions as heat flow pathways to develop these local thermal anomalies.

The subsurface imaging result of Figure 4.62a has superimposed aeromagnetic data on it and this was achieved by exaggerating the height of the magnetic data to about a distance of 19278.31 m ASL in order to incorporate both plots. This shows the responses of the aeromagnetic anomalies from the varying depths of occurrence of the models. The very low residual magnetic anomalies between Awgu and Okigwe (-35.2 to 5 nT) shows underlying shallow spherical structures between 100 m^{-2} km depths causing such response. It could be faults and/or fractures capable of hosting metallic sulphides embedded within the sedimentary piles of the Asu River Group. Disseminated deposits with varying degrees of magnetic properties have shortwavelength responses on the aeromagnetic map. At the extreme Northeastern part of section A, the deposits are very close to the surface. The models with higher MVI values occuring at about >5 km depths at extreme Southeastern part of the section around Afikpo environs, show higher magnetic responses on the magnetic anomaly map. These are affirmed by the fact that intra-sedimentary volcanics and magnetic massive sulphide deposits, disseminated pyrrhotite in shales and siltstones, Ilmenite, and Maghemite have been identified as geologic units that can cause magnetic responses in a sedimentary basin (Gunn & Dentith, 1997; Clark & Tonkin, 1994).

The same subsurface imaging result of figure 4.62a had 3D computed geothermal gradient data superposed on it. The 3D data had its height exaggerated to about 35307.10 m in order to accommodate both plots. The models obtained from the 55×55 km window of part A inversion result, range from 100 to 9900 m depth. Areas of high geothermal gradients coincide with models of higher magnetic properties about 7-8 km depth at extreme NE while low geothermal gradients coincide with subsurface deposits of low magnetic values. Figure 4.63a reveals a lot of models obtained from this window size, Most of the models of high MVI values denote deposits with more magnetic properties because of very high residual anomaly responses observed over them, and they are quite surfacial going by their depths of occurrences between <100 m to <5 km as corroborated from shallow CPDs <10 km depth. At extreme North to Northwest and South to Southeast of the study area, surfacial deposits on the average occur between depths of about 150 m to 4500 m while the rest occur as deep as >9500 m. There is a

visible NW-SE trend of occurrence of these sub-surface deposits around environs South of Ikom, almost at the Central part of the study area Northwest and West of Ikom. North, Northeast and Northwest of Obubra and Ugbodo, there are both shallow and deeper occurrences of some of the deposits. This is most likely caused by stress fields from Charcot fault systems, accompanied by igneous activities that pre-date the Santonian deformational regime. Albian and early Cenomanian fractured basements which have possibly resulted from this phenomenon and overlain by silted Odukpani and ARG sediments provided migration pathways for intruding basalts and igneous veins at varyng depths within the host sediments. Low residual magnetic anomalies occur between 30-45 nT at Ikom environs, denotative of possible vein lodes of skarns created between contacts of intruding basalts within formations of New Netim Marl.

The inversion results of Part B anomalous geothermal gradient falls within late Albian and early Cenomanian fractured basements which have also served as pathways to conduct heat across formations. Some areas of high geothermal gradients in the Eastern flank occur at Nta-Nselle, Nnam, Akorfornor e.t.c. The inversion result from Part B of the 55×55 km window has the aeromagnetic data superposed on it as represented on figure 4.63b. The 3D aeromagnetic data plot was exaggerated also to a height of 19202.65 m in order to accommodate both plots of the 3D aeromagnetic data and model extract. The models with higher magnetic values which are closer to the surface reflect on the aeromagnetic data as short wavelengths in red to purple colourations of high magnetic response while models with lower magnetic values and at greater depths >4km are reflected on the aeromagnetic data as blue of low magnetic responses.

The window size of Fig.4.64a accommodates more deposits at depth and towards the subsurface and reveals the inclination of these deposits from depths >7km with models <6km. From observation, there are intrusives at depths >5km and approaching the surface, they loose their high susceptibility values, this basically occurs due to subsurface erosional activities. The higher magnetic responses from the aeromagnetic data correspond to high values from MVI models at depth while lower responses correspond to subsurface deposits of lower magnetic values. The aeromagnetic data with combinations of varying wavelength distributions have corresponding

responses from both higher magmatic models at depth and lower magmatic models at the subsurface from the Magnetic Vector Inversion MVI result (fig.4.64b). The plot of Fig.4.64 c was done using a 2000m offset and the relief scaled at 500. From this representation, areas with shallow magmatic models of the CPD plot occurring between 1-2 km depth have corresponding high geothermal gradients while high magmatic models at a greater depth >4km have corresponding low geothermal gradient. This is most probably guided by an existing relationship whereby geothermal gradient and heat flow values increase with reduction in curie point depth. There is an inverse relationship between geothermal gradient and curie point depth and between heat flow and curie point depth.

Pb-Zn ores in the ASU River Group sediments exhibit poor magnetic properties (Ogundipe & Obasi 2016), hence, associating mineralized zones with low magnetic susceptibility was considered feasible. However, the Asu River Group shales which host these ores contain some gangues as iron minerals in form of pyrite, chalcopyrite, marcassite, and siderite (Agumanu, 1989; Umeji 2000, and Arinze, Emedo & Ngwaka**,** 2019) showing higher susceptibility values when they exist independently without the occurrence of sulphide lodes. Based on the scope of this work and as previously interpreted, subsurface intrusives, vein lodes in fractures containing ores and gangues, yield magnetic susceptibility contrasts. The interest in mineralization shown by varying magnetic susceptibilities, guided the selection of anomaly windows. Based on the varying susceptibility contrasts, prominent anomaly windows P-Y in Fig.4.65 were captured on the geomagnetic anomaly map for wider and more detailed probe using the Magnetic Vector Inversion modeling. Modelling result from window P as in Figures 4.66a(i). The models or deposits delineated within this window occur at near surface and at depths between 2 km and 7 km. At the extreme NE part of the window where the environs of Nsukka and environs, outcropping almost very close to the surface between 500 m to 2 km are low magmatic models most likely of shale, clay or sand origin. South of this has adjacent occurrences of models/deposists with varying magnetic intensities between 2 km to 7 km depths. Figure 4.66a (ii) shows that low susceptibilities from aeromagnetic anomaly at the Northeastern part of the window area, are responses from near-surface low magnetic models while a higher

magnetic anomaly responds to deposits >7 km BSL depth with higher magnetic vector inversion values. These models may likely occur as placers of magnetites or heavy iron deposits up to 300m to 1 km controlled by Adaoru stream which cross-cuts Nsukka and its environs (see Fig.1.7). The intra-sedimentary magnetic deposits however occur and cross-cut the sandstones and shales of Ajali and Nsukka formations respectively, hence the variation of high magnetic susceptibility from the ore and host rocks.

4.66b (i) reveals Q window which captures NorthWest of Ogoja and Northeast of Ugbodo. spaced, nucleated deposits and varying shapes of models delineated, which are steep, inclined and curved. At extreme left, is a conspicuous and an almost spherical deposit and variegated magnetic vector inversion values from the model yield and correspond with mixed magnetic anomaly responses from the superimposed aeromagnetic anomaly data [Fig. 4.66b(ii)]. The vertically inclined models with varying magnetic intensities at the central part of the window directly have undulating magnetic responses, basically very low and a bit of higher magnetic anomaly responses. These models with higher magnetic intensities at depth in the Northwestern part of the window have higher magnetic anomaly responses. This window contains both high and low residual magnetic susceptibilities. The inclined steep models occurring almost at shallow depths (1-3) km, are outcropping basalt intrusives within the Coniacian to Turonian Awgu shale host rocks, which give high residual anomaly responses. These shallow intruding basalts occur as discontinuities within the shale host rocks (Fig.1.7), and may likely house important lodes of galena, sphalerites, marcasites as telethermal to epithermal deposits, with gangues amidst calcite, dolomites and shales. These lodes within shallow tectonic structures remarkably give low residual susceptibilities.

R is a window represented in figure 4.66 c(i) which captures the environs of Gaki and Ogoja. The models obtained here have MVI values between 0.01646 to 0.04037 and occur about 200 m to 3 km BSL depths. These models are of varying higher magnetic values and occur mainly in the NE part of the window. From the superimposed aeromagnetic anomaly data on it [Fig.4.66c(ii)], higher magnetic anomaly corresponds with these subsurface deposits with higher MVI values. This window contains models of high MVI values >0.03339, reflecting low residual magnetic susceptibilities on the aeromagnetic anomaly map and which are almost surficial. This high

anomaly responses come from late Paleozoic plutons of biotite-garnet-shists and banded gneisses around the environs of Gaki and Ogoja between 100 m to 3 km BSL. Lindgren, 1933 associates acid plutonic rocks in old Precambrian terranes as often associated with faulting and having replacement ore bodies, broadly tabular and in veins. The low residual susceptibilities are likely denotative of replacement ore bodies enriched in Gold, Tin, Molybdenum, Wolframite, Copper, Lead, Zinc, Arsenic and as such, may have important occurrence of ore minerals such as magnetite, pyrrhotite, cassiterite, bornite, chalcopyrites, pyrites, galena and gold.

S window in Figures 4.66 d(i), captures Udi and its environs. Here, horizontal models with varying MVI values were delineated. Horizontal models >30 km width were mostly delineated at >7km BSL. At the Eastern section of this window area, sub-surface horizontal models became more reduced in width, occurring at about 500 m to a bit more > 4 km. The aeromagnetic anomaly data was superimposed on the inversion modelling result of the window. Over the rows of N-S trending horizontal deposits with varying MVI values occurring at varying depths, are corresponding high magnetic intensity anomalies on the aeromagnetic anomaly map [Fig.4.66d(ii)]. This window captures Udi environs and contains N-S trending tabular models which occur within the Anambra basin. From the east, the horizontal models occur within Awgu shales, contact zones of Nkporo and Awgu shales, contact zones of Nkporo and sub-bituminuous shales of Mamu formation, Ajali sandstones and contact zones of Ajali sandstones and sub-bituminous shales of Nsukka formation. The varying magnetic susceptibility responses, occur over the Coniacian to lower Paleocene allochthonous sediments of the basin's depocentre. Stanton (1972), in his environment-rock association scheme, classifies the important deposits in such environment to be Iron and Manganese deposits. The elongated models are likely going to be strata-bound deposits of banded iron formation oriented in N-S direction in the geosynclinal environment. The basin's westward flecture and alignment of the Santonian stress fields in the N-S direction must have repositioned the lodes in a N-S direction. These BIFs in the environment will most likely occur in gangues of Sulphide and Silicate facies because of their formations in shallow water facies.

T window represented in Figures 4.66 e (i), captures Abakaliki and environs. A lot of nucleated but concentrated clusters on the subsurface occur at about 100 m to 4.5 km BSL depth with varying but dominant high MVI values at the extreme Northeastern part of the window field. The aeromagnetic anomaly data directly overlying this window has a corresponding high magnetic anomaly response over the clusters. [Fig. 4.66e(ii)]. The area windowed mainly occurs within the ASU River shale group which contains baked shales of the formation as seen from intermediate susceptibility of ≤ 20nT. The sparse and disseminated ores occur as result of the shales' association with the intruding basalt. These porpheries most likely occur at alteration zones within shale host rocks coincident on the contact zones with the basalt intrusives. These models may likely exist as porpheries as hypogene mineralization.

U is a window represented in Figures 4.66f(i) which captures Ikom and environs within Mamfe embayment of the Calabar flank. The model delineated around the environs of Ikom with varying range of MVI values, outcrops to the surface as much as >300 m ASL as seen at the extreme right of windows U and occurring also at depth <6 km BSL. Overlying this in Fig. 4.66f (ii), is the aeromagnetic anomaly data whose variegated short wavelength anomalies correspond with the underlying model. High magnetic anomalies also correspond with near-surface models. This window captures Awgu shales and marls of Mamfe embayment. The high residual susceptibility reflects the presence of intruding subsurface basalts. The overlying variegated susceptibility responses from the anomaly map occur over spherical subsurface deposits at extreme East, which are likely carbonate-rich pellitic to clay-rich gangues (occurrence of protolithic deposits may be high here). Depending on the pressure-temperature ratio, the carbonate minerals here are likely going to be associated with those of the green schist facies.

V is a window represented in Fig. 4.66g(i) which captures environs of Okigwe and Awgu. An inclined model attached to an almost spherical model was delineated here. This inclined steep model of very low MVI value range between 0.00031 and 0.00032 and occupy as much as >80 m ASL. The near-spherical model has a range of MVI values between 0.00034 to 0.00049 and occurs between >1.5 km to <7 km depth. Figure 4.66g(ii) shows superposition of aeromagnetic anomaly data on inversion modeling results, the downward deflection of low

magnetic anomaly corresponds to the low value ranges of MVI values from the almost spherical lump. The V window accommodates the Albian ASU River group, Coniacian Awgu shales, Campanian to Paleocene sediments of the Anambra basin and Imo shale equivalents of the Akata formation. The window shows two regions of residual anomaly intensities, the zero contours demarcate boundaries between sediments of Afikpo and Anambra basin. The deposits are likely weathered doleritic intrusives which emanate from the ASU River group sediments, into the Awgu shales. The high residual intensity depicts iron deposits within allochthonous sediments of the Maastrichtian.

Figure 4.66h(i) shows window W which captures Okposi and environs. Here, the models are of higher intensityand MVI values within the range of 0.00031 and 0.00053. At the extreme right window, at a depth about >5km, stacks/groups of cylindrical models in a N-S direction can be seen to occur. At a depth >7km around the environs of Afikpo, there is an E-W occurrence of models with varying MVI value range. Other smaller models occur at a depth of 2-6 km. The inversion models were overlain with the aeromagnetic data [fig.4.66 h(ii)] directly and from this superimposition, elongated and smaller circular models occurring towards the Southeastern part of the window with higher MVI values, have corresponding higher aeromagnetic anomaly response value, while towards the Northwestern parts of the window region, models with lower MVI values have corresponding lower aeromagnetic anomaly. The varying residual intensities most likely demarcates the formation of the ARG with Awgu shales (see Fig.1.7). The sediments of the Afikpo basin contain as seen from the magmatic models of high MVI values, residual placers which are most likely, magnetites.

Window X captures environment Northwest of Biase around the Calabar flank as represented in Fig. 4.66I(i). At the extreme Western part of the window and more than 10m ASL, there is a steep depression greater than 4km BSL. Above the models with high MVI values > 0.00038, overlies those of lower MVI values <0.00024. At the extreme right of the window are smaller cluster deposits lying horizontally and above at 100 m ASL and on deep seated models at 4-7 km depth BSL. There are various magnetic intensities of the models at the extreme right evident from the varying MVI values of the surface outcropping models between 0.00015 to 0.00031 MVI and

the spherical ones overlain by the outcropping models at about 4-7 km BSL. The aeromagnetic anomaly data superposed on the inversion modeling results as represented in fig. 4.66I(ii) shows very short wavelengths of high magnetic anomalies corresponding with deposits of varying MVI values at the extreme rights. The surface deposits at the northernmost part with high and low MVI values have corresponding high and low magnetic anomaly responses respectively. This window accommodates various litho-stratigraphic sequences of the late Paleozoic basements of the Calabar flank, the Cenomanian sediments of the Odukpani, Turonian to Coniacian sediments of the Afikpo basin and Campanian-Maastrichtian sediments of the Anambra basin. Diagenetic to low-grade metamorphism most likely emanates between the contacts of Biase's migmatites (metasomatic rocks) with shales and marls around Biase environs, hence the models at the extreme right might be carbonate rich gangues which are sub-surficial deposits from hydrothermal alterations. At the extreme left, the models may also represent intruding volcanics of magnetic origin which precipitates iron-copper-zinc minerals.

Figure 4.66j(i) shows window Y which captures the environs of Owerri and Umuahia. There are basically sub-surface deposits revealed in this window which occurs less than100 m ASL to at most less than 5 km BSL. The deposits are almost spherical and nodular and dispersed all through the window area and the models have equally varying MVI values between 0.00048 to 0.00069. The superimposition of aeromagnetic anomaly data over it yields a high response of the aeromagnetic anomaly data over the deposits at the extreme right of the Study area [Fig. 4.66j(ii)]. This window accommodates shales and sandstones of Paleocene to Oligocene. The susceptibility contrasts represent lithologic transition from shale to sandstone units. The shale most likely reflects high residual susceptibility >120 nT arising from the ferruginized Nsukka and Imo shale units and sandstones of Aimeke and Nsugbe. The disseminated deposits represent propheries with varying MVI values depict shallow lenses of magnetite gangue minerals such as; Iron, pyrites, chalcopyrite, e.t.c.

4.2.3. Discussion of Results from Airborne Radiometric Data

A. Discussion of Results from Radioelement Concentrations

There is relativity between the geology and the radiometric data sets. The shales of the Abakaliki-Benue Trough (Afikpo Basin) and Mamfe Basin have high Potassium (K), Thorium (Th) and Uranium (U) concentrations. K, U and Th radioelements are usually dominant in acid igneous rocks, pegmatites and around basement regions. However, high content of the three radioelements within Afikpo syncline having ASU River group sediments, Mfamisong limestone, New Netim Marl, EzeAku formation, Amasiri sandstone and Awgu formation suggests allocthonous sediments within the syncline. The basin serves as a placer where valuable mineral deposits accumulate through hydrothermal alteration processes from contacts of intrusives and basement source rocks with the ASU River group sediments. The marls, shales and black shales most likely contain vein deposits significantly denser than sand components or quartz in the form of alluvial deposits of Ag, Pb, Zn, Cu. (Oha *et al.*, 2017). The radioelement concentration maps (total count and tenary maps) are useful in discriminating zones of consistent lithology and contacts between contrasting lithologies (Duval, 1983), hence mineral colonies and geological boundaries are easily inferred. The disintegration of parent materials increase the radioelement concentrations, a lot of detrital feldspar of the ARG sediments will likely reflect on anomalous TC and ternary image maps. Etim *et al.* (1988) suggested that the most credible lead source for Abakaliki mineralization, corresponds to detrital feldspars eroded from the basement and re-concentrated within sandstone-shale series. The three radioelement concentrations are commonly present as well around Ikom. There is more of Potassium concentration than Uranium and Thorium concentrations within basement rocks of Calabar flank (comprising of Oban Massifs extrusives and Obudu plateau). The gneiss and granite outcrops of these extrusives have high potassium content, usually, this is the basic radioelement constituent around altered acid volcanics and areas of saline deposits in sediments (after Dickson & Scott, 1997). The sequences of sandstones, limestones, shales and calcareous sandstones of the Odukpani Formation most likely contribute to more potassium content.

Nkporo shales have high Thorium and Uranium concentrations which depict shale-rich zones. These carbonaceous formations most likely have high radon potentials in these mudrocks which are unstable to help contribute, by disintegrating, to higher Thorium and Uranium concentrations. The Mamu Formation, Ajali

sandstone and Nsukka Formation which constitute parts of the Anambra basin, show very low K, U and Th contents. This is because of the sedimentation of thick carboniferous sediments of the Anambra basin evident from coalification and kerogenization processes within the Formation under high heat and pressure. As a result of this, radioactivity seems to have a downturn, establishing an inverse relationship between radioactivity and carbonization.

B. Discussion of Results from Radioelement Ratio Composites

K, K/eTh and K/eU all have similar appearances and show dominance of the the K-radioelement around the

SouthEastern part of the study area comprising of the Afikpo syncline and the Calabar flank of the basements. The potassium composites reveal the dominance of this element around the Oban massifs up to the Mamfe basin, denoting presence of acid volcanic, saline deposits, heavy mineral deposits, evaporates and feldspars e.t.c. The Uranium ratio composites show clearly the deficiency of Uraninites or Uranium radioelement within the Anambra Basin and the basements of the Calabar flank, especially the environs of the Oban massif. From Uranium plots of Figures 4.68h and 4.68i, shales of Nkporo formation display high Uranium concentrations equivalent to the ranges of those possessed by typical Archaen shales (Dickson & Scott, 1997). Thorium ratio composites; eTh/eU and eTh/K are represented in Figures 4.68(e) and 4.68(f) respectively. They reveal the concentration of Thorium element around the basements of the Calabar flank and within Mamfe, Anambra and Afikpo Basins. Figure 4.68g shows combination of radioactive results which was established from combination of each of the three radioelement ratio composites for three radioactive elements (combination of three radiometric ratios). According to Duval, 1983, red is assigned to eU/eTh, green to eU/K and blue to eTh/K.

C. Discussion of Ternary Image Results

The ternary image gives a comprehensive distribution of the three radioelements and corroborates the earlier descriptrions of what their various dominances entail within the study area.This technique is very proficient towards the delineation of ore deposits often associated with hydrothermal alteration apparent through

accentuated changes in K, eTh and eU especially for K count (Duval, 1983). Radioelements are always possible indicators of mineralization because they are contained in economic minerals such as Uranium ores, heavy minerals, feldspars, evaporates e.t.c. and heatflow from radioactive isotope decay usurps on continental margins constituting continental heat flows, thus high isotope concentrations are denotative of high heat flow (Holmberg, Naess & Evensen, 2012), the heat of the Earth is replenished by radioactive decay at a rate of 30 TW (Perry, 1895).

4.2.4. Discussion of Results from Map Composites

A. Discussion of Results from Clay Alteration on Magnetic Lineament Map

Figure.4.70 shows contact regions of clay alterations and magnetic lineaments which are believed to have resulted from leaching properties of hydrothermal/ore fluids, actively circulated through dilated fractures. They are possibly generated from heat of subsea magma chamber from upwelling magmatic plumes which intrude into sediments and precipitate SEdEX minerals by metasomatic reactions and are saturated by saline sea waters of high Sulpho-salts from the Atlantic. These encircled zones therefore approximate shallow to deeper accrued ores from mineralizing fluids in contact with these dilated fractures as revealed from magnetic lineaments and most likely have sustainable Iron, Manganese, Lead and Zinc e.t.c ores.

B. Discussion of Results from Magnetic and Landsat Lineament Maps on Iron Oxide Map

The red iron rich zones in Figs. 4.71a & 4.71b which coincide with surface and deep seated lineaments are likely potential ore fields. The magnetic and Landsat lineaments coincide almost together though the surface lineaments appear distributed over the whole study area more than the magnetic lineaments. Veins and mineral lodes dominate in such coinciding regions.

C. Discussion of Magnetic and Landsat Lineament Maps on Mineral Map

The superimposition of the magnetic and Landsat lineaments (Fig. 4.72) show dense lineation of the study area which serves as good conduits for hydrothermal fluid migration, wall rock alteration and ore precipitation. Mineral map of the study area superimposed on Figure 4.72 reveals areas with occurrence of few existing minerals

are seen where surface and deep-seated lineament co-occur, hence it is likely that fields with mineral deposits can be anticipated.

D Discussion of Results from Evaluation of Zones Viable for Ore Deposits

From Figure 4.73, most shallow subsurface to surface basement bodies occur dominantly in Eastern parts and other dispersed parts, in the West as represented by variegation of colours. These variegated colours occurring at Ogoja, Obudu, Ikom, Oban likely denote felsic to mafic surface intrusives within the study area. They are dominant around basements adjacent to the Mamfe basin. Most likely, east of the study area are viable regions for ore accretion because from the NTilt map, variegations of short wavelength anomalies are dominant here. High radian values in purple color most likely represents deeper magnetic responses occurring within the surface area. Comparison of part B modelled results from the geomagnetic anomaly field data with the NTilt map in Fig.4.74, shows that NTilt technique resolves adjacent anomalies and enhances shallow and deep structures as much as the 3D MVI inversion modelling does, but the inversion modelling goes a step further to estimate greater depths and model geometries of structures. Figure 4.74 relates the fact that mineralization within the study area is structurally controlled, as almost all the minerals are clearly seated on the delineated structures. High temperature hydrocarbon deposits such as coal and graphite occupy zones of moderate to high geothermal gradients (Fig.4.75).

Mineral occurrences in the country are closely related to lineaments linked to offshore trans-oceanic fracture zones, this is corroborated by Figs. 4.71a&b and 4.72. The mineral maps were further superposed on geothermal gradient and NTilt derivative maps (Figs.4.74 & 4.75) to observe how temperature and geologic structures influence their occurrences. High temperature non-renewable organic resources outside the interest of this study, may likely occur in Calabar and Enugu respectively, which are regions of moderate to high geothermal gradients. From Table 4.5, it can be concluded that zones of ore deposits are dominant in environs of Nsukka, Enugu, Udi, Awka, Owerri, Okigwe, Umuahia, Aba, Okposi, Afikpo, Ugbodo, Abakaliki, Obubra, Ikom. The study reveals that dense lineaments from deformational events and intrusives amidst high temperature gradient from Cretaceous

magmatism, makes the study area a viable ore field. Structures from inferred fault zones compare well with occurrence trend of delineated minerals (Fig.4.76 b). Results from predictive map (Fig.4.76 a) show good correlation between areas of high lineament density and existing minerals as a guide to predict mineral occurrences. This correlation suggests that primary mineralization is tectonically controlled and that it occurs through conduits such as faults, fissures and lineaments by which magma or mineralizing fluids get to the surface as intrusives (Ananaba & Ajakaiye, 1987). In the course of evaluating anomalous zones, thresholds for residual anomaly intensities (nT) were given in the range of - 35 to 20 as very low; 21 to 49 as low; 50 to 79 as moderate; 80 to 99 as high and >100 as very high due to the fact that contrasts in susceptibility ranges ushered in geologic contacts as corroborated from Euler structural index of 0. For geothermal gradient (°C/km), it was given in the range of 16.2 to 21.2 as very low; 22.2 to 26.2 as low; 27.2 to 36.2 as moderate; 37.2 to 46.2 as high and > 47.2 as very high. For heat flow (mW/m^2), it was given as 24.7 to 44.7 as very low; 45.7 to 54.7 as low; 55.7 to 74.7 as moderate; 85.7 to 94.7 as high and > 95.7 as very high (based on the given range from Onuoha & Ekine, 1999 and Sharma, 2004). For total count from radiometric data (ppm), 450 to 759.81 was given as very low, 760 to 1069.00 as low, 1070 to 1599 as moderate; 1600 to 2265.85 as high and >2266.00 as very high, given by similar ranges from Duval, 1983. Based on this afore-mentioned evaluation, a comprehensive catalogue was deduced from study results of Table 4.5, model results from Fig.4.65, results from Figs. 4.70 and 4.72b and inferences from Fig.4.72a, was developed in Table 4.6 to infer regions of potential ore deposits.

4.2.5. Discussion of Results from Electrical Data

A. Discussion of SP and Image Results from Umuobom

Areas of mineralization are depicted by very negative amplitude peaks from total field array curves and at amplitude crossover points at origins from gradient array curves (Olorunfemi. 2014). Profiles from gradient configuration along traverse 2 and total field array along traverse 1 of Umuobom were developed. Usually for a gradient array, when a target dips at less than 30°, the anomaly is asymmetrical (Reynolds, 1997; Olorunfemi, 2014) and the body dips in the degree of asymmetry, where amplitude of the shoulder body is higher but when the target dips at 90°, the anomaly becomes symmetrical, showing both equal arms adjacent to the cross-over

point (Olorunfemi, 2014 and Adeyemi *et al.,* 2006; see Fig.3.6a). The SP plot made from the tabularized SP readings (Table 4.8a) shows that the distance between the two cross-over points from 50 m to 220 m along traverse 2 given in Fig. 4.77b, was used to calculate half width and estimate depth to the ore body.

Depth of burial of pyrite deposit was estimated from amplitude inflection points from the Gradient Array plot:

$X_D = Z^2\sqrt{3}$ (Adeyemi *et al*., 2006) 4.1

$Z^2 = \frac{X_D}{\sqrt{3}} = 0.58X_D$ 4.2

$Z = \sqrt{0.58X_D}$ 4.3

$Z^2 = \frac{220-50}{\sqrt{3}} = \frac{170}{\sqrt{3}}$

$Z^2 = 0.58 \times 170 = 98.6$

$Z = \sqrt{98.6} = 9.9$ m

From estimation, it can be said that pyrite mineralization occurs at most 10 m which is also evident from the shallow pit dug at > 4m, (see Fig.4.78b). Along Traverse 2 Umuobom, pyrite sample (see Figs.4.78 a&d) was

picked at this location, N05°52'03.0" E007°10'16.0", in dried river embayment which was certainly an environment favorable for accumulation of sulphide mineral under anoxic conditions and within the dark shale beds it occurred in (Fig.4.78 c&e). Meanwhile a hand dug pit by the locals had already been made at about 7m wide and at >4m depth. Samples obtained and lithology seen around the area of pyrite deposit, corroborates Petters findings in 1982 of grey calcareous shales, siltstones with bands of sandstone and ironstones of Paleocene Imo Shales. The dark grey shales are silty and powdery when felt between the index finger and the thumb and it leaves a smell of carbide which points to it being both calcareous and carbonaceous. The grey shales have iron stains on them probably because of their close association with pyrites. The area grades into the sandstone and shale sequences of Ameki formation.

B. Discussion of SP and Image Results from Nsude

The plots in Figs. 4.79a&b give a 1D presentation along each individual traverse line. The signature of the anomaly from total field curve is symmetrical about the x-axis which estimates the half width as distance from

origin to point where you have peak displacement of the anomaly and it is used to estimate depth to the ore deposit (Olorunfemi, 2014) (see Fig.479a). From qualitative evaluation of the anomaly generated along traverse 1, the target is likely going to be located from the cross-over point at 230 m up to 350m where negative amplitudes occupy. The cross-over point was extrapolated at about 351 m to make it relatively symmetrical about the x-axis. Zones with the occurrence of peak negative amplitudes are diagnostic of a very metallic ore, most likely iron stones, which are also exposed to the surface. Along traverse 2, the deflection of the peak negative would have been very symmetrical about the x-axis of the curve is extrapolated to cross over at 0 origin. The depth of occurrence of ironstones was as much as between 35.09 to 78.30 m. Depth to the iron ore occurrence at traverse 1, Nsude:

$$X_{\frac{1}{2}} = \sqrt{3}z \qquad 4.4$$

$$Z = \frac{X_{\frac{1}{2}}}{\sqrt{3}} = 0.58X_{\frac{1}{2}} \qquad 4.5$$

$$X_{\frac{1}{2}} = \frac{351-230}{2} = \frac{121}{2} = 60.5$$

$$Z_1 = 0.58X_{\frac{1}{2}} = 0.58\times60.5 = 35.09 \text{ m}$$

Depth to the iron ore occurrence at traverse 2, Nsude:

$$X_{\frac{1}{2}}(1) = \frac{270-0}{2} = \frac{270}{2} = 135$$

$$Z_2 = 0.58X_{\frac{1}{2}} = 0.58\times135 = 78.30 \text{ m}$$

In all of these, anomaly is single peak negative, but there seems to be a vertical flow of water, such as a Spring water flow because the potential polarity became positive towards the end of the second traverse, it could mean a scenario of water being pumped out of a well (Olorunfemi, 2014). This survey is associated with ore and ore-bearing rocks and its focus is on mineral exploration. Here, the amplitude voltage of the potential is higher and ranges from few millivolts to one thousand volts but for the mineralization potential, the polarity is negative. For mineral survey, mineralization potential of 200mV is accepted as threshold value (Olorunfemi, 2004). Mineralization of iron stones are surficial and will have a depth of occurrence to as much as 35-80 m.

The ironstones are mainly hosted by the regressive sands of Ajali Formation. The ironstone deposits influence the ferruginization of the sands in Nsude, some of the red earth sands dated to the cretaceous age have great thickness and constitutes friable and poorly sorted sandstones (Fig.4.80d). Most of these iron stones are massive and occur in-situ in their zones of major occurrences but reduce in sizes and geometry farther away from their areas of occurrence. This can be explained better as weathering, erosion and transport, playing a very major role in the dispersion of the iron stones. The clay and sandstones of this area are highly ferruginized and the lateritic clay remains an indication of its occurrence in an iron-rich environment. The ironstone gotten here likely has more than 20% iron based on the hardness, which is more likely to come from aggregate of quartz grains and aluminous alumino-silicates. The dark brown surface of the stone is as a result of oxidation of iron with oxygen of the air and its dark grey interior is as a result of the unoxidized part. This metallic rock does not fall into the category of Banded Iron Formations (BIFs) but in the class of ironstones, as it shows clearly, no bands on the ironstone. (Fig.4.80c).

C. Discussion of VES Results from Nnam Alok, Ikom

The pseudo-section reveals the occurrence of material resistivity >1000 Ωm which is suspected galena/barite,

occurring within fractured shale between 5-15 m (fig.4.82b). The combination of 2D imaging and VES section shows the Albian granites being overlain by the fractured Odukpani sediments which informs the lithology of consolidated shale and dolomitic limestone (Reynolds, 1997). The late Albian and early Cenomanian fractured basements have possibly resulted from folding accompanied by igneous activities, pre-dating the Santonian deformational regime. The intruding plugs of fresh basement rocks within the sedimentary sequence could have also caused resistivity increase >5000 Ωm. From the works of Akpan, Ebong, Ekwok & Joseph **(**2014); Obi, Ekwueme & Akpeke (2014), Luaano, Horacio, Mario, Marta & Ricardo. (2012), Egeh, Ekwuemeka & Akpeke (2004), resisitivity of Barite mineralized vein, has been noted to occur from 1300-3999 Ωm. These geologic materials must have been emplaced in faulted rocks by space fillings. The composite map in Fig.4.72 shows environs of Alok as viable for barytes or gangues of lead/Zinc occurrence. Akpeke & Ekwueme (2012) showed

typical barte-bearing dolerite dykes, occupying the boundary between sandstone and basement, and also reported occurrence of barite precipitation within calcareous sandstone and carbonaceous shale host rocks as a result of reaction of mineralizing fluids with calcareous sandstone, in Agoi Ibami, Cross River State which occurs almost in same study location. Ehirim, Ebeniro & Ofoegbu. (2016) theorized that usually, high resisitivity signatures are diagnostic of barite vein structures which have higher resistivity relative to their host rocks, and that they also exist as gangue minerals associated with lead-zinc mineralization in fractures, fissures and open space fillings in sedimentary and igneous rocks. Nshor Efor Spring (Fig.4.83) at Ikom's environment of high geothermal gradient was visited. The spring has its water source emanating from medium grained granites and it most likely emanates from an outcropping sand body (aquifer, aquiclude or aquitard) cut through by fractured granites overlying Odukpani sediments. Considering the environment of occurrence of the Nshor Efor Spring, the spring was visited in the morning to ascertain the temperature of water but it was a bit below the normal body temperature of 37°C as it felt cold while touched, however some of the enlightened locals talked about the dramatic increase in temperature of the water in early mornings of the raining season to as much as 42°C which was later measured. The dramatic increase in temperature of Nshor Efor spring especially during the rainy season, is a clear indication that there is abnormal temperature changes within these region, which could be considered a surface manifestation of temperature variations in the subsurface. From the VES study, it was observed that within the vicinity of Alok area delineated as having high potential for geothermal resource, there occurs near-surface emplacement of basement rocks with little shale stringes sitting on top of the basement. This can be encapsulated that a befitting model of the proposed geothermal resource in this area is the Hot Dry Rock (HDR) model. Thermal subsurface heat sources, 500 m or less below the surface produce measurable thermal anomalies at the surface and thermal anomalies due to local subsurface heat sources are impossible to detect at the surface or at depths of only a few feet (Lovering & Goode, 1963) except by examining drilled hole temperatures. Nevertheless, diurnal effects, time and weather of the day, time of the year, thermal property and surface temperature of the granite rock from sun's heat, local heat sources such as an oxidizing sulphide or conductive mineral body, may have played a role in the

temperature change. Some of the very low resistivity values point out fractures, a structure which could have possibly aided subsurface heat flow.

D. Discussion of VES Results from Amagunze

The low resisitivity values obtained in Fig.4.84 from VES results, when compared to the range of nominal resistivity values by Reynolds, 1997, are diagnostic of clay, ferruginized limestones and conglomerates, while high results >35000Ω relate to laterites and iron oxides. Amagunze hosts a series of vesicular Awgu massifs by the river bank of Isi Ube, occurring alongside clastics and chemical sediments of Awgu Formation within the Afikpo Basin. This has cementing iron oxides from the pyroclastics of Abakaliki and Awgu massifs binding the conglomerate of trangressive sediment matrix (ironstone, sand and silt stone). From 2D image, the rather dolomitic basement rocks occur between 50 to >100m and outcrops to the surface as seen at the river bank of Isi Ube (Fig.4.86). They may likely contain fractured rock salts which influence heat flow dispersions through ion interractions with pathway openings. Faults and fractures within the adjacent regions of this syncline, regionally emplaced during the Santonian, may be well developed with lodes for mineralization, within the sediment host rocks from reactions between clastic and chemical sediments.

Considering temperature gradient in this region, the closest aforementioned spring to the locations of the VES survey was visited and temperature of the water equivalent to normal body temperature of 37°C was detected. Deductions from the study using resistivity approach shows that thick deposits of sedimentary rocks of mainly sand and shale intercalations. This sedimentary rocks should be under intense pressure by the overburden, thus, the likely geothermal resource within this area is proposed to be geopressured of geothermal resource.

4.2.6 Discussion of Results from Field Images and Secondary Data

The image results show evidences of mineralized zones visited within the study area. Secondary data from double dipole results, corroborates findings of delineated viable zones as well. These zones represented in blue in tables 4.6 encompass, Obinagu in Enugu which shows deposits of Iron stone, Nkalagu and Ishiagu in Ebonyi State which have mineralizations of limestone and dolerites respectively and Nkaliki and Ameka which show

mineralizations of Lead/Zinc (Figs. 4.87 to 4.92). 2D dipole dipole imaging result in Egudinego was gotten from dipole length of 10 m occupied at 23 stations with expansion factor, n, varied from 1 to 5. The resistivity structure with varying range of 2 and 64 Ωm in fig.4.93a, shows two subsurface layers in purple to reddish brown and yellow on the eastern flank between stations 14 and 25, whose thickneses vary from 5-6 m with modelled resistivity values of 40-64 Ωm, depictive of lateritic shale. The second layer is low resistivity clay layer in blue/green colour, which seems to outcrop between stations 0-14 and is indicative of pockets of plastic clay. Ceramics manufactures have benefitted from the development of refined plastic clays and calcinated plastic clays (chamotte) in their sanitary ware productions. At depth of 10-27 m between stations 2-4, there seems to be localized deposits of higher resisitivity values greater than 50 Ωm, which from table 2.9, is depictive of galena rich zones within the ASU river group sediments. From Fig.4.94b, the low resistivity (4-40 Ωm) clay in blue/green outcrops between stations 17 and 25 and extends to depth of over 30 m and the thickness of the top lateritic shale varies from 5-10 m, which occurs between stations 0-17. However, the localized relatively high resistivity ore body suspected to be galena is seen to occur between stations 18-21.

CHAPTER FIVE

5.0. SUMMARY, CONCLUSION AND RECOMMENDATIONS

5.1. Summary

The study involving the interpretation of aeromagnetic, remote sensing and air-borne radiometric data and use of resistivity technique as a non-major technique in this work, to ground-truth these positive results has broadened an understanding towards the proliferation of ore bodies and subsurface structures and their mode of occurrences for futuristic explorations. NGSA's airborne magnetic residual data were analyzed

to delineate zones and structures of anomalous responses from variegated long and short wavelengths denotative of mineralizations or intrusive bodies. OASIS MONTAJ has really been relevant so far in airborne data transformation that has yielded desired outputs, ranging from the production of derivative and magnetic lineament maps, 3D inverse modelling results, 3D source parameter imaging and Euler depth results. Thermal systems and heat regimes that have been determined through spectral analysis, radioelement ratios, PCA, ternary and composite maps from airborne radiometric data. In the same vein, ENVI and ArcMap software packages were helpful in transforming Landsat 8 data to produce band ratios, combination and composite maps that are indicative of hydrothermally altered host rocks. Thermal regimes from temperature gradients prove to be useful in influencing ore field proliferation.

East of the study area is more viable regions for ore accretion because from NTilt map, variegations of short wavelength anomalies are dominant here. High radian values in purple colour most likely represents deeper magnetic responses occurring within the subsurface. Over 600 lineaments were extracted from both true colour composite of the Landsat image and the RTE-TMI map of the aeromagnetic data. These dense combination of all lineaments reveal both surface and deep seated structures. The Southeastern sedimentary basin reveals that about 70% of the area is covered by surface and deep-seated lineaments >2km BSL. About 50% of the basin contains shallow magmatic deposits in developed host rock lineaments within the range of 50-500 m and deep-seated ones occur at most >3km depths. These deposits

have been modelled for their respective geometries which informs that most shallow deposits exist as spherical models, sills, inclined and horizontal cylindrical dykes and seep-seated ones greater than 5km, exist as cylindrical and lenticular deposits. Magnetic lineaments with a predominant NE–SW trend appear to be more densely distributed around basement rocks of the Calabar flank due to how old in origin this pre-dominant lineament trends relate to Chain and Romanche transcurrent fault systems from Atlantic

ocean into the country (Ajakaiye *et al.,* 1986). They specifically initiated fractures within the pre-Cambrian basements overlain by cretaceous sediments. 3D standard Euler deconvolution, Magnetic Vector Inversion modelling and Source Parameter Imaging (SPI^{TM}) techniques were employed for depth estimation of possibly mineralized structures. Results from SPI and Euler methods show similar depth estimates which probes subsurface magmatic models in the range of >0.5 to <2.5 km. Generally, magnetic lineaments have a predominant E-W amd surbodinate ENE-WSW trend but younger surfical structures in dominant NE-SW trend from Landsat lineaments, indicate NE-SW stress fields from tectonic activities, and extirpate older lineaments in E-W trend. Few mineral occurrences from digitized mineral map of the area, are situated mainly at regions where these lineament types co-occur and inferring from these zones of co-occurrences and anomalous responses from analysis of various map composites, an updated mineral catalogue of the study area has forth-with been generated. Sabin's ratio composites delineates alteration zones in the basin as represented in light green to yellow areas. The clay alteration and iron oxide maps all highlight same regions of alterations and inclusions. Regions of magnetic lineaments and clay alteration (6/7 map) contacts, are denotative of alteration zones which are areas of prospect. They are likely to host lodes (mineral veins) in dominant NE-SW and E-W trends and extend to as much greater depths as revealed by Euler and MVI techniques.

Environs of Nsukka, Enugu, Udi, Awka, Owerri, Okigwe, Umuahia, Aba, Okposi, Afikpo, Ugbodo, Abakaliki, Obubra, Ikom e.t.c are zones of mineral prospects as represented in the encircled zones of figure 4.70 and almost co-located anomaly windows of figure 4.65. The horizontal gradient magnitude of

the TMI-RTE also confirms an ENE-WSW and NE-SW anomaly trends from presence of varying basement structural complexities as seen from the amplitudes of the gradients >0.067nT/m and as high as 0.093nT/m. Magnetic susceptibility differences are measured from the degree of varying amplitudes.

Subsurface mafic rocks >0.0005nT/m delineated from the 2D map invariably distinguishes varying lithologic boundaries and units as the area is an interesting mix of sedimentary and basement environment.

The geologic environment of the area favours the occurrence of renewable energy-mineral resources. The thermal maturity of the rocks in some areas will not encourage the development of hydrocarbon resources because the presence of high geothermal and heat flow resources in areas like Amagunze, Okposi, Udi, Enugu, Ugbodo, Obudu, Alok and Oban Masif encourage the potentiality of geothermal and mineral resources in these fields. This is so because a change in temperature affects not only the physical properties of rocks and minerals but changes the rate of reactions of chemicals usually prevalent in clay mineral transformation. High geothermal gradients are conspicuous within the silted Afikpo and Anambra basins and Mamfe embayments. NTilt responses from edges of shallow and deep-seated structures, show high values in the Calabar flank, Ugbodo and the Synclinous arm of the Afikpo Basin. Folds and faults may have localized or channeled the emanating riftogenic-based intruding saline fluids which prograded into ore zones, particularly in ARG environs, causing the formation of lodes of intrusive bodies. Large magnitude magnetic anomalies reflect over these surficial lodes and this connotes a response from iron-rich minerals (Elliot, 1982). Increased geothermal gradient garnered from the upwelling magma phenomenon of the Albian times which initiated most igneous activities must have influenced subsurface hydrothermal deposits. These deposits formed at shallow depths of 100 m - 2.5 km as revealed from 3D MVI results, were triggered by resultant heat flow above 70mW/m^2 threshold. Most of the hydrothermal deposits delineated by the modelling approach reveal their occurrences at shallow depths of <200 m up to >6 km BSL depth around environs of high heat flow and geothermal gradient. These intrusives are

epithermal and replacement deposits based on depth and temperature of deposition, hence their vertical and diagonal discontinuities (see 3D model and NTilt results). These exceedingly iron-rich discontinuities signify epithermal bonanzas which are likely going to encompass Silver and Lead deposits, copper

porphyries, clay minerals, magnetites and skarns especially in Mamfe basin of the Calabar flank because of the immediate adjacent intrusive igneous rocks in this region having silica and iron mix. Appropriate structures and geologic environments favour the occurrences of base metal epithermal ore systems and also gives history of its geothermal system. The pre-Santonian folded and fractured Southern Benue trough likely hosts mineral generations in its cavities. The varying wide temperature ranges within the area promises a suitable environment and stability for alteration minerals to develop in discontinued regimented mineral colonies and epithermal deposits. Inclusion studies of vein minerals from Abakaliki and Ishiagu ore bodies has confirmed the epigenetic Pb-Zn deposits of the Southern Benue Trough (Olade & Morton, 1985) and it invariably detects the thermal history of the LBT.

The airborne radiometric survey revealed values of equivalent uranium to be in the range of 0.36 to 5.21 parts per million (ppm), 3.74 to 19.04 ppm for equivalent Thorium and 0.07 to 1.35% Potassium. Shales of the Southern Benue trough and Nkporo have high Uranium and Thorium anomalies denoting metamorphosed shales which have increased radioactivity from greater amounts of these released radioelements within the subsurface. These radioelements were included into reactive hydrothermal ore fluids amidst shaly or carbonaceous wall rocks. Regions with intense radioactivity from the three radioelements have corresponding increased heat flow because the decay rates of radioelements replenishes earth's heat flow in deca terrawatts (Perry, 1895). It is justified to say that the prolific ore fields of the Southeastern sedimentary basin of the LBT has always been induced by anomalous and varying geothermal fields which set ore fluids into migration. Low to moderate temperatures in geothermal systems of the subsurface cool high temperature ore fluids from higher geothermal gradients hence the occurrences of most discontinuous subsurface intrusives within the Study area. These deposits

are most likely to occur in regions with very low to moderate geothermal gradients between 20-27°C/Km such as Okigwe, Ikom, Obubra, Ugbodo, Udi, Afikpo, Abakaliki, Apiapum e.t.c. Deposits occurring in

these vicinities would most likely occur as replacements or stockworks in basement regions, vein deposits especially in the sedimentary sequences (Berger, 1982). In many ways, the thermal renewable energy resource is favourable to mineralization.

Visitation to four sites confirms the results of mineralization in Umuobom, Imo State and Nsude, in Enugu, as revealed by negative mineralization potential values obtained over the traverses ran on each of these locations. The VES-Schlumberger resistivity conducted at Amagunze, Enugu and Alok in Cross River State, has thus confirmed fractured high resistivity basement rocks constituted by highly conductive materials as likely going to encourage high geothermal gradients by ionization processes.

5.2 Conclusion

A full fledged 4 combo study approach consisting of transformation and interpretation of airborne magnetic data, landsat image scenes, VES and SP-resistivity data and air-borne radiometric data were used to evaluate new ore fields in parts of Southeastern sedimentary basin. This research has shown good responses to surface and deep seated dense lineations, moderate to high geothermal gradients, moderate to high radioelement counts, anomalous magnetic fields and from 3D modelled geometries of ore bodies in the range of >2-7 km. The prospectivity and viability of the study area is very high especially around the environs of the ASU River Group sediments because of some reasons such as dual geology and past to present geodynamicity of the area.

5.3 Recommendations

Several other approaches such as geochemical and petrographic studies of rock samples within the area, need to be adopted by other researchers to probe ore grades. Other geophysical techniques such as well-logging and seismic surveys need to be undertaken, to further corroborate depth, width and thickness of occurrence of these deposits in the afore-listed areas of deposits. Recent well logs need to be obtained in

regions of high geothermal gradients, to ascertain thermal conductivities from drilled-hole temperatures of the existing formations within the study area and harness the reserves.

CONTRIBUTION TO KNOWLEDGE

The Research, 'Evaluation of Mineral and Geothermal Resources of Parts of Southeastern Nigerian Sedimentary Basin', has contributed to the existing body of scholarly knowledge, as it has been able to;

1. Develop a modified catalogue of ore fields from co-occurrence of surface and deep-seated lineaments and generate improved/updated mineral map of the study area by adopting new techniques of magnetic data transformation using MVI and NTilt approaches.

2. Establish a relationship between the geometries of ore deposits and their depth of occurrence by revealing that shallow deposits exist as spherical, sills, inclined and horizontal cylindrical dykes while deep-seated ones greater than 5km exist as cylindrical and lenticular deposits. The depth and geometries are sure guides for resource estimation.

3. Reveal two regimes of geothermal gradient anomalies in N-S and E-W trends and delineate places of renewable geothermal energy resource in environs of Amagunze, Okposi, Ugbodo, Obubra, Alok and Mamfe, whose approximate models of geothermal resources within the area are proposed as Hot Dry Rock (HDR) for Alok area in Cross River State and geopressured model for Amagunze in Enugu State.

REFERENCES

Abdullahi, M. & Raj, K. (2020). Curie depth estimated from high resolution aeromagnetic data of parts of Lower and Middle Benue Trough, Nigeria. Acta Geodactica et Geophysica, 55(4), doi:10.1007/S40328-020.

Abdulrahman, A.K. (2010). Remote Sensing. Republic of Iraq , Ministry of Higher Education and Scientific Research University of Technology, Department of Applied Sciences, University of Technology. Pp.15-17.

Abraham, E.M.; Itumoh, O.; Chukwu, C. & Onwe, R. (2019). Geothermal Energy Reconnaissance of Southeastern Nigeria from Analysis of Aeromagnetic and Gravity Data, *Pure Appl. Geophys.Springer Nature Switzerland AG,* https://doi.org/10.1007/s00024-018-2028-1.

Adagunodo, T.A.; Sunmonu, L.A. & Adeniji, A.A.(2015). An overview of magnetic method in mineral exploration, *Journal of Global Ecology and Environment,* 3(1), 13-28.

Ademila, O.; Akingboye A.S. & Ojamomi A.I. (2018). *Vietnam Journal of Earth Sciences,* 40(3), 288-298, Doi: 10.15625/0866-7187/40/3/12619

Adepelumia, A.A & Falade, A. H. (2017). Combined high-resolution aeromagnetic and radiometric mapping of uranium mineralization and tectonic settings in Northeastern Nigeria. *Acta Geophysica,* ISSN 1895-6572, DOI 10.1007/s11600-017-0080-3.

Adewumi, T. & Salako, K.A. (2018). Delineation of mineral potential zone using high resolution aeromagnetic data over part of Nasarawa State, North Central, Nigeria. *Egyptian Journal of Petroleum,* 27,759–767.

Adeyemi, A.A.;Idornigie, A.I. & Olorunfemi, M.O. (2016).Spontaneous Potential and Electrical Response Modelling for a Thick Conductor. *Journal of Applied Science Research.* 2(10), 691-702.

Aggarwal, S. (2004). Photogrammetry and Remote Sensimg Division, Indian Institute of Remote Sensing Dehra Dun. *Satellite remote sensing and GIS application in agricultural meterology,* 39-65; Geneva: World Meteorological Organization. Pp.23-28.

Agumanu, A.E. (1989). The Abakaliki and Ebonyi Formations: subdivisions of the Albian Asu River Group in the southern Benue Trough, Nigeria. *J Afr Earth Sci.*, 9, 195-207.

Ajakaiye, D.E. (1981). Geophysical Investigation of the Benue Trough. *A Review of Earth Evol. Sc.*,1, 26-136.

Ajakaiye, D.E.; Hall, D.H. Millar, T.W.; Verheijen, PJT; Awad, MB. & Ojo, S.B. (1986). Aeromagne tic anomalies and tectonic trends in and around the Benue Trough, Nigeria. *Nature*, 319, 582-584.

Akande, S.O; Hoffknecht, A. & Erdtmann, B.D. (1992). Rank and petrographic composition of selected upper Cretaceous and tertiary coals of Southern Nigeria. *International Journal of Coal Geology*, 20, 209-224.

Akande, S.O. & Mucke, A. (1993). Co-existing Copper Sulphides and Sulphosalts in the Abakaliki Pb–Zn deposit, Lower Benue Trough and their genetic implications; *J. Mineral. Petrol.,* 47, 183–192.

Akinlalu, A.A.; Adelusi, A.O.; Olayanju, G.M.; Adiat, K.A.N.; Omosuyi, G.O.; Anifowose, A.Y.B. and Akeredolu, B.E. (2018). Aeromagnetic mapping of basement structures and mineralization characteristics of Ilesa Schist Belt, Southwestern Nigeria, *Journal of African Earth Sciences*, 138, 383-391. DOI: https//doi.org/10.1016/j.jafrearsci.2017.11.033.

Akinsunmade, A.; Dinh, C.N.; Wojas, A. & Tomecka- Suchoń, S. (2020). Characterization of lithological zones of the Isanlu sheet 225, North Central Nigeria, using aerogeophysical datasets. *Acta Geophysica*, 68, 651–665, https://doi.org/10.1007/s11600-020-00411-6.

Akpan, A.E; Ebong, D; Ekwok, S.E & Joseph, S. (2014). Geophysical and Geological studies of the spread and industrial quality of Okurike baryte deposit. *American Journal of Environmental Science,* 10(6), 566-574.

Alhumimidi, M.S.; Aboud, E.; Alquahtani, F.; Al-Battahien, A.; Saud, R.; Alquahtani, H.H.; Aljuhani, N.; Alyousif, M.M. & Alyousef, K.A. (2021). Gammar ray spectrometric survey for mineral exploration at Baljurashi area, Saudi Arabia. *Journal of Radiation Research and Applied Sckiences*, 14(1), 82-90.

Amajor, L.C.(1985). The Cenomanian hiatus in the Southern Benue Trough, Nigeria. *Geological magazines*, 122(01), 39-50. Doi: 10.1017/s0016756800034063.

Amin, B.P & Mazlan, H. (2015).Regional Hydrothermal Alteration Mapping Using Landsat 8 Data Conference: ICONSPACE 2015. At. Langkari, Malaysia. DOI:/ Iconspace.2015.7283788.

Ananaba, S. E. & Ajakaiye, D. E. (1987). Evidence of tectonic control of mineralization of Nigeria from lineament density analysis: A Landsat study; *Int. Journal. Rem. Sensing*, 1(10), 1445-1453.

Anderson, H. & Nash, C. (1997). Integrated lithostructural mapping of the Rossing area, Namibia using high resolution aeromagnetic, radiometric, Landsat data and aerial photographs, *Exploration Geophysics*, 28, 185-191.

Anyanwu, G. & Mamah, L. (2013). Structural Interpretation of Abakiliki-Ugep, using Airborne Magnetic and Landsat Thematic Mapper (TM) Data. *Journal of Natural Sciences Research ISSN 2224-3186.*

Arinze J.I.; Emedo O.C. & Ngwaka A.C.(2019). Analysis of aeromagnetic anomalies and structural lineaments for mineral and hydrocarbon exploration in Ikom and its environs southeastern Nigeria. *Jour. Afri. Earth Sci.,* 151, 274-285.

Arisoy, M.O.& Dikmen, U. (2013). Edge detection ofmagnetic sources using enhanced total horizontal derivative of the tilt angle, *Bull. Earth Sci. Appl. Res. Cent. Hacet. Univ.*, 34(1), 73–82.

Azaiez, H.; Gabtni, H.; Chabaane, A.; Sayem, G. & Bedri, M. 2020. Geophysical study of Hanimam Sidi Maamar geothermal site in Central Tunisia for sustainable development. *Journal of African Earth Sciences.* https://doi.org/10.1016 /j.jafrearsi.2020.103897.

Bamidele, O.E. (2020). Assessment of relationship between mineralization and structures within the Ijero mining field, southwestern Nigeria. *Unpublished* PhD *thesis*, Obafemi Awolowo university, Ile-Ife. Osun State, Nigeria. 463pp.

Barker, R.D. (1975). A Note on the Induced Polarization of the Bunter Sandstone, *Geoexploration,* 13, 227-233.

Beardemore, G. R. & Cull, J. P. (2001). Crustal Heat Flow: A Guide to Measurement and Modelling. New York, NY: Cambridge University Press.

Bierwirth P.N., 1997. The use of airborne gamma-emission data for detecting soil proper-ties. *Proceedings of the Third International Airborne Remote Sensing Conference and Exhibi-tion.*Copenhagen, Denmark.

Benkhelil, M. J. (1989). The origin and evolution of the Cretaceous Benue Trough, Nigeria. *J.Afric. Earth Sci*., 8, 251-282.

Benkhelil, J. (1986). Caracteristiques structurales et evolution geodynamique du basin intracontinentale de la Benoue (Nigeria).Thesis d_etat, Nice, p. 275.

Berger, B.R. (1982). The Geological attributes of Au-Ag-base metal epithermal deposits., In Erickson, R.L.,ed.,Characteristics of mineral deposit occurrences: *US Geological Survey Open File Report*, 82-795, 248.

Binks, R.M. & Fairhead, J.D. (1992). Aplate tectonic setting for Mesozoic rifts of West and Central Africa.*Tectonophysics*, 213(1-2), 141-151.

Blakely, R.J (1995). Potential Theory in Gravity and Magnetics Applications, Cambridge. University Press, Cambridge 464.

Blakely, R.J. & Simpson, R.W. (1986). Approximating edges of source bodies from magnetic or gravity anomalies, *Geophysics*, 51, 1494-1498.

Butler, K. (2013). Band combinations for Landsat 8 imagery and remote sensing. ARC GIS blog, ESRI USER conference.

Bukola, A.S.; Abbass, A.; Rafiu , A.; Adewuyia,A.; Ejepu, J. & Adewumi, T.(2021). Delineating and Interpreting the Gold Veins Within Bida and Zungeru Area, Niger State Nigeria, Using Aeromagnetic and Radiometric Data. *Pakistan Journal of Geology (PJG),* 5(2). *DOI: 10.2478/pjg-2021-0006* ISSN: 2521-2915 (Print) ISSN: 2521-2923 (Online).

Brun, J.P.(1999). Narrow Rifts Versus Wide Rifts: Inferences for the mechanics of rifting from laboratory experiments, *Philos, Trans. R.Soc.A,* 357(1753), 695-712.

Chabaane, A.; Redhaounia, B. & Gabtni, H. 2017. Combined application of vertical electrical sounding and 2D electrical resistivity imaging for geothermal groundwater characterisation: Hammam Sayala Hot Spring case study (NW Tunisia). *Journal of African Earth Sciences*, 134, 292 – 298. http://dx.doi.org/10./ 016/j.jafrearsci. 2017.07.003

Charbonneau, B.W.; Holman, P.B. & Hetu, R.J. (1997). Airborne Gamma Spectrometer Magnetic-VLF Survey of Northeastern Alberta. *In* Exploring for minerals in Alberta: *Geological Survey of Canada Geoscience Contributions, edited by MacQueen, Canada-Alberta Agreement on Mineral Development Geological Survey of Canada Bulletin,* 500, 107-132.

Chukwu, G.U.; Ekine, A.S & Ebeniro, J.O. (2008). SP Anomalies Around Abakaliki Anticlinorium of Southeastern Nigeria. *Pacific Journal of Science and Technology*, 9(2), 552-557.

Clark D.A. & Tonkin .C. (1994). Magnetic anomalies due to pyrrhotite: examples from the Cobar area, N.S.W. *Applied Geophysics,* 32. 11-32.

Coker, J.O.; Mustapha, A.O.; Makinde, V. & Adesodun, K. (2013). Application of Radiometric Surveys to Delineate between Sedimentary Terrain and Basement Complex: A case study of Sagamu and Abeokuta, South Western Nigeria, *Journal of Natural Sciences Research* www.iiste.org, 3(13), 13-17. ISSN 2224-3186 (Paper) ISSN 2225-0921 (Online).

Cook, S.E.; Corner, R.J.; Groves, P.R. & Grealish, G.J. (1996). Use of Airborne Gamma-Radiometric Data for soil mapping. *Aust. J. Soil Res., 34, 183–194.*

Corti, G.; Bonini, M.; Conticelli, S.; Innocent, F.; Manetti, P. & Sokoutis, D. (2003). Analogue Modellling of Continental Extension: A review focused on the relations between the patterns of deformation and the presence of magma. *Earth Sci. Rev.*, 63, 169-247.

Coward, M.P; Dewey, J.F. & Hancock, P.L.(1987). Continental Extensional Tectonics. *Geological Societyof London Special Publication,* 28, 637.

Cratchley, L.R. & Jones, C.P.(1965). An interpretation of the geology and gravity anomalies of the Benue Valley, Nigeria. Overseas geological surveys, *Institute of Geol. Sciences, London Geophysics,* 1-26.

Day-Stirrat, R. J.;Hiller, S.; Nikitin, A.; Hofmann, R.; Mahood, R. & Mertens, G. (2021). Natural Gamma-ray spectroscopy (NGS) as a proxy for distribution of clay minerals and bitumen in the Cretaceous McMurray Formation, Alberta, Canada. *Science Direct:Fuel, 288, 119513.*

De Swardt, A.M.J. (1964). Laterization and Landscape Development in Parts of Equatorial Africa. *Zeitsch.f. Geomorphologie* NF8, 313-333.

Dickin, A.P. (2005). Radiogenic Isotope Geology. Publisher: Cambridge University Press ISBN: 9780521823166. DOI: 10.1017/CB09781139165150.

Dickson, B.L & Scott, K.M. (1997). Interpretation of Aerial Gamma-Ray Surveys, Adding the Geochemical Factors. *Journal of Australian Geology and Geophysics,* 17, 187-200.

Dobrin, M. & Savit, C. (1988). Introduction to Geophysical Prospecting, McGraw Hill, 4th edn.

Drury, S.A. (1986). Remote sensing of geological structure *in* European agricultural terrain, *Geol. Mag.*, 123, 113-121.

Drury, S.A. (1993). Image interpretation in Geology. Second Edition, Allen and Unwin, London.

Duval, J.S. (1983). Composite colour images of aerial gammar ray spectrometric data, *Geophysics*, v.48, pp.722-735.

Egbelehulu, P.; Mallam, A.; Abdulsalam, N. & Adewumi, T. (2021). A Review of Electrical Methods as a Worthy Tool for Mineral Exploration, *Sciendo,* 97-100, DOI: htttps://doi.org/10.2478/pjg-2020-0011.

Egboka, B.C. & Uma, K.O. (1986). Hydrochemistry, contaminant transport and tectonic effects in the Uburu-Okposi salt lake area of Imo State*, Nigeria. Hydrol. Sci. Journ.,* 31(2), 205-221.

Egeh, E.U.; Ekwuemeka, B.N. & Akpeke, B.G. (2004). The appraisal of a proposed proposed barite quarry in Akpet area, Cross River State from resistivity investigation*, Global Journal of Geological Science,* 2(2), 171-175.

Ehirim, C.N.; Ebeniro, J.O. & Ofoegbu, C.O. (2016). Baryte mineral exploration in parts of Lower Benue Trough, Nigeria. *International Journal of Physical Sciences*, 11(21), 279-286.

Ekwok, S.E.; Akpan, A.E.; Ebong, E.D. & Eze, O.E. (2021). Assessment of depth to magnetic sources using high resolution aeromagnetic data of some parts of the Lower Benue Trough and adjoining areas, Southeast Nigeria. *Advances in Space Research*, 67(7), 2104-2119.

Ekwueme, B.N. & Akpeke, G.B. (2012). Occurrence and distribution of barite mineralization in Cross River State, southeastern Nigeria, *Global Journal of Geological Sciences*, 10(1), 85- 98.

Eldosouky,A.M.; Pour, A.B.; Hamed,A.; Taha, A.; Gamal, M.; Mahmoud, A. & Pham. L.T. (2021). Utilization of Landsat-8 Imagery and Aeromagnetic Data for Deciphering Alteration Zones and Structures: Implications for Mineral Exploration in the Southeastern Desert of Egypt, *Frontiers in Scientific Research and Technology,* 2, 19-28.

Elkhateeb, O.S.; Abdellatif, M.A.G. & Elkhateeb, O. S. (2018). Delineation potential gold mineralization zones in a part of Central Eastern Desert, Egypt using Airborne Magnetic and Radiometric data. *NRIAG Journal of Astronomy and Geophysics*, https://doi.org/10.1016/j.nrjag.2018.05.010.

Elliot, J.E. (1982). Model for contact metasomatic tungsten/copper/ gold deposits, In Erickson, R.L., ed., Chararacteristics of mineral deposit occurrences: US Geological Survey Open-File Report, 82-795, 248.

El-Qady, G. 2006. Exploration of a geothermal reservoir using geoelectrical resistivity inversion; case study of Hammam Mousa, Sinai, Egypt. *J. Geophysics. Eng*. 3, 114 – 121 doi. 10.1088/1742–2132/3/2/002.

Encarta, Microsoft archived from *The Original.* (2009).

ENVI® and IDL ®. ITT Coorporation: Harris Geospatial, Registered in the United States Patent and Trademark Office. ION^{TM}, ION Script^{TM}, ION Java^{TM} and ENVI Zoom^{TM}.

Etim, O. N.; Louis, P. & Maurin, J. C. (1988). Interpretation of electrical soundings on the Abakaliki Lead-Zinc and barite prospects, S.E. Nigeria: Geological and genetic implications. *Journal of African Earth Sciences*, 7, 743-747.

Ezepue, M.C. (1981). Lead-Zinc mineralization at Ishiagu, Eastern Nigeria. *Trans. Inst. Min. Metall.* (abstract), 90, B87.

Eze, M.O.; Mamah, L.I.; Madu, A.J.C. & Onuba, L. (2017). Geological and Structural Interpretation of Possible Mineralization Zones of part of Anambra Basin and Southern Benue Trough Using

Airborne Geophysical Data. *International Journal of Research in Engineering and Applied Sciences (IJREAS)*, 7(5), 70-80.

Ezepue, M.C. (1984). The Geologic Setting of Lead-Zinc Deposits at Ishiagu, Southeastern, Nigeria. *Journal of African Earth Sciences*, 2(2), 97-101.

Falade, M.O (2016). A Profile of Nigeria's Solid Minerals. Overview of Minerals in Nigeria. In: Report of the Vision 2020, National Technical Working Group on MINERALS AND METALS DEVELOPMENT,2009.In:http://en.wikipedia.org/wiki/Mining_industry_ofNigeria. (Accessed October, 2018).

Farrington, J.L. (1952). A preliminary description of the Nigerian Lead-Zinc field. *Econ. Geol*., 583-608.

Fatoye, F.B & Gideon, Y.B. (2013). *Africa Geosciences Review, 20(1), 35 – 42.*

Fatoye, F.B.; Ibitomi, M.A. & Omada, J.I. (2014). Lead-Zinc-Barytes mineralization in the Benue Trough, Nigeria: Their geology, occurrences and economic prospective. *Advances in Applied Science Research*, 5(2), 86-92.

Faure, G. & Mensing, T.M.(2005). Isotope Principle and Applications, 3rd Edition , John Wiley and Sons, Hoboken.

Ford, S.O. (1981). The Economic Mineral Resources of the Benue Trough. *Earth Evolution Sciences.*, 1, 154-163.

Franto, Pramumijoyo, S. & Setijadji, L.G.(2021). Alteration mineral mapping to identify primary tin potential using Landsat 8 images and geographic information system in Rimba Kulit Area, Southern Bangka Island, *IOP Conf. Ser.: Earth Environ. Sci.,* 212 012021.

Frutuoso, Rui, Lima, A.; Teodoro, A.C. (2021). Application of remote sensing data in gold exploration:targeting hydrothermal alteration using Landsat 8 imagery in Northern Portugal. *Arabian Journal of Sciences,* 14, 459.

FUGROAirborne Surveys (2007). All Airborne Geophysical Data Acquired in the Part II Survey.

Gao, X.; Xiong, S.; Yu, C.; Zhang, D. and Wu, C. (2021). The Estimation of Magnetite Prospective Resources Based on Aeromagnetic Data: A Case Study of Qihe Area, Shandong Province, China. *Remote Sens.,* 2021, 13, 1216. https://doi.org/10.3390/rs13061216.

Gao, J. (2009). Digital Analysis of Remotely Sensed Imagery. The McGraw Hill Companies, Inc., ISBN: 9780071604659.

Georgsson, L. S. (2009). Geophysical methods used in geothermal exploration. Presented at Short Course IV on *Exploration for Geothermal Resources*, organized by UNU-GTP, KenGen and GDC, at Lake Naivasha, Kenya, November 1–22.

Georgsson, L.S. 2013. Geophysical methods used in geothermal exploration. Paper presented at Short Course VIII on Exploration for Geothermal Resource. Organised by (UNU – GTP, GDC and KenGen, at Lake Bogoria and Lake Naivasha, Kenya. Oct. 31 – Nov. 22, 2013.

Geosoft Oasis Montaj, Oasis Montaj How-to-Guide (2010).

Ghoneim, S.M.; El Nabi,A. S.H.; Yehia, S.A.& Salem, S.M. (2021).Using airborne gamma ray spectrometry and remote sensing data for detecting alteration zones around Wadi Saqia area, Central Eastern Desert, Egypt. *Journal of African Earth Sciences,*178, 104181. https://doi.org/10.1016/j.afrearsci.2021.104181.

Githenya, L.K.; Mathu, E.M.; Kariuki, P.C. & Waita, J. (2021). Integration of Remote Sensing and Geological Mapping for Economic Mineralization Mapping in Mwitika-Makongo Area, Kitui County. *J Remote Sens GIS.,* 10(2), 281.

Glatzmaier, G. A. & Roberts, P.H. (1995). "A three-dimensional self-consistent computer simulation of a geomagnetic field reversal", *Nature,* 377 (6546), 203-209.

Goetz, A.F.H. & Rowan, L.C. (1981). *Geologic remote sensing science,* 211, 781-791.

Graham, D.F. & Bonham-Carter, G.F. (1993). Airborne Radiometric Data: A Tool for Reconnaissance Geological Mapping using a GIS. *Photogrammetric Engineering and Remote Sensing.*, 58, 1243-1249.

Grant, F.K. (1971). South Atlantic, Benue Trough and Gulf of Guinea Cretaceous Triple Junction. *Geological Society American Bulletin,* 82, 2295-2298.

Grasty, R.L. & Shives, R.B.K. (1997). Applications of Gamma Ray Spectrometry to Mineral Exploration and Geological Mapping, Workshop presented at Exploration 97: Fourth Decennial Conference on Mineral Exploration.

Grauch, V.J.S.; Hudson, M.R.; Minor, S.A. & Caine, J.S. (2006). Sources of Along Strike Variations in Anomalies Related Intrasedimentary Faults: A Case Study from the Rio Grande Rift, USA: *Exploration Geophysics,* 37, 372-378.

Gunn, P.J.(1997). Application of Aeromagnetic Survey to Sedimentary Basin Studies. AGSO. *Journal of Australian Geology and Geophysics*, 17(2), 133-144.

Gunn, P.J & Chisholm, J. (1984).Non-conductive volcanogenic massive sulphide mineralization in the Phiara area of Western Australia. Exploration Geophysics, 15, 143-153. https://doi.org/10.1071/EG984143.

Gunn PJ, & Dentith M.E. (1997). Magnetic responses associated with mineral deposits. AGSO *Journal of Australian Geology & Geophysics*, 17(2), 145-158.

Guo, C.; Sun, Y.; Jia, Q.; Jiang, Z.; Jiang, D.; Wang, G.; Xu, Y.; Wang, T.; Tian,J. & Wu, Z.N.(2009). Wide Spectrum Responsivity Detectors from Visible to Mid -Infrared based on Antimonide. *Infrared Physics & Technology*, 96, 1-6.

Haruna, I.V, (2017). Lithologic Features and Uranium Possibilities of the Granites of Pupule, Adamawa Massif, N.E.Nigeria. *Global Journal of Geological Sciences*, 15(57-64).

Holmberg, H.; Naess, E & Evensen, J.E. (2012). Thermal modeling in the Oslo rift Norway. Proceedings of the 37th workshop on Geothermal Reservoir Engineering Stanford University, Stanford California, January 30-February 1, 2012.

Hoover, H.C. & Hoover LH. Georgius Agricola *De Re Metallica* translated from the first Latin edition of 1556. New York: Dover, 1912; reprinted 1950.

Hoover, D.B.; Klein, D.P. &Campell, D.C. (1995). Geophysical methods in exploration and mineral environmental investigations. In: Edward, A. Ed.) Preliminary compilation of descriptive geoenvironmental mineral deposit models, *US Department of the Interior, US Geological Survey, Open-file Report*, 95-831, 19-.23.

IAEA. (1991). Airborne gamma ray spectrometer survey-ing, International Atomic Energy Agency, *Technical Report Series*, 323.

IAEA. (2003). Guidelines for Radioelement Mapping using Gammar Ray Spectometry Data. *International Atomic Energy Agency.*

IAEA. (2007). International Atomic Energy Agency. Safety Glossary, Terminology used in Nuclear Safety and Radiation Protection-2007 Edition.

IEA. (2019). Global solar PV market set for spectacular growth over next 5 years. Press Release.

Ibraheem, I.M; Haggag, M. & Tezkan, B. (2019).Edge Detectors as Structural Imaging Tools UsingAeromagnetic Data: A Case Study of Sohag Area, *Egypt.Geosciences*, 9,211, doi:10.3390/geosciences 9050211.

Ijeh, B.I.; Anyadiegwu, F.C. & Okeiyi, D.C. (2018). Interpretation of Airborne Magnetic Data Over Afikpo and Environs. *IOSR Journal of Applied Geology and Geophysics* (IOSR-JAGG), 6(3), 51-60.

Ikeh, J.C.; Ugwu, G.Z & Asielue, K. (2017). Spectral depth analysis for determining depth to basement of magnetic source rocks over Nkalagu and Igumale areas of the Lower Benue Trough, Nigeria. *International Journal of Physical Sciences,* 12(19), 224-234.DOI: 10.5897/IJPS2017.4668.

Illies, J.H. (1981). Graben Formation-the Maltese islands –a case history, In: J.H. Illies (Editor), Mechanism of graben formation. *Tectonophysics,* 73: 151-168.

Imam, E. (2019). Remote Sensing Platforms and Sensors. *Remote Sensing and GIS, Pathshala,* RS & GIS VI. https://www.researchgate.net/publication/330212930.

Imbroane, M.A.; Melenti, C & Gorgan, D. (2007). Mineral Explorations by Landsat Image Ratios. Conference: Proceedings of the North International Symposium on Symbolic and Numeric Algorithms for Scientific Computing, SYNASC 2007, Timisoara, Romania. September 26-29.

Ishola, K.S.; Oluwaseyi, P.; Akerele, O. & Adeogun, Y. (2020). Application of aeromagnetic data to map subsurface structural features in Ewekoro, southwestern Nigeria, *Springer Links: Modelling Earth Systems and Environment,* 6, 2291-2302.

Jain, S. (1988). Total Magnetic Field Reduction-The Pole or Equator?: A Model Study. *Canadian Journal of Exploration Geophysics,* 24(2), 185-192.

Jaques, A.L.; Wellman, P.; Whitaker, A.& Wyborn, D. (1997). High Resolution Geophysics in Modern Geological Mapping. *AGSO Journal of Australian Geology & Geophysics*, 17, 159-174.

Jhabvala, M.; Choi, K.; Waczynski, A. & Arun, N.la (2011). Performance of the QWIP focal plane arrays for NASA's Landsat Data Continuity Mission . *Proceedings of SPIE-The International Society for Optical Engineering.* DOI:10.1117/12.886.

Joseph, G. (1996). Imaging Sensors for Remote Sensing, *Remote Sensing Reviews*, 13, 257-342.

Kana, J.D.; Djongyang, N.; Raidandi, D.; Nouck,P.N. & Dadje, A. 2015. A review of geophysical methods for geothermal exploration. *Renewable and Sustainable E n e r g y R e v i e w s* , 4 4 , 8 7 - 9 5 . http://dx.doi.org/10.1016/j.rser.2014.12.026.

Kaura, M.A & Mohammad, M.A. (2017). Geophysical Study of Brine Deposits Using Electrical Resistivity Technique in Awe, Awe Local Government Area of Nasarawa State in Nigeria, Pdfs. Semanticscholar.org.

Keary, P.; Brooks, M. & Hill, I. (2002). An Introduction to Exploration, 3rd Edition. Blackwell Science, 2002, ISBN0632049294.

Keen, C.E.; Stockmal, G.S.; Welsink, H & Mudford, B. (1987). Deep Custal Structure and Evolution of the Rifted Margin Northeast of Newfoundland: results from LITHOPROBE East, *Can J. Earth Sci*, 24, 1537-1549.

Keller, G.V. & FrischKnecht, F.C. (1966). Electrical Methods in Geophysical Prospecting. First Edition. Pergamon Press, London, pp.519.

Kendall, A.C. (1984). Evaporites. In: Walker, R.G (ed.). Facies models: Geoscience Reprint Series 1, New foundland, Canada, *Geological Association of Canada,* 259-296.

Khain, V.Yu. (1992). The role of rifting in the evolution of the Earth's Crust. In: P.A.Ziegler(Ed.). Geodynamics of Rifting, vol.III. Thematic Discussions, *Tectonophysics,* 215,1-7.

Kumar, P.L.K.K.; Veeraswamy, G.; Raghubabu, K. & Balaji, E. (2020). Geochemical characteristics of iron ore deposits and processing of Landsat-8 data (geology, geomorphology and lineaments) in semi-arid region and using geospatial techniques. *Modeling Earth Systems and Environment*, ISSN 2363-6203, 6(2), 1245-1252, DOI 10.1007/s40808-020-00754-5.

Landsat 8 United State Geological Survey (USGS) (2015). Landsat Missions Factsheet: https://pubs.usgs.gov/fs/2015/3081/fs20153081.pdf.

Ladipo, K.O.(1998). Paleogeography, sedimentation and tectonics of the upper cretaceous and tectonics of the upper cretaceous Anambra basin, Sotheastern Nigeria. *Journal of African Earth Sciences* 7, 865-871.

Lawal, T.O.; Sunday, J.; Fawale, K.; Salami. M & Adewumi, T. (2021). Use of Magnetic anomaly data to delineate subsurface structures and depth characterization of Lafiagi and its environs, Northcentral Nigeria, *NRIAG Journal of Astronomy and Geophysics,* 10(1), 157-169, DOI: 10.1080/20909977.2021.1900526.

Lawal, T.O.; Omar, D.M.; Salami, M.K.; Adewumi,T.; Sunday, J.A. & Fawale, O. (2021). Detection of Concealed Mineral Deposits using Magnetic Data in parts of Osun State and its Environs, Southwestern Nigeria. 64th International Conference on Science and Sustainable Development (ICSSD 2020), IOP Conf. Series: *Earth and Environmental Science,* 655, doi:10.1088/1755-1315/655/1/012074.

Leborgne, R.; Rivett, M.O.; Wanangwa, G.J.; Sentenac, P. & Kalin, R.M.(2021). True 2-D Resistivity Imaging from Vertical Electrical Soundings, to Support More Sustainable Rural Water Supply Borehole Siting in Malawi. *Appl. Sci.,* 11, 1162. https://doi.org/10.3390/app11031162.

Leilesand, T.M & Keifer, R. (1993). Remote sensing and image imterpretation, third edition, John Villey, New York.

Lo, B.H. & Pitcher, D.H.(1996). A case history on the use of regional aeromagnetic and radiometric data sets for lode gold exploration in Ghana. *Annual meeting expanded abstracts, Society of Exploration Geophysicists*, 592-595.

Lovering, T.S & Goode, H.D. (1963). Measuring geothermal gradients in drill holes less than 60 feet Deep East Tintic District, Utah Washington: United States Government Printing Office.

Lowrie, W. (2007). Fundamentals of Geophysics. Cambridge: Cambridge University Press, New York.1st, edition.

Luaano,L.; Horacio, E.; Mario, T.;Marta, A. & Ricardo,E.(2012).Geoelectric explorationof the Purisima-Kumicruze district, Jukay Province, Argentina. *International Journal of Geophysics*, 2012: 1-12.

Maden, N., 2010. Curie-point depth from spectral analysis of magnetic data in Erciyes stratovolcano (Central TURKEY). *Pure Appl. Geophys.* 167, 349–358.

Magill, J. & Galy, J. (2005). Archaeology and Dating. Radioactivity Radionuclides Radiation. *Springer Berlin Heidelberg*, 105-115, doi:10.1007/3-540-26881-2-6. ISBN 978-3-540-26881-9.

Manea, M., & Manea, V. C. (2011). Curie point depth estimates and correlation with subduction in Mexico. Pure and Applied Geophysics, 168, 1489. https://doi.org/10.1007/s00024-010- 0238-2.

Mbah, V.O.; Onwuemesi, A.G.; Aniwetalu & Emmanuel, U. (2015). Exploration of Lead-Zinc (Pb-Zn) Mineralization Using Very Low Frequency Electromagnetic (VLF-EM) in Ishiagu, Ebonyi State. *Journal of Geology & Geophysics.*, 4(4).1000214, DOI:10.4172/2329-6755.1000214, ISSN: 2329-6755 JGG.

McBratney, A.B.; Mendoça, S. & Minasny, M.L. (2003). On Digital Soil Mapping. *Geoderma*, 117, 3-52.

McCay, A.T.; Harley, T.L.; Younger, P.L.; Sanderson, D.C. W. & Cresswell, A.J. (2014). Gammar-ray Spectometry in Geothermal Exploration: State of the Art Techniques. *Energies*, 7(8), 4757-4780. https://doi.org/10.3390/en7084757.

McGinn, A. & Schneer, K. (2019). Fact Sheets: Jobs in Renewable Energy, Energy Efficiency and Resilience. Environmental and Energy Study Institute. Ideas. Insights. Sustainable Solutions. amcginn@eesi.org.

Merti, P.J. (1970). Structural Geology of the Cenozoic Niger Delta. African Geology, *Proceedings of Ibadan conference on African Geology,* Ibadan, Nigeria.

Mia, B. & Fujimitsu, Y. (2012). Mapping hydrothermal altered mineral deposits using Landsat 7 ETM+ image in and around Kuju volcano, Kyushu, Japan. *Journal of Earth System Science,* 121, 1049-1057.

Milsom J. (2003). Field Geophysics: The geological field guide series, John Milsom University College, Lon-don. Published by John Wiley and Sons Ltd. Third edition, 51-70.

Mirianrita, N.; Obiora, D.N.; Ossai & Okwoli, E. (2015). A Case Study of Aeromagnetic Data Interpretation of Nsukka area, Enugu State, Nigeria, for hydrocarbon exploration. *International Journal of Physical Sciences, 10(17), 503-519.*

Mohamed, M.T.A.; Al- Naimi, L.S.; Mgbeojedo, T.I. & Agoha, C.C.(2021). Geological mapping and mineral prospectivity using remote sensing and GIS in parts of Hamissana, Northeast Sudan. *Journal of Petroleum Exploration and Production*, 11, 1123–1138, https://doi.org/10.1007/s13202-021-01115-3.

Morgan, P. & Baker, B.H.(eds)(1983a). Process of continental rifting. *Tectonophysics* Spec Issue 94:680.

Morgan, P. & Baker, B.H.(1983b). Introduction-Processes of continental rifting. *Tectonophysics* 94:1-10.

Murat, R.C. (1972). Stratigraphy and palaeography of the Cretaceous and Lower Tertiary in Southern Nigeria. *In: T.F.J Dessauvagie and A.J. Whiteman (Eds.),* African Geology, University of Ibadan, Nigeria, 251-266.

Nabighian, M.N.; Grauch, V.J.S.; Hansen, R.O.; LaFehr, T.R.; Li, Y.; Peirce, J.W.; Philips, J.D. & Ruder, M.E. (2005). The historical development of the magnetic method in exploration; *Geophysics,* 70, 33-61.

Nash, C.R., Boshier, P.R., Coupard, M.M., Theron, A.C. & Wilson, T.G. (1980). Photogeology and satellite image interpretation in mineral exploration. *Mineral Science Eng*.,12,.216- 244.

Ndougsa-Mbarga, T.; Meying, A.; Bisso, D.; Sharma, K.K., Layu, D.Y. & Manguella-Dicoum, E.(2011). Audiomagnetotelluric (AMT) Soundings Based on the Bostick and Evidence of Tectonic Features along Northern Edgeof the Congo Craton, In the Messamena/Abong Mbang. *J. Ind. Geophys. Union,* 15(3), 145-159.

Nelson, S. A. (2015). Streams and Drainage Systems, Physical Geology, EENS 111.

Neugebauer, H.J. (1983). Mechanical Aspects of Continental Rifting. *Tectonophysics,* 94(1-4),91-108.

Neumann, E.R. & Ramberg, I.B. (eds.) (1978). Petrology and Geochemistry of Continental rifts. Proc NATO Adv Stud Inst Reidel, Dordrecht, 296.

Nigerian Geological Survey Agency (2010). Digitized Map of the Geology of Lower Sedimentary Basin from Geologic Map of Nigeria.

Nwachukwu, S.O. (1972). The tectonic evolution of the southern portion of the Benue Trough, Nigeria, *Geological Magazine,* 109, 411-419.

Nwachukwu, S. O. (1974). Temperatures of formation of vein minerals in the southern portion of the Benue Trough, Nigeria. *J Mining Geol*., 11, 45-54.

Nwajide, C.S. (2013). Sequence Stratigraphy of the Lower Benue Trough in Geology of Nigeria's Sedimentary basin. Published by CSS Bookshop limited. pp.287.

Nwegbu, A. (2014). Uranium Exploration in Nigeria: Nigerian Geological Survey Agency.

Nwobodo, A.N.; Ikeri, H.I. & Chikeleze, P.C. (2020). Geological Studies on Uranium, Thorium, Potassium Based On Airborne Radiometric Geophysical Data of Wukari And Donga Middle Benue Trough Nigeria. *The International Journal of Engineering and Science*, 9(6), 34-41, ISSN(e): 2319-1813 ISSN (p): 20-24-1805 DOI:10.9790/1813-0906013441.

Obaje, N.G. (2009). Geology and Mineral Resources of Nigeria. Springer Dordrecht Heidelberg London New York, 2009.

Obande, G. E., Lawal, K. M., & Ahmed, L. A. (2014). Spectral analysis of aeromagnetic data for geothermal investigation ofWikki Warm Spring, north-east Nigeria. *Geothermics*, 50, 85–90.

Obi, A.A; Ekwueme, B.N & Akpeke, G.B (2014). Reserve estimation of barite deposits using geologicaland geophysical investigation, in Cross River, Southeastern Nigeria, *Journal of Environmental Earth Science,* 4(10): 16-31.

Obi, D. A.; Okereke C. S.; Obei B. C. & George A. M. (2009). Aeromagnetic Modeling of Subsurface Intrusives and its Implication on Hydrocarbon Evaluation of the Lower Benue Trough, Nigeria. *European Journal of Scientific Research*, 47(3), 347 -361.

Obiora, S. C., & Charan, S. N. (2010). Tectonomagmatic origin of some volcanic and sub-volcanic rocks from the Lower Benue rift. Nigeria. *Journal African Earth Sciences.,* 58, 197–210.

Odoh, B,; Utom, A.U. & Obini, N.S. (2012). Groundwater Prospecting In Fractured Shale Aquifer Using an Integrated Suite of Geophysical Methods: A Case History from Presbytaerian Church, Kpiri-Kpiri, Ebonyi State, Southeastern Nigeria. *Journal of Geosciences,* 2(4): 60-65: DOI: 10.5923/j.geo.20120204.01.

Odoma, A.N.; Obaje, N.G.; Omada, J.I.; Idakwo, S.O. & Erbacher, J. (2013). Paleoclimate Reconstruction During Mamu Formation (Cretaceous) Based on Clay Mineral Distributions. IOSR *Journal of Applied Geology and Geophysics* (IOSR-JAGG) e-ISSN: 2321–0990, p-ISSN: 2321–0982.1(5), 40-46.

Ogundipe, I.E. & Obasi, R.A. (2016). Geology and mineralization in the Albian sediments of the Benue Trough, Nigeria. *British Journal of Earth Sciences Research. 4(3), 1-15.*

Ofoegbu, C.O. (1984). Interpretation of Magnetic Anomalies over the Lower and Middle Benue Trough of Nigeria, *Geophysical Journal Royal Astronomical Society,* 79, 813-823.

Ofoegbu, C. O. (1985). Interpretation of an aeromagnetic profile across the Benue Trough of Nigeria. *Journal of African Earth Science,* 3, 293 – 296.

Ofoegbu, C. O. (1988). An Aeromagnetic Study of Part of the Upper Benue Trough, Nigeria. *Journal of African. Earth Science*, 7, 77- 90.

Ogundipe, I.E. & Obasi, R.A. (2016). Geology and mineralization in the Albian sediments of the Benue Trough, Nigeria. *British Journal of Earth Sciences Research. 4(3), 1-15.*

Oha, I.A.; Onuoha, K.M.; Nwegbu, A.N. & Abba, A.U. (2016). Interpretation of High Resolution Aeromagnetic Data over Southern Benue Trough, South Eastern Nigeria. *J. Earth Syst. Sci., 125(2),* 369–385.

Oha, I.A.; Onuoha, K.M. & Dada, S.S. (2017). Contrasting styles of lead-zinc-barium mineralization in the Lower Benue Trough, Southeastern Nigeria, *J. Earth Syst. Sci., 21(1),* 7–16.

Okafor, E.G. & Uwadiale, G.G.O.O. (1997). Process mineralogy of the Ishiagu lead-zinc deposit, Nigeria. *Mining, Metallurgy & Exploration,* 14, 45-48.

Okeke, C. J.; Ukaegbu, V. U. & Egesi, N. (2019). Remote sensing signature of geological structures inferred on landsat imagery of Afikpo area Southeastern Nigeria, *Journal of Geology and Mining Research,* 11(1),1-13, DOI: 10.5897/JGMR2018.0305, C249FDC59935, ISSN: 2006-9766.

Okeke, F.I.; Ibrahim, A.A. & Echeonwu, E.C. (2020). Application of Remote Sensing and Machine Learning Methods for Coal Seam Distribution Mapping at Lower Benue Trough, *Journal of Research in Environmental and Earth Sciences,* 6(6), 42-56, ISSN(Online):2348-2532.

Okereke, C.N.; Onu, N.N.; Ibe, K.K.; Selemo, A.O.I.; Opara, A.I.; Ikoro, D.O.; Ibeneme, S.I. & Oha, I.A. (2012). Analysis of Landsat and Aeromagnetic Data for Mapping of Linear Structures: A

Case Study of Yola Area, Upper Benue Trough, Nigeria. *International Journal of Engineering Research and Application*, 2(3), 1968-1977.

Okiyi, I.M.; Olorunfemi, M.O.; Ojo, J.S,., Akintorinwa, O.J. & Bayode, S. (2015). Geoelecrtic Investigation of a Site for a Proposed Airport in Ebonyi State, Southeastern, Nigeria. Unpublished M.Sc Thesis.

Okonkwo, A.C & Ezeh, C.C. (2012). A Ground Integrated Geophysical Exploration for Sulphide Ore Deposits. Case Study: EPL A40 Mine Field, Lower Benue Trough, Nigeria. International Research, *Journal of Geology and Mining (IRJGM),* 2(8), 214-221.

Okoyeh, E.I.; Akpan, A.E.; Egboka, B.C.E; Okolo, M.C. & Okeke, H.C (2015). Geophysical Delineation of Sub-surface Fracture Associated with Olposi-Uburu Salt Lake, Southeastern Nigeria.*International Research Journal of Environmental Sciences,* 4(2), 1-6.

Okpoli, C.C.(2019). Delineation of high resolution aeromagnetic survey of Lower Benue Trough for lineaments and mineralization: Case study of Abakaliki sheet 303. *Malaysian Journal of Geosciences* 3(1): pp.51 – pp.60. ISSN: 2521-0920.

Okubo, Y., Graf, R.J., Hansen, R.O., Ogawa, K. &Tsu, H. (1985). Curie point depths of the island of Kyushu and surrounding areas, Japan. *Geophysics* 50, 481–494.

Olade, M.A. (1976). On the genesis of lead-zinc deposits in Nigeria's Benue rift (aulacogen); A re-interpretation. *Nig. Journ. Min. Geol*.,13, 20-27.

Olade, M.A. (1978) Early Cretaceous Basaltic volcanism and initial continental rifting in Benue trough. *Nature Phy. Sci.*, 27 (3), 458-459.

Olade, M.A & Morton, R.D. (1980). Temperature of Ore Formation and Origin of the Ishiagu Lead-Zinc Deposit, Southern Benue Trough. *Nigeria Jour. Min. Geol*., 17, 19-127.

Olade, M.A & Morton, R.D. (1985). Origin of lead-zinc mineralization in the Southern Benue Trough, Nigeria: Fluid Inclusion and Trace element studies. *Mineralum Deposita*,20, 76- 80.

O'Leary, D.W; Friedman, J.D and Pohn, H.A. (1976). Lineaments, Linear, Lineations: Some proposed new standards for old terms. *Geol. Soc. Am. Bull.* 89, 1463-1469.

Ologun, J.A.A. (2004). Geological Mapping of Parts of Jos Plateau Using Nigeria Sat1-Image. NARSDA News. pp. 35-37.

Olorunfemi (2014). Electricals and Electromagnetics. Resistivity and Induced Polarization Techniques. Obafemi Awolowo University, Ile-Ife, Osun State, Unpublished.

Olorunsola, K. & Aigbogun, C. (2017). Assessment of aero-radiometric data of Southern Anambra Basin for the Prospect of Radiogenic Heat Production. *Journal of Applied Science Environmental Management*, 21(4), 743-748, JASEM ISSN 1119-8362.

Olorunsola, K. & Aigbogun, C. (2017). Correlation and Mapping of Geothermal and Radioactive Heat Production from the Anambra Basin, Nigeria. *African Journal of Environmental Science and Technology*,10,517-531.

Olowofela, J.A; Ajani, O.O & Oladunjoye, M.A. (2007). Application of Induced Polarization Method to Delineate Sulphide Ore Deposits in Oshina Area of Benue State, Nigeria. *Ife Journal of Science.* 10(1), 137-145.

Olugbenga, A.F.(2009). Preliminary Investigationof Some Radiometric Anomalies at Kufena Ring Complex, Zaria, Kaduna State, Using Gammar Scintillometer. *The Pacific Journal of Science and Technology,* 10(1).591-601.

Omada, J.I. & Echefu, C.I. (1996). On the Economic Appraisal and Genesis of the Barite Mineralization and Saline Springs in the Middle Benue Trough, Nigeria. *Journal of Mineralogy, Petrology and Economic Geology*, 91(3), 109-115.

Onu, F.K (2017). The Southern Benue Trough and Anambra Basin, South Eastern Nigeria: A Stratigraphic Review. *Journal of Geography, Environment and Earth Science International*, 12(2), 1-16, Article no. JGEESI.30416. ISSN:2454-7352.

Onuba, L.N.; Anudu, G.K.; Chiaghanam, O.I. & Anakwuba, E.K. (2011). Evaluation of Aeromagnetic Anomalies Over Okigwe Area, Southeastern Nigeria. *Research Journal of Environmental and Earth Sciences*, 3(5), 498-507.

Onuba, L.N.; Onwuemesi, A.G.; Egboka, B.C.; Anudu, G.K. & Omali, A. (2013). A Review of Hydrocarbon Prospects in the Lower Benue Trough, Nigeria: Another Insight from Potential Field Study. *Search and Discovery Article,* 20194.

Onuoha, K. M., & Ekine, A. S. (1999). Subsurface temperature variation and heat flow in the Anambra Basin, Nigeria. *Journal of African Earth Sciences,* 28(3), 641–652.

Onwubuariri, C.N ; Mgbeojedo, T.I.; Al-Naimi, L.S. & Agoha, C.C.(2018). Analyzing Neo-Tectonic Effects on Gully Development Within Orlu and Environs, Southeastern Nigeria from Landsat Imagery and Azimuthal Sounding Data. *International Journal of Development Research,* 08(06), 21038-21045.

Onyedim, G. C.; Awoyemi, M. O.; Ariyibi, E. A. & Arubayi, J. B. (2006). Aeromagnetic imaging of the basement morphology in part of the Middle Benue Trough, Nigeria. *Journal of Mining And Geology*, 42 (2), 157-163.

Onyewuchi, R.A.; Opara, A.I.; Ahiarakwem, C.A. & Oko, F.U. (2012).Geological Interpretations Inferred from Airborne Magnetic and Landsat Data: Case Study of Nkalagu Area, Southeastern Nigeria. *International Journal of Science and Technology,* 2(4), 178-191.

Onyewuchi, R.A & Ugwu, S.A. (2016). Geological Interpretation of the High Resolution Aeromagnetic Data over Okigwe-Udi Area, Anambra Basin, Nigeria, Using 3-D Euler Deconvolution and 2-D Spectral Inversion Methods. *Journal of Geography, Environment and Earth Science International,* 10(1), 1-22.

Opara, A.I. (2011). Estimation of the depth to magnetic basement in parts of the Dahomey Basin, Southwestern Nigeria. *Australian Journal of Basin and Applied Sciences, 5(9), 335-343.*

Opara, A.I.; Ekwe, A.C.; Okereke, C.N.; Oha, I.A. & Nnosiri, O.P. (2012). Integrating airborne magnetic and Landsat data for geological interpretation over parts of Benin basin, Nigeria. *The Specific Journal of Science and Technology.* 556-571.

Opara, A.I.; Onyewuchi, R.A.; Onyekuru, S.O.; Okonkwo, A.C.; Nwosu, I.E.; Embarga, T.T.& Nosiri, O.P. (2014). Structural interpretation of the Afikpo sub-basin:evidences from airborne magnetic and Landsat ETM data. *Elixir Earth Science*. 71, 24546-24552.

Orajaka, S. (1965). Geology of Enyigba, Ameri and Ameka Lead Zinc Mines; *J. Geol.*, 3, 49–51.

Orajaka, S. (1972). Salt Water Resources of East Central State of Nigeria. *Nig. Journ. Min. Geol.*, 7, 35- 41.

Osinowo,O.O.; Gomy, A. & Isseini, M. (2021). Mapping hydrothermal alteration mineral deposits from Landsat 8 satellite data in Pala, Mayo Kebbi Region, Southwestern Chad, *Scientific African* 11 (2021) e00687, www.elsevier.com/locate/sciaf.

Ourhzif, Z.; Algouti, A.; Algouti, A.; Hadach, F. (2019). Lithological Mapping Using Landsat 8 OLI AND ASTER Multispectral Data In Imini-Ounilla District South High Atlas of Marrakech. *The International Archives of the Photogrammetry, Remote Sensing and Spatial Information Sciences,* Volume XLII-2/W13, 2019 ISPRS Geospatial Week 2019, 10–14 June 2019, Enschede, The Netherlands.

Palmason, G.(ed.).(1980). Continental and Oceanic rifts. *Am Geophys Un Geodyn* 8: 309.

Patnode, H.W. & Willie, MR.J.(1950). The Presence of Borehole Geophysics to Water Resource Investigation.of the USGS, Book2, Chapter E1.

Payamani, A.; Babaei, B, Dehghan, S. & Harouni, H.A. (2020).Applying various satellite image processing methods on Aster and LandsatETM+ data to identify and separate the alteration zones around gold mine of Akhtarchi, Khomein, Iran. *Revista Cientifica*, 33(2), 490-510.

PCI Geomatic (2015). Info @ PCI Geomatics.com.

Perry, J. (1895a). On the Age of the Earth: *Nature*, v.51, p.224-227.

Perry, J. (1895b). On the Age of the Earth: *Nature*, v.51, p.341-342.

Perry, J. (1895b). On the Age of the Earth: *Nature*, v.51, p.582-585.

Petters, S.W. (1978). Stratigraphic Evolution of the Benue Trough and Its Implications for the Upper Cretaceous Paleogeography of West Africa. The Journal of Geology. 86(3), 311–322. *Bibcode*:*1978JG.....86..311P*. *doi*:*10.1086/649693*. *JSTOR 30061985*.

Petters, S.W. (1978). Stratigraphic Evolution of the Benue Trough and Its Implications for the Upper Cretaceous Paleogeography of West Africa. The Journal of Geology. 86(3), 311–322. *Bibcode*:*1978JG.....86..311P*. *doi*:*10.1086/649693*. *JSTOR 30061985*.

Petters, S.W. (1982). Central West African Cretaceous-Tertiary benthic Foraminifera and stratigraphy. Paleontographica. Abt A 179, 1-104.

Petters, S.W. & Ekweozor, C.M. (1982). Origin of Mid Cretaceous Black Shales in the Benue Trough, Nigeria. Paleogeography, Paleoclimatology, Paleoecology, 40, 311-319.

Philips, J.D. (1998). Processing and Interpretation of aeromagnetic data for the Santa Cruz Basin-Patahonia Mountains Area, South-Central Arizona. US Geological Survey Ope File Report, Arizona, 02-98.

Pilkington, M &Bardossy, Z. (2015). DSIM3D: Software to perform unconstrained 3D inversion of magnetic data. Geological Survey of Canada, Open File 7749, 1.zipfile.doi:10.4095/295611.

Pour, A.B & Hashim, M. (2014). Hydrothermal Alteration Mapping from Landsat 8 Data, Sar Cheshmeh Copper Mining District, Southeastern Islamic Republic of Iran. *Journal of Taibah Uni. for Science,9,155-166.*

Prayudi, S.D.; Arrofi, D. & Ali, R.K. (2019). Identifying of geothermal manifestation existence and characterization of sulphidation type using Landsat-8 image processing results: Case study of Mount Papandayan area, Garut Regency, West Java Province. Proceedings: *The 7th Indonesia International Geothermal Convection and Exhibition (IIGCE).* Assembly Hall-Jakarta Convention Center Indonesia, August 13-15, 2019.

Prost, G.L. (2014). Remote Sensing for Geoscientists-Image Analysis and Integration, 3rd ed., CRC Press.

Rajesh (2004). Application of Remote Sensing and GIS in mineral resource mapping – An overview. Journal of mineralogical and petrological sciences. 99(3). DOI: 10.2465/jmps.99.83.

Ran, L.; Zhang, Y.; Wei, W. & Zhang, Q. (2017). A Hyperspectral Image Classification Framework with Spatial Pixel Pair Features. Sensors, 17(10), 2421.

Ravat, D.; Pignatelli, A.; Nicolosi, I. and Chiappini, M. (2007). A Study of spectral methods of estimating the depth to the bottom of magnetic sources from near surface magnetic anomaly data. Geophysical Journal International, 169(2): 421-434.

Reeves, C. (2005). Aeromagnetic Surveys: Principles, practice and Interpretation. Earth-Works, Washington DC, GEOSOFT 1-10.

Reford, S. (2010). Nigeria's Nationwide High Resolution Airborne Geophysical Surveys, 72nd EAGE Conference and Exhibition-Workshops and Fieldtrips, DOI:10.3997/2214-4609.20149924.

Reid, A. (2007). Semi-Automated Methods of Potential Field Interpretation- Innovations and Recent and Future Developments. EGM 2007 International Workshop, Innovation in EM, Grav and Mag. Methods: a new Perspective for Exploration. Capri, Italy.

Reijers, T. J. A. & Nwajide, C.S. (1998). Geology of the Southern Anambra Basin. Unpublished Report for Chevron Nigeria Limited. Field Course Note, pp.66.

Rekhibi, S., Wadi, M., & Said, A. (2015). Remote Sensing & GIS Techniques for Gold Exploration. In *International Conference on Advances in Science, Engineering, Technology and Natural Resources (ICASETNR-15) Aug. 27-28, 2015 Kota Kinabalu (Malaysia)*. International Institute of Chemical, Biological, EnvironmentalEngineering.https://doi.org/10.15242/IICBE.C081506.

Reynolds, R.L.; Rosenbaum, J.G.; Hudson, M.R. & Fishman, N.S. (1990). Rock magnetism, the distribution of magnetic minerals in the Earth's crust, and aeromagnetic anomalies. United State Geological Survey Bulletin,1924, 24-25.

Reynolds, J.M. (1997). An Introduction to Applied and Environmental Geophysics. Chichester: John Wiley and Sons, p.796.

Ridwan, M.A.; RAdzi, N.A.M . Ahmad, W.S.H.M.W.; Mustafa, I.S; Din, N.M.; Jalil, Y.E.; Isa, A.M; Othman, N.S &Zaki, W.M.D.W.(2019). Applications of Landsat 8 Data: A Survey Science Publishing Corporation, 7,438.

Riwayat, A.I.; Ahmad Nazri, M.A.& Abidin, M.H.Z. (2018). Application of Electrical Resistivity Method (ERM) in Groundwater Exploration. IOP Conf Series: Journal of Physics: Conf Series, 995(2018)012094, doi:1088/1742-6596/995/1/012094.

Robbins, E.I. (1983). Accumulation of fossil fuels and metallic minerals in active and ancient rifts. Tectonophys, 94, 633-658.

Robinson, E.S. and Coruh, C. (1988). Exploration Geophysics, John Wiley & Sons, New York, USA.

Rockwell, B.W., Gnesda, W.R., & Hofstra, A.H.(2021). Improved automated identification and mapping of iron sulfate minerals, other mineral groups, and vegetation using Landsat 8 Operational Land Imager data, San Juan Mountains, Colorado, and Four Corners Region: *U.S. Geological Survey Scientific Investigations Map*, 3466, 1 sheet, scale 1:325,000, 37. pamphlet, https://doi.org/ 10.3133/ sim3466.

Rowan, C.C. &Bowers, T.L. (1995). Analysis of linear features mapped in Landsat Thematic Mapper and side-looking airborne radar images of the Reno, Nevada 18 by 28 quadrangle, Nevada and California – Implications for mineral resources studies. *Photogramm. Eng. Remote Sensing*, Vol..61, 749-759.

Ruppel, C. (1995). Extensional Processes in Continental Lithosphere, *Journal of Geophysical Research,* 100 Part B.P.(24187-24215).

Ryan, Carbotte, Coplan, O' Hara, Melkonian, Arko, Weissel, Ferrini, Goodwillie, Nitsche, Bonczkowski & Zemsky (2009). Topographical Map of the Study Area. Multi-Resolution Topography Synthesis, *Geochem. Geophys. Geosyst*., 10, Q03014, doi: 10.1029/200).

Sajjad, M. & Mohammad, R.H. (2018). The Early Cretaceous Mansourabad Shale-Carbonate Hosted Zn-Pb-C-Ag Deposits, Central Iran: An example of vent proximal subsea floor replacement SEDEX mineralization. Ore Geology Reviews, 95, 20-39.

Sawkins, F.J. (1976). Massive Sulphide deposits in relation to geotectonics. *In: Strong, D.F (ed) Metallogeny and plate tectonics. Spec. Pap. Geol. Assoc. Can*. 14, 221.

Schowengerdt, R.A. (2007). Remote sensing: Models and methods for image processing (3rd ed.). Academic press. p.2. ISBN 978-0-12-3694007-2.

Shah, A.K.; Ryan, D; Taylor, Gregory, J.; Walsh & Phillips, J.D.(2021) Integrated geophysical imaging of rare earth element-bearing iron oxide-apatite deposits in the Eastern Adirondack Highlands, New York, *Geophysics*, 86(1), 37-54, 10.1190/GEO2019-0783.1.

Shah, M.; Sircar, A.; Vaidya, D.; Sahajpal, S.; Chaudhary, A. and Dhale, S. 2015. Overview of Geothermal Surface Exploration Methods. IJARIIE – ISSN (0) – 2395 – 4396, 1(4), 55 – 64. (www. ijariie.com)

Shaole, A.; Zhixin, Z.; Kefa, Z. & Jinlin, W. (2021). Subsurface structures of the Xiaorequanzi deposit, NW China: New insights from gravity, magnetic and electromagnetic data. *Geophysical prospecting*, 69(02), 434-447.

Sharma, P. V.(1987). Magnetic Method Applied to Mineral Exploration. *Ore Geology*. Review, 2, 323-357.

Sharma, P. V. (2004). Environmental and engineering geophysics (p. 475). Cambridge: Cambridge University Press.

Shuey, R.T.; Schellinger, D.K.; Tripp, A.C. and Alley, L.B.(1997). Curie depth determination from aeromagnetic spectra: Geophysical *Journal of the Royal Astronomical Society*. 50, 75-101.

Singh, A. and Harrison, A. (1985). Standardized Principal Components. *International Journal of Remote Sensing*, 6, 883-896.

Smith, R.S.; Thurston, J.G.; Dai, T.F. & Macleod, I.N.(1998). SPI-The Improved Source Parameter Imaging Method. *Geophysics Prospects*. 46:141-151.

Spector, A. & Grant, F.S. (1970). Statistical Models for Interpreting Aeromagnetic Data. *Geophysics*,35, 293-302.

Stampolidis, A., Kane, I., Tsokas, G.N. & Tsourlos, P., 2005. Curie point depths of Albania inferred from ground total field magnetic data. Surv. *Geophys.* 26, 461– 480.

Stanton, R.L. (1972). Ore petrology, New York: McGraw-Hill.

Suleiman, T.; Okeke, F. N.; Obiora, N.D. & Tunga, U.S.(2020). Review of Combined Magnetic and Radiometric Methods of Geophysical Survey in Nigeria, *International Journal of Earth Science and Geophysics*, 6(32), DOI: 10.35840/2631-5033/1832.

Sulemana, I.A; Quaye-Ballard, J.; Ntori, C.; Awotwi, A.; Okrah, M.T & Asare-Ansah, A.(2020).Location Mappimg of Hydrothermal Alteration Using Landsat 8 Data: A Case Study in Prestea Huni Valley District, Ghana. *International Journal of Geography and Geology, Conscientia Beam*, 19(1), 13-37.

Taiwo, A.M.; Towolawi, A.T; Olanigan, A.A; Olujimi, O.O & Arowolo, T.A.(2015). Comparative Assessment of Groundwater Quality in Rural and Urban Areas of Nigeria. Research and Practices in Water Quality, Teang Shui Lee, In Tech Open, DOI: 10.5772/59669.

Tanaka, A.; Okubo, Y. & Matsubayashi, O. (1999). Curie Point Depth based on Spectrum Analysis of the Magnetic Anomaly Data in East and South East Asia. T*ectonophysics* 306, 461-470.

Tattam, C. M. (1930). Geophysical investigation upon the lead-zinc lodes of Ogoja Province. *Geological Survey of Nigeria, Annual Report*., 14-23.

Telford, W.M.; Geldart, L.P.; Sheriff, R.E & Keys, D.A. (1990).Applied Geophysics (Second Edition: Cambridge University Press, pp. 344-536.

Tesfaye, K.M. (2004). Interpretation and Geodatabase of Dykes using Aeromagnetic Data of Zimbabwe and Mozambique. International Institute for Geo-Information Science, Earth Observation

Enschede, the Netherlands.

Thompson, D.T. (1982). EULDPH: A new technique for making computer-assisted depth estimates from magnetic data. *Geophysics*, 47, 31–37.

Tissot, B.P & Welte, D.H. (1978). Petroleum formation and occurrence: A new approach to oil and gas exploration, XVIII +5385, 241 Abb., 70 Tab. Berlin-Heidelberg-New York1978. Springer-Verlag. DM 7900.

Tompolidi, A-M.; Sykioti, O, Koutroumbas, K & Parcharidis, I. (2020). Spectral Unmixing for Mapping a Hydrothermal Field in a Volcanic Environment Applied on ASTER, Landsat-8/OLI, and Sentinel-2 MSI Satellite Multispectral Data: The Nisyros (Greece) Case Study *Remote Sens*., 2020, 12, 4180; doi:10.3390/rs12244180.

Turcotte, D.L.& Schubert, G. (1982). *Geodynamics.* Cambridge University Press, New York.

Ugwu, G.Z.; Ezema, P.O. & Ezeh, C.C (2013). Interpretation of aeromagnetic data over Okigwe and Afikpo areas of the Lower Benue Trough, Nigeria. *International Research Journal of Geology and Mining* (IRJGM) (2276-6618), 3(1), 1-8.

Ugwu, G.Z. and Ezema, P.O. (2014). Geophysical investigation for locating buried iron slag at Lejja, Enugu State, Nigeria. *Journal of Natural Science, 2(1),* ISSN 2308-5061. www. Journal-of-natural science. Darsghah-e-ahlebait.com.

Uma, K.O; Onuoha, K.M & Egboka, B.C. (1990). Hydrochemical facies, groundwater flow pattern and origin of saline waters in parts of the western flank of the Cross River basin, Nigeria. In: *The Benue Trough, Structure and Evolution.* (ed. C.O.Ofoegbu), 115-134; Braunschweig, Vieweg.

Uma, K.O. & Loehnert, E.P (1992). Research on the Saline Groundwaters in the Benue Trough, Nigeria: Preliminary Results and Projections. Zbl. *Geol. Palaont. Teil I, H*. 11, 2751-2756, Stuttgart.

Uma, K.O. (1998). The Brine Fields of the Benue Trough, Nigeria: A Comparative Study of Geomorphic, Tectonic and Hydrochemical Properties. *Journal of African Earth Sciences. 26(2), 261-275.*

Umeji, A.C. & Caen-Vachette, M. (1983). Rb-Sr Isochron from Gboko and Ikyen Rhyolites and its Implications for the age and Evolution of the Benue Trough, Nigeria. *Geol. Mag.,* 120, 529-533.

Umeji (1988). Trace fossils from Eze-Aku formation (Turonian) Sotheastern Nigeria. *Journal of mining and geology.* 24 (1&2). 79-80.

Umeji, A.C.(2000) Evolution of the Abakaliki and Anambra sedimentary basins southeastern Nigeria. A report submitted to the shell Petrol. Dev. Co. Nig Ltd 147.

Ward, S.H. (1990). Resistivity and Induced PolarizationMethods. In: WARD,S.H.(Ed.): Geotechnical and Environmental Geophysics, I: Review and Tutorial. *Societyof Exploration Geophysics,* Tulsa Okhlahoma, 147-189.

Watanabe, H. & Matsuo, K. (2003). Rock type Classification by Multi-Band TIR of ASTER, *Geoscience Journal*, 7(4),347-358.

Whitmarsh, R.B., Manatschal, G. & Minshull, T.A. (2001). Evolution of Magma poor Continental margins from rifting to seafloor spreading, *Nature,* 413(6852), 150-154.

Wilford, J.R., Bierwirth, P.N. & Craig, M.A. (1997). Application of airborne gamma-ray spectrometry in soil/regolith mapping and applied geomorphology, *AGSO Journal of Australian Geology and Geophysics*, 17, 201-216.

Wilson, P.A. (1997). Rule Based Classification of Water in Landsat MSS Images, Using Variance Filter, *Photogrammetric Engineering and Remote Sensig.* 63(5), 485-491.

Wright, J.B. (1968). South Atlantic Continental Drift and the Benue Trough. *Tectonophysics.* 6(4):301-310.

Wright, P.M. (1981). Gravity and Magnetic Methods in Mineral Exploration, *In Skinner, B.J, ed., Economic Geology,* 75th Anniversary.829-839.

Youssef, M.A.S & Shadia T. E. (2013). Utilization of airborne gamma ray spectrometric data for geological mapping, radioactive mineral exploration and environmental monitoring of southeastern Aswan city, Southeastern Desert, Egypt, *Geophys. J. Int.,* 195, 1689–1700 doi: 10.1093/gji/ggt375.

Ziegler, P.A. (1992). Plate tectonics, plate moving mechanisms and rifting. In: P.A. Ziegler (Ed.), Geodynamics of Rifting , vol.III. Thematic Discussions, *Tectonophysics*, 215, 9-34.

APPENDICES

I - OTHER LANDSAT RATIOS AND THEIR RATIO COMPOSITES

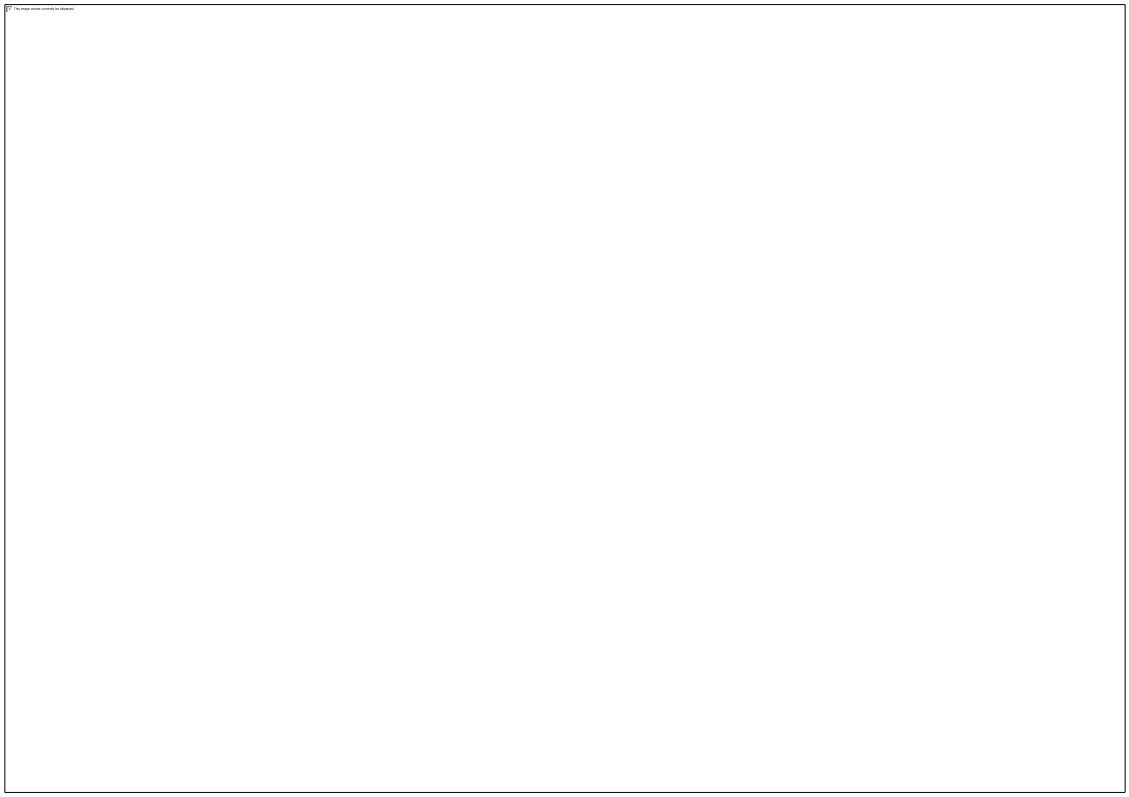

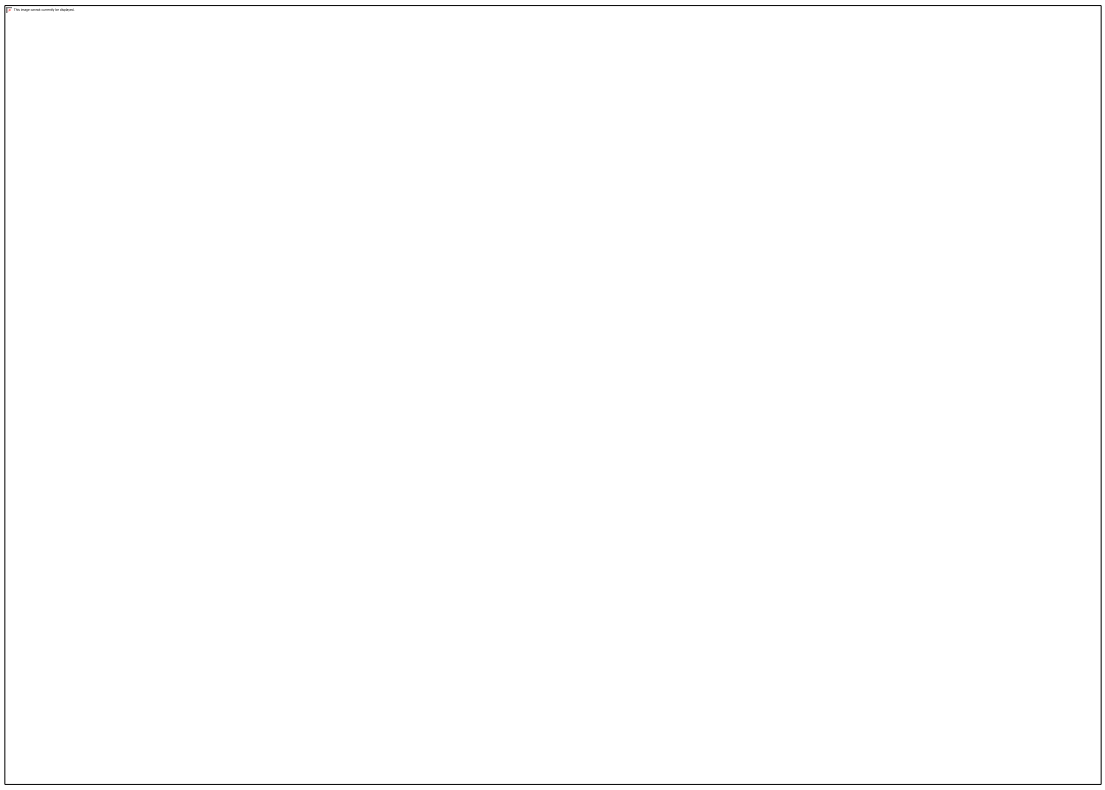

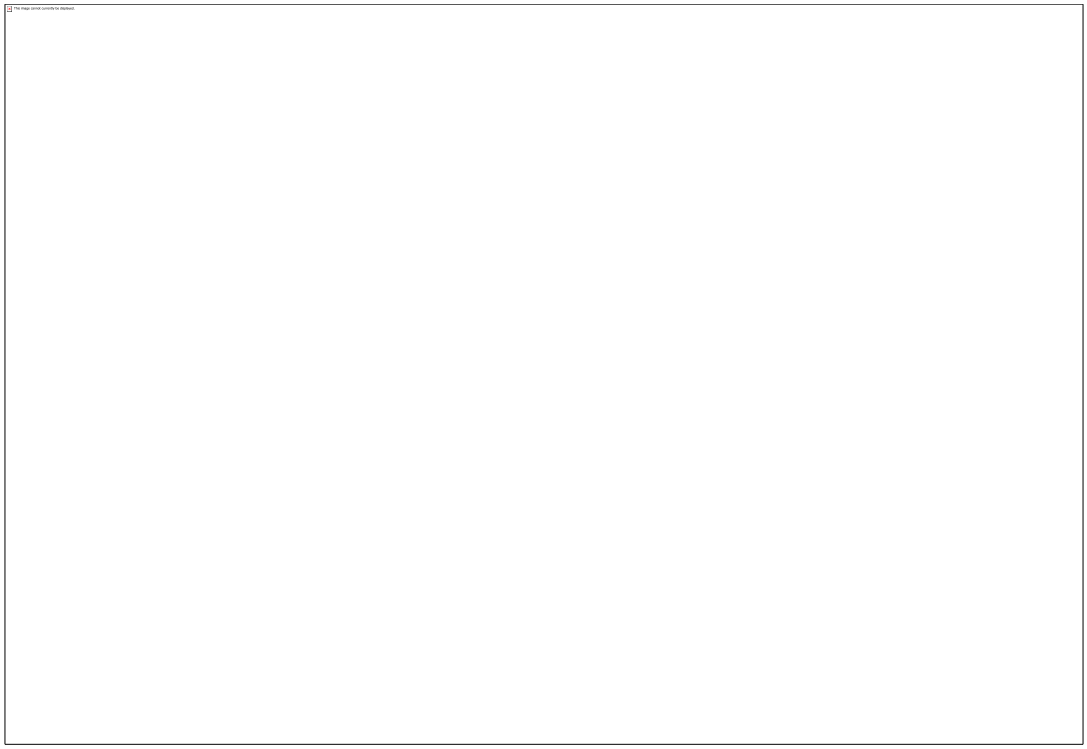

TWEAKED SABIN'S RATIO

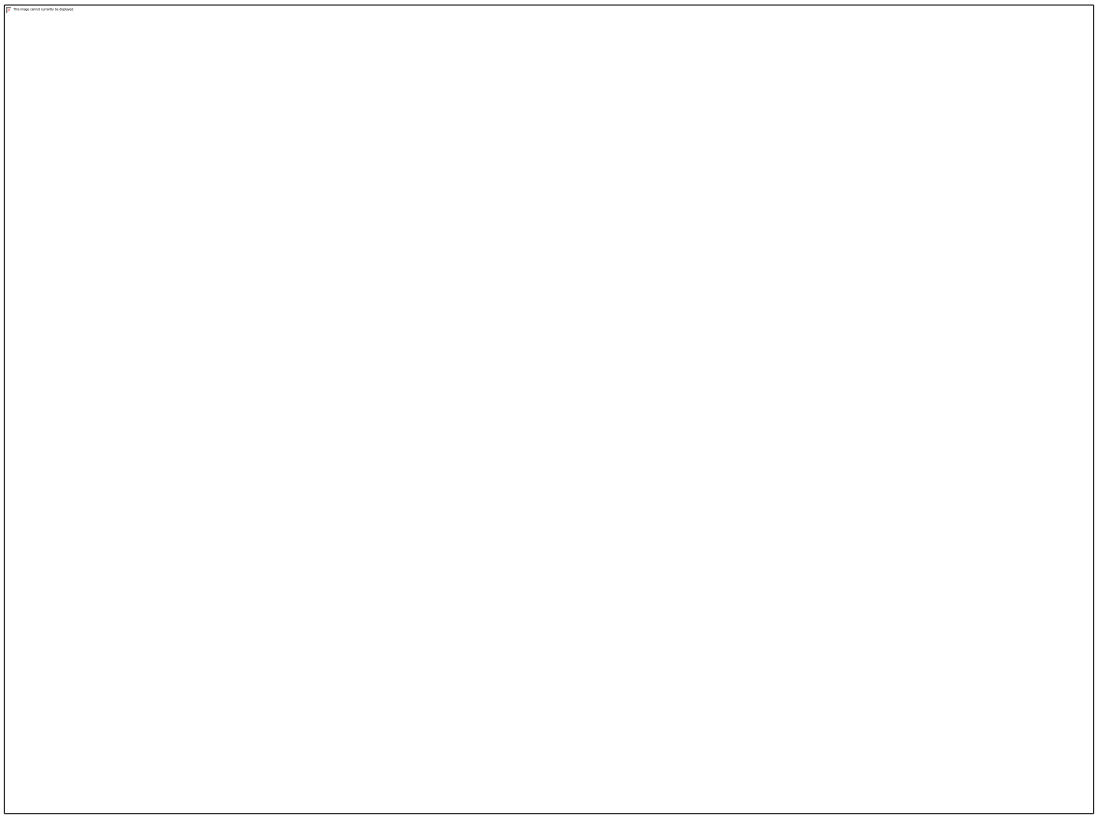

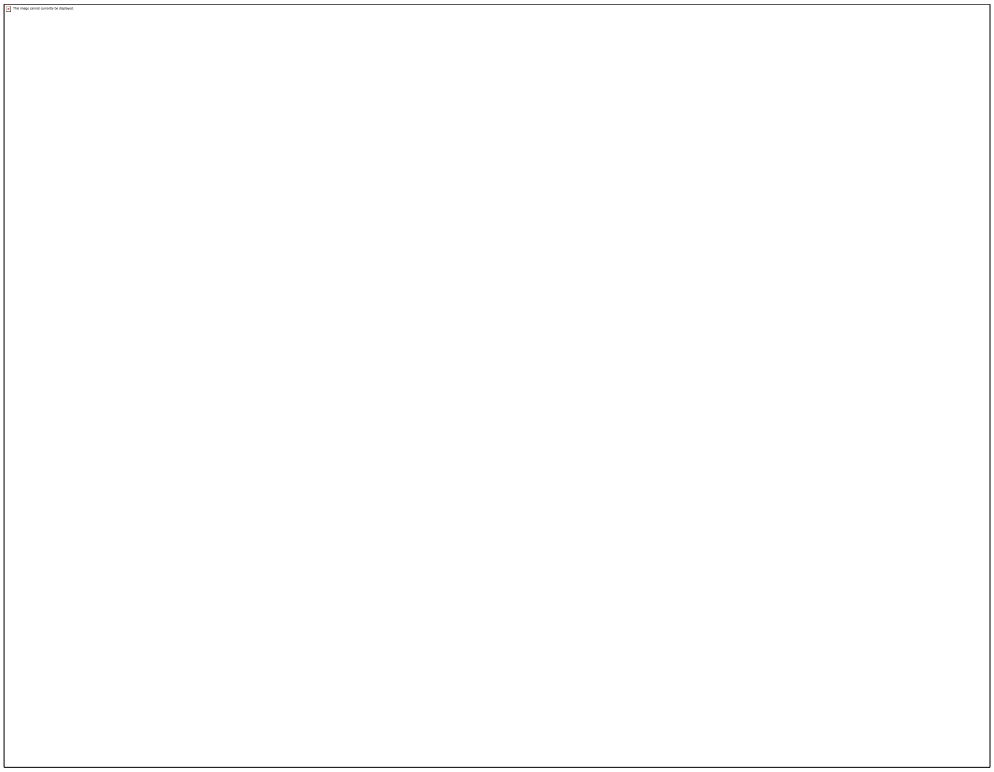

PCA IRON AND CLAY RATIO PLOTS

II - SPECTRAL PLOTS

35 SPECTRAL PLOTS USED TO CALCULATE DEPTH TO THE TOP OF MAGNETIC SOURCES

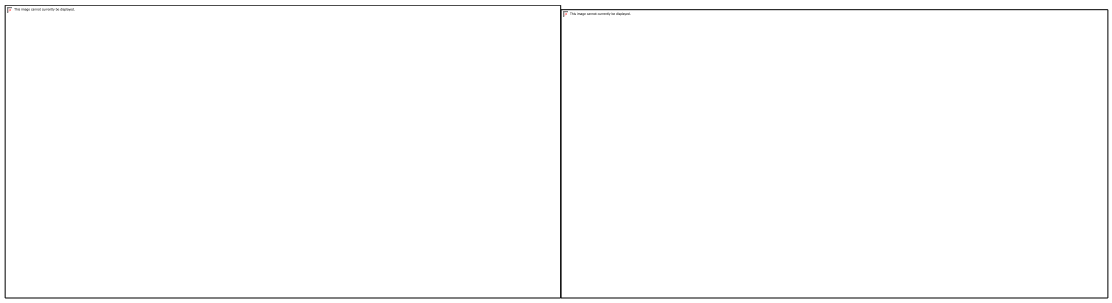

(i) (ii)

(iii)

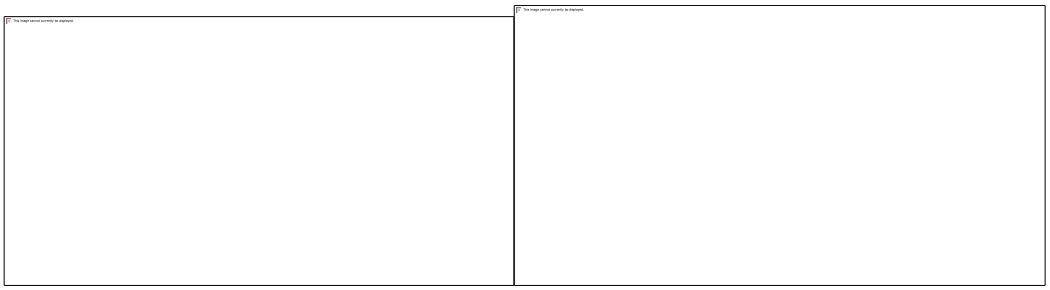

(iv)

(v)

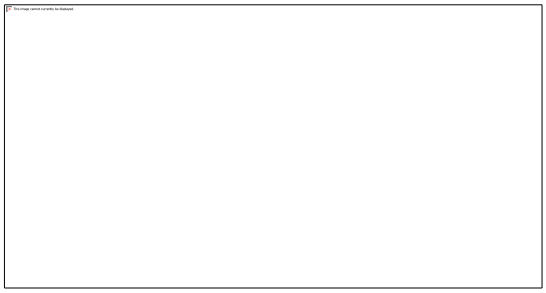

(vi)

(vii)

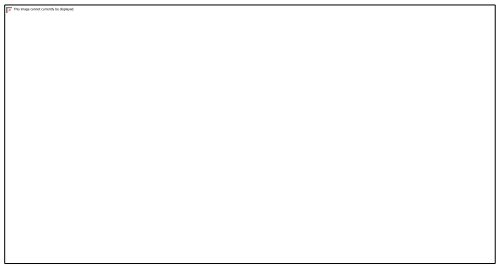

(viii)

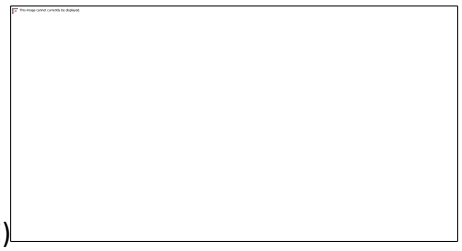

(ix)

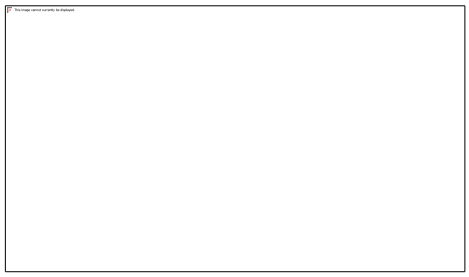

(x)

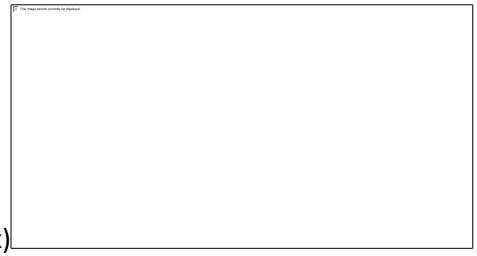

(xi) 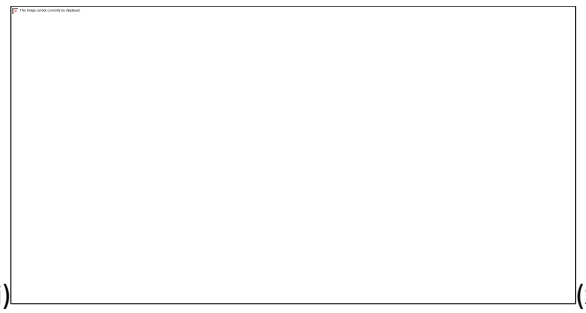

(xii) 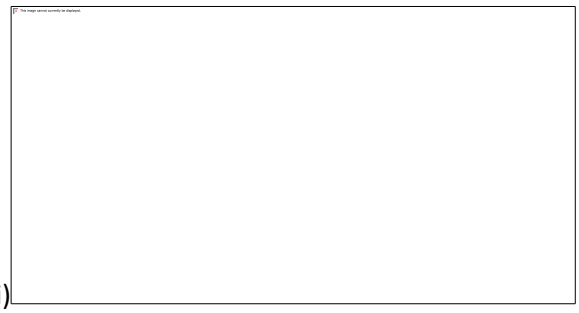

(xiii) 

(xiv) 

(xv) 

(xvi) 

(xvii) 

(xviii) 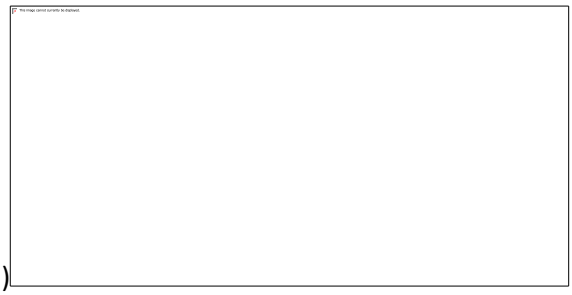

(xix) 

(xx) 

(xxi) 

(xxii) 

(xxiii) 

(xxiv) 

(xxv) 

(xxvi) 

(xxvii) 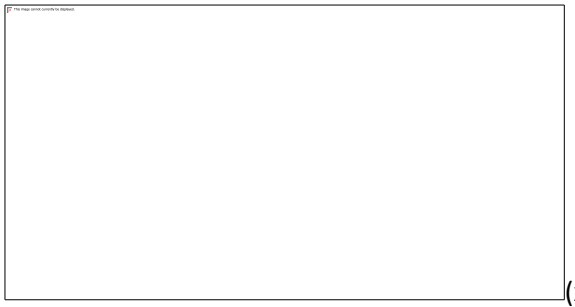

(xxviii) 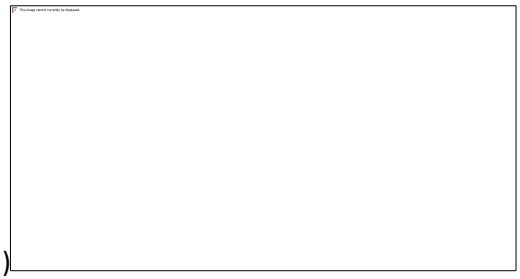

(xxix) 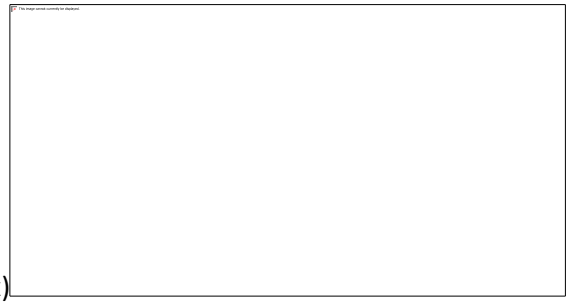

(xxx) 

(xxxi) 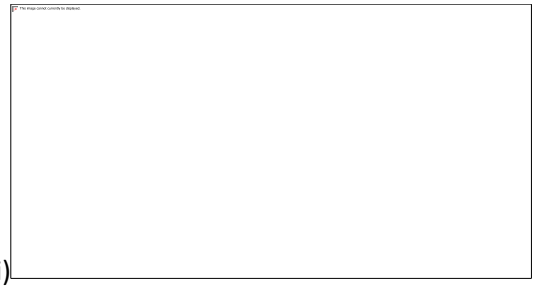

(xxxii) 

(xxxiii) 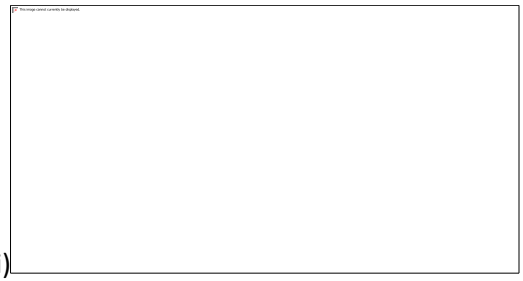

(xxxiv) 

(xxxv) 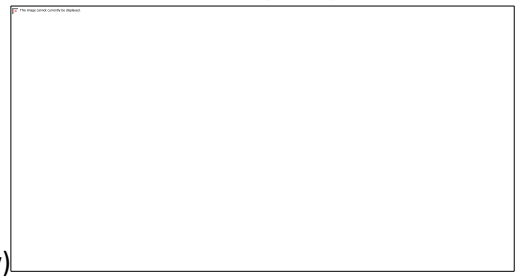

SPECTRAL PLOTS USED TO CALCULATE DEPTH TO THE CENTROID OF MAGNETIC SOURCES

(i) 

(ii) 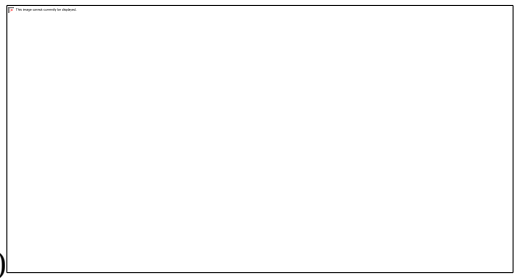

(iii) 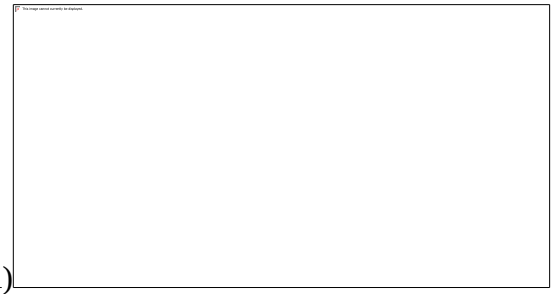

(iv) 

(v) 

(vi) 

(vii) 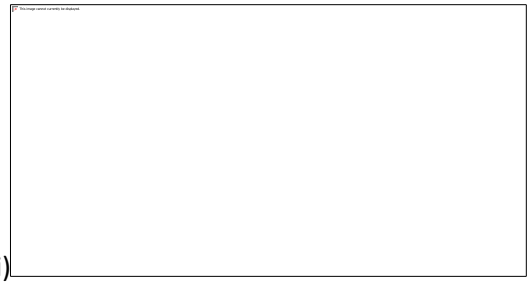

(viii) 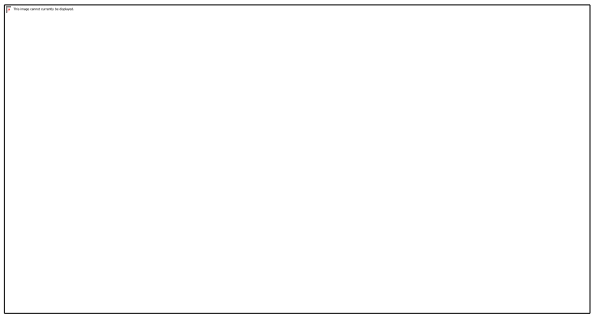

(ix) 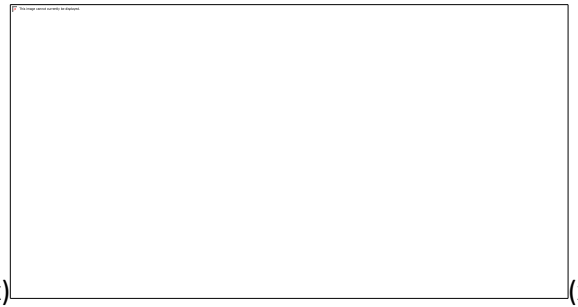

(x) 

(xi) 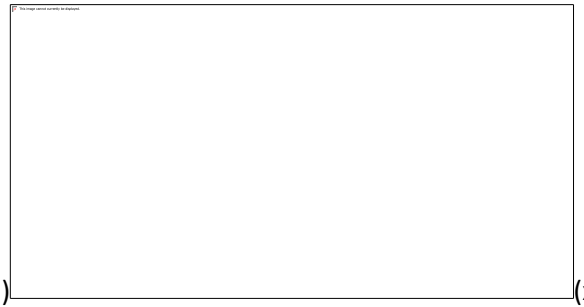

(xii) 

(xiii) (xiv)

(xv) 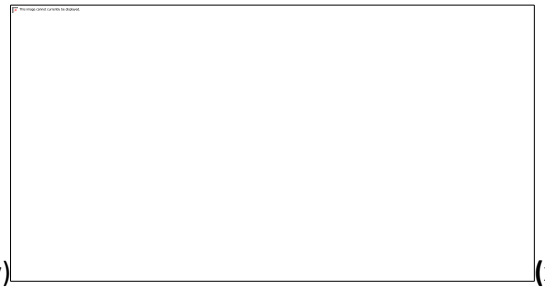

(xvi) 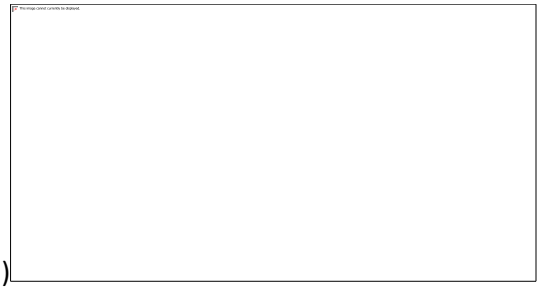

(xvii) 

(xviii) 

(xix) 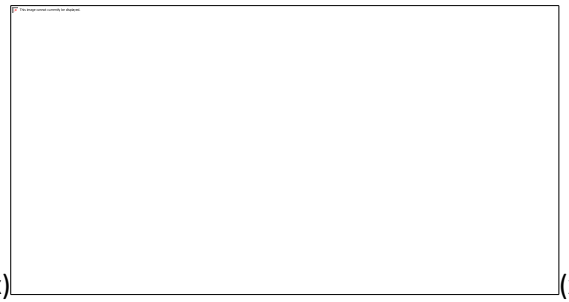

(xx) 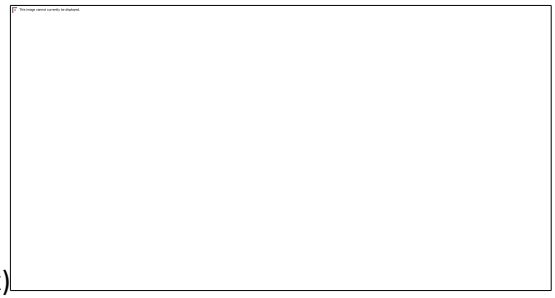

(xxi) 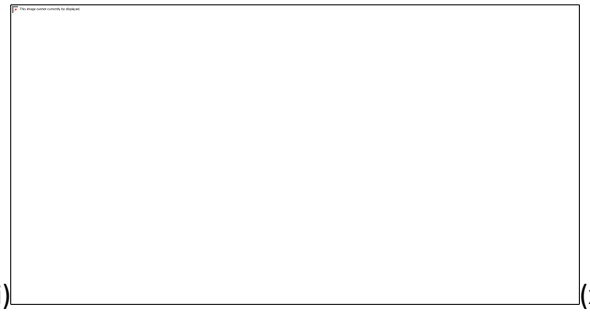

(xxii) 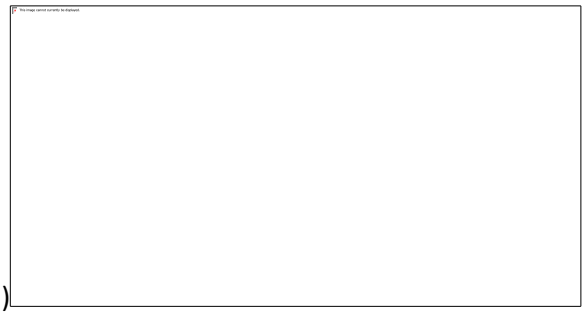

(xxiii) 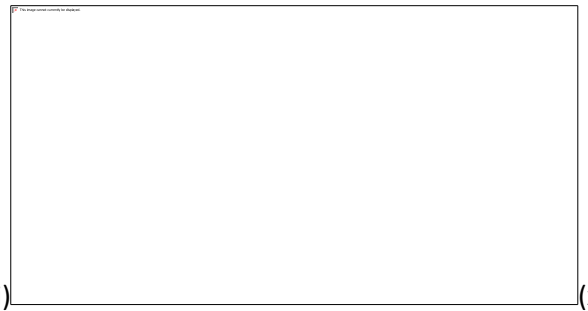

(xxiv) 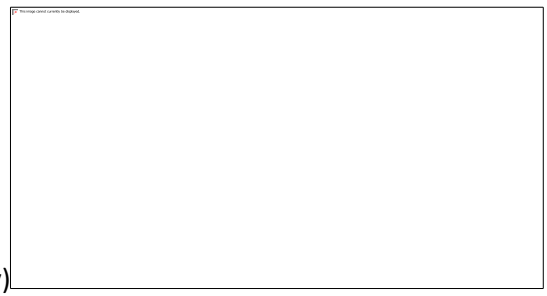

(xxv) 

(xxvi) 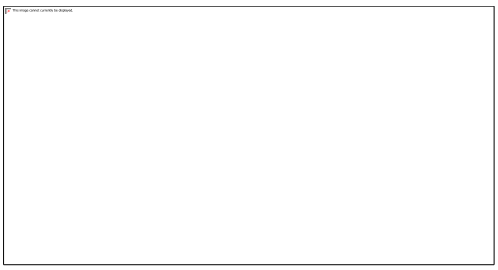

(xxvii) 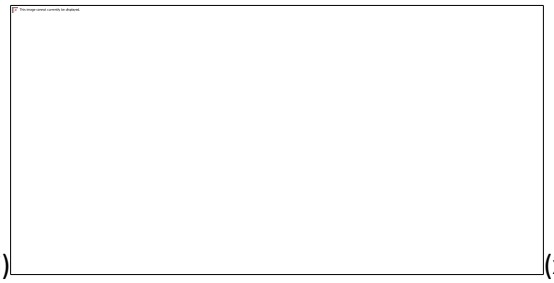

(xxviii) 

(xxix) 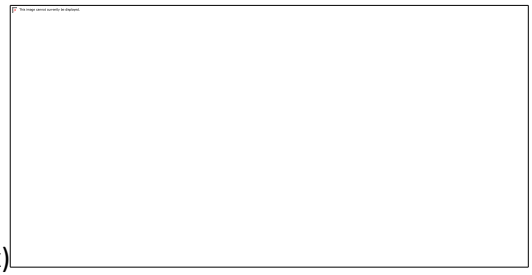

(xxx) 

(xxxi) 

(xxxii) 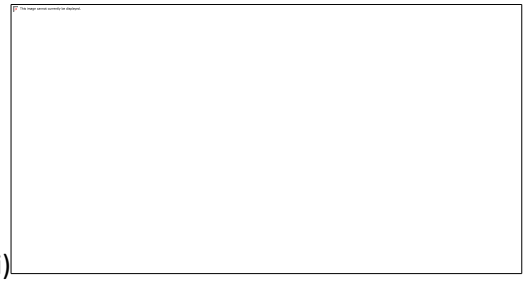

(xxxiii) 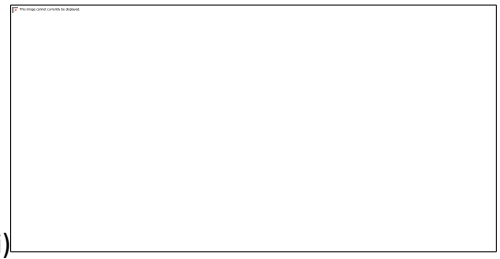

(xxxiv) 

(xxxv) 

III – EULER SOLUTION

3D EULER DEPTH SOLUTION FOR SI = 2

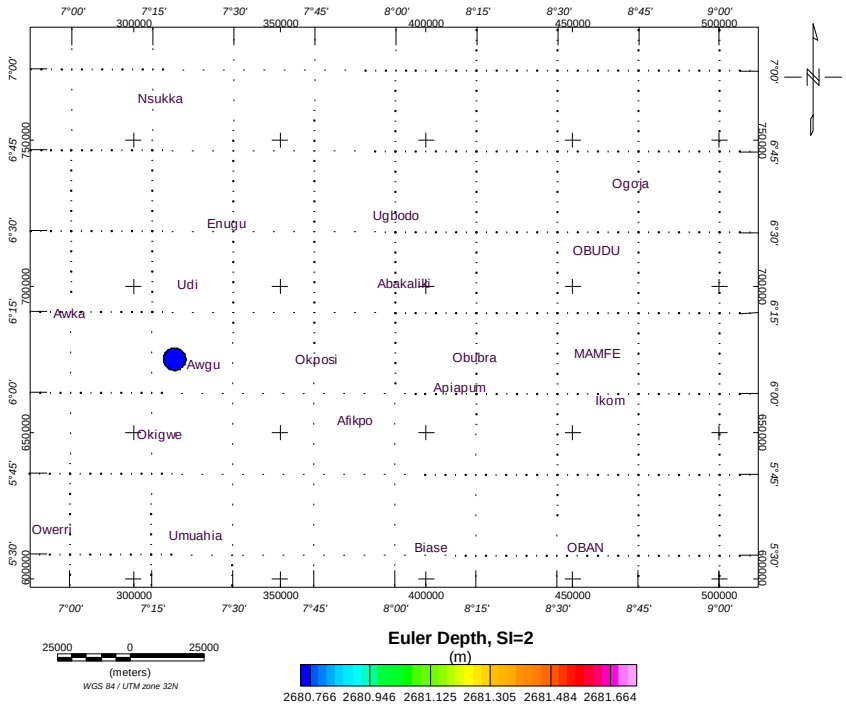

IV – FIRST VERTICAL DERIVATIVE WITH SUPER IMPOSED LINEAMENTS


This image cannot currently be displayed.